Effects of Aging on the Cyclic Stress Strain and Fatigue Behaviors of Lead-free Solders

by

Muhannad Mustafa

A dissertation submitted to the Graduate Faculty of
Auburn University
in partial fulfillment of the
requirements for the Degree of
Doctor of Philosophy

Auburn, Alabama
August 2, 2014

Keywords: Lead-free Solder, Aging, Fatigue, Finite Element Modeling, Microstructure, Constitutive Modeling

Approved by

Jeffrey C. Suhling, Chair, Quina Distinguished Professor of Mechanical Engineering
Pradeep Lall, Thomas Walter Professor of Mechanical Engineering
Hareesh V. Tippur, McWane Professor of Mechanical Engineering
Michael J. Bozack, Professor of Physics

Abstract

The microstructure, mechanical response, and failure behavior of lead free solder joints in electronic assemblies are constantly evolving when exposed to isothermal aging and/or thermal cycling environments. While the effects of aging on solder constitutive behavior (stress-strain and creep) have been examined in some detail, there have been no prior studies on the effects of aging on solder failure and fatigue behavior. Aging leads to both grain and phase coarsening, and can cause recrystallization at Sn grain boundaries. Such changes are closely tied to the damage that occurs during cyclic mechanical loading.

In this investigation, the effects of aging on the cyclic stress-strain and fatigue behaviors of lead free solders have been investigated. Solder test specimens (SAC105 and SAC305) have been prepared and subjected to cyclic stress/strain loading for various prior aging conditions. Both uniaxial specimens subjected to cyclic tension/compression and Iosipescu lap shear samples subjected to cyclic positive/negative shear have been studied. A four-parameter hyperbolic tangent empirical model has been used to fit the entire cyclic stress-strain curve, and the hysteresis loop size (area) was calculated using definite integration for a given strain limit. This area represents the energy dissipated per cycle, which can be correlated to the damage accumulation in the joint. Samples were subjected to cyclic loading over a particular strain range until fatigue failure occurred, and then various popular empirical failure criteria such as the Coffin-Manson model and

the Morrow model have been used to estimate the fatigue life. Fatigue failure was defined to occur when there was a 50% peak load drop during mechanical cycling.

Prior to testing, the specimens were aged (preconditioned) at 125 C for various aging times, and then the samples were subjected to cyclic loading at room temperature (25 C). It has been observed that aging decreases the mechanical fatigue life, and the effects of aging on the peak load drop have been studied. It has also been observed that degradations in the fatigue/failure behavior of the lead free solders with aging are highly accelerated for lower silver content alloys (e.g., SAC105). From the recorded cyclic stress-strain curves, the evolution of the solder hysteresis loops with aging have been characterized and empirically modeled. Similar to solder stress-strain and creep behavior, there were strong effects of aging on the hysteresis loop size. Comparisons have been made between isothermal uniaxial fatigue life and shear fatigue life and good agreement has been found. A microstructural adaptive fatigue model has been proposed that includes aging effects via consideration of grain/sub-grain coarsening, recrystallization, and IMC particle growth.

Acknowledgments

It is indeed a great pleasure and proud privilege for the author to express his deepest sense of sincere thanks and gratitude to his major advisor Dr. Jeffrey C. Suhling for his continuous guidance, supervision and untiring support that were a constant source of inspiration throughout this research work. The author also would like to his appreciation to his advisory committee members including Dr. Hareesh V. Tippur, Dr. Pradeep Lall, Dr. John L. Evans, and Dr. Michael J. Bozack for their insightful instruction and discussion regarding this research. Special thanks are also extended to all my co-workers and friends, Dr. Zijie Cai, Jordan Roberts, Dr. Mohammad Motalab, Nusrat Jahan Chhanda, Safina Hussain, Kun-yen Wang, Md. Hasnine, Munshi Mahbubul Basit, Sudan Ahmed, Promod Roy Chowdhury, Nianjun Fu, Michael Palmer, and John Marcell for their help, encouragement, and friendship.

The author is in debt to his parents Dr. A. K. M. Golam Mustafa and Dr. Shamsun Nahar Begum for their endless love and support to his life and study. Lastly, the author solemnly dedicates this dissertation and all achievements in pursuit of his doctoral degree to his wife Nusrat Jahan Chhanda and daughter Ajrin Jahan Muhannad, for their endurance, perseverance, and heartfelt consideration.

Table of Contents

Abstract ii
Acknowledgments iv
List of Figures x
List of Tables xvii
CHAPTER 1
INTRODUCTION AND GENERAL SCIENCE 1
1.1 Lead Free Electronics: Overview 1
1.2 Sn-Ag-Cu Solder Alloy as Popular Choices 4
1.3 Mechanical Properties of Solder Materials 8
1.3.1 Tensile 8
1.3.2 Creep 11
1.3.3 Shear 14
1.3.4 Fatigue 15
1.3.5 Cyclic Stress-Strain Behavior 18
1.4 Micro-structural Damage Mechanisms 19
1.4.1 Dislocation 19
1.4.2 Slip 22
1.4.3 Plasticity 23
1.5 Objectives of This Research 25
1.6 Organization of the Dissertation 26
CHAPTER 2
LITERATURE REVIEW 28
2.1 Introduction 28
2.2 Aging Effects on Solder Material Properties 28
2.3 Effect of Fabrication and Testing Conditions on Solder Material Properties 35
2.4 Cyclic Stress-Strain Behavior of Solder Materials 36
2.5 Isothermal and Thermomechanical Fatigue Criteria for Solder Materials 39
2.6 Summary and Discussion 43

CHAPTER 3

SPECIMEN PREPARATION AND EXPERIMENTAL TESTING 46

3.1 Introduction 46

3.2 Uniaxial Test Specimen Preparation Procedure 46

3.3 Mechanical Testing System 52

3.4 Load Train Calibration 54

3.5 Summary and Discussion 55

CHAPTER 4

EMPIRICAL MODELS FOR UNIAXIAL AND CYCLIC STRESS STRAIN BEHAVIOR OF SOLDER MATERIALS 56

4.1 Introduction 56

4.2 Overview: Uniaxial Stress-Strain Relationship 56

4.3 Existing Stress-Strain Models for Viscoplastic Materials 58

4.3.1 J-C Model 59

4.3.2 Z-A Model 60

4.3.3 K-H Model 61

4.3.4 Anand Model 62

4.3.5 Other Models 63

4.4 Hyperbolic Tangent Empirical Model for Solder Stress-Strain Behavior 64

4.5 Calculation of Hysteresis Loop Area 73

4.6 Summary and Discussion 75

CHAPTER 5

EFFECTS OF AGING ON CYCLIC STRESS-STRAIN BEHAVIOR OF LEAD FREE SOLDER MATERIALS 76

5.1 Introduction 76

5.2 Overview of Cyclic Stress-Strain Behavior 77

5.3 Hysteresis Loop During Cyclic Loading 78

5.4 Effects of Aging for Strain Controlled Cyclic Testing 80

5.5 Effects of Aging for Stress Controlled Cyclic Testing 95

5.6 Comparisons of Hysteresis Loops for Different SAC Alloys 102

5.7 Effects of Testing Temperature on Hysteresis Loop Size 105

5.8 Summary and Discussion 108

CHAPTER 6

EFFECTS OF AGING ON THE UNIAXIAL FATIGUE BEHAVIOR OF LEAD FREE SOLDER MATERIALS 110

6.1 Introduction 110
6.2 Fatigue Phenomena 111
6.3 Fatigue Life Prediction 113
6.4 Fatigue Test Matrix Description 118
6.5 Evolution of Hysteresis Loops during Cyclic Loading 119
6.6 Effects of Aging on Fatigue Life 122
6.7 Effects of Silver Content on Fatigue Life of Lead-free Solder 133
6.8 Effects of Solidification Temperature Profile on the Fatigue Life 136
6.9 Reduction of the Fatigue Life of SAC Solder for Long-term Aging 142
6.10 Summary and Discussion 144
CHAPTER 7
SHEAR SPECIMEN PREPARATION AND DEVELOPMENT OF EXPERIMENTAL TEST SYSTEM 145
7.1 Introduction 145
7.2 Shear Specimen Design 146
7.3 Finite Element Analysis of Shear Specimens 148
7.3.1 Ball Shear Specimen 148
7.3.2 Lap Shear Specimen (Iosipescu Shear Specimen) 155
7.4 Design and Development of a Mold Assembly for Specimen Preparation 165
7.5 Procedure for Iosipescu Shear Sample Preparation 167
7.5.1 Surface Polishing 168
7.5.2 Surface Cleaning 168
7.5.3 RMA Flux 168
7.5.4 Placing Materials in the Mold Assembly 168
7.5.5 Reflow Soldering 170
7.5.6 Inspection and Measurement of Joint Dimension 171
7.6 Mechanical Testing System 173
7.7 Load Train Calibration 174
7.8 Shear Cyclic Stress-Strain Data Processing 178
7.9 Summary and Discussion 179
CHAPTER 8
EFFECTS OF AGING ON SHEAR CYCLIC STRESS-STRAIN AND FATIGUE BEHAVIOR OF LEAD FREE SOLDERS 180
8.1 Introduction 180
8.2 Test Matrix Description 180

8.3 Effects of Aging on Shear Cyclic Stress Strain Behavior 181
8.4 Effects of Aging on the Shear Fatigue Behavior 187
8.5 Equivalency Between Uniaxial and Shear Fatigue Data 193
8.6 Summary and Discussion 199
CHAPTER 9
MICROSTRUCTURE BASED FATIGUE MODEL INCLUDING AGING EFFECTS 200
9.1 Introduction 200
9.2 Review of Available Fatigue Models 202
9.2.1 Plastic Strain Fatigue Models 204
9.2.2 Creep Strain Fatigue Models 205
9.2.3 Energy-based Fatigue Models 206
9.2.4 Damage Fatigue Models 207
9.3 Microstructural Damage Evolution 207
9.4 Microstructural Adaptive Fatigue Model 215
9.4.1 Aging Induced Fatigue Model 216
9.4.2 Derivation of Shift Function 216
9.4.3 Grain/Sub-grain Coarsening during Static Annealing [233] 217
9.4.4 Grain/Sub-Grain Coarsening during Plastic Deformation [233] 218
9.4.5 Determination of Material Constants 222
9.5 Band of Fatigue Life 222
9.6 Relation between Isothermal Fatigue Life and Thermal Fatigue Life 230
9.7 Application of Isothermal Fatigue Data in Reliability Prediction 231
9.8 Summary and Discussion 234
CHAPTER 10
SUMMARY AND CONCLUSIONS 235
10.1 Empirical Model for Uniaxial and Cyclic Stress-strain Behavior for Solder Material 235
10.2 Effects of Aging on Cyclic Stress-strain behavior for Lead-free Solder Materials… 235
10.3 Effects of Aging on Fatigue behavior for Lead-free Solder Materials 237
10.4 Shear Specimen Preparation and Development of Experimental Set-up 238
10.5 Effects of Aging on Shear Cyclic Stress-Strain and Fatigue Behaviors for Lead-free Solder Materials 239
10.6 Microstructure Based Fatigue Model including Aging Effects 240

10.7 Conclusions 240
REFERENCES 242
APPENDIX A 262
OTHER PROPOSED EMPIRICAL MODELS FOR VISCOPLASTIC STRESS-STRAIN BEHAVIOR FOR SOLDER ALLOYS 262
A.1 Model #1: Hyperbolic Tangent Model with Linear Term 262
A.2 Model #1: Non-linear Regression Fit 262
A.3 Model #2: Polynomial Hyperbolic Tangent Model 263
A.4 Model #2: Non-linear Regression Fit 263
A.5 Model #2: Examples (4^{th} Order Polynomial) 265
A.6 Model #2: Examples (4^{th} Order Polynomial) for True Stress-Strain Behavior 266
A.7 Model #3: Dual Polynomial Hyperbolic Tangent Model 267
A.8 Model #3: Non-linear Regression Fit 267
APPENDIX B 269
COMPUTER CODE IN MATLAB 269
B.1 Example Code For Calculation of Area of Hysteresis Loop 269
B.2 Example Code For Determination of Peak Cyclic Stress 275

List of Figures

Figure 1.1 Lead Free Solder Market Share [13] 4

Figure 1.2 Prevailing Lead Free Choices and Their Applications 5

Figure 1.3 Sn-Ag-Cu Ternary Phase Diagram 7

Figure 1.4 SEM Micrograph of Typical Sn-Ag-Cu Solder [21] 7

Figure 1.5 Typical Stress-Strain Response for Ductile Materials 10

Figure 1.6 Typical Creep Response for Ductile Materials 12

Figure 1.7 Creep Deformation Mechanism Map for Eutectic Sn-Pb Solder [28] 13

Figure 1.8 Typical Shear Stress-Strain Response for Ductile Materials 15

Figure 1.9 Depiction of the Effects of the Accumulating Fatigue Damage [32] 16

Figure 1.10 Typical S-N Curve for Ductile Materials 17

Figure 1.11 Schematic Representation of the fatigue process [34] 18

Figure 1.12 Cyclic Stress-Strain behavior of Alloys (a) Cyclic hardening (b) Cyclic Hardening and Softening (c) Cyclic softening 19

Figure 1.13 Crystal Lattice showing Atoms and Lattice Planes 20

Figure 1.14 Schemes of (a) Edge Dislocation (b) Screw Dislocation 21

Figure 1.15 Edge dislocation caused by an extra partial plane of atoms in the crystal 21

Figure 1.16 Scheme of Screw Dislocation 22

Figure 1.17 Schematic View of Slip Mechanism 23

Figure 1.18 Plasticity Under a Spherical Nanoindenter in (111) Copper. 24

Figure 2.1 Partial Deformation Behavior in aged Sn3.5Ag Specimen 30

Figure 2.2 Degradation of the Material Properties of SAC405 Under 31

Figure 2.3 Effect of Dopants on the Evolution of Creep Rate with Aging (SACX, SAC105, SAC205, Aging up to 6 Months) 34

Figure 2.4 Distribution of IMC Particles in SACX before/after Aging [21] 34

Figure 2.5 As-Solidified Macrostructures of SAC387 [60] 36

Figure 2.6 Isothermal and Thermal Cycling Hysteresis Loops at N near 0.5 N_f [65] 38

Figure 3.1 Specimen Preparation Hardware 48

Figure 3.2 Specimen Cooling/Reflow Profiles 50

Figure 3.3 Heller 1800EXL Reflow Oven 51

Figure 3.4 Solder Uniaxial Test Specimens 51

Figure 3.5 X-Ray Inspection of Solder Test Specimens (Good and Bad Samples) 52

Figure 3.6 MT-200 Testing System with Solder Sample 54

Figure 4.1 Uniaxial stress-strain diagrams: (a) low-carbon steel curve, (b) conventional definition of yield-point stress on stainless steel curve, (c) stress-strain curve of aluminum with effects of unloading and reverse loading 57

Figure 4.2 Typical Trend of Stress-strain Curve for Viscoplastic Solder Material 67

Figure 4.3 Non-linear Regression Fit of Experimental Data of SAC405 Solder Alloy Using Hyperbolic Tangent Model with Different Hyperbolic Tangent Terms 68

Figure 4.4 Non-linear Regression Fits to Experimental Data for Different Types of Solder Alloys Using the Two Term Hyperbolic Tangent Model 70

Figure 4.5 Comparisons of Regression Fits for Different Empirical Models 72

Figure 4.6 SAC105 Stress-Strain Curves and Empirical Model 72

Figure 4.7 Typical Cyclic Stress-Strain Test Results for 74

Figure 4.8 Typical Hysteresis Loop and Area Calculation 75

Figure 5.1 Typical Cyclic Stress-Strain Test Results for 79

Figure 5.2 Variation of Hysteresis Loop Area with Number of Cycles 79

Figure 5.3 Strain Limit Controlled Cyclic Test 81

Figure 5.4 Stress Limit Controlled Cyclic Test 81

Figure 5.5 Hysteresis Loops for Cyclic Stress-Strain Testing 85

Figure 5.6 Hysteresis Loops for Cyclic Stress-Strain Testing 86

Figure 5.7 Variation of the Hysteresis Loop Area with Aging 87

Figure 5.8 Reduction of Solder Material Strength Due to Aging (SAC105, RF) 89

Figure 5.9 Evolution of Hysteresis Loop Due to Damage Accumulation in the Material for both Stress and Strain Controlled Cyclic Tests 89

Figure 5.10 Hysteresis Loops for Cyclic Stress-Strain Testing 93

Figure 5.11 Variation of the Hysteresis Loop Area with Aging 94

Figure 5.12 Comparison of Hysteresis Aging Behaviors of 94

Figure 5.13 Hysteresis Loops for Cyclic Stress-Strain Testing 98

Figure 5.14 Variation of the Hysteresis Loop Area with Aging 100

Figure 5.15 Increase of Plastic Strain Due to Aging (SAC105, RF) 100

Figure 5.16 Optical Microscopic Image of Void Formation along Sub-Grain Boundaries in an Aged Sample (SAC105, RF, Aging for 210 Days at 125 C) 101

Figure 5.17 Cyclic Stress-Strain Curves for SACN05 104

Figure 5.18 Comparison of Hysteresis Loop Areas for 105

Figure 5.19 Evolution of Hysteresis Loop Size at Different Testing Temperatures for SAC405 Solder Alloy (Stress Controlled Cyclic Tests) 106

Figure 5.20 Hysteresis Loop Areas for SAC405 at Different 106

Figure 5.21 Evolution of Hysteresis Loop Size at Different Testing Temperatures for SAC405 Solder Alloy (Stress Controlled Cyclic Tests) 107

Figure 6.1 Depiction of Cyclic Loading in Solder Joints during Thermal Cycling 111

Figure 6.2 Hysteresis Loop Evolution during a Fatigue Test 121

Figure 6.3 Typical Peak Stress Drop during a Fatigue Test 121

Figure 6.4 Fatigue Data (Plastic Strain Range vs. Cycles to 123

Figure 6.5 Fatigue Data (Energy Dissipation vs. Cycles to 126

Figure 6.6 Cyclic Curves for Non-Aged Samples with Different ΔW (SAC105) 127

Figure 6.7 Cyclic Curves for Aged Samples with Different ΔW 128

Figure 6.8 Evolution of Hysteresis Loop Shape with Number of Cycles 130

Figure 6.9 Evolution of Hysteresis Loop Area with Number of Cycles 130

Figure 6.10 First Cycle Hysteresis Loops for Cyclic Stress-Strain Testing 130

Figure 6.11 Fatigue Data (Plastic Strain Range vs. Cycles to 131

Figure 6.12 Fatigue Data (Plastic Strain Range vs. Cycles to 132

Figure 6.13 Fatigue Data (Plastic Strain Range vs. Cycles to 134

Figure 6.14 Fatigue Data (Strain Energy Density vs. Cycles to 134

Figure 6.15 Comparison of Fatigue Life for Water 138

Figure 6.16 Comparison of Fatigue Life for Water 139

Figure 6.17 Comparison of Fatigue Life for Water 140

Figure 6.18 Comparison of Fatigue Life for Water 141

Figure 6.19 Fatigue Data (Plastic Strain Range vs. Cycles to 143

Figure 6.20 Fatigue Data (Strain Energy Density vs. Cycles to 143

Figure 7.1 Typical Configuration of Iosipescu Shear Specimen 146

Figure 7.2 Effects of BGA Ball Geometry and Chip Size on 148

Figure 7.3 Finite Element Modeling of Solder Ball Shear Test Assembly 149

Figure 7.4 Solder Ball Assembly 150

Figure 7.5 Finite Element Mesh Near a Solder ball 150

Figure 7.6 Material Properties of Solder Ball Assembly Model 151

Figure 7.7 Shear Stress τ_{xy} Distribution in the Solder Balls 152

Figure 7.8 Normal and Shear Stress Distributions for the Center Solder Ball 153

Figure 7.9 Normal and Shear Strain Distributions for the Center Solder Ball 154

Figure 7.10 Iosipescu Shear Test Specimen Assembly and Loading Fixture..... 156

Figure 7.11 Finite Element Meshing near Solder Layer (SOLID95 Brick Element) 156

Figure 7.12 Normal and Shear Stress Distributions within the 157

Figure 7.13 Uniformity of the Shear Stress Distribution within the..... 157

Figure 7.14 Normal and Shear Stress Distributions within the 158

Figure 7.15 Effects of Thickness and Size of Solder Bump on Fatigue Life [204]..... 159

Figure 7.16 Iosipescu Shear Specimen with Solder Layer having Different Thicknesses 159

Figure 7.17 Stress Distributions within a Solder Layer of Thickness 0.75 mm 160

Figure 7.18 Stress Distributions within a Solder Layer of Thickness 0.50 mm 161

Figure 7.19 Stress Distributions within a Solder Layer of Thickness 0.125 mm 162

Figure 7.20 Stress Concentration at the Side of the Solder 163

Figure 7.21 Comparison between Simple Lap Shear Specimen and Iosipescu Shear Specimen (Layer Thickness = 0.50 mm) 164

Figure 7.22 Stress Concentrations for Simple Lap Shear Specimen and 165

Figure 7.23 Mold Assembly for Iosipescu Shear Specimens 166

Figure 7.24 Iosipescu Shear Specimen 167

Figure 7.25 Flow Chart for Preparing Iosipescu Shear Specimen Assemblies 169

Figure 7.26 Heller 1800EXL Reflow Oven 170

Figure 7.27 Reflow Profile for Iosipescu Shear Specimen Assemblies 170

Figure 7.28 Defects during Shear Sample Preparation 171

Figure 7.29 Good Quality Iosipescu Shear Specimen Assembly 172

Figure 7.30 Olympus BX60 Optical Microscope and Measuring Scale..... 172

Figure 7.31 Design and Development of Testing System for..... 174

Figure 7.32 Modified Design for Specimen Grips (Two-Point Holding)..... 174

Figure 7.33 Iosipescu Shear Specimen having no Solder Layer 175

Figure 7.34 Load Train Equivalent System 176

Figure 7.35 Load Train Stiffness Measurement 177

Figure 7.36 Shear Stress-Strain Curve Before and 177

Figure 7.37 Shear Hysteresis Loops Before and..... 177

Figure 7.38 Typical Shear Cyclic Stress-Strain Test Results 178

Figure 8.1 Hysteresis Loops for Cyclic Shear Stress-Strain..... 185

Figure 8.2 Evolution of the Shear Hysteresis Loop Area of the..... 186

Figure 8.3 Variation of the Shear Hysteresis Loop Area with..... 186

Figure 8.4 Hysteresis Loop Evolution During a Shear Fatigue Test 188

Figure 8.5 Shear Fatigue Data (Plastic Shear Strain Range vs. 190

Figure 8.6 Shear Fatigue Data (Energy Dissipation vs. Cycles to..... 192

Figure 8.7 Variation of Peak Shear Stress with Cycling 193

Figure 8.8 Fatigue Life Curves (Equivalent Plastic Strain Range vs. 197

Figure 8.9 Fatigue Life Curves (Energy Dissipation vs. 198

Figure 9.1 Microstrutural Damage Evolution for SAC105 (No Aging)..... 208

Figure 9.2 Microstrutural Damage Evolution for SAC105 212

Figure 9.3 Transgranular Cracking Through Many..... 213

Figure 9.4 Intergranular Cracking Through Few Large..... 213

Figure 9.5 Optical Microscopic Images on Crack Propagation Modes..... 214

Figure 9.6 Fractured Surface of SAC105 (No Aging Condition) 215

Figure 9.7 Number of Failure Cycle at Particular Strain Range 223

Figure 9.8 Shift Function with Aging Time for SAC305 224

Figure 9.9 Non-linear Regression of number of Adjusted Failure Cycle Data 225

Figure 9.10 Modified Coffin-Manson Model with Shift Function for SAC105 225

Figure 9.11 Modified Coffin-Manson Model with Shift Function for SAC305 226

Figure 9.12 Modified Morrow Model with Shift Function for SAC105 226

Figure 9.13 Modified Morrow Model with Shift Function for SAC305 227

Figure 9.14 Band of Fatigue Life for SAC105 based on Plastic Strain Range 228

Figure 9.15 Band of Fatigue Life for SAC305 based on Plastic Strain Range 228

Figure 9.16 Band of Fatigue Life for SAC105 based on Plastic Strain Energy 229

Figure 9.17 Band of Fatigue Life for SAC305 based on Plastic Strain Energy 229

Figure 9.18 Crack Initiation Fatigue Data for SAC305 233

Figure 9.19 Reliability Prediction of 19 mm PBGA Package 233

List of Tables

Table 4.1 Empirical Models for Stress Strain Behavior 65

Table 4.2 Coefficient of Variation (r^2) Values for Hyperbolic Tangent 69

Table 6.1 Fatigue Ductility Exponent of Plastic Strain Range 116

Table 6.2 Fatigue Ductility Exponent of Plastic Strain Energy Based 117

Table 6.3 Fatigue Test Matrix (X = Completed) 119

Table 6.4 Coffin-Manson Coefficients for SAC105 123

Table 6.5 Morrow Model Coefficients for SAC105 126

Table 6.6 Coffin-Manson Coefficients for SAC305 131

Table 6.7 Morrow Model Coefficients for SAC305 132

Table 6.8 Coffin-Manson Model Coefficients and Number of 138

Table 6.9 Morrow Model Coefficients and Number of 139

Table 6.10 Coffin-Manson Model Coefficients and Number of 140

Table 6.11 Morrow Model Coefficients and Number of 141

Table 8.1 Aging Test Matrix for Iosipescu Shear Specimens (X = Completed) 181

Table 8.2 Coffin-Manson Coefficients for SAC105 190

Table 8.3 Morrow Model Coefficients for SAC105 192

Table 8.4 Coffin-Manson Coefficients for SAC105 197

Table 8.5 Morrow Model Coefficients for SAC105 198

Table 9.1 Fatigue Models and Classification 202

Table 9.2 Summary of Solder Fatigue Models 203

Table 9.3 Shift Factors at Different Aging Conditions 223

Table 9.4 Constants K_1 and K_2 for Crack Initiation 233

CHAPTER 1

INTRODUCTION AND GENERAL SCIENCE

1.1 Lead Free Electronics: Overview

Lead-based solders date to 3800 BC, when they were used for artistic purposes to produce ornaments [1]. From the 1960s to early 1990s, eutectic 63Sn-37Pb was the most extensively used soldering alloy in electronic packaging. Its advantages include relatively higher ductility, less intermetallic compounds (IMC), low surface and interfacial energies, outstanding reliability, superior wettability and compatibility with most substrates and devices [1-2], and a low melting temperature (183 C).

Various social, environmental, and health concerns have driven the push to lead-free solder technologies [3-6]. Proposed and enacted legislations in the forms of international and national laws, standards, and local initiatives have sought to control the use of lead in electronics manufacture. Advantages of lead-free technologies are providing manufacturers with opportunities to make process changes to incorporate different components and materials. Of course, some manufacturers are motivated to be environmental stewards for ethical or perhaps public relations reasons.

Manufacturers are assessing the effects of lead-free technologies on market differentiation. Some question the logic of eliminating lead in electronics, suggesting that market forces are the sole driver of the change. Initial consumer reaction to lead-free products has been positive, and early successes in marketing lead-free products suggest

that informed consumers are choosing environmentally considerate products. However, effecting such a fundamental change will require more than market pressure to be implemented successfully.

On January 27, 2003, the European Parliament and the Council of the European Union passed a pair of directives aimed at minimizing the risks and impacts that the production, use, treatment, and disposal of waste electrical and electronic equipment have on human health and the environment. Directive 2002/95/EC on the restriction of the use of certain hazardous substances in electrical and electronic equipment (RoHS) [8] and Directive 2002/96/EC on waste electrical and electronic equipment (WEEE) [9] had been considered and debated for years. Together they indentify lead as a material prohibited in electrical and electronic equipment to after July 1 2006. Other materials facing the same restriction are mercury, cadmium, hexavalent chromium, polybrominated biphenyls, and polybrominated diphenyls ethers. Additionally, the directives guide the prevention of waste electrical and electronic equipment and foster the development of reuse and recycling methods in order to reduce the amount of waste for disposal. Besides new restrictions on industry, the directives propose new policies and practices to assist manufacturers in meeting the objectives. The goal is to improve the environmental performance of all operating companies that are directly involved in the handling of waste electrical and electronic equipment, particularly those companies that are involved in the treatment of the waste.

Several Japanese electronics manufacturers have successfully created a market differentiation and increased market share based on “green” products that use Pb-free solders [10]. One effort to transfer technical knowledge was a visit of United Kingdom

(UK) technical representatives to Japan to observe Japanese practices in the incorporation of lead-free solders. The UK Department of Trade and Industry's (DTI) International Technology Service sponsored the visit made by the Surface Mount and Related Technologies (SMART) Group. The SMART Group consisted of industrial, governmental, and academic representatives with expertise in electronics manufacture. As the visiting team members prepared for their mission, they indentified their preconceptions as to why Japan has been leading the change to lead-free solder. Therefore, the conversion to Pb-free solders in the global electronics assembly business appears imminent [11].

Applications of lead-free solder in microelectronic packaging have been continuously increasing in recent years. Although it becomes challenging for engineers, scientists, and manufacturers to find a "perfect" replacement for eutectic Sn-Pb, some lead-free solders features good characteristics that make them appreciate candidates for next generation microelectronic packaging:

- Physical behavior (melting temperature, etc) similar to eutectic Sn-Pb
- Adequate wettability for the metallization used in the electronics industry
- Good fatigue resistance, electrical performance and reliability
- Compatibility with existing liquid flux systems
- Adequate shelf life and performance as a solder paste
- Low dross formation when used in a wave soldering operation
- Low cost

Material scientists and researchers around the world have developed about 70 lead-free solder alloy compositions to date including binary, ternary, and even quaternary

alloys [12]. Most of the lead-free solder alloys are Sn-based alloys. Although researchers have not yet found any "drop in" replacements for eutectic Sn-Pb solder in all applications, mostly lead-free solder alloys containing Sn, Ag, Cu, Bi, and Zn are recognized as promising candidates for next generation microelectronic packaging. Among the most popular lead-free solders, Sn-rich lead free alloys have occupied more than 80% of the wave solder market share and more than 90% of the reflow solder market share as shown in Figure 1.1.

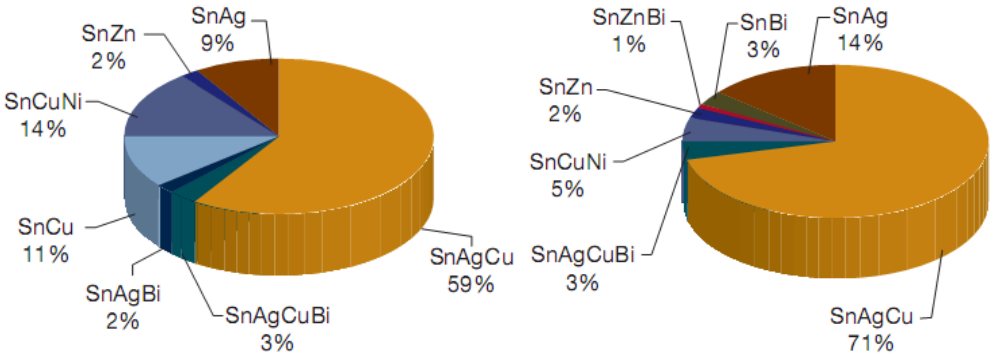

(a) Wave Solders (b) Reflow Solders

Figure 1.1 Lead Free Solder Market Share [13]

1.2 Sn-Ag-Cu Solder Alloy as Popular Choices

As depicted in Figure 1.1, Sn-Ag-Cu solder alloys are the most common Pb-free materials, and are regarded as the best alternative to eutectic Sn-Pb solder so far. The Sn-Ag-Cu (SAC) alloy family has been the prevailing alloy system used to replace tin-lead alloy because it is near eutectic, with adequate thermal fatigue properties, strength, and wettability. Most lead free solder candidates originated from binary alloy systems that were further optimized by adding small amounts of third chemical elements in order to lower the melting point and/or increase the wettability and reliability [14]. Popular lead

free choices based on availability on the market and their current applications are tabulated in Figure 1.2. As shown in Figure 1.1, SnAgCu (SAC) has been the most popular, and is widely used lead free solder in today's market.

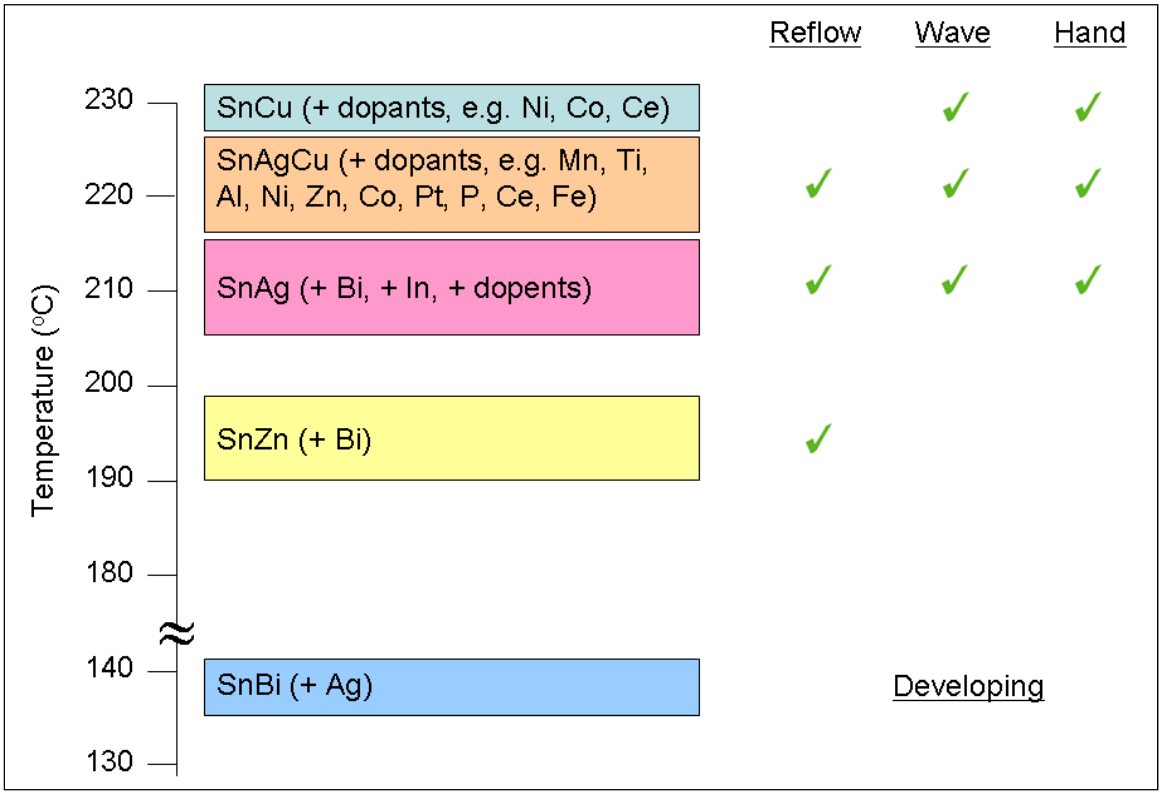

(Lee, C. N., Professional Development Course, ECTC 2011)

Figure 1.2 Prevailing Lead Free Choices and Their Applications

Although they are still not regarded as the perfect replacement for all applications, a variety of SAC alloys with different chemical compositions have been the proposed by various user groups and industry experts. These include: SAC105 (98.5Sn-1.0Ag-0.5Cu), SAC205 (97.5Sn-2.0Ag-0.5Cu), SAC305 (96.5Sn-3.0Ag-0.5Cu), and SAC405 (95.5Sn-4.0Ag-0.5Cu), known as the SACN05 series; SAC387 (95.5Sn-3.8Ag-0.7Cu), SAC396 (95.5Sn-3.9Ag-0.6Cu), and SAC357 (95.2Sn-3.5Ag-0.7Cu), identified as near eutectic

SAC choices; SAC3810 (95.2Sn-3.8Ag-1.0Cu), SAC3595 (95.55Sn-3.5Ag-0.95Cu), SAC0307 (9Sn-0.3Ag-0.7Cu), and SAC107 (98.3Sn-1.0Ag-0.7Cu), designed for special needs such as high temperature applications, drop and shock optimization, etc. The main benefits of the various SAC alloy systems are their relatively low melting temperatures compared with the 96.5Sn-3.5Ag binary eutectic alloy, as well as their superior mechanical and manufacturability properties when compared to other lead free solders [15]. SAC solders have outperformed high-Pb solders C4 joints in ceramic ball grid array (CBGA) systems, where better results were obtained in thermal cycling for Pb-free alloys. The findings also showed that SAC alloys are proportionately better in thermal fatigue as the thermal cycling range decreases. Another advantage of SAC is that it appears to be more resistant to gold embrittlement than Sn-Pb. In test results, the strengths of the joints were substantially higher for the SAC alloys than for the Sn-Pb alloy. Also, the failure mode was changed from a partially brittle joint separation to a ductile tearing with SAC [16].

It is known that the eutectic SAC alloy composition is near Sn-3.5Ag-0.9Cu, with a melting temperature of 217 C [17, 18]. Figure 1.3 contains the Sn-Ag-Cu ternary phase diagram near the pure Sn side with an enlarged scale. The contours in the figure represent the isothermal lines. The red boxed region indicates the region containing SAC alloy compositions currently available on the market.

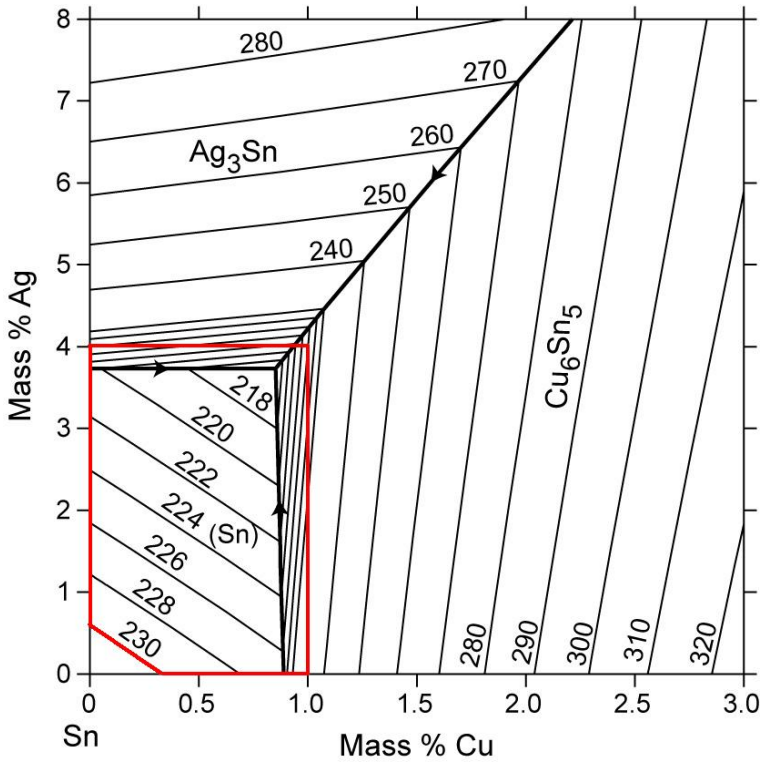

(http://www.metallurgy.nist.gov/phase/solder/agcusn-ll.jpg)

Figure 1.3 Sn-Ag-Cu Ternary Phase Diagram

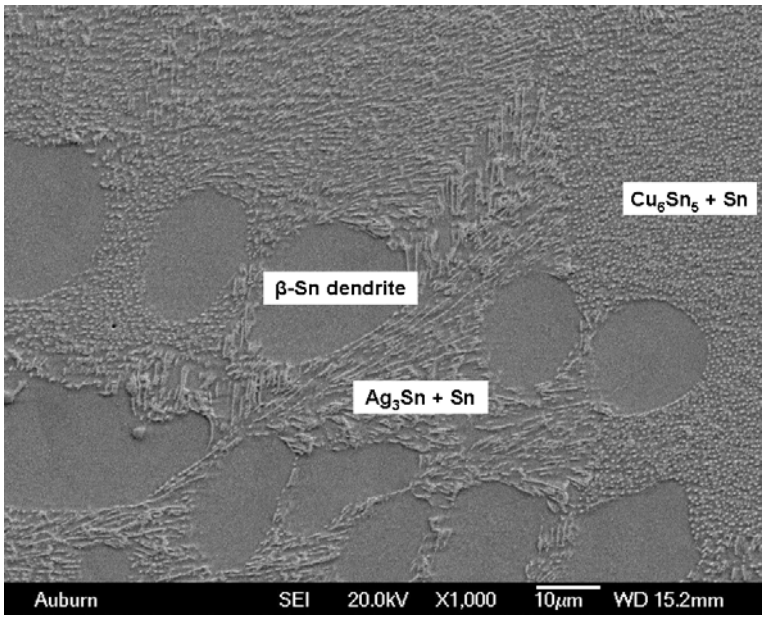

Figure 1.4 SEM Micrograph of Typical Sn-Ag-Cu Solder [21]

The ternary phase diagram shows two possible precipitates near the eutectic Sn-Ag-Cu region: Ag_3Sn and Cu_6Sn_5. The ternary eutectic microstructure of SAC solders consists of β-Sn dendrites (primary phase), eutectic Sn-Ag regions (needle-shape Ag_3Sn intermetallics dispersed within the β-Sn matrix), and eutectic Sn-Cu regions (scallop-shape Cu_6Sn_5 intermetallics dispersed within the β-Sn matrix), as shown in Figure 1.4. These interspersed fine intermetallic particles are capable of pinning and blocking the movement of dislocations, and will thus enhance mechanical strength and reliability of lead free solder joints when compared to eutectic Sn-Pb alloy [19-20].

Despite the benefits mentioned above, SAC family solders sometimes are still questionable as complete substitutes for eutectic Sn-Pb because of cost, some patent issues (particularly outside Europe), aesthetic considerations (dross problems), and a relatively high melting temperature (217 C vs. 183 C).

1.3 Mechanical Properties of Solder Materials

In electronics, solder joints are used to mount chips and components onto printed circuit boards (PCB) and thus create an electrical circuit. Therefore, an ideal solder material needs not only excellent conductivity to transmit signals, but also adequate strength to provide mechanical support and connection. Since most failures in electronic packages are caused by fatigue/fracture under certain thermal conditions [22], complete understanding of the mechanical behavior of solder materials is extremely critical.

1.3.1 Tensile

Tensile properties indicate how the material will react to forces being applied in uniaxial tension. Although solder joints are rarely under pure tensile/compressive loading, tensile properties are still crucial indicators for design purposes. Through tensile

tests, several material properties can be determined, such as effective modulus, yield strength (YS), ultimate tensile strength (UTS), elongation, etc. The tensile behavior of a solder material is usually described by a load vs. elongation curve, which is then converted into a uniaxial stress vs. strain curve. Engineering stress-strain curves are mostly employed instead of "true" stress-strain curves because the physical size and shape changes of the material are neglected.

Figure 1.5 shows a typical engineering stress strain curve. In engineering practice, the engineering stress and engineering strain are defined as follows [23]:

$$\sigma_e = \frac{F}{A_0} \tag{1.1}$$

$$\varepsilon_e = \frac{\Delta L}{L} = \frac{L_f - L_0}{L_0} \tag{1.2}$$

where F is the applied force, A_0 the original (unstressed) cross-sectional area, L_f the final (current) length, and L_0 the initial gage length.

Note that the stress and strain initially increase with a linear relationship. This is the linear-elastic portion of the curve where no plastic deformation has occurred. This means that when the stress is reduced, the material will return to its original shape. In this linear region, the material obeys the relationship defined by Hooke's Law where the ratio of stress to strain is a constant:

$$\sigma = E\varepsilon \tag{1.3}$$

where E is called the effective elastic modulus, which is the slope of initial part of a stress-strain curve. However, since the elastic modulus includes small inelastic deformations or time-dependent deformations such as creep, it is usually smaller than the

dynamic modulus measured by the acoustic or ultrasonic wave methods, which largely eliminate the inelastic deformation due to rapid wave propagation [24-26].

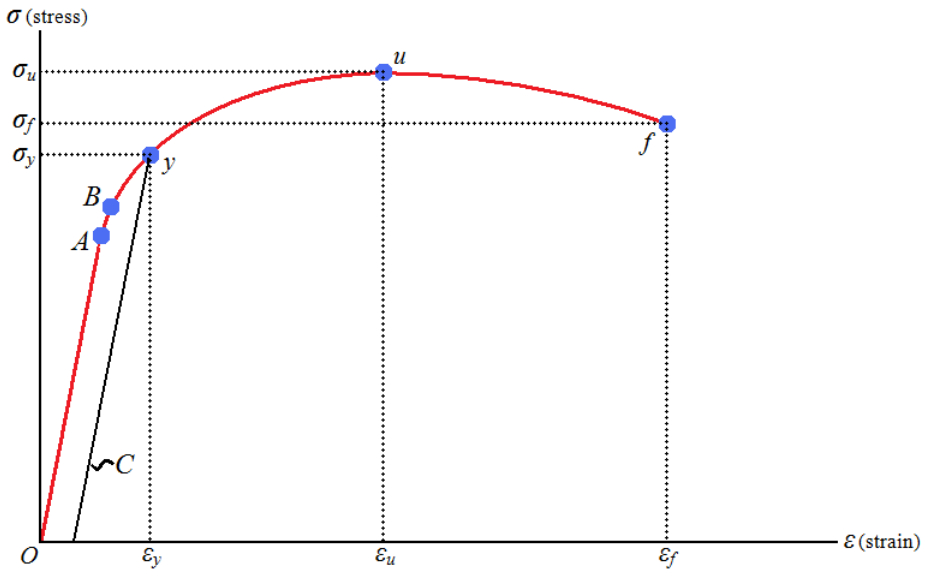

(http://www.engineeringarchives.com/les_mom_stressstraindiagram.html)

Figure 1.5 Typical Stress-Strain Response for Ductile Materials

As the strain progresses, many materials (e.g. solder) eventually deviate from this linear proportionality, the point of departure being termed the proportional limit. This nonlinearity is usually associated with stress-induced plastic flow in the specimen. At this stage the material is undergoing a rearrangement of its internal molecular or microscopic structure, in which atoms are being moved to new equilibrium positions. Such plasticity requires a mechanism for molecular mobility, which in crystalline materials can arise from dislocation motion. A closely related term is the yield stress, denoted σ_y in Figure 1.5; which is the stress needed to induce plastic deformation in the specimen. Since it is often difficult to pinpoint the exact stress at which plastic deformation begins, the yield stress is usually taken to be the stress needed to induce a specified amount of permanent strain, typically 0.2%. By drawing a parallel line to the

elastic portion of the engineering stress-strain curve but offset from the origin by a strain of 0.002, the "0.2% offset yield stress" is then determined as the intersection between the stress-strain curve and the offset line.

The ultimate tensile strength (UTS) or, more simply, the tensile strength, is the maximum engineering stress level reached in a uniaxial tension test. The strength of a material is its ability to withstand external forces without breaking. In ductile materials, the UTS will be well outside of the elastic portion into the plastic portion of the stress-strain curve. The engineering stress will decrease after the UTS is reached due to occurrence of necking in the specimen. However, this type of localized deformation is beyond the research scope here, and will not be further discussed in this dissertation.

1.3.2 Creep

Solder joints are often placed in service in variable temperature environments, and mechanical stresses are often developed due to the Coefficient of Thermal Expansion (CTE) mismatches between silicon chip and other assembly materials. These stresses can cause transient deformations to take place, particularly over a long period of service time. Time-dependent deformation of a material while under a constant applied stress that is below its yield strength is known as creep deformation. Creep is often regarded as one of the major failure modes of solder joints in microelectronic packaging modules [27].

In engineering practice, creep data are usually obtained under conditions of constant uniaxial loading and constant temperature. Results of tests are plotted as strain vs. time up to rupture. As indicated in Figure 1.6, the response begins with a quick transition to the initial "elastic" strain level, followed by three stages; namely, primary, secondary, and tertiary creep. In the primary stage, strain occurs at a relatively rapid rate

(high slope) after the instantaneous elastic strain. Then the strain rate gradually decreases until it becomes approximately constant during the secondary stage. This constant creep rate due to the dynamic balance of strain hardening and recrystallization is defined as the steady state creep rate [23]. It is often used by practicing engineers as one of the key material parameters for solder in Finite Element (FE) simulations used to predict solder joint reliability. The tertiary creep region occurs when rupture is imminent, and typically features an abrupt change to a nearly constant but significantly increased creep rate.

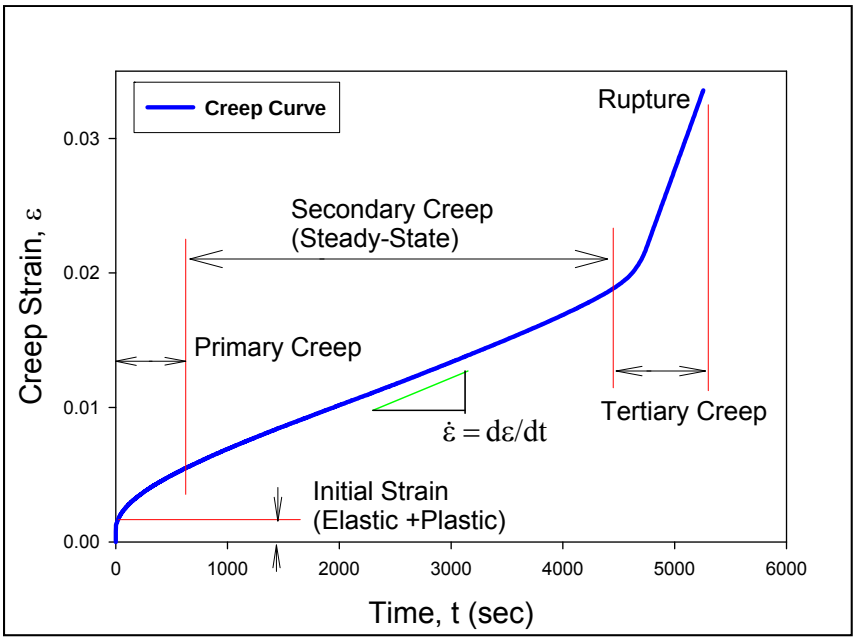

Figure 1.6 Typical Creep Response for Ductile Materials

In spite of similar shapes of creep responses, the deformation mechanism of creep varies with applied load and service temperature. Figure 1.7 maps the possible creep deformation mechanisms for eutectic Sn-Pb solder material. This diagram features axes of normalized stress, τ/G, and homologous temperature, T/T_M, where τ is shear stress, G the shear modulus, T the ambient temperature, and T_M the melting temperature. The map

is divided into fields, that show the regions of stress and temperature over which each of the deformation mechanisms is dominant. Superimposed on the fields are contours of constant strain-rate, which show the net strain-rate (due to an appropriate superposition of all the mechanisms) that a given combination of stress and temperature will produce. For most cases, creep is considered critical with a homologous temperature larger than 0.5. Therefore, creep is not negligible for most solder materials even at room temperature (RT) due to their large homologous temperatures:

$$H_T = \frac{T}{T_M} = \frac{298K}{456K} = 0.65 \qquad \text{for eutectic Sn-Pb} \tag{1.4}$$

$$H_T = \frac{T}{T_M} = \frac{298K}{490K} = 0.61 \qquad \text{for Sn-Ag-Cu} \tag{1.5}$$

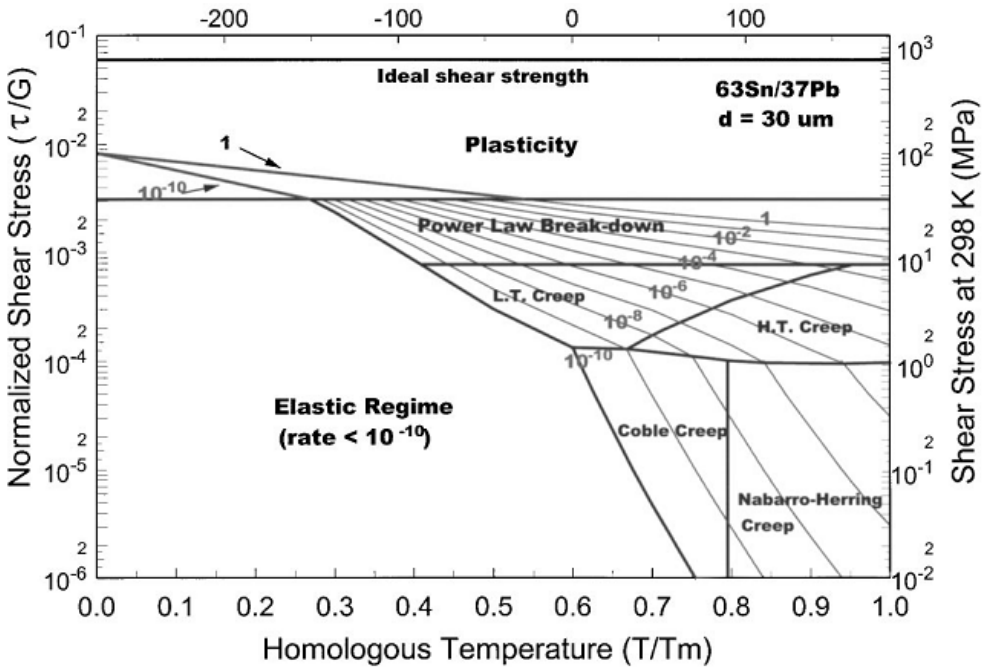

Figure 1.7 Creep Deformation Mechanism Map for Eutectic Sn-Pb Solder [28]

In practice, solder joints are subjected to high ambient temperatures and/or high stress levels in most cases. Thus, it is believed that dislocation-controlled creep and

lattice diffusion-controlled creep are the major deformation modes for eutectic Sn-Pb solder [28]. At high homologous temperatures, the thermally activated dislocations are able to move along preferred slip plans or cut through dislocation barriers [29-30], and the interstitial atoms and lattice vacancies tend to migrate along the gradient of a grain boundary in the presence of tensile or compressive pressure in reversed directions [31].

1.3.3 Shear

It is known that solder joints in microelectronics systems often experience shear loading due to the CTE mismatches. Similar to tensile stress-strain curves, a linear relation also holds for shear stress-strain responses at small shear strains, as shown in Figure 1.10:

$$\tau = G\gamma \tag{1.6}$$

Here shear stress and shear strain, τ and γ, can be similarly obtained by:

$$\tau = \frac{F}{A_0} \tag{1.7}$$

$$\gamma = \frac{\Delta x}{h} \tag{1.8}$$

where F is the applied shear force, A_0 the cross-sectional area, Δx the transverse displacement, h the initial length.

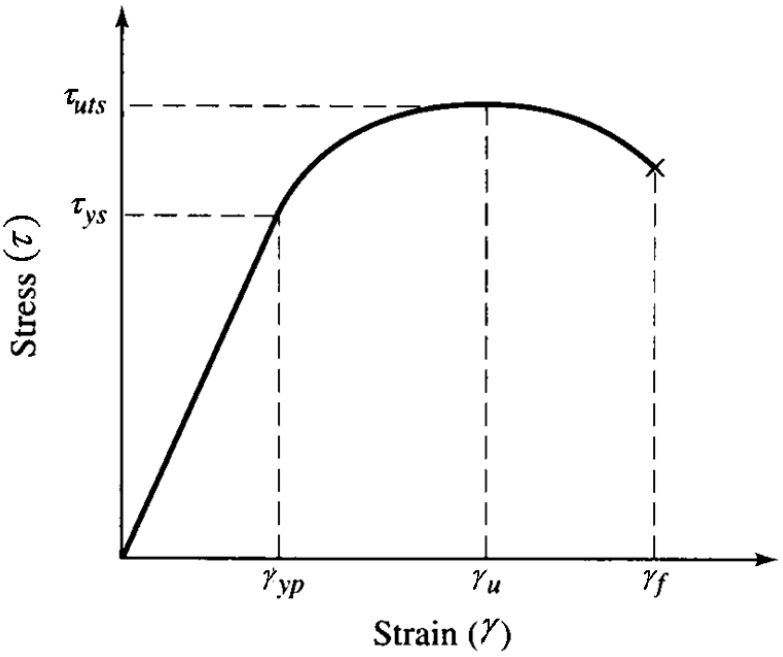

(http://www.benbest.com/cryonics/lessons.html)

Figure 1.8 Typical Shear Stress-Strain Response for Ductile Materials

In Eq. 1.6, G is called the shear modulus or modulus of rigidity, measured as the slope of the linear portion on the shear stress-strain response. For isotropic materials, the shear modulus can also be estimated from the elastic modulus and Poisson's ratio [23]:

$$G = \frac{E}{2(1+v)} \tag{1.9}$$

1.3.4 Fatigue

Thermally cycling induced solder joint fatigue is a common failure mode in electronic packaging. When subjected to temperature changes, stresses in electronic assemblies are typically developed due to the mismatches in CTE of the soldered components and the Printed Circuit Board (PCB). Cyclic temperature changes, either due to external environment or power switching, can therefore lead to substantial alternating stresses and strains within the solder joints. During cyclic loading, micro

cracks form within the solder material followed by macro cracks which leads to damage and ultimately to fatigue failure (see Figure 1.9). The facts that the original bulk design strengths are not exceeded and the only warning sign of an impending fracture is an often indiscernible internal crack, make fatigue damage especially dangerous for electronic packages.

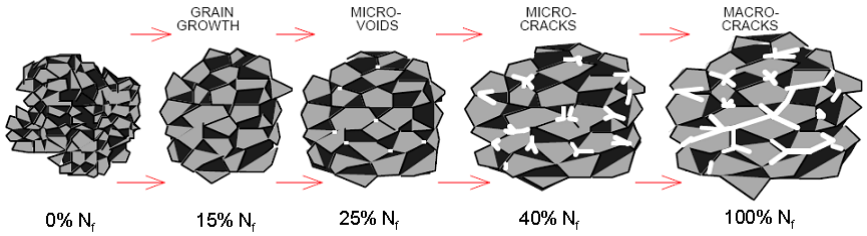

Figure 1.9 Depiction of the Effects of the Accumulating Fatigue Damage [32]

Fatigue test results are obtained by cycling smooth or notched specimens until failure, and are presented in a form of S-N diagram (where S is the stress amplitude, and N the number of cycles to failure) as shown in Figure 1.10. Since the 1950s, researchers have developed several models to predict the number of cycles to failure of solder materials including the Engelmaier-Wild equation [32], Palmgren-Miner linear damage law, Coffin-Manson relation [33], etc.

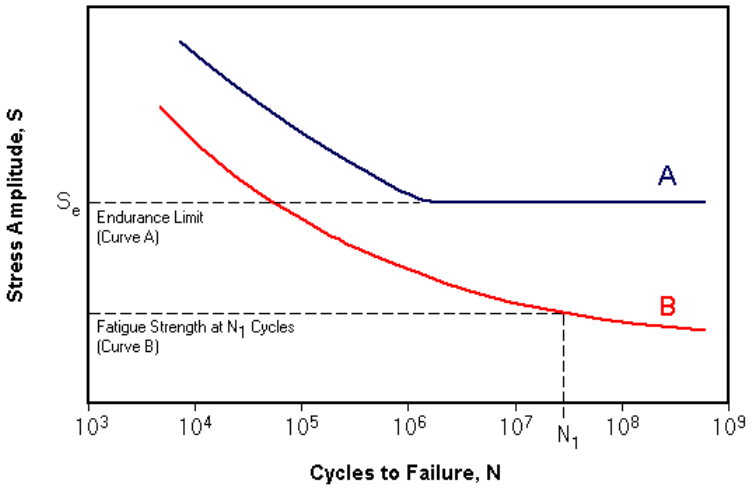

(http://www.mdme.info/MEMmods/MEM30007A/properties/Properties.html)

Figure 1.10 Typical S-N Curve for Ductile Materials

The typical stages of the fatigue damage process are summarized schematically in Figure 1.11. In general, slip occurs first, followed by cracks that can be seen only at high magnification. These cracks continue to grow under cycle loading and eventually become visible to the unaided eye. The cracks tend to combine such that just a few major cracks grow. These cracks (or crack) reach a critical size, and sudden fracture occurs. The higher the stress magnitude, the sooner all processes occur. Cracks may also stop without further growth as a result of compressive residual stress fields or as a crack grows out of a high-stress region such as a notch. Thus fatigue generally consists of crack nucleation, growth, and final fracture. At high stress levels, a large portion of the total fatigue life is associated with microcrack and macrocrack growth. At low stress levels, a great deal of the total fatigue life is spent in the nucleation of the crack and microcrack growth.

Fatigue substantially involves the nucleation and growth of cracks. Only the nucleation stage can be absent in a fatigue fracture. Thus, fatigue failures can be overcome by preventing the nucleation and growth of cracks.

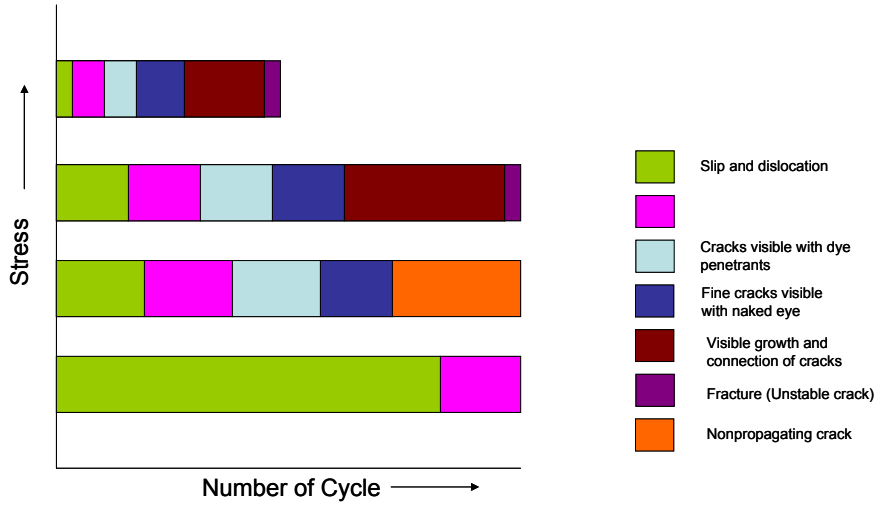

Figure 1.11 Schematic Representation of the fatigue process [34]

1.3.5 Cyclic Stress-Strain Behavior

The stress-strain behavior obtained from a monotonic tension or compression test can be quite different from that obtained under cyclic loading. This was first observed during the late nineteenth century by Bauschinger [35]. His experiments indicated that the yield strength in tension or compression was reduced after applying a load of the opposite sign that caused inelastic deformation. Therefore, one single reversal of inelastic strain can change the stress-strain behavior. Three types of cyclic stress-strain behavior can be obtained for most of metal alloys at different initial conditions [36] as shown in Figure 1.12: (a) cyclic hardening for fully annealed condition, (b) both cyclic hardening and softening for partially annealed condition, and (c) cyclic softening for cold-worked condition. The mechanism of hardening and softening can be described in

terms of dislocation substructure, motion, and slip. If dislocations are constrained to move or glide and slip is minimized, the material is said to cyclically harden. Reconfiguration of the dislocation structure can also tend to promote greater dislocation mobility. Therefore, dislocations are able to circumnavigate around microstructural barriers that generally tend to restrict deformation, such as precipitates and grain boundaries. Thus, such a material is said to cyclically soften.

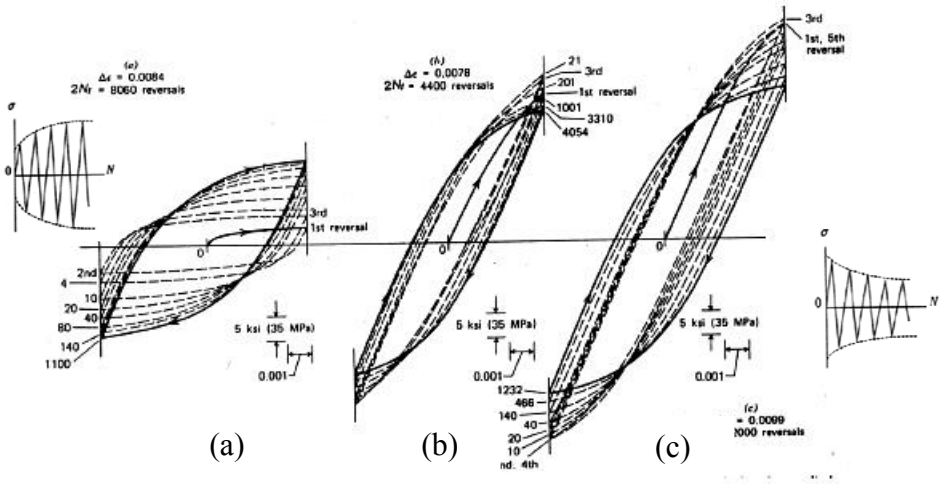

Figure 1.12 Cyclic Stress-Strain behavior of Alloys (a) Cyclic hardening (b) Cyclic Hardening and Softening (c) Cyclic softening

1.4 Micro-structural Damage Mechanisms

1.4.1 Dislocation

Line imperfections within crystal structure are called dislocations. A linear disturbance, i.e. a one dimensional imperfection in the geometrical sense of the atomic arrangement, which can very easily occur on the slip plane through the crystal, is such a dislocation. The most important kinds of linear defects are edge and screw dislocations. Both of these types are formed in the process of their deformation. Both of these defects

are the most striking imperfections, and are responsible for the useful property of ductility in metals, ceramics, and crystalline polymers. Crystalline materials can be either in the form of single crystal or as an aggregate of many crystals usually known as polycrystalline, where the pure crystals are separated by well-defined boundaries known as grain boundaries. Polycrystalline materials are often stronger than ordinary amorphous materials because crystals have different orientations with respect to each other, and the grain boundaries can obstruct the movement of dislocations. Polycrystalline materials are typically isotropic because they exhibit the same properties in every plane and direction, whereas single crystals are often called anisotropic with directional properties.

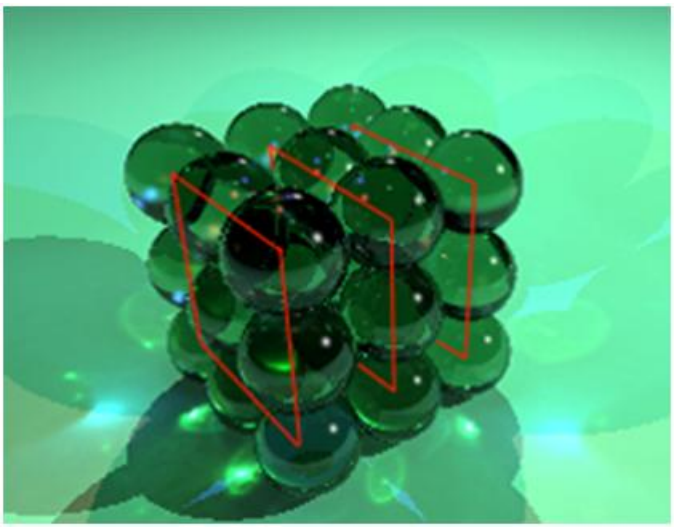

Figure 1.13 Crystal Lattice showing Atoms and Lattice Planes

1.4.1.1 Edge Dislocation

This type of dislocation is formed by adding an extra partial plane of atoms to the crystal [Fig. 1.14(a)]. An edge dislocation in its cross-section is essentially the edge of an

'extra' half-plane in the crystal lattice. The lattice around a dislocation is elastically distorted. Figure 1.15(a) shows a cross-section of a crystal where atoms (shown by dots) are arranged in a perfect orderly manner. When an extra half plane is inserted from the top, the displacement of atoms is shown in Fig. 1.15(b). The top and bottom of the crystal above and below the line XY appear perfect. When the extra half plane is inserted from the top, the defects so produced are represented by ⊥ (inverted tee), and if the extra half plane is inserted from the bottom, the defects so produced are represented by T (Tee).

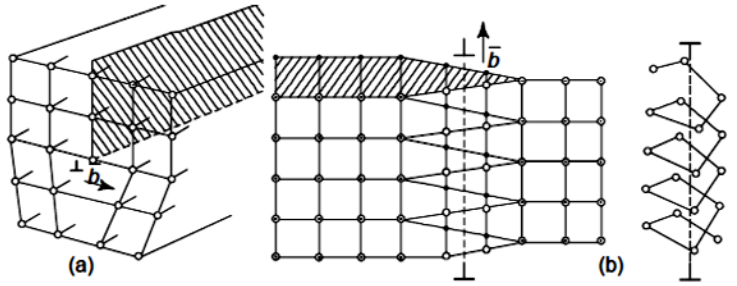

Figure 1.14 Schemes of (a) Edge Dislocation (b) Screw Dislocation

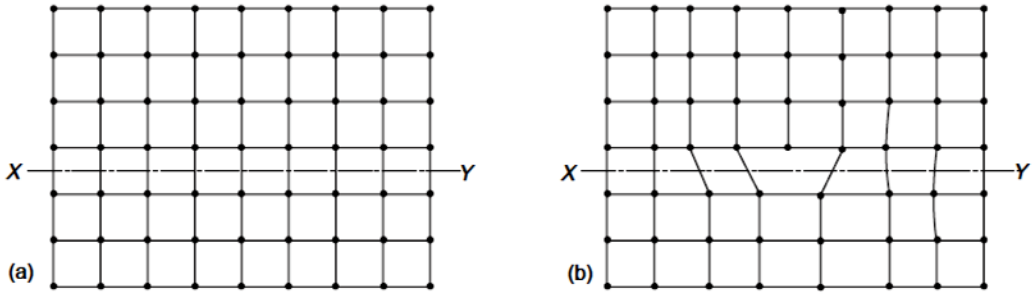

Figure 1.15 Edge dislocation caused by an extra partial plane of atoms in the crystal

1.4.1.2 Screw Dislocation

The formation of a screw dislocation is shown in Fig. 1.14(b). In this type, the atoms are displaced in two separate planes perpendicular to each other. An isomeric

view of a perfect crystal is shown in Fig. 1.16(a). The displacement of atoms in the region ABC is shown in Fig. 1.16(b). The arrangement of atoms in screw dislocations appears like that of a screw or a helical surface.

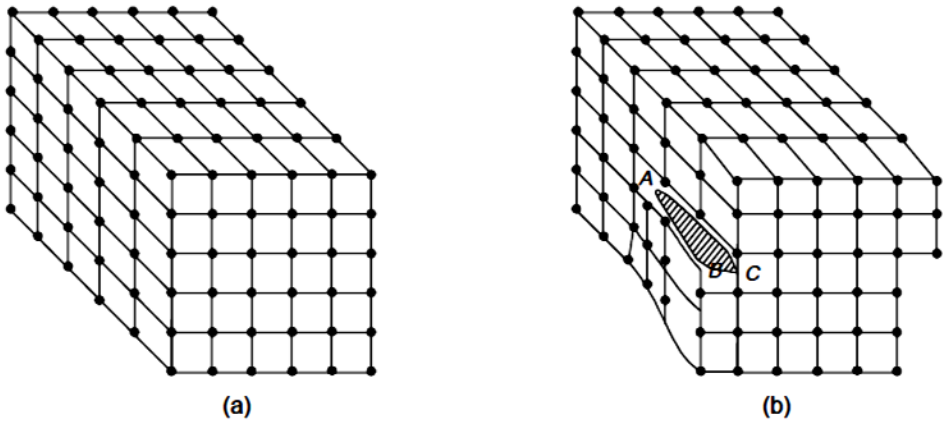

Figure 1.16 Scheme of Screw Dislocation

1.4.2 Slip

The movement of atoms from their original positions in the metal is termed as slip. In materials science, slip is the process by which a dislocation motion produces plastic deformation. An external force makes parts of the crystal lattice glide along each other, changing the material's geometry. Depending on the type of lattice, different slip systems are present in the material. More specifically, slip occurs between planes containing the smallest Burgers vector. A schematic view of a slip mechanism is shown in Figure 1.17. The ease with which atoms move or slip in a metal is an indication of hardness.

Figure 1.17 Schematic View of Slip Mechanism

The slip planes and slip directions in a crystal have specific crystallographic forms. The slip planes are normally the planes with the highest density of atoms, i.e., those most widely spaced, and the direction of the slip is the direction in the slip plane that corresponds to one of the shortest lattice translation vectors. Often, this is the direction in which atoms are most closely spaced. A slip plane and a slip direction constitute a slip system. A characteristic shear stress is required to initiate a slip. Slip is an important mode of deformation mechanism in crystals. Slip induces plasticity in most metals.

1.4.3 Plasticity

Plasticity describes the deformation of a material undergoes non-reversible changes of shape in response to applied forces. For example, a solid piece of metal being bent or pounded into a new shape displays plasticity as permanent changes occur within the material itself. In engineering, the transition from elastic behavior to plastic behavior is called yield. Plastic deformation is observed in most materials including metals, soils, rocks, concrete, foams, bone and skin. However, the physical mechanisms that cause

plastic deformation can vary widely. At the crystal scale, plasticity in metals is usually a consequence of dislocations.

In most crystalline materials such defects are relatively rare. But there are also materials where defects are numerous and are part of the very crystal structure, in such cases plastic crystallinity can result. In brittle materials such as rock, concrete, and bone, plasticity is caused predominantly by slip at micro cracks. An example of plasticity occurred during nano-indentation is shown in Figure 1.18.

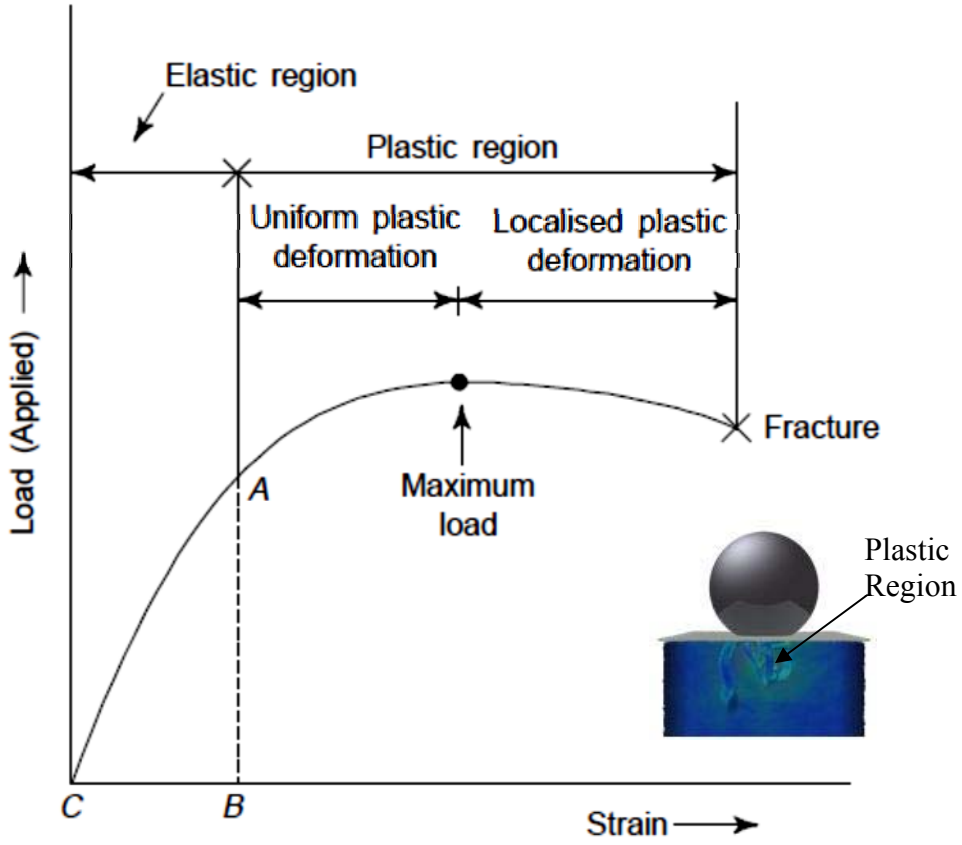

Figure 1.18 Plasticity Under a Spherical Nanoindenter in (111) Copper.

1.5 Objectives of This Research

The motivation of this research is to the need to understand the effects of aging on the cyclic stress-strain and mechanical fatigue behaviors, and microstructural damage evolution during cyclic loading of lead free solder alloys. The current database of fatigue behavior of solder material properties has been expanded including aging effects in order to predict fatigue life and reliability of microelectronic packages based on established reliability models. The objectives for this research include:

(1) Develop specimen preparation procedures that produce uniaxial testing coupons with consistent microstructures comparable to actual lead free solder joints in commercial electronic packages

(2) Develop constitutive models for the cyclic stress-strain behavior of lead free solders to calculate area of the hysteresis loop generated during cyclic loading

(3) Understand cyclic stress-strain behavior including aging effects for lead free solder alloys in terms of energy dissipation per cycle and evolution of hysteresis loops with aging

(4) Perform uniaxial fatigue test for different lead free solders over a wide range of aging conditions, and study uniaxial fatigue behavior including aging effects

(5) Design, develop, and calibrate of shear testing fixture for solder with the help of computer aided drawing and finite element analysis

(6) Develop shear specimen preparation procedures that produce shear testing coupons with consistent microstructures comparable to actual lead free solder joints in commercial electronic packages

(7) Understand shear cyclic stress-strain behavior including aging effects for lead free solder alloys, including the evolution of hysteresis loops with aging

(8) Perform shear fatigue tests for different lead free solders over a wide range for aging conditions, and correlate shear fatigue data with uniaxial fatigue data

(9) Examine the microstructural damage evolution occurring during cyclic loading with and without aging effects

(10) Develop microstructural adaptive fatigue models for lead free solders for predicting long term fatigue life including aging effects

1.6 Organization of the Dissertation

This dissertation focuses on understanding aging effects on cyclic stress-strain and fatigue behavior of lead free solder materials and is presented in the following chapters:

Chapter 1: Introduction to lead free solders alloys and mechanical properties of solder materials.

Chapter 2: Literature review on isothermal aging effects, cyclic stress-strain and fatigue behavior, and microstructure damage evolution for lead free solder alloys.

Chapter 3: Experimental procedure for uniaxial specimen preparation

Chapter 4: Empirical model for uniaxial and cyclic stress-strain behavior for solder materials

Chapter 5: Effects of aging on the uniaxial cyclic stress-strain behavior for lead free solders

Chapter 6: Effects of aging on the uniaxial fatigue behavior of lead free solders

Chapter 7: Shear specimen preparation and development of an experimental shear stress-strain loading fixture

Chapter 8: Effects of aging on the shear cyclic stress-strain and fatigue behavior of lead free solders

Chapter 9: Development of microstructure based fatigue model including aging effects

Chapter 10: Summary and conclusions

CHAPTER 2

LITERATURE REVIEW

2.1 Introduction

Thermally cycling induced solder joint fatigue is a common failure mode in electronic packaging. When subjected to temperature changes, stresses in electronic assemblies are typically developed due to the mismatches in the coefficients of thermal expansion (CTE) of the soldered components and the PCB. Cyclic temperature changes, either due to external environment or power switching, can therefore lead to substantial alternating stresses and strains within the solder joints. Energy dissipation occurs during such cyclic loading due to yielding and occurrence of viscoplastic deformations, and the strain energy density dissipated per cycle can be calculated from the area of stress-strain hysteresis loops. The cycling eventually leads to micro cracks being formed within the solder material, followed by macro cracks which leads to damage progression and ultimately to fatigue failure. Aging of solder materials degrades their mechanical and creep properties, and will exacerbate the rate of damage accumulation during cycling loading.

2.2 Aging Effects on Solder Material Properties

Several studies have been performed on degradation of solder material properties when the alloys are exposed to isothermal aging. For example, Medvedev [37] observed in the 1950s that material properties of a solder alloy degraded while it was exposed to

isothermal aging. He reported that a 30% reduction occurred in the tensile strength of bulk Sn-Pb solder, while a 23% reduction in tensile strength occurred for solder joints after 450 days of room temperature (RT) aging. Similar observations were also reported by Lampe [38]. He observed that up to a 20% loss occurred in both strength and hardness of Sn-Pb and Sn-Pb-Sb solders after 30 days of RT aging.

The effects of aging on tensile properties of Pb-free solders have also been studied extensively in recently years. Ding, et al. [39] examined the influence of aging treatment on the microstructure, mechanical properties, and fracture mechanisms of Sn3.5Ag solder as shown in Figure 2.1. In their investigation, crack initiation and propagation in the Sn3.5Ag eutectic solder were recorded, and the corresponding mechanisms were analyzed in detail. They also reported a rapid softening effect on solder samples subject to 180 C isothermal exposure for 120 hours. Xiao, et al. [40] investigated the tensile behavior of SAC396 solder alloy subjected to both room temperature aging and elevated temperature (HT) aging at 180 C for various aging periods. They observed a 25% reduction of tensile strength for 35 days of RT aging, and even larger reductions for elevated temperature aging.

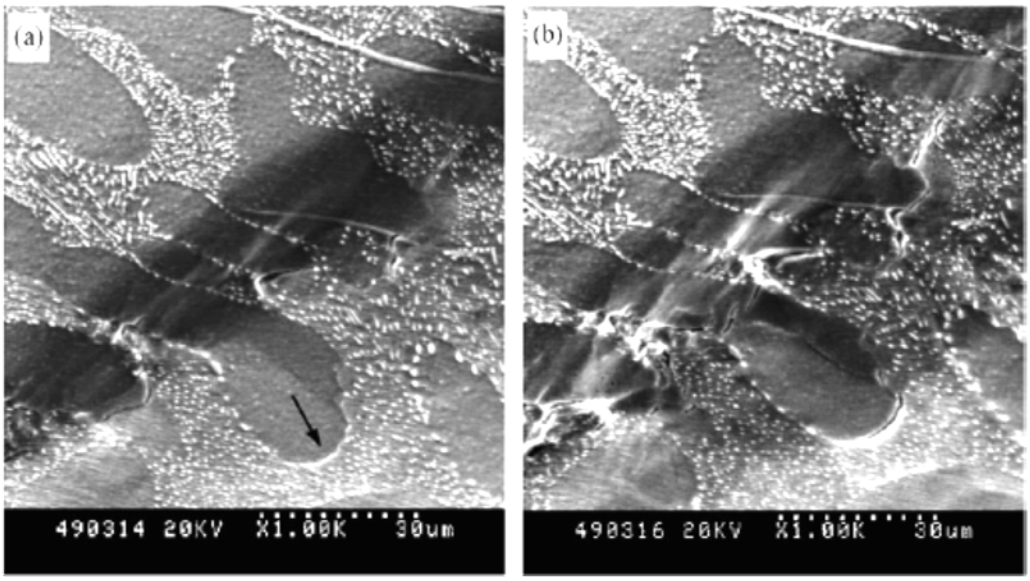

Figure 2.1 Partial Deformation Behavior in aged Sn3.5Ag Specimen
Strained to (a) 2.3% (b) 3.8% [39]

Ma, et al. [41] studied the effects of aging on effective elastic modulus, yield strength, and ultimate tensile strength of SAC305 and SAC405 solder alloys under various aging conditions. They observed a significant drop of the material properties in the first 20 days for both room temperature and elevated temperature aging, followed by a linear degradation as shown in Figure 2.2. Zhang, et al. [42] also systematically studied the aging effects on tensile properties of SACN05 (N = 1, 2, 3, 4) series solders. They performed several uniaxial tensile tests on micro-scale bulk solder samples with a full aging test matrix. Different empirical models were proposed in their study to correlate the degradation in tensile properties with aging.

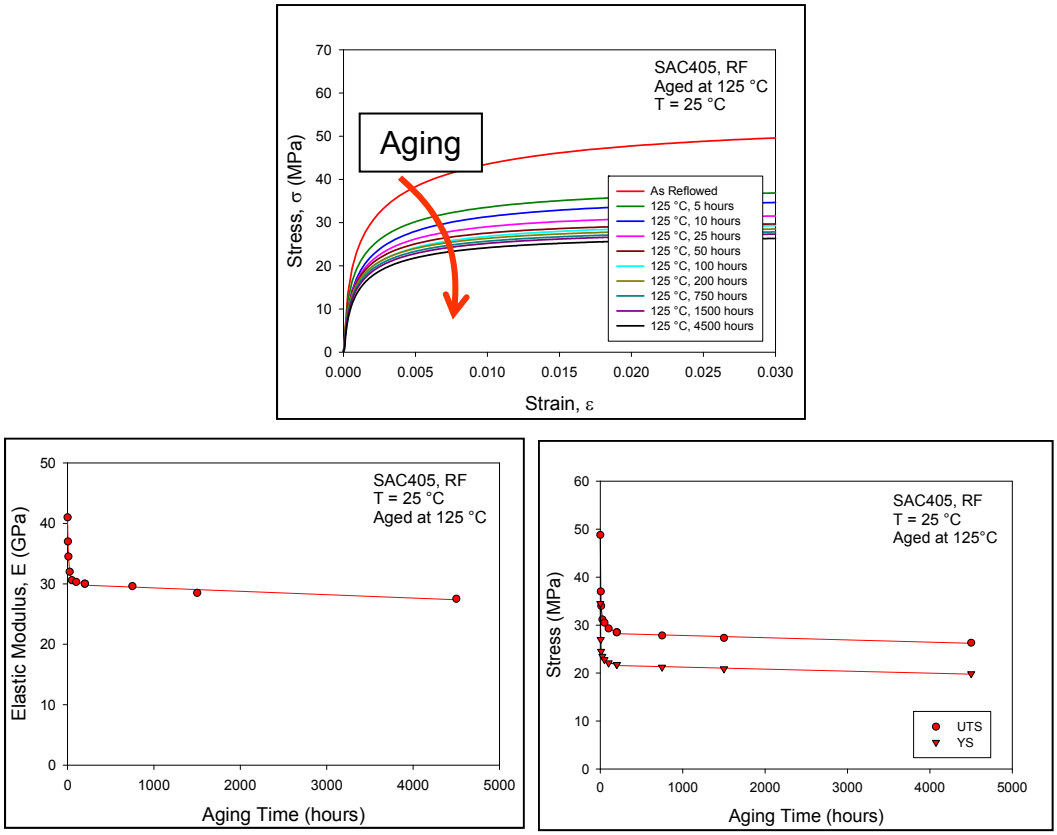

Figure 2.2 Degradation of the Material Properties of SAC405 Under Various Aging Conditions [41]

Various studies have also suggested that isothermal aging causes significant reductions in the shear strength and changing of the failure modes of lead free solder joints. Chen, et al. [43] studied and measured the variations in shear strength of solder bumps with aging for both Sn-Pb and Sn-3.5Ag solders. They concluded that after thermal aging at 150 C for 1500 hours that the shear strengths decreased 8.9% for Sn-Pb solder and 5.3% for Sn-3.5Ag solder. For the first 200 hours of aging, the shear strength decreased at a higher rate than for longer aging times. Similar results were found by Kim, et al. [44]. They observed an average 5% decrease in joint strength in stud bump samples for the first 300 hours of aging at 150 C. For longer aging times, they reported that the

degradation was almost negligible. Anderson, et al. [45] extended the study to a wide selection of SAC alloys, including SAC305, SAC3810, SAC379, and SAC396. All of the solder materials were severely softened with long term high temperature aging. They also reported that joints in the as-soldered and 100 hour aged conditions experienced shear failure in a ductile manner by either uniform shear of the solder matrix (in the strongest solders) or by a more localized shear of the solder matrix adjacent to the Cu_6Sn_5 interfacial layer, consistent with other observations.

The literature has also documented the significant influence of aging on the creep behavior of lead free solder alloys. Ma, et al. [41] initiated a parametric study of aging on SAC305 and SAC405 solders, and found that the secondary creep rates were increased by up to 10X and 100X, respectively. A more systematic study was conducted by Zhang, et al. [42]. They recorded the evolution of the creep curves and corresponding steady state creep rates as a function of aging (aging temperature and aging time), and observed up to a 9,700X deterioration of the secondary creep rate for aging up to 6 months. Similar aging induced degradations in creep properties were also reported in bulk samples by Xiao, et al. [46] and Mysore, et al. [47], and in solder joints by Chavali, et al. [48].

Chou, et al. [49] reported on degradation of BGA ball shear strength with elevated temperature aging at 125C or 150 C. Their investigation documented both microstructure coarsening and intermetallic layer growth during aging. In addition, Hasegawa, et al. [50] measured elastic modulus reductions with aging by testing thin solder wires, while Chiu and co-workers [51] found significant reductions in drop reliability after elevated temperature aging. Pang and co-workers [52] measured microstructure changes,

intermetallic layer growth, and shear strength degradation in SAC single ball joints subjected to elevated temperature aging.

The effects of room temperature (25 C) and elevated temperature (50, 75, 100, and 125 C) aging on the mechanical properties and creep behavior of SAC alloys have been extensively discussed by researchers at Auburn University [21, 40-41, 53-54]. Cai, et al. [21, 55] have reported on effects of aging on the mechanical behavior of doped SAC solder materials (i.e., SACX). Smaller creep rate degradations from aging were reported for the doped SAC alloy. The changes in the creep rate of SAC-X were approximately 10X smaller than those for SAC105 at several different aging temperatures (25 C, 50 C, 75 C, 100 C and 125 C). For example, the creep rate of SAC105 increased by a factor of 9700X after 6 months aging at 125 C, while the creep rate of SACX0307 increased by 954X for the same exposure time (See Figure 2.3). Cai [21] also investigated the evolution of SAC microstructure with aging and found that the IMC particles gradually dispersed away from their original locations to the grain boundaries and conglomerated as aging progressed (Figure 2.4).

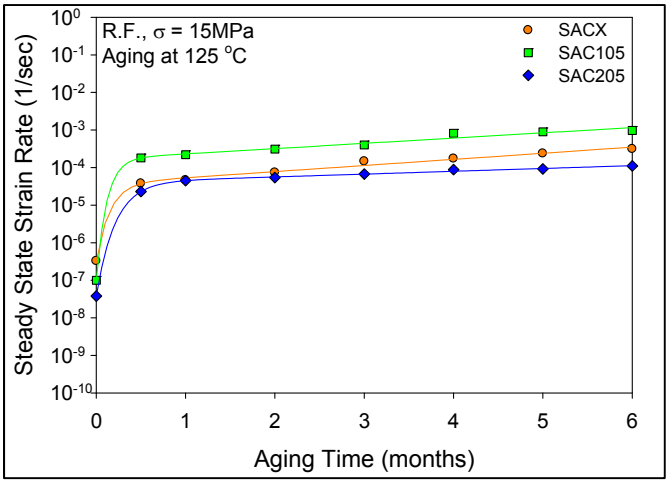

Figure 2.3 Effect of Dopants on the Evolution of Creep Rate with Aging (SACX, SAC105, SAC205, Aging up to 6 Months)

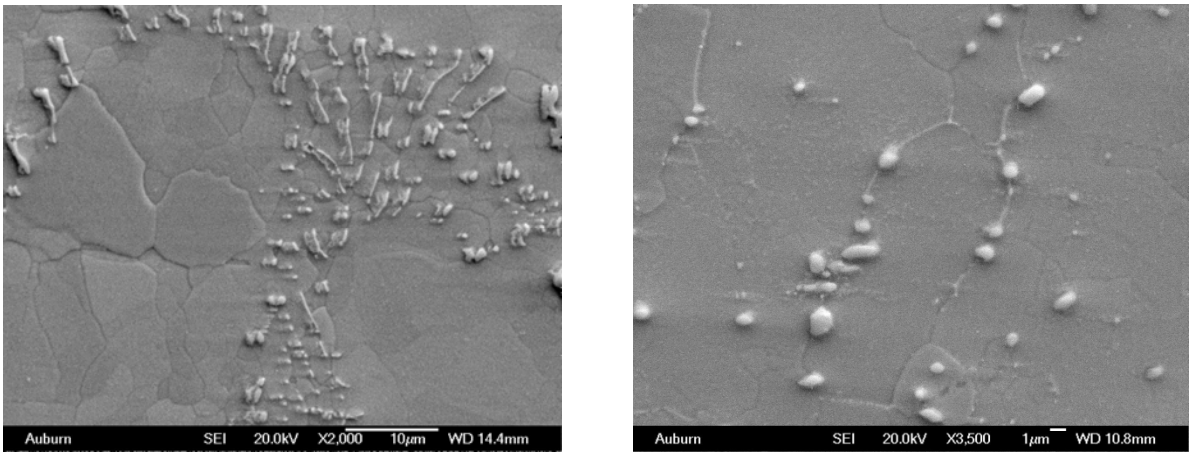

Figure 2.4 Distribution of IMC Particles in SACX before/after Aging [21]

Motalab, et al. [56] performed uniaxial tensile testing of SAC305 lead free solder for specimens subjected to 7 different sets of aging conditions prior to testing: 0, 1, 5, 20, 60, 120, and 180 days of aging at 100 C. For each aging time, stress-strain data were measured at three strain rates (.001, .0001, and .00001 sec^{-1}) and five temperatures (25, 50, 75, 100, and 125 C). It was observed that the majority of the changes in the material

properties at each temperature occurred during the first 20 days of aging, with slower degradations occurring from 20 to 180 days of aging. Hasnine, et al. [57] explored aging phenomena in actual solder joints by nano-mechanical testing of single SAC305 solder joints extracted from PBGA assemblies. They observed that the creep rate increased by 17X for a single grain solder joint subjected 30 days of aging at 125 C.

2.3 Effect of Fabrication and Testing Conditions on Solder Material Properties

The solidification cooling rate has a significant effect on the microstructure of solder materials by determining the initial size, distribution, and morphology of IMC phases (e.g. Ag_3Sn and Cu_6Sn_5) [58]. For bulk solder, fast cooling rates result in relatively thin and planar IMCs, while slow cooling rates lead to a relatively thick and scalloped IMC morphology. For a solder/substrate interface, fast cooling rates reduce the thickness of the interfacial IMC layer, as well as the size of IMC particles [59]. Liang, et al. [60] compared the mechanical properties and macro/micro-structure of SAC387 formed with different cooling rates. Figure 2.5 illustrates their results for the typical macrostructures of as-solidified test samples (etched by 10% HCl) for different cooling rates. They found that fast solidification could significantly lower the Sn dendrite arm spacing and enhance the creep resistance of the solder material.

Tensile properties of solder materials are known to be strongly rate and temperature dependent. In the 1980s, Anand [61] proposed a unified plastic/creep constitutive model for describing the viscoplastic behavior of metals. The flow equation in the Anand model establishes the relationship between flow stress and plastic strain, with strain rate and ambient temperature as parameters. This model has been shown to work well on solder materials and is widely used in finite element simulations. Pang, et

al. [62] modified the Ramberg-Osgood model by introducing testing temperature and strain rate, in an attempt to predict the stress-strain behavior for SAC387. Nie, et al. [63] characterized the rate-dependent behavior of SAC387 solder over a wide range of strain rates, from 10^{-6} to 10^{-2} sec^{-1}. Although two different experimental setups were utilized, their test results demonstrated a remarkably consistent relationship between the yield stress and the strain rate over eight decades of strain rate. It has also been demonstrated by several researchers [11, 24, 28, 45], that both stress level and testing temperature have a strong effect on the steady state creep rate of solder materials. In general, higher values of stress and/or temperature significantly accelerates creep and reduces the strain-to-rupture.

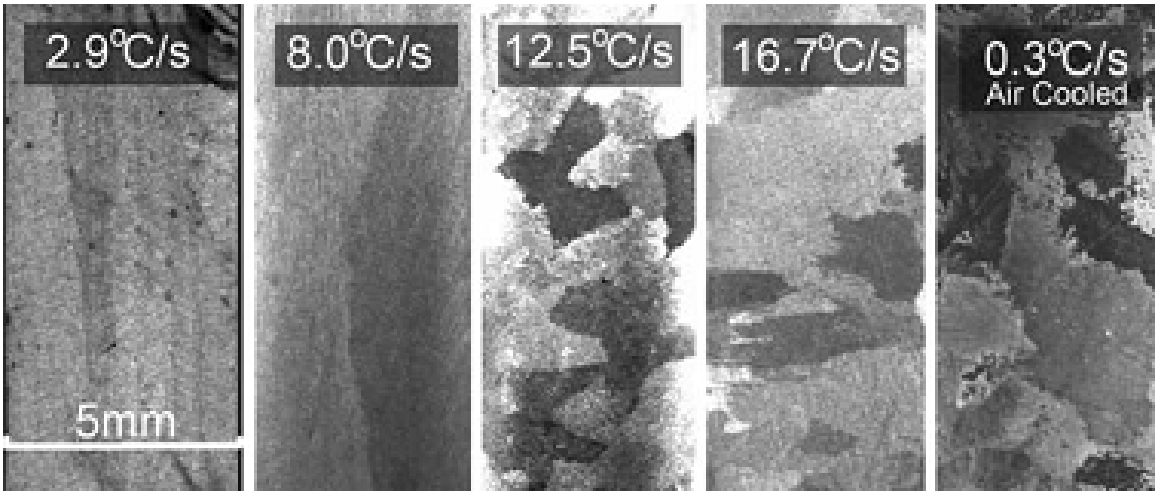

Figure 2.5 As-Solidified Macrostructures of SAC387 [60]

2.4 Cyclic Stress-Strain Behavior of Solder Materials

The stress-strain behavior obtained from a monotonic tension or compression tests can be quite different from that obtained under cyclic loading. This was first observed during the late nineteenth century by Bauschinger [35]. His experiments indicated that

the yield strength in tension or compression was reduced after applying a load of the opposite sign that caused inelastic deformation. Thus, one single reversal of inelastic strain can change the stress-strain behavior of metals. In the early 1960s, Morrow [36] reviewed several experimental techniques and methods for interpreting results and also illustrated typical phenomenological cyclic-dependent deformation and fracture behavior. He observed that a stable hysteresis loop quickly developed under cyclic conditions. Based on this observation, he also developed a descriptive theory of fatigue based upon cumulative plastic strain energy as a criterion for fatigue damage, and elastic strain energy as a criterion for fracture. He demonstrated quantitatively that the fatigue properties of a metal can be related to its cyclic stress-strain properties.

Many prior researchers have studied the cyclic stress-strain behavior of solder materials. Models to predict fatigue life of solder alloys under thermal cycling or thermomechanical fatigue loading have been developed in several investigations [64-71]. For example, Guo, et al. [65] investigated the evolution of the hysteresis loops for both thermomecanical fatigue and isothermal fatigue for 63Sn-37Pb solder, and also compared the hysteresis loops found at various failure cycles. They performed mechanical cyclic tests at 25 C and 80 C under strain control for strain limits of 0.3% to 3%. For thermal cycling, they tested between 25 C and 80 C, with a 120 second ramp. They also developed a mathematical correlation between the sizes of the isothermal hysteresis loop and thermal cycling hysteresis loop.

Busso, et al. [66] studied cyclic stress-strain behavior of 60Sn-40Pb solder using cyclic torsion tests performed on a feedback controlled servo-hydraulic testing machine. They also developed a viscoplastic constitutive model that included a strong Bauschinger

effect exhibited by solder during cyclic loading. Frear, et al. [67] observed that under conditions of cyclic strain, the microstructure of 60Sn-40Pb alloy experienced a heterogeneous coarsening. They then developed a microstructure based finite element simulation methodology for the prediction of solder joint fatigue life. Yang, et al. [71] investigated cyclic stress-strain behavior of 63Sn-37Pb solder under triangular waveform, trapezoid waveform, and multi-level dwell time waveform cyclic loading.

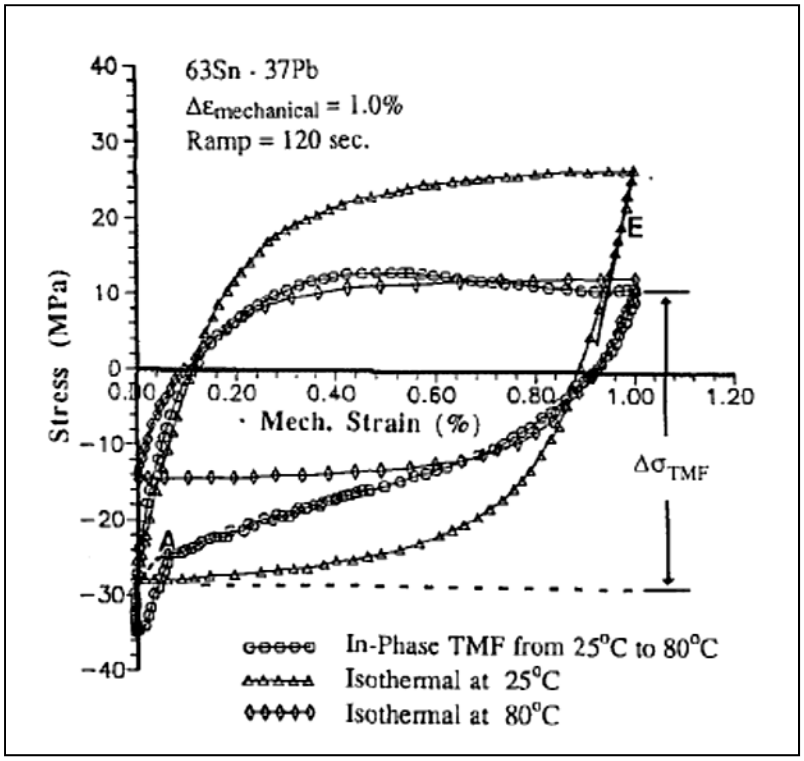

Figure 2.6 Isothermal and Thermal Cycling Hysteresis Loops at N near 0.5 N_f [65]

Measurement of deformations during thermal cycling and stress-strain hysteresis in solder joints have also been examined. For example, Hall [72-73] measured deformations and hysteresis experimentally for the case of a leadless ceramic chip carrier soldered to an FR4 printed wiring board and subjected to thermal cycling. Pao [74-76]

used a 2-beam geometry to successfully measure the thermo-mechanical hysteresis of a variety of Sn-based alloys. Haacke, et al. [77] described a test assembly and reported both hysteresis and thermomechanical fatigue data for Sn based solder, while Raeder and co-workers [78] reported thermomechanical deformation behavior of Sn-Bi eutectic solder under fatigue loading in terms of plastic strain energy density. Dusek, et al. [79] studied the stress vs. strain behavior and evolution of the hysteresis loops of Sn3.5Ag0.5Cu solder during isothermal fatigue at several different temperatures (24, 30, 60, and 125 C). They reported that with slow cycling, where creep and stress relaxation play dominant roles, the number of cycles to failure increases with higher temperatures.

Hu, et al. [80] reported that under constant strain range, the stress range decreased during cyclic testing of Sn-Pb solder. They also observed the fifth hysteresis loops at 22 C for total strain ranges of 1%, 2%, and 5%, and reported that with increasing strain range, the area of the hysteresis loops increased. The stress range was found to have decreased by 85% as the temperature was increased from 22 C to 50 C. Shi, et al. [81] studied the effects of frequency and temperature on hysteresis loops during cyclic loading. They reported that the area of the hysteresis loops decreased with the reduction of the frequency from 1 Hz to 0.0001 Hz, and that the area of hysteresis loop also decreased with the increasing testing temperature from 25 C to 150 C.

2.5 Isothermal and Thermomechanical Fatigue Criteria for Solder Materials

Several previous studies have been conducted on the fatigue behavior of lead free solders. Herkommer, et al. [82] have developed a damage model that is capable of predicting material behavior under both mechanical shear cycling and thermal cycling loading conditions. Zhang and Dasgupta [83, 84] have discussed the mechanical and

thermal cycling durability of selected lead-free solders (Sn3.9Ag0.6Cu, Sn3.5Ag, and Sn0.7Cu), and developed a mechanical fatigue damage criterion. They demonstrated good correlation between predictions of their criterion and experimental cycles to failure under different strain rates and temperature conditions. Whitelaw, et al. [85] have determined the parameters of the Bonder-Partom model from uniaxial cyclic stress-strain tests for both lead-free and Sn-Pb solders. They have also verified their model under isothermal mechanical cycling conditions. Korhonen, et al. [86] conducted uniaxial cyclic tests at various temperatures for near eutectic Sn-Ag-Cu alloy to understand the isothermal fatigue behavior. Nucleation and growth mechanisms of fatigue damage were also observed using optical microscopy, scanning electron microscopy (SEM), and the Electron Back-Scattering Diffraction (EBSD) method.

Kanchanonai, et al. [87] performed uniaxial strain controlled cyclic testing to investigate fatigue failure and mode II crack growth behavior of Sn-3.5Ag eutectic solder alloy for different strain ranges, load drop parameters, and times to failure. Fatigue failure behavior and cyclic creep deformation were observed by Shang, et al. [88], and they related the fatigue behavior to cyclic stress amplitude, number of cycles, stress ratio, frequency, temperature, alloy composition, and microstructure for different lead-free solders. Both uniaxial cyclic tests and shear cyclic tests were carried out by Andersson, et al. [89] to establish a comparison between the isothermal mechanical fatigue properties of lead free solder joints and bulk solders.

Uniaxial cyclic tests were performed by Pang, et al. [90] for SAC387 (95.5Sn-3.8Ag-0.7Cu) and Sn-Cu (99.3Sn-0.7Cu) solder alloys. In their study, the Coffin-Manson model and the Morrow model were used to describe the low cycle fatigue

behavior of the solder materials. The fatigue ductility exponent in the Coffin-Manson law for a Sn-Ag-Cu micro-solder joint was investigated by Kanda, et al. [91] in terms of the cyclic strain-hardening property and inelastic strain energy in fracture for isothermal fatigue. They established a relationship between the equivalent inelastic strain range and the fatigue life under triangular and trapezoidal waves for both as-soldered and aged specimens. Shang, et al. [88] reviewed the recent fatigue studies of Sn-rich Pb-free solder alloys to provide an overview of the current understanding of cyclic deformation, cyclic softening, fatigue crack initiation, fatigue crack growth, and fatigue life behavior in those alloys.

Kim, et al. [92] observed that the lead-free solder (95,5Sn4.0Ag0.5Cu) has a stronger fatigue resistance than the 63Sn37Pb under low loading levels in both thermal and bending tests. However, when the applied load increased, the Sn-Pb solder had the longer fatigue life. Chen, et al. [93] investigated the low cycle fatigue behavior of 63Sn-37Pb solder under strain controlled uniaxial and torsional loading. They reported that the fatigue ductility exponent did not change with the amount of load drop, but that the fatigue ductility coefficient changed in a linear manner with load drop. The Coffin-Manson equation constants for fatigue life estimation of Sn-8Zn-3Bi solder joints were determined by Sun, et al. [94]. The Sn-8Zn-3Bi solder had a melting temperature of around 199 C, which is close to that of the conventional Sn-Pb solder.

Fossum, et al. [95] proposed a practical viscoplastic damage model to characterize 95.5Sn-3.9Ag-0.6Cu lead free solder under cyclic thermomechanical loading conditions. The low cycle fatigue behavior of Sn-3.5Ag, Sn-0.7Cu, and 63Sn-37Pb were investigated by Takahashi, et al. [96] with a non-contact extensometer at room temperature. He

reported that surface features in the low-cycle fatigue test did not appear until 90% of the fatigue life for Sn-3.5Ag, 90% of the fatigue life for Sn-0.7Cu, and, 80% of the fatigue life for 63Sn-37Pb. Isothermal low cycle mechanical fatigue tests of solder joints for 63Sn-37Pb, Sn-3.7Ag, Sn-4.0Ag-0.5Cu and Sn-8Zn-3Bi solders were performed by Andersson, et al. [97]. They found that Sn-4.0Ag-0.5Cu lead free solder exhibited the best isothermal fatigue properties. Lee, et al. [98] found similar results.

Kanchonmai, et al. [99] performed low cycle fatigue tests of Sn-3.5Ag eutectic lead free solder under various temperatures and frequencies, and then used three different prediction models including the Coffin-Manson model, Smith-Topper model, and Morrow model. Lau, et al. [100] investigated the thermal cycling fatigue life of lead-free solder joints in a plastic ball grid array (PBGA) package assembly. They concluded that the thermal-fatigue life of the solder joints would be over-estimated based on a pure-shear theory. In addition to pure shear, bending, twisting and expansion/contraction deformations were needed to be included. Pang, et al. [101] investigated isothermal low cycle fatigue for 95.5Sn-3.8Ag-0.7Cu bulk solder specimens over a range of test temperatures (-40 C, 25 C, 75 C and 125 C) and frequencies (1Hz, 0.01 Hz and 0.001 Hz). They proposed frequency modified Coffin-Manson model and Morrow model relationships for 95.5Sn-3.8Ag-0.7Cu lead free solder at 125 C and over the entire range of test frequencies. Li, et al. [102] studied the effects of tin diffusion, silver and palladium dispersion, and intermetallic compound growth on the shear fatigue life-time and shear strength of 62Sn-36Pb-2Ag solder joints between thick film Pd-Ag conductors.

Bansal, et al. [103] observed a significant degradation in reliability after 500 hours of aging at 150 C for both SAC105 and SAC305 solder joints in 0.5 mm pitch

BGAs and MLF packages. Elevated temperature aging effects on shear fatigue behavior was studied by Venkatadri and coworkers [104] on a SMD test vehicle with SAC305 solder joints. A decrease of more than 70% in fatigue resistance was observed after 3000 hours of aging at 125 C. A more systematic study of aging induced evolution of hysteresis loops and fatigue behaviors of lead free solders was conducted by Mustafa, et al. [105-108]. They reported a decrease in loop area with aging for all SACN05 alloys, indicating reduction of energy dissipation in the material.

2.6 Summary and Discussion

In this chapter, an extensive review has been performed on three major topics in solder material characterization including aging effects, cyclic stress-strain behavior and fatigue behavior of solder material.

Aging effects are the primary reason for the large discrepancies existing in the mechanical property databases for solder materials. Isothermal aging causes significant evolution of microstructure of lead free solders that increases the plasticity of the material behavior. Most lead free solders, especially the Sn-Ag-Cu solder family, experience dramatic loss in strength (both tensile and shear), stiffness, creep and fatigue resistance as aging progresses. This effect was found to be intensified at elevated temperature aging exposures. With respect to soldered components on substrates, aging has also been extensively reported to accelerate unfavorable interfacial IMC growth, cause the formation of Kirkendall voids, and result in the coarsening of the phases in bulk solder joints.

The effects of cooling profile and testing conditions on mechanical properties of solder alloys were also discussed. In general, fast cooling rates (i.e. water quenching)

during solidification yield finer/smaller phases in the microstructure, which in turn strengthens the solder material. However, quickly cooled samples may also exhibit more brittle behavior when subject to deformation, indicating a loss in strain-to-failure. Testing conditions such as strain rate, stress level, and testing temperature are also known to be key factors affecting the mechanical properties of solders. In general, higher strain rates during tensile tests cause strain hardening, and thus increase the strength and stiffness of the material. In creep testing, the response is highly accelerated by small increases in the applied stress loading. Softening effects in material properties have been reported for both tensile and creep tests performed under elevated temperatures.

Previous studies on cyclic stress-strain behavior of solder alloys were also discussed. Several experimental investigations, and developed theories for cyclic stress strain behavior of different solder alloys were presented for various testing conditions. Studies on the dependence of hysteresis loop shape and size for different frequencies and testing temperatures were also discussed. It has been demonstrated that the area of the hysteresis loop decreases with increasing frequency of cyclic loading, whereas the area of the hysteresis loop decreases with the increasing testing temperature. It is also reported in the literature that with increasing strain range, the area of the hysteresis loop increases. Several attempts have also been made to establish a correlation between isothermal mechanical loading hysteresis loops and thermal cycling hysteresis loops for lead free solders.

Lastly, isothermal mechanical fatigue behavior and thermal cycling fatigue behavior of different types of solder materials were discussed. It has been reported that Sn-4.0Ag-0.5Cu lead free solder exhibited the best isothermal fatigue properties. Several

fatigue life prediction models such as, the Coffin-Manson model, Smith-Topper model, and Morrow model have been used by researchers. Fatigue tests have been performed for the solder alloys under strain controlled uniaxial, shear, and torsional loadings. Nucleation and growth mechanisms of fatigue damage were also observed using optical microscopy, scanning electron microscopy (SEM), and the Electron Back-Scattering Diffraction (EBSD) method. Finally, a short discussion of the literature regarding aging effects on fatigue behavior for solder materials has been presented.

CHAPTER 3

SPECIMEN PREPARATION AND EXPERIMENTAL TESTING

3.1 Introduction

In this chapter, a novel specimen preparation technique is presented to fabricate solder uniaxial test specimens. This unique approach is able to fabricate micro-scale uniaxial tensile specimens without further modification and machining. The test specimens are formed in glass tubes with rectangular cross-section by using a vacuum suction system, and then cooled by either a water quenched cooling profile or a specifically designated reflow profile. In the current work, uniaxial samples with nominal dimensions of 80 (length) × 3 (width) × 0.5 (height) mm were utilized. Uniaxial tensile stress-strain and creep tests were then carried out by using a micro tension torsion testing system. Several empirical constitutive models were adopted to represent the collected raw data, and to extract the desired mechanical properties for the solder materials of interest.

3.2 Uniaxial Test Specimen Preparation Procedure

Solder uniaxial samples have been fabricated by machining of bulk solder material [109], or by melting of solder paste in a mold [39, 45, 110-111]. Use of a bulk solder bars is undesirable, because they will have significantly different microstructures than those present in the small solder joints used in microelectronics assembly. In

addition, machining can develop internal/residual stresses in the specimen, and heat generated during turning operations can cause localized microstructural changes on the exterior of the specimens. Reflow of solder paste in a mold causes challenges with flux removal, minimization of voids, microstructure control, and extraction of the sample from the mold. In addition, many of the developed specimens have shapes that significantly deviate from being long slender rods. Thus, undesired non-uniaxial stress states can be produced during loading.

Other investigators have attempted to extract constitutive properties of solders by direct shear or tensile loading [52, 112-113], or indenting [114], of actual solder joints (e.g. flip chip solder bumps or BGA solder balls). While such approaches are attractive because the true solder microstructure is involved, the unavoidable non-uniform stress and strain states in the joint make the extraction of the correct mechanical properties and stress-strain curves from the recorded load-displacement data very challenging. Also it can be difficult to separate the various contributions to the observed behavior from the solder material and other materials in the assembly (bond pads, silicon die, PCB/substrate, etc.).

In an attempt to avoid many of the specimen preparation pitfalls identified above, a novel specimen preparation procedure has been developed at Auburn University. Compared with other specimen fabrication approaches, this unique technique is able to make micro-scale uniaxial tensile specimens with no requirement of further machining/cutting. The solder specimens in this study were formed in high precision rectangular cross-section glass tubes using a vacuum suction process. The tubes were first cooled by water quenching, and then sent through a SMT reflow oven to re-melt the

solder in the tubes and subject them to any desired temperature profile (i.e. same as actual solder joints). The process begins by melting the solder in a quartz crucible using a pair of circular heating elements (see Figure 3.1). A thermocouple attached on the crucible and a temperature control module is used to direct the melting process. One end of the glass tube is inserted into the molten solder, and suction is applied to the other end via a rubber tube connected to the house vacuum system. The suction forces are controlled through a regulator on the vacuum line so that only a desired amount of solder is drawn into the tube. The specimens are then cooled to room temperature via water quenching.

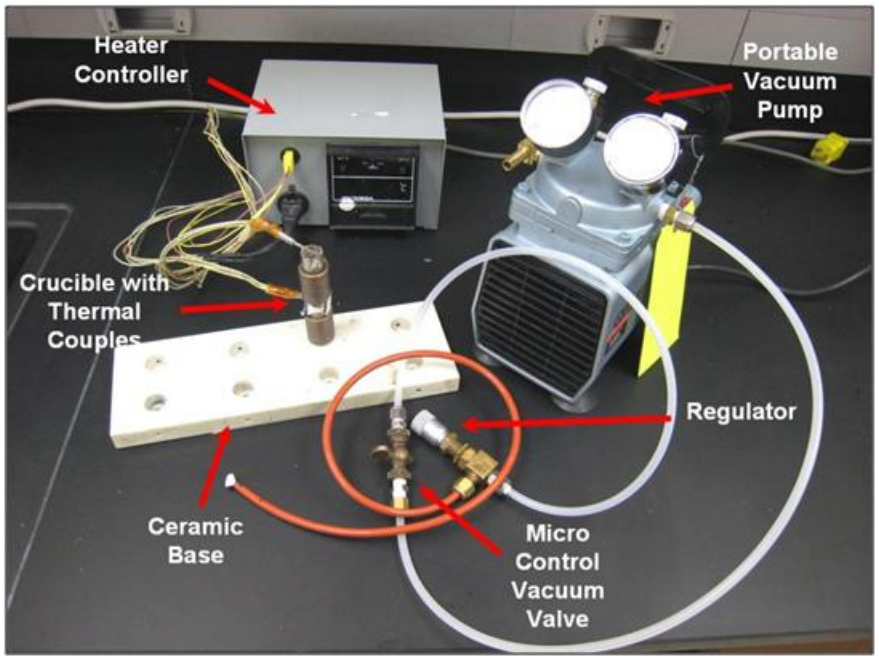

Figure 3.1 Specimen Preparation Hardware

In order to see the extreme variations possible in the mechanical behavior and microstructure, two different cooling profiles were employed in this work:

(1) Water Quenching (W.Q.): water quenching of the tubes (fast cooling rate),

(2) Reflowed (R.F.): controlled heating and cooling using a surface mount technology solder reflow oven.

A typical temperature versus time plot for the water quenching profile is shown in Figure 3.2(a). For the reflow oven controlled cooling, the tubes were first cooled by water quenching, and they were then sent through a reflow oven (9 zone Heller 1800EXL, see Figure 3.3) to re-melt the solder in the tube and subject it to the desired temperature profile. Thermo-couples were attached to the glass tubes and monitored continuously using a radio-frequency KIC temperature profiling system to ensure that the samples were formed using the desired temperature profile (same as actual solder joints). Figure 3.2(b) illustrates the reflow temperature profile used in this work for lead free solder specimens.

Typical glass tube assemblies filled with solder and final extracted specimens are shown in Figure 3.4. For some cooling rates and solder alloys, the final solidified solder samples could be easily pulled from the tubes due to the differential expansions that occur when cooling the low CTE glass tube and higher CTE solder alloy. Other options for more destructive sample removal involve breaking the glass or chemical etching of the glass. The final test specimen dimensions are governed by the useable length of the tube that can be filled with solder, and the cross-sectional dimensions of the hole running the length of the tube. In the current work, uniaxial samples were formed with nominal dimensions of 80 x 3 x 0.5 mm. A thickness of 0.5 mm was chosen because it matches the height of typical BGA solder balls. The specimens were stored in the aging oven immediately after the reflow process to eliminate possible room temperature aging effects.

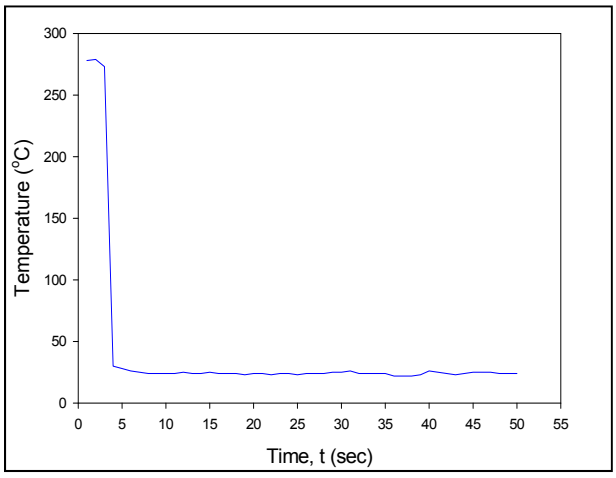

(a) Water Quenching Profile, W.Q.

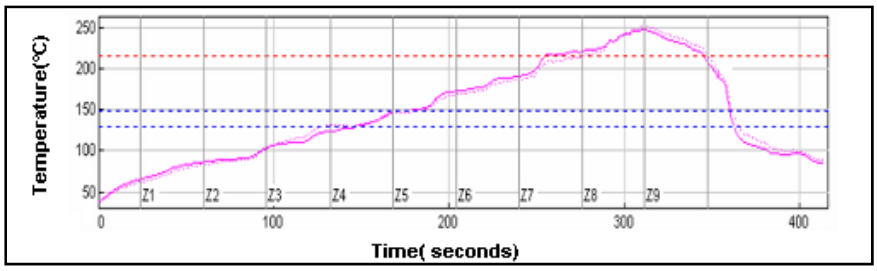

(b) Reflow Profile, R.F.

Figure 3.2 Specimen Cooling/Reflow Profiles

Figure 3.3 Heller 1800EXL Reflow Oven

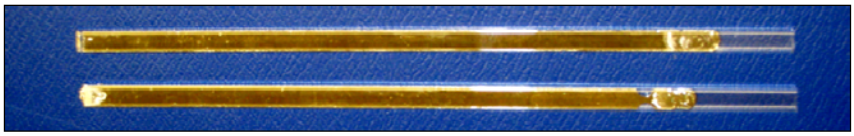

(a) Within Glass Tubes

(b) After Extraction

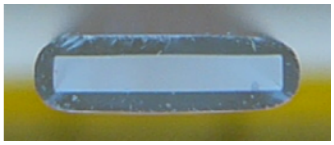

(c) Cross-Section

Figure 3.4 Solder Uniaxial Test Specimens

The described sample preparation procedure yielded repeatable samples with controlled cooling profile (i.e. microstructure), oxide free surface, and uniform dimensions. By extensively cross-sectioned on several specimens, the microstructure of any given sample was proven to be very consistent throughout the volume of the sample. In addition, the specimen preparation method has been demonstrated to yield repeatable

sample microstructures for a given solidification temperature profile. Samples were inspected using a micro-focus x-ray system to detect flaws (e.g. notches and external indentations) and/or internal voids (non-visible). Figure 3.5 illustrates results for good and poor specimens. With proper experimental techniques, samples with no flaws and voids were generated.

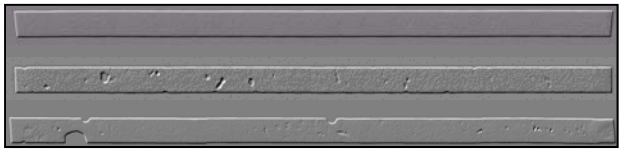

Figure 3.5 X-Ray Inspection of Solder Test Specimens (Good and Bad Samples)

3.3 Mechanical Testing System

A MT-200 tension/torsion thermo-mechanical test system from Wisdom Technology, Inc., as shown in Figure 3.6, has been used to test the samples in this study. The system provides an axial displacement resolution of 0.1 micron and a rotation resolution of 0.001°. Testing can be performed in tension, shear, torsion, bending, and in combinations of these loadings, on small specimens such as thin films, solder joints, gold wire, fibers, etc. Cyclic (fatigue) testing can also be performed at frequencies up to 5 Hz. In addition, a universal 6-axis load cell was utilized to simultaneously monitor three forces and three moments/torques during sample mounting and testing. Environmental chambers, which were added to the system, allow samples to be tested over a temperature range of -185 to +300 C.

The axial stress and axial strain were calculated from the applied force and measured cross-head displacement using:

$$\sigma = \frac{F}{A} \qquad \varepsilon = \frac{\Delta L}{L} = \frac{\delta}{L} \tag{3.1}$$

where σ is the uniaxial stress, ε is the uniaxial strain, F is the measured uniaxial force, A is the original cross-sectional area, δ is the measured crosshead displacement, and L is the specimen gage length (initial length between the grips). The gage length chosen in this study for cyclic tension/compression loading was 10 mm. A short specimen length was necessary so that buckling could be prevented during the compressive part of the cyclic testing. The buckling force was estimated prior to testing using Euler's Formula:

$$F_{cr} = \frac{\pi^2 EI}{L_{eff}^2} \tag{3.2}$$

where E is initial elastic modulus of solder material, and the effective length $L_{eff} = L/\sqrt{2}$ was used for the clamped-clamped end conditions present in the grips of the mechanical testing system.

All short term (no failure) uniaxial cyclic stress-strain tension-compression tests in this paper were conducted using a strain rate of $\dot{\varepsilon} = 0.0001\ sec^{-1}$ for both strain limit controlled and stress limit controlled cyclic tests. Long term fatigue tests to failure were conducted using a constant strain rate of $\dot{\varepsilon} = 0.001\ sec^{-1}$ and several different applied strain ranges. All tests were conducted at room temperature (25 C).

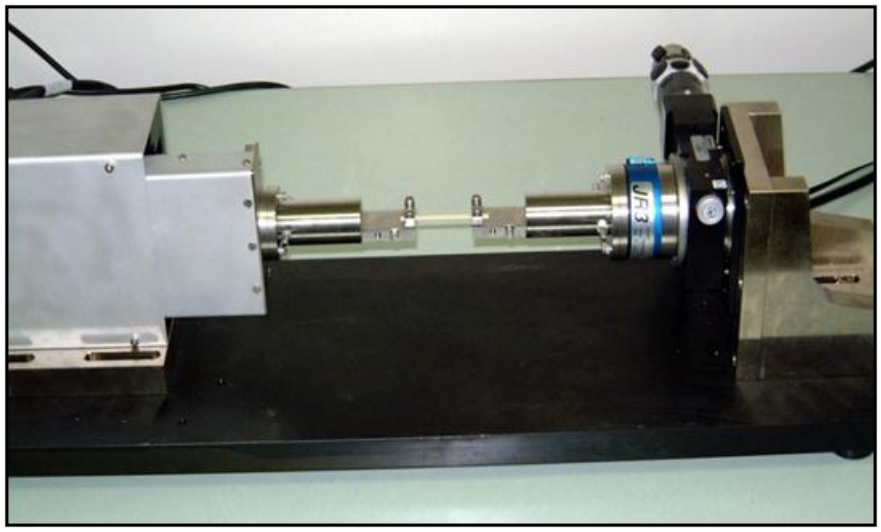

Figure 3.6 MT-200 Testing System with Solder Sample

3.4 Load Train Calibration

During uniaxial testing, forces and displacements were measured. The total displacement includes the displacement due to sample extension and the displacements occurring within the gripping fixtures and load cell. These non-specimen deformations are referred to as load train displacements, and must be either eliminated or compensated for to measure the sample extension accurately. For load train calibration, a very rigid bar was placed between the two microtester (MT-200 Testing System) grips. The load train stiffnesses were measured from the force divided by displacement after applying both tension and compression loads separately. Due to the high rigidity of the bar, all displacements occurring during this calibration could be considered to be from grips and load cell assembly. The load train stiffnesses measured from the tension and compression tests were found to be equal. During loading of a specimen, the measured displacement is

$$\delta = \delta_s + \delta_{LT}$$

Where δ is the total displacement, δ_s is the specimen displacement, and δ_{LT} is the load train displacement. The load train displacement can be evaluated from the applied force in the calibration experiment:

$$F = k_{LT}\delta_{LT} \tag{3.3}$$

where k_{LT} is the load train stiffness. Combining these results, the actual sample displacement can be determined as [115],

$$\delta_s = \delta - \frac{F}{k_{LT}} \tag{3.4}$$

For the present MT-200 test system, the measured value of the load train stiffness was very high, and it caused only 0.01% error during calculation of sample displacement. Thus, the correction term is Eq. (3.4) could be neglected, and the cross-head displacements were assumed to be equal to the specimen displacements.

3.5 Summary and Discussion

A unique specimen preparation procedure was used in this study to fabricate micro-scale solder uniaxial tensile specimens. All solder specimens were formed in glass tubes with rectangular cross-section by using a vacuum suction system. Two cooling profiles were adopted in this study, including water quenching and controlled reflow oven cooling. A short sample (10 mm) was used to avoid buckling during cyclic loading. Typical uniaxial samples with nominal dimensions of 10 × 3 × 0.5 mm have been utilized. The load train stiffness was determined and found to be very high. Therefore, the strain in the sample could be calculated accurately from the cross-head displacement.

CHAPTER 4

EMPIRICAL MODELS FOR UNIAXIAL AND CYCLIC STRESS STRAIN BEHAVIOR OF SOLDER MATERIALS

4.1 Introduction

The irreversible plastic work or plastic strain energy density dissipated in solder materials during a loading cycle can be calculated from the area of the cyclic stress-strain hysteresis loop. This quantity is often used for fatigue assessment under cyclic loading. Energy based failure criteria require the determination of the change of strain energy density accurately for one cycle of the fatigue loading. This necessitates calculating the area of the hysteresis loop, and having a good empirical model for the observed uniaxial cyclic stress-strain behaviors of the material. In this chapter, an empirical model is proposed to characterize the uniaxial and cyclic stress-strain behavior for lead free solders. Comparisons are also shown between proposed empirical model and other models available in the literature.

4.2 Overview: Uniaxial Stress-Strain Relationship

The most common test in plasticity is the uniaxial tension test. Some representative tension test diagrams are shown in Figure 4.1, where the nominal stress σ_N, defined as the load per unit original area cross-section $\frac{P}{A_0}$, is plotted against the conventional strain ε^c. The nominal stress σ_N is proportional to the applied force P, and the conventional strain ε^c to the elongation ΔL. Therefore, the $\sigma_N - \varepsilon^c$ curve is generally

similar to the $P - \Delta L$ diagram obtained from the testing machine. For a typical metal such as low-carbon steel (as shown in Figure 4.1a), the characteristics points and curve portions may be distinguished:

- 1: The proportional limit σ_{PL}
- 2: The elastic limit σ_E
- 3^u and 3^l : The upper σ_Y^u and the lower σ_Y^l yield points
- $3^l - 4$: The region of the perfectly plastic flow
- 4 – 5 : Plastic hardening
- 5: The tensile or the ultimate strength σ_u (the maximal nominal stress or the point of instability)
- 5 – 6: The region of unstable deformation (triaxial deformation resulting in "necking" of the specimen)
- 6: The fracture stress σ_f

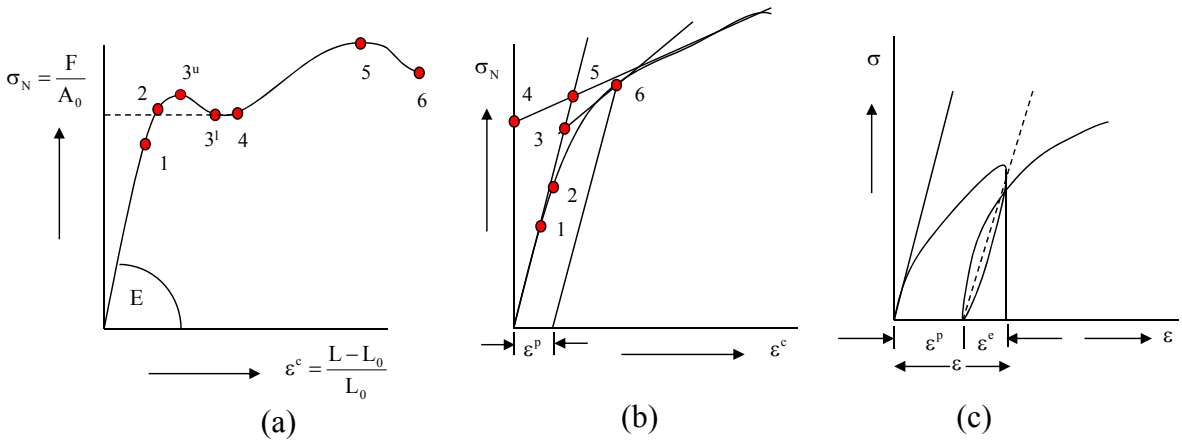

Figure 4.1 Uniaxial stress-strain diagrams: (a) low-carbon steel curve, (b) conventional definition of yield-point stress on stainless steel curve, (c) stress-strain curve of aluminum with effects of unloading and reverse loading

Many materials such as stainless steels, aluminum alloys, and tin alloys do not exhibit the phenomenon of perfectly plastic flow. Therefore, an additional definition of the yield stress based on a defined strain offset must be introduced. These concepts are illustrated in Figure 4.1 (b), where the characteristics points are:

1. The proportional limit (the termination of linearity)
2. The elastic limit
3. The back extrapolation to the zero plastic strain
4. The fixed fraction of the elastic modulus
5. The back extrapolation to the elastic modulus
6. The offset yield strength [116]

Furthermore, some materials do not exhibit any proportional stress-strain curve regions (e.g. annealed copper, brass, etc.). Upon unloading and reloading, a thin curvilinear hysteresis loop is formed, where the average slope is equal to the initial slope at the origin [117].

4.3 Existing Stress-Strain Models for Viscoplastic Materials

It is widely acknowledged that solder materials exhibit elasto-viscoplastic behavior when subject to large deformations. In general, the expression for the total strain can be partitioned into elastic and plastic parts:

$$\varepsilon = \varepsilon_e + \varepsilon_{vp} \tag{4.1}$$

where ε_e is the elastic strain; ε_{vp} is the viscoplastic strain. If the strain hardening effect (the stress continues to increase after yielding) is also taken into consideration, the constitutive model may be expressed in generic terms as:

$$\begin{aligned} \varepsilon = \varepsilon_e = \frac{\sigma}{E} & \qquad \text{for } \|\sigma\| < \sigma_Y \\ \dot{\varepsilon} = \dot{\varepsilon}_e + \dot{\varepsilon}_{vp} = \frac{\dot{\sigma}}{E} + f\left(\sigma, \sigma_Y, \varepsilon_{vp}\right) & \qquad \text{for } \|\sigma\| \geq \sigma_Y \end{aligned} \tag{4.2}$$

Based on the fact that the mechanical properties, such as yield stress, ductility, and tensile strength will change with strain rate and temperature, an ideal viscoplastic constitutive model for solder materials should have the following form:

$$\sigma_{vp} = f\left(\varepsilon_{vp}, \dot{\varepsilon}_{vp}, T\right) \tag{4.3}$$

where σ_{vp} is the von-Mises flow stress; ε_{vp} is the equivalent plastic strain; $\dot{\varepsilon}_{vp}$ is the equivalent plastic strain rate; and T is the temperature. In the past few decades, several physically and phenomenologically based models have been proposed for use in material characterization, including tensile and creep responses. In this section, four constitutive models with approximately the same number of material constants will be discussed including the Johnson-Cook (J-C) model, Zerilli-Armstrong (Z-A) model, Khan-Huang (K-H) model, and Anand model.

4.3.1 J-C Model

In 1983, Johnson and Cook [118] proposed a constitutive model for metals subjected to large strains, high strain rates, and high temperatures. Although it is purely empirical, their model is widely used due to its simplicity and the availability of parameters for various materials of interest. In the J-C model, the flow stress σ is expressed as:

$$\sigma\left(\varepsilon, \dot{\varepsilon}, T\right) = \left(A + B\varepsilon^n\right)\left(1 + C \ln \dot{\varepsilon}^*\right)\left(1 - T^{*m}\right) \tag{4.4}$$

where A, B, C, m, n are material constants; $\dot{\varepsilon}^* = \dot{\varepsilon}/\dot{\varepsilon}_0$ is the dimensionless strain rate ($\dot{\varepsilon}_0$ is normally taken to be 1.0 sec^{-1}), and $T^* = (T - T_r)/(T_m - T_r)$ where T_r is the reference temperature (lowest temperature of interest) and T_m is the melting temperature of the material. With merely one term, the J-C model in its multiplication form is appropriate for describing the temperature dependence of metals. However, this model will be invalid for modeling any metals where the work hardening rate decreases with an increased strain rate. In addition, this model exhibits unrealistically small strain-rate dependence at high temperatures.

4.3.2 Z-A Model

In 1987, Zerilli and Armstrong [119] proposed constitutive relations based on a dislocation mechanism. The Z-A model includes the effects of strain hardening, strain-rate hardening, and thermal softening based on the thermal activation analysis. The general form of the equation for the flow stress is:

$$\sigma(\varepsilon, \dot{\varepsilon}, T) = \sigma_a + B\exp(-\beta\dot{\varepsilon}T) + B_0\sqrt{\varepsilon}\exp(-\alpha\dot{\varepsilon}T) \tag{4.5}$$

In this model, σ_a is the thermal component of the flow stress given by:

$$\sigma_a = \sigma_g + \frac{k_h}{\sqrt{l}} + K\varepsilon^n \tag{4.6}$$

where σ_g is the contribution due to solutes and initial dislocation density, k_h is the microstructural stress intensity, l is the average grain diameter, and K, B, B_0 are material constants. Note that in the thermally activated terms, the functional forms of the exponents α and β are

$$\begin{aligned} \alpha &= \alpha_0 - \alpha_1 \ln(\dot{\varepsilon}) \\ \beta &= \beta_0 - \beta_1 \ln(\dot{\varepsilon}) \end{aligned} \tag{4.7}$$

where α_0, α_1, β_0, β_1 are material parameters that depend on the crystal structure (e.g. FCC, BCC, HCP).

4.3.3 K-H Model

Based on the study of Bordner and Partom [120], Khan and Huang [121] developed a new constitutive model to predict the mechanical behavior of 1100 aluminum in the strain rate range from 10^{-5} to 10^{4} sec^{-1}. In their study, the model proposed was:

$$J_2 = f_1(\varepsilon_2) f_2(D_2) \tag{4.8}$$

where ε_2 is the equivalent plastic strain defined by:

$$\varepsilon_2 = \frac{1}{2}\varepsilon_{ij}\varepsilon_{ij} \tag{4.9}$$

Considering the one dimensional case, Eq. 4.9 can be rewritten as:

$$\sigma = g_1(\varepsilon) g_2(\dot{\varepsilon}) \tag{4.10}$$

where g_1 and g_2 are expressed as:

$$\begin{aligned} g_1(\varepsilon) &= \left[3 f_1\left(\frac{3}{4}(\dot{\varepsilon})^2 \right) \right]^{1/2} \\ g_2(\dot{\varepsilon}) &= \left[f_2\left(\frac{3}{4}(\dot{\varepsilon})^2 \right) \right]^{1/2} \end{aligned} \tag{4.11}$$

Examples of the particular forms of g_1 and g_2 were given in their study:

$$\begin{aligned} g_1(\varepsilon) &= \sigma_0 + E_\infty \varepsilon - a e^{-\alpha\varepsilon} \\ g_2(\dot{\varepsilon}) &= \left(1 - \frac{\ln(\dot{\varepsilon})}{\ln(D_0)} \right)^{-n} \end{aligned} \tag{4.12}$$

where n, E_∞, σ_0, a and α are constants, and D_0 was chosen to be 10^{6} sec^{-1} in their work. Compared to the J-C model, the K-H model is more capable of predicting strong work-

hardening behavior over a large strain-rate range. However, since the K-H model does not incorporate temperature effects into the proposed equations, modifications are needed so that the temperature-dependent characteristics of a material can be fully predicted.

4.3.4 Anand Model

In 1985, Anand [122] proposed a set of constitutive equations for large isotropic viscoplastic deformations but small elastic deformations. This constitutive model has been embedded in commercial finite element simulation software such as ANSYS, and is now widely used for modeling of solder materials. There are three equations in the Anand model; namely the stress equation, flow equation, and evolution equation.

The stress equation is defined by:

$$\sigma = cs \qquad (c < 1) \tag{4.13}$$

where s is the deformation resistance, and c is a parameter defined as:

$$c = \frac{1}{\xi}\sinh^{-1}\left[\left(\frac{\dot{\varepsilon}}{A}e^{Q/RT}\right)^{m}\right] \tag{4.14}$$

where ξ is the multiplier of stress, $\dot{\varepsilon}$ is the inelastic strain rate, A is the pre-exponential factor, Q is the activation energy, m is the strain rate sensitivity, R is the universal gas constant, and T is the absolute temperature.

The flow equation was selected to accommodate the strain rate dependence on the stress, and is given by:

$$\dot{\varepsilon} = A\exp\left(-\frac{Q}{RT}\right)\left[\sinh\left(\xi\frac{\sigma}{s}\right)\right]^{1/m} \tag{4.15}$$

Note that temperature dependence has been incorporated into the model via an Arrhenius term.

The evolution equation for the internal variable s is assumed to be:

$$s = f(\dot{\varepsilon}, \varepsilon, T) \tag{4.16}$$

An explicit form of evolution equation is expressed as:

$$\dot{s} = \left[h_0 \left(1 - \frac{s}{s^*} \right)^a \operatorname{sign}\left(1 - \frac{s}{s^*} \right) \right] \dot{\varepsilon} \qquad (a > 1) \tag{4.17}$$

where h_0 is a constant for the dynamic process, a is the strain rate sensitivity of the dynamic process, and s* represents a saturation value of s associated with a given set of testing conditions given by:

$$s^* = \hat{s} \left[\frac{\dot{\varepsilon}}{A} \exp\left(-\frac{Q}{RT} \right) \right]^n \tag{4.18}$$

where $\hat{s}$ is a constant, and n is the strain rate sensitivity for the saturation value of deformation resistance.

To summarize, the Anand model has nine material constants, i.e. s_0, Q, A, ξ, m, h_0, $\hat{s}$, n, and a (note that s_0 is the initial value of deformation resistance). These constants can be determined from either stress-strain responses or creep responses characterized over a wide temperature range. The Anand model successfully unifies both rate-dependent creep behavior and rate-independent plastic behavior occurring concurrently, and it has been demonstrated to work well on solder materials. On the other hand, there are still some limitations of the Anand model, such as incapability of predicting the primary and tertiary creep responses, no incorporation with aging effects, etc.

4.3.5 Other Models

Several other empirical models are available in the literature for representing uniaxial stress-strain relationships. Some simple empirical formulae called

schematizations of the stress-strain diagrams were introduced for theoretical computations such as the Mises model [123], Prandtl model [124], and Ilyushin model [125]. Nonlinear empirical plastic hardening schematizations may also be obtained by fitting the experimental data. Some useful proposals for the power plastic hardening materials are available in the literature including the Ludwik model [126], Swift model [127], and Ramberg-Osgood model [128]. Generalized asymptotic approximations for uniaxial stress-strain relationship were proposed by Szuwalski [129] and Betten [130]. Similar to the Anand viscoplastic model, McDowell [131] proposed a unified constitutive model for viscoplastic materials. These models are tabulated in Table 4.1.

4.4 Hyperbolic Tangent Empirical Model for Solder Stress-Strain Behavior

Although, several different mathematical models can be used to represent the constitutive behavior of solder, an empirical hyperbolic tangent model has been used in this work to accurately represent the stress-strain behavior. Hyperbolic tangent terms were first used by Anderson and Berkyto [132], and then later by Suhling [133] for representing stress-strain behavior of cellulosic materials. In the present work, it has been demonstrated that hyperbolic tangent functional terms are also useful for the representation of the nonlinear stress-strain behavior of solder alloys.

Table 4.1 Empirical Models for Stress Strain Behavior

(a) Schematizations of Stress Strain Curves

$\sigma = \sigma_0$	(Mises, 1913)
$\sigma = \begin{cases} E\varepsilon & \left(\varepsilon \le \dfrac{\sigma_0}{E}\right) \\ \sigma_0 & \left(\varepsilon \ge \dfrac{\sigma_0}{E}\right) \end{cases}$	(Prandtl, 1928)
$\sigma = \begin{cases} E\varepsilon\left(\varepsilon \le \dfrac{\sigma_0}{E}\right) \\ E\varepsilon\left[1-\omega(\varepsilon)\right]\left(\varepsilon \ge \dfrac{\sigma_0}{E}\right) \end{cases}$ $\omega(\varepsilon) = \dfrac{E-E_1}{E}\left(1-\dfrac{\sigma_0}{E\varepsilon}\right)$	(Ilyushin, 1946)
$\sigma = k\varepsilon^n$	(Ludwik, 1909)
$\sigma = C(m+\varepsilon)^n$	(Swift, 1952)
$\dfrac{E\varepsilon}{\sigma_0} = \dfrac{\sigma}{\sigma_0} + k\left(\dfrac{\sigma}{\sigma_0}\right)^m$	(Ramberg-Osgood, 1943)

(b) Unified Constitutive Model

$\dot{\sigma} = E\left(\dot{\varepsilon} - \dot{\varepsilon}^{IN}\right) + \left[\varepsilon - \varepsilon^{IN} - \alpha\left(T - T_0\right)\right]\dot{E}$ $- E\left[\left(T - T_0\right)\dot{\alpha} + \alpha\dot{T}\right]$	(McDowell, 1994)

(c) Generalized Asymptotic Approximations

$\varepsilon = \dfrac{\sigma}{E\left(1-\dfrac{\sigma}{\sigma_0}\right)^n} \qquad n \ge 0$	(Szuwalski-Życzkiwski, 1973)
$\dfrac{\sigma}{\sigma_0} = \dfrac{E\dfrac{\varepsilon}{\sigma_0}}{\left[1+\left(\dfrac{E\varepsilon}{\sigma_0}\right)^m\right]^{\frac{1}{m}}}$	(Betten, 1975)

The hyperbolic tangent function "tanh(ε)" can be expressed as power series expansion using:

$$\tanh(\varepsilon) = \varepsilon - \underbrace{\frac{\varepsilon^3}{3} + \frac{2\varepsilon^5}{15} - \frac{17\varepsilon^7}{315} + ...}_{\text{Non-Linear Term (Plastic Region)}} = \sum_{n=1}^{\infty} \frac{2^{2n}\left(2^{2n}-1\right)B_{2n}\varepsilon^{2n-1}}{2n!}, \varepsilon < \frac{\pi}{2} \qquad (4.19)$$

Linear Term (Elastic Region)

The typical appearance of a solder stress-strain curve and desired boundary conditions are shown in Figure 4.2. For boundary condition 1, the initial slope $\frac{d\sigma}{d\varepsilon}$, should be nearly constant for small ε as the initial stress-strain curve is approximately linear. For boundary condition 2, σ(ε) should be nearly constant when the value of ε is very large as the stress-strain curve saturates at the level of the ultimate strength for large strains.

The initial slope (effective elastic modulus) of the tanh(ε) function can be calculated by taking the derivative of σ(ε) with respect to ε at ε = 0:

$$\left.\frac{d\sigma(\varepsilon)}{d\varepsilon}\right|_{\varepsilon=0} = \left.\frac{d(\tanh(\varepsilon))}{d\varepsilon}\right|_{\varepsilon=0} = \left.1 - \frac{3\varepsilon^2}{3} + \frac{10\varepsilon^4}{15} - \frac{119\varepsilon^6}{315} + ...\right|_{\varepsilon=0}$$
$$\Rightarrow \left.\frac{d\sigma(\varepsilon)}{d\varepsilon}\right|_{\varepsilon=0} = 1(\text{Constant}) \qquad (4.20)$$

For large strain, the tanh(ε) function becomes

$$\lim_{\varepsilon \to \infty}\left[\tanh(\varepsilon)\right] = \lim_{\varepsilon \to \infty}\left[\frac{e^{\varepsilon} - e^{-\varepsilon}}{e^{\varepsilon} + e^{-\varepsilon}}\right] = \frac{1 - \frac{1}{e^{\infty}}}{1 + \frac{1}{e^{\infty}}} = 1(\text{Constant}) \qquad (4.21)$$

From Eqs. 4.20 and 4.21, it is clear that the hyperbolic tangent term tanh(ε) has the ability to fulfill the boundary conditions of a typical solder stress-strain curve.

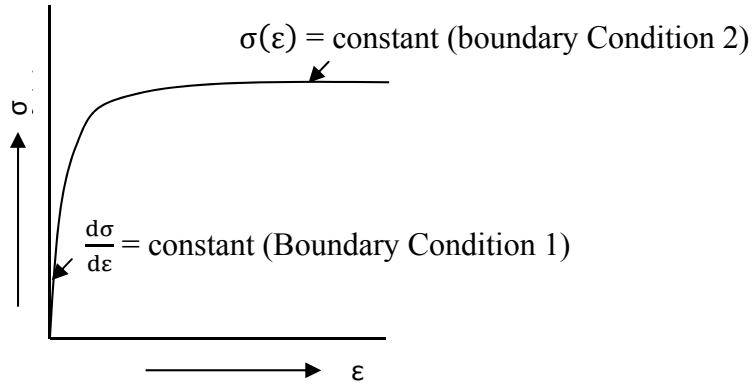

Figure 4.2 Typical Trend of Stress-strain Curve for Viscoplastic Solder Material

A general series of hyperbolic tangent terms can be written as,

$$\sigma(\varepsilon) = \sum_{n=1,3,5...}^{N} C_n \tanh(C_{n+1}\varepsilon) \tag{4.22}$$

The constants C_1, C_2, …., C_{N+1} can be chosen by nonlinear regression analysis to fit this function to a set of solder stress-strain data. For example, a set of 52 stress vs. strain data points were measured for a SAC405 solder sample. The curve fitting tool in Matlab was used to fit Eq. (4.22) to this data with various values of N. The results are illustrated in Figure 4.3 for N=1, 2, 3, 4. It was observed that extremely good fits ($r^2 \geq 0.999$) were obtained for $N \geq 2$.

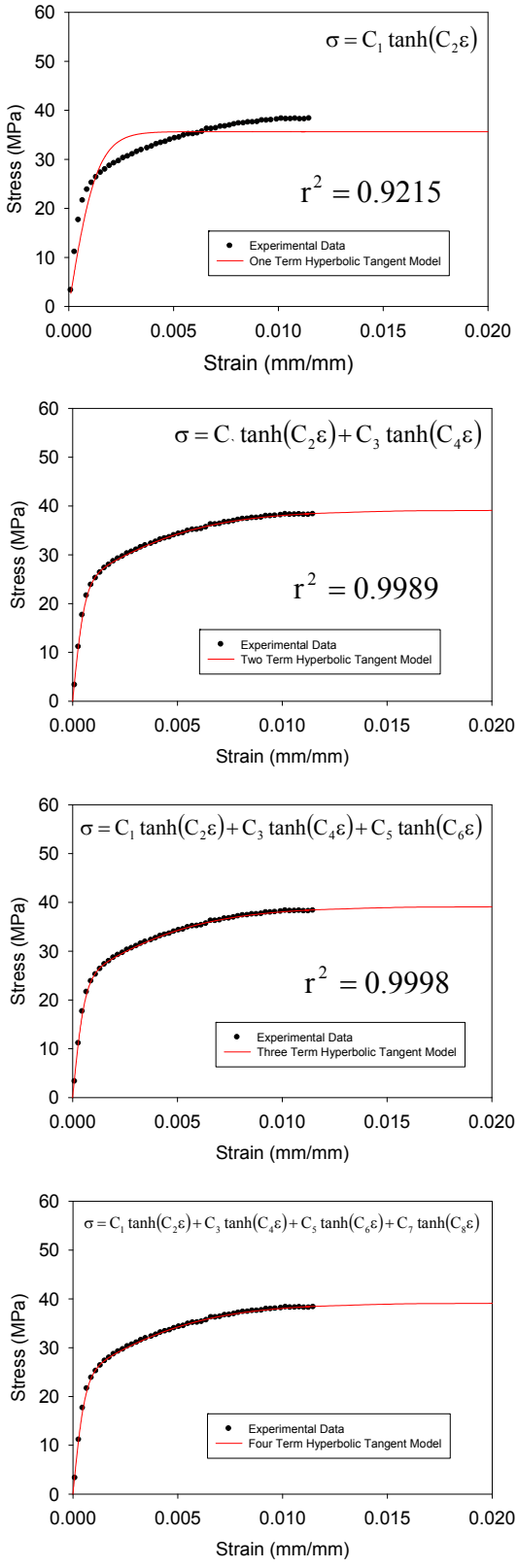

Figure 4.3 Non-linear Regression Fit of Experimental Data of SAC405 Solder Alloy Using Hyperbolic Tangent Model with Different Hyperbolic Tangent Terms

Similar results were found for other sets of SAC405 stress-strain data as illustrated in Table 4.2. In addition, the 2-term hyperbolic tangent model (C_1, C_2, C_3, C_4) was found to fit lead free solder data well for a variety of lead free solder alloys as shown in Figure 4.4. Additional discussion on empirical models for solder is presented in Appendix A.

Table 4.2 Coefficient of Variation (r^2) Values for Hyperbolic Tangent Model Fits to SAC405 Data

Test No.	One Term	Two Terms	Three Terms	Four Terms
Sample 1	0.9215	0.9989	0.9998	0.9998
Sample 2	0.9187	0.9980	0.9997	0.9997
Sample 3	0.9095	0.9972	0.9995	0.9996

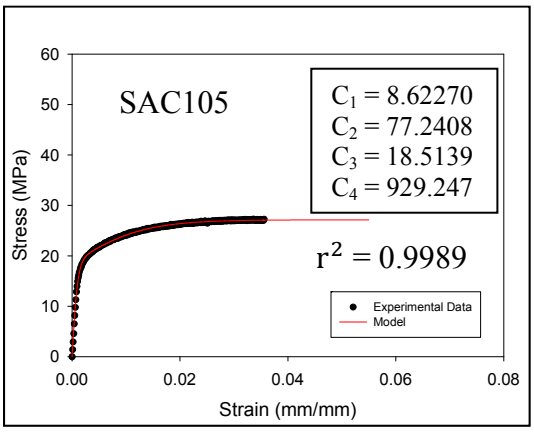

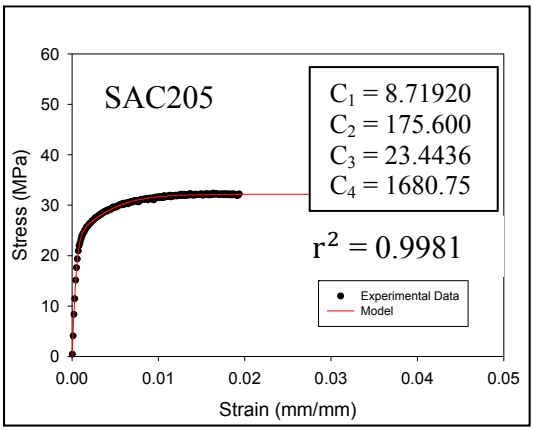

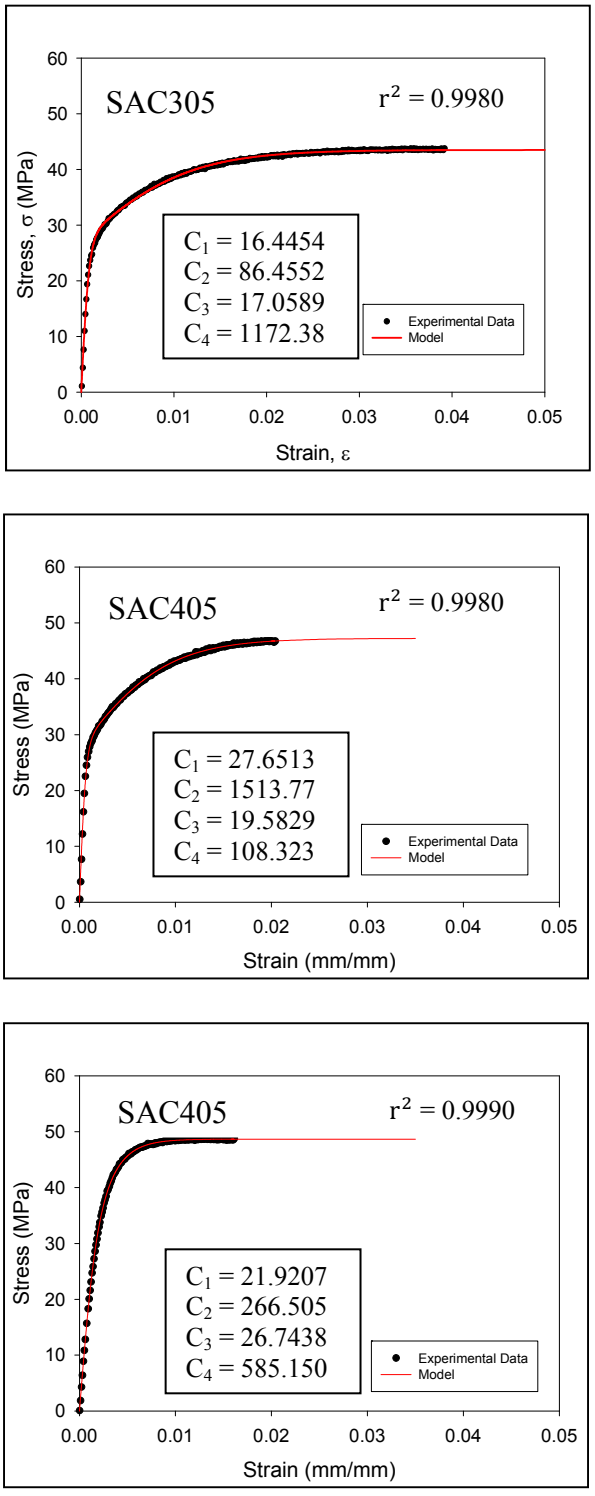

Figure 4.4 Non-linear Regression Fits to Experimental Data for Different Types of Solder Alloys Using the Two Term Hyperbolic Tangent Model

Since the four parameter hyperbolic tangent model has worked well for all solder alloys, it has been used to represent solder stress-strain data in the remainder of this work. It can be expressed as:

$$\sigma = C_1 \tanh(C_2\varepsilon) + C_3 \tanh(C_4\varepsilon) \tag{4.23}$$

where, C_1, C_2, C_3, C_4 are the material constants to be determined using nonlinear regression analysis. For this model, the effective elastic modulus (E) can be estimated as:

$$E = \lim_{\varepsilon \to \infty}\left[\frac{d\sigma(\varepsilon)}{d\varepsilon}\right] = \lim_{\varepsilon \to \infty}\left[C_1C_2\left\{\left(1-\tanh^2(C_2\varepsilon)\right) + C_3C_4\left(1-\tanh^2(C_4\varepsilon)\right)\right\}\right] \tag{4.24}$$

$$E = C_1C_2 + C_3C_4$$

and the ultimate tensile strength (UTS) can be found using:

$$\sigma = \lim_{\varepsilon \to \infty}\left[\sigma(\varepsilon)\right] = C_1 + C_3 \tag{4.25}$$

Comparisons are shown in Figure 4.5 for 5 different empirical models including the two term hyperbolic tangent model, Weibull model, Ludwik model [126], Ramberg-Osgood model [128], and Swift model [127]. For this set of solder data, the accuracy (r^2 value) for the four parameter hyperbolic tangent model fit was the highest among all of the empirical models. Figure 4.6 illustrates a set of example stress-strain curves for SAC105 (Sn-1.0Ag-0.5Cu) lead free solder tested at room temperature for a strain rate of 0.0001 sec^{-1}, and the corresponding fit of Eq. (4.22) to the data. The excellent representation provided by the hyperbolic tangent empirical model suggests that it provides an accurate mathematical description for the "average" stress-strain curve through a set of multiple experiment curves measured under the same conditions.

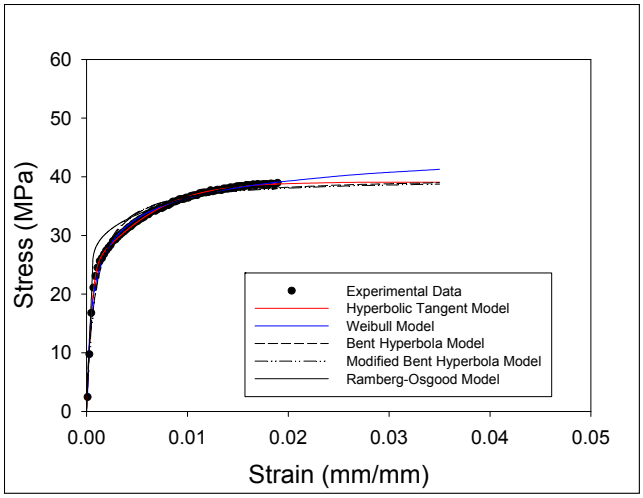

Model	r^2
Hyperbolic Tangent Model	0.998
Weibull Model	0.990
Ludwick Model	0.985
Ramberg-Osgood Model	0.973
Swift Model	0.984

Figure 4.5 Comparisons of Regression Fits for Different Empirical Models

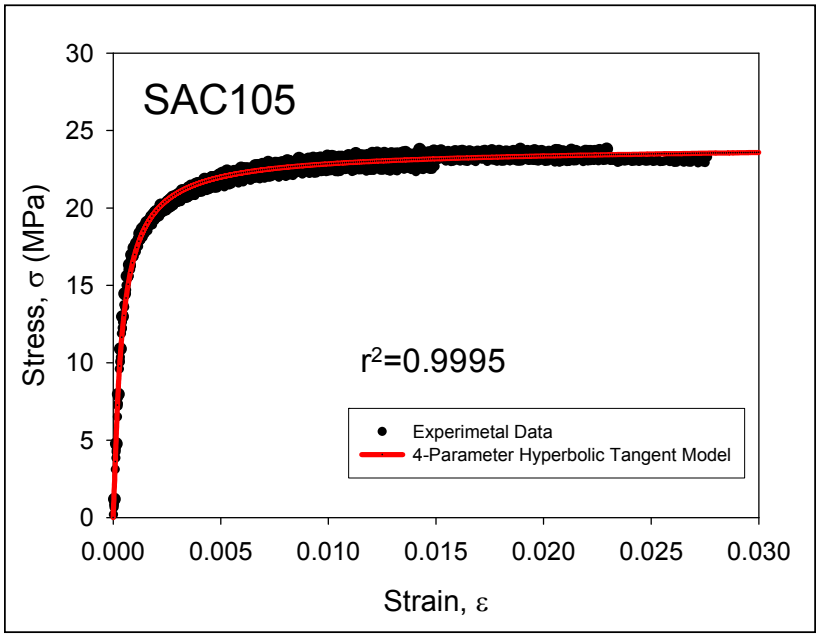

Figure 4.6 SAC105 Stress-Strain Curves and Empirical Model

4.5 Calculation of Hysteresis Loop Area

In past years, a number of relationships have been proposed relating the low- and high-cycle fatigue life to the plastic strain energy stored in the material during a load cycle (area of the hysteresis loop) [134]. To unify both low and high cycle fatigue, the total cyclic strain energy density, ΔW_t (plastic and elastic), has been proposed as a promising damage parameter [134]. This is also consistent with non-linear fracture mechanics approaches to fatigue crack propagation. Since the plastic strain energy density is calculated from the area of the hysteresis loop generated during cyclic loading. It is important to calculate this area accurately using appropriate empirical models to represent the cyclic stress-strain curve.

In this work, the four-parameter hyperbolic tangent model was used to calculate the area of the hysteresis loop generated during cyclic loading. To process the cyclic stress-strain data and calculate the areas of the associated hysteresis loops, a pair of empirical models have been used to represent the tension portion (C to B, top as shown in Figure 4.7) and the compression portion (B to C, bottom as shown in Figure 4.7) of the stress-strain behavior in each cycle. Figure 4.7 illustrates the definitions of the two portions of the stress-strain cycle and the empirical fits $f_1(\varepsilon)$ for the compression loading region (bottom of the hysteresis loop) and $f_2(\varepsilon)$ for the tensile region (top of the hysteresis loop). Extending the hyperbolic tangent expression in Eq. (4.23), the following empirical models were found to fit our experimental cyclic stress-strain data well:

$$f_1(\varepsilon) = -A_1 \tanh(A_2(-\varepsilon+\varepsilon_2)) - A_3 \tanh(A_4(-\varepsilon+\varepsilon_2)) + \sigma_1$$

$$f_2(\varepsilon) = B_1 \tanh(B_2(\varepsilon-\varepsilon_1)) + B_3 \tanh(B_4(\varepsilon-\varepsilon_1)) + \sigma_2 \qquad (4.26)$$

where

$$\varepsilon_1 \le \varepsilon \le \varepsilon_2$$

From the stress-strain data for each cycle, the constants in the empirical models in Eq. (4.26) can be determined through a nonlinear regression analysis. The hysteresis loop area can then be evaluated analytically or numerically using

$$\Delta W = \int_{\varepsilon_1}^{\varepsilon_2} \left[f_2(\varepsilon) - f_1(\varepsilon) \right] d\varepsilon \tag{4.27}$$

This area represents the plastic energy density dissipated per cycle during the cyclic loading.

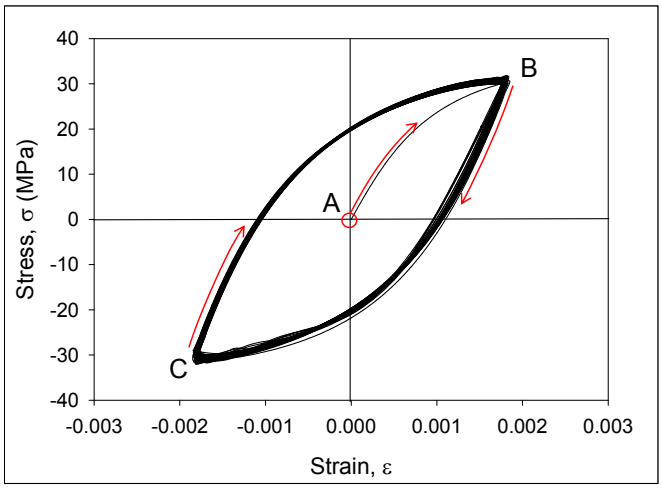

Figure 4.7 Typical Cyclic Stress-Strain Test Results for SAC Solder (Strain Controlled)

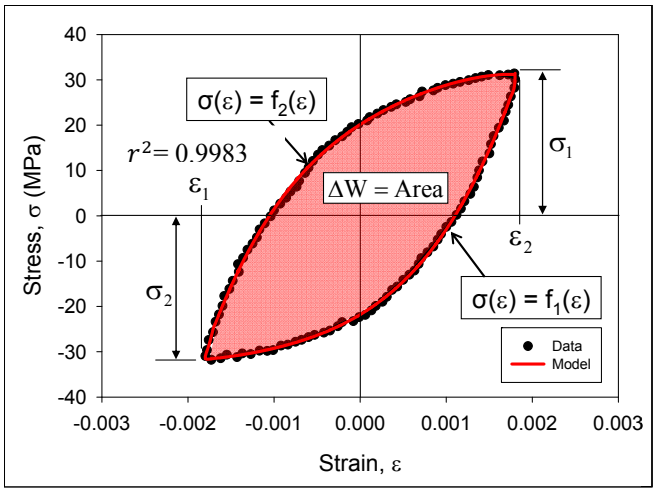

Figure 4.8 Typical Hysteresis Loop and Area Calculation

4.6 Summary and Discussion

In summary, a four-parameter hyperbolic tangent model was developed to represent uniaxial and cyclic experimental solder stress-strain data. Other models available in the literature were also discussed. Comparisons were made between the proposed four-parameter hyperbolic tangent model and the literature models. Based on the r^2 values of the non-linear regression fits, the four-parameter hyperbolic tangent model was found to be superior for representing solder experimental data. A mathematical technique was also developed to calculate the area of the hysteresis loop generated during cyclic loading using the hyperbolic tangent model.

CHAPTER 5

EFFECTS OF AGING ON CYCLIC STRESS-STRAIN BEHAVIOR OF LEAD FREE SOLDER MATERIALS

5.1 Introduction

While the effects of aging on solder constitutive behavior (stress-strain and creep) have been examined in some detail, there have been no prior studies on the effects of aging on solder failure/fatigue behavior. In this chapter, the effects of several parameters (aging, temperature, strain/stress limits, and solder alloy composition) on the cyclic stress-strain behavior of lead free solders are investigated. Uniaxial SAC lead free solder specimens were subjected to cyclic (tension/compression) mechanical loading under both strain control (constant positive and negative strain limits) and stress control (constant positive and negative stress limits). The hysteresis loop size (area) was calculated from the measured cyclic stress-strain curves for a given solder alloy and temperature, and then empirical models were used to represent the evolution of the solder hysteresis loops with aging. Most tests in this investigation were performed with SAC105 solder alloy. However, the effect of solder composition was examined in a limited way by testing four SAC alloys (SAC105, SAC205, SAC305, SAC405) with varying silver content (1-4%) under strain controlled cycling. In addition, the effect of the testing temperature has also been studied by performing cyclic testing of SAC405 samples at four different temperatures (25, 50, 75, and 100 C).

5.2 Overview of Cyclic Stress-Strain Behavior

Analysis of cyclic stress-strain behavior of solder material is important for the determination of fatigue characteristics and modeling of the fatigue damage process. Based on the literature, there are two basic approaches for description of the fatigue process using energy approaches. In the first case, the total energy accumulated in the fatigue process is taken into account. This energy is comparable with the energy dissipated in static tension tests. Suggestions for such an approach can be found for example in the papers by Feltner and Morrow [135], and Lin [136], Lin and Haicheng [137].

In the second approach, the accumulation of dissipated energy in particular cycles of variable loading is taken into accoacunt. Three groups of suggestions can be observed in this approach. These take into account:

a) Plastic strain energy density W_p solely; This approach was presented in the papers by Gołoś [138], Kaleta [139], Mroziński and Topoliński [140]. Based on the literature information, it can be stated that this type of fatigue model is accurate for low-cycle fatigue.

b) Sum of Plastic strain energy density W_p and elastic strain energy density W_e; This approach can be found in the papers by Ellyin [141]. Gołoś [142], and Gołoś and Ellyin [143]. This type of approach is more accurate for high-cycle fatigue.

c) Plastic-elastic strain energy density W_t; In this approach, the separation of the total strain energy into elastic and plastic

components is omitted. Such an approach was suggested in the papers by Łagoda [144], and Smith et al. [145].

Fatigue graphs in the energy-life approach with the use of W_p, W_e and W_t parameters are mostly obtained using cyclic stress-strain tests performed under controlled stress or strain limits. The strain energy density is calculated from the area of the hysteresis loop generated during cyclic loading. Therefore, sufficient studies on cyclic stress-strain behavior and hysteresis loop evolution are needed before finding fatigue characteristics and developing fatigue model of solder materials.

5.3 Hysteresis Loop During Cyclic Loading

Typical cyclic stress-strain testing results for a SAC solder uniaxial specimen are shown in Figure 5.1. In this case, the specimen was tested in strain controlled cycling with strain limits of ±0.0018. The sample was initially relaxed (unloaded, point A), and then a tensile loading was applied to generate the initial portion of the stress-strain curve (similar to the initial portion of the monotonic test results in Figure 4.6). Tensile loading was continued until the strain reached +0.0018 (point B). At that time, the loading direction and the direction of cross-head motion were reversed. The sample was then compressed until the strain reached -0.0018 (point C), when the direction of loading and extension was reversed again (to be tensile). Testing continued in tension until the strain again reached +0.0018 (point B) and the first hysteresis loop was completed. Further loops (between points B and C) were generated by continuing the alternating compressive and tensile loadings in a similar manner. The variation of the hysteresis loop area with cycle number for the first 100 cycles in Figure 5.1 is shown in Figure 5.2.

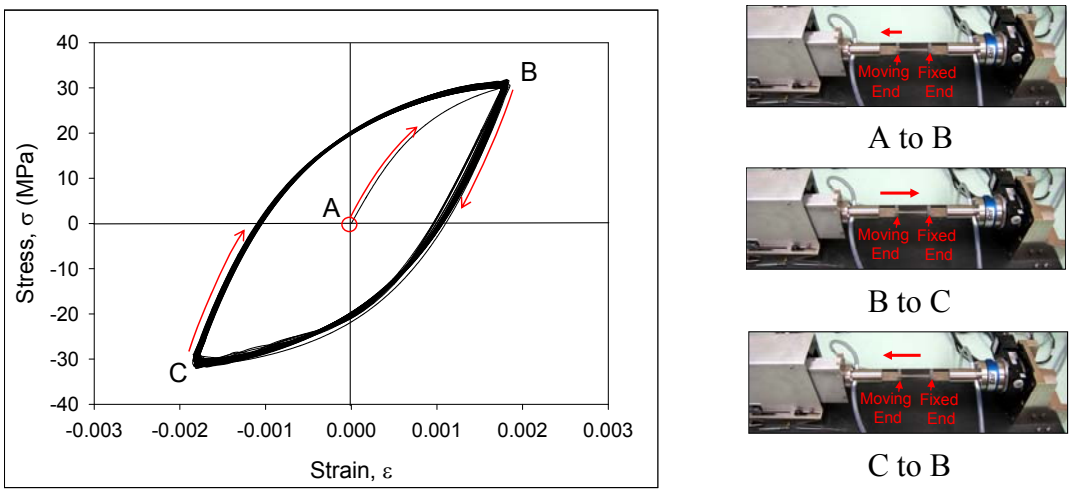

Figure 5.1 Typical Cyclic Stress-Strain Test Results for SAC Solder (Strain Controlled)

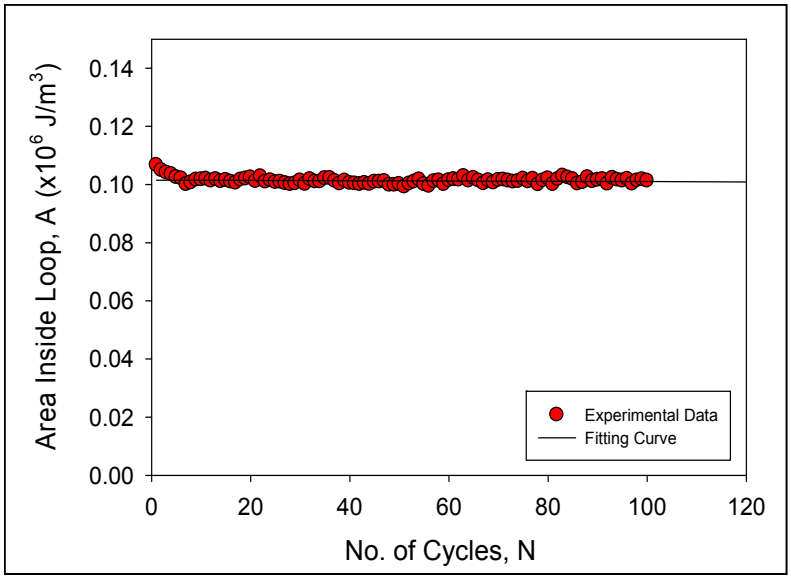

Figure 5.2 Variation of Hysteresis Loop Area with Number of Cycles

A triangular strain vs. time or stress vs. time waveform with a constant strain rate of 0.0001 sec^{-1} has been employed for all cyclic tests as shown in Figure 5.3 and Figure 5.4. For strain limit controlled cyclic tests, the strain limits were ±0.0018, and for stress limit controlled cyclic tests, the stress limits were ±10 MPa. As a constant strain rate was maintained, a frequency of 0.85 Hz was employed for the strain limit controlled cyclic tests. For the stress limit controlled cyclic tests, the frequency of the strain waveform varied from 0.93 Hz to 3 Hz. As shown in Figure 5.2, stabilization occurs after initial cyclic softening, and the hysteresis loop area remains nearly constant for the first 100 cycles.

5.4 Effects of Aging for Strain Controlled Cyclic Testing

Strain controlled cyclic testing has been performed on a SAC105 samples (WQ and RF) subjected to aging at 125 C. The WQ and RF solidification cooling profiles used in the sample preparation yielded two distinctly different initial microstructures for the samples (WQ samples have finer microstructures and higher/better mechanical properties). After solidification, the samples were subjected to aging at 125 C for various durations including 0, 5, 10, 30, 60, 90, 120, 150, 180, 270 and 360 days (0-12 months). The 0-day aging specimens represented non-aged samples, which were tested within a few minutes after solidification. There were 5 specimens in each leg of the test matrix. Each set of 5 specimens had a fixed sample cooling profile (WQ or RF) and aging time (one of 9 different durations). The strain controlled testing was performed with strain limits of ±0.0018, and the testing temperature was 25 C.

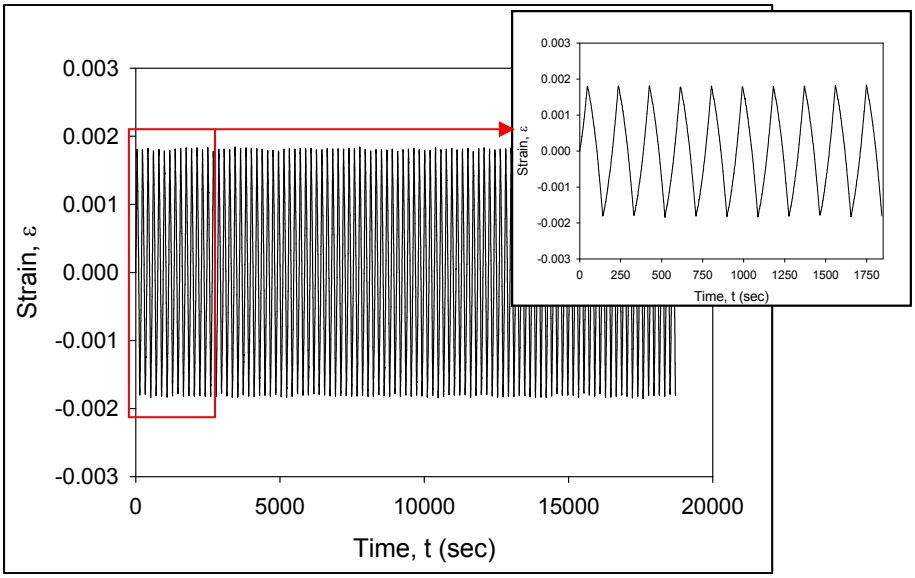

Figure 5.3 Strain Limit Controlled Cyclic Test

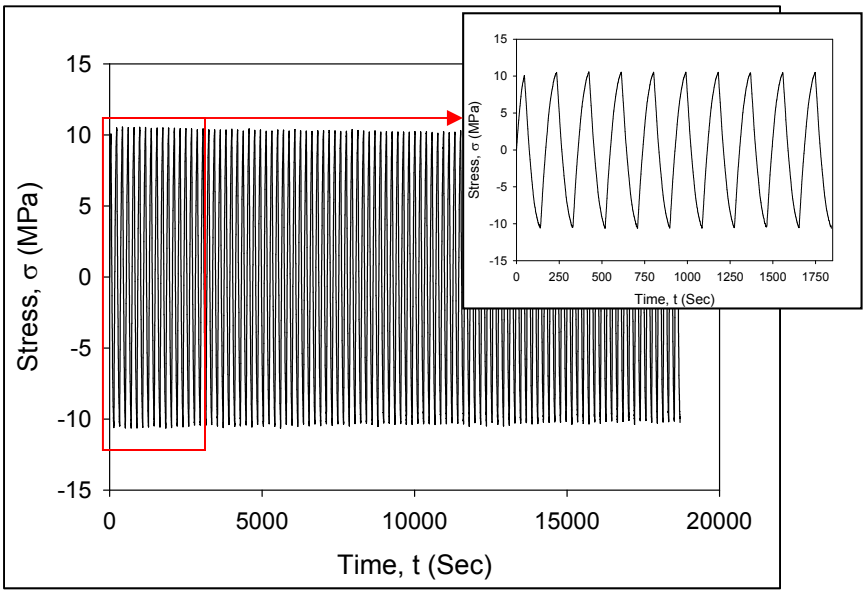

Figure 5.4 Stress Limit Controlled Cyclic Test

Figure 5.5 illustrates example plots of the cyclic stress-strain behavior for WQ samples subjected to the 10 different aging times. Each plot contains one of the five test results obtained for a particular aging duration. Results for the other 4 samples were remarkably similar, and the data showed a high level of consistency and repeatability from sample to sample as shown in Figure 5.6 for samples with no aging and for samples with 60 days of aging at 125 C. Similar results were found for other aging conditions.

It is observed that the hysteresis loops rotate and become smaller in height as aging progresses. From the recorded data, the hysteresis loop areas were calculated using the procedure outlined in Chapter 4. A plot of the evolution of the hysteresis loop area with aging time is shown in Figure 5.7. In this graph, each data point represents the average value of the 5 tests performed for a particular aging duration. The area of hysteresis loop denotes the energy density (volumetric) dissipated per cycle, and is related to the damage accumulated per cycle. The units are in J/m^3 (energy per unit volume).

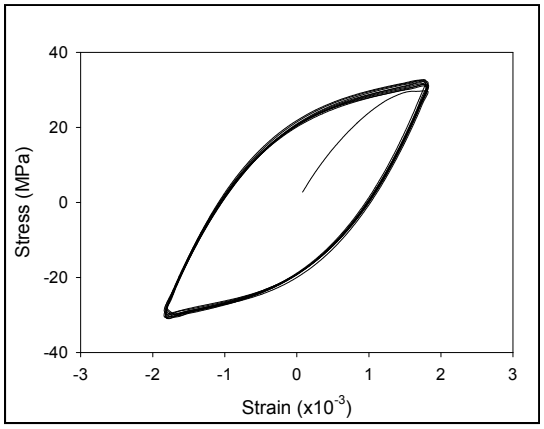

(a) No Aging

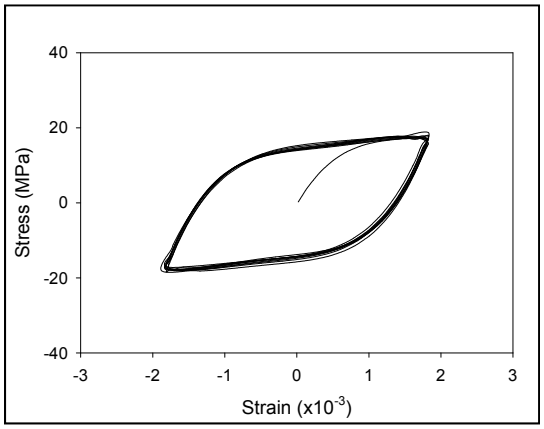

(b) 5 Days Aging

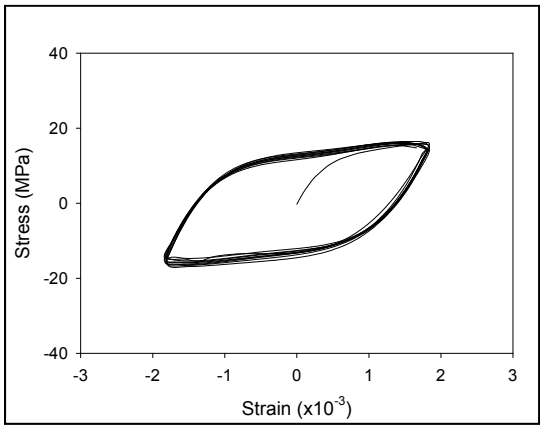

(c) 10 Days Aging

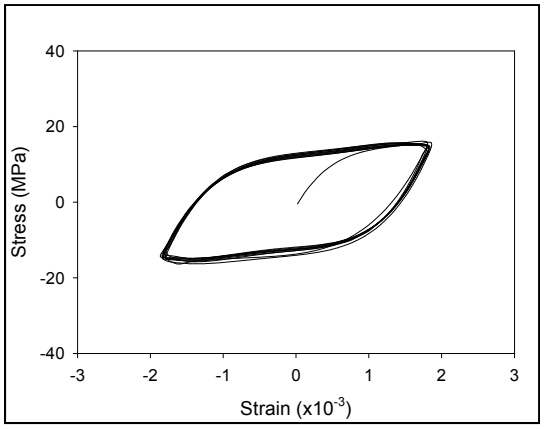

(d) 30 Days Aging

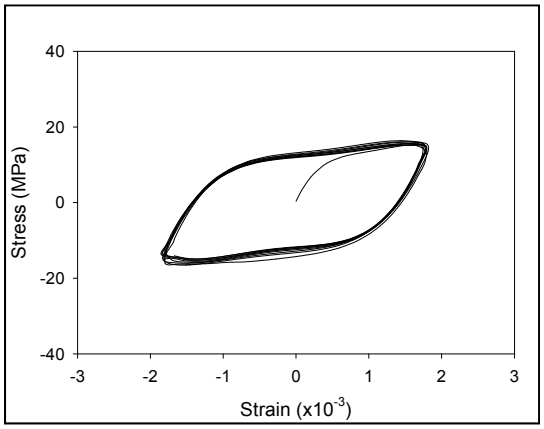

(e) 60 Days Aging

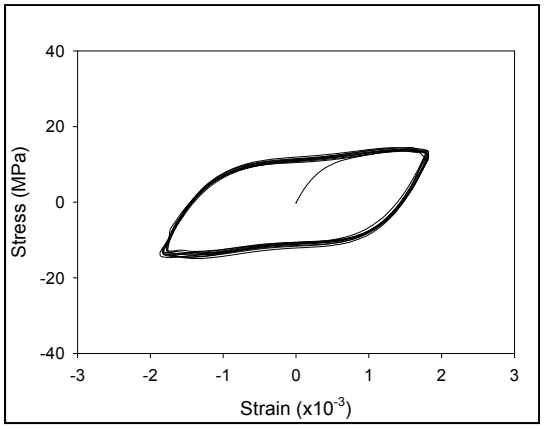

(f) 90 Days Aging

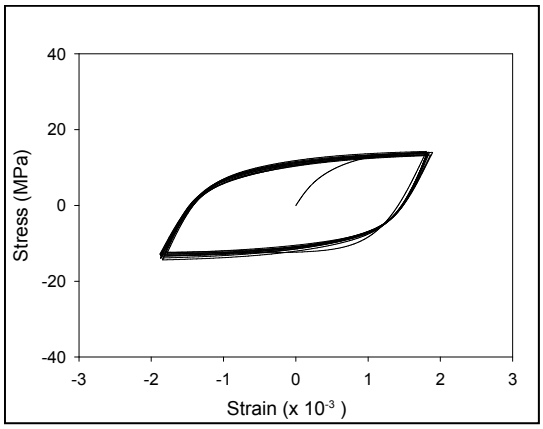

(g) 120 Days Aging

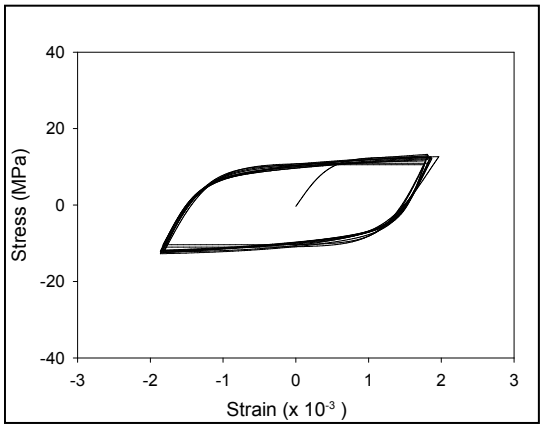

(h) 150 Days Aging

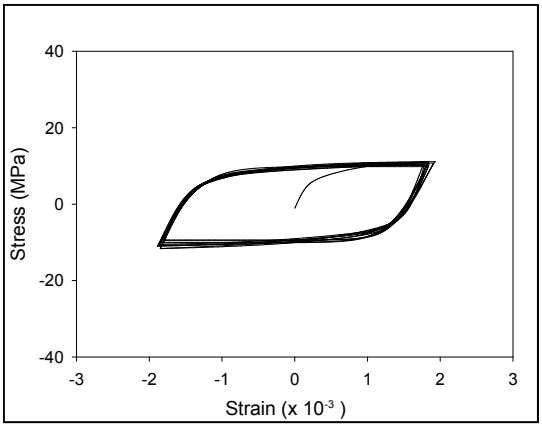

(i) 180 Days Aging

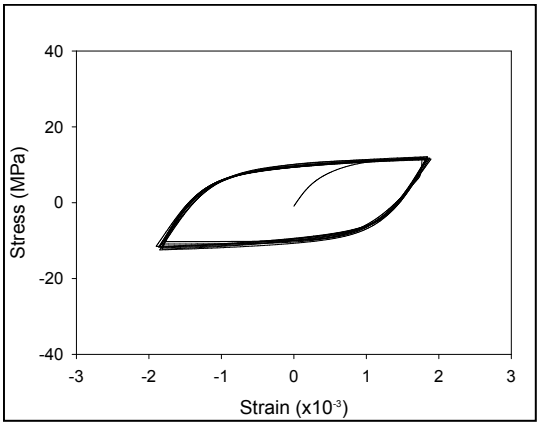

(j) 360 Days Aging

Figure 5.5 Hysteresis Loops for Cyclic Stress-Strain Testing
of SAC105 (Strain Controlled, WQ Samples)
Aging for 0-12 Months at 125 C

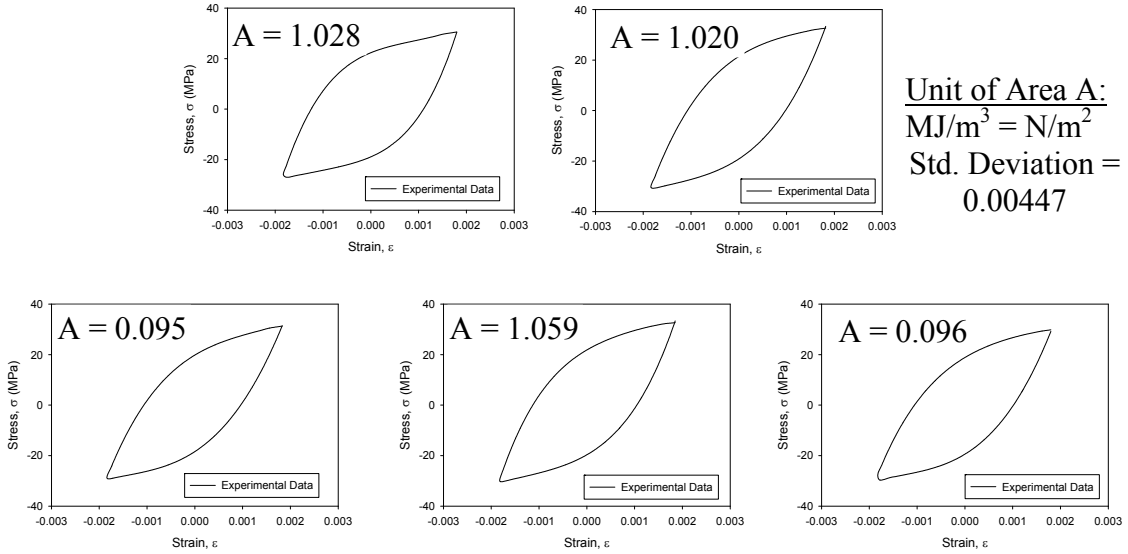

(a) No Aging

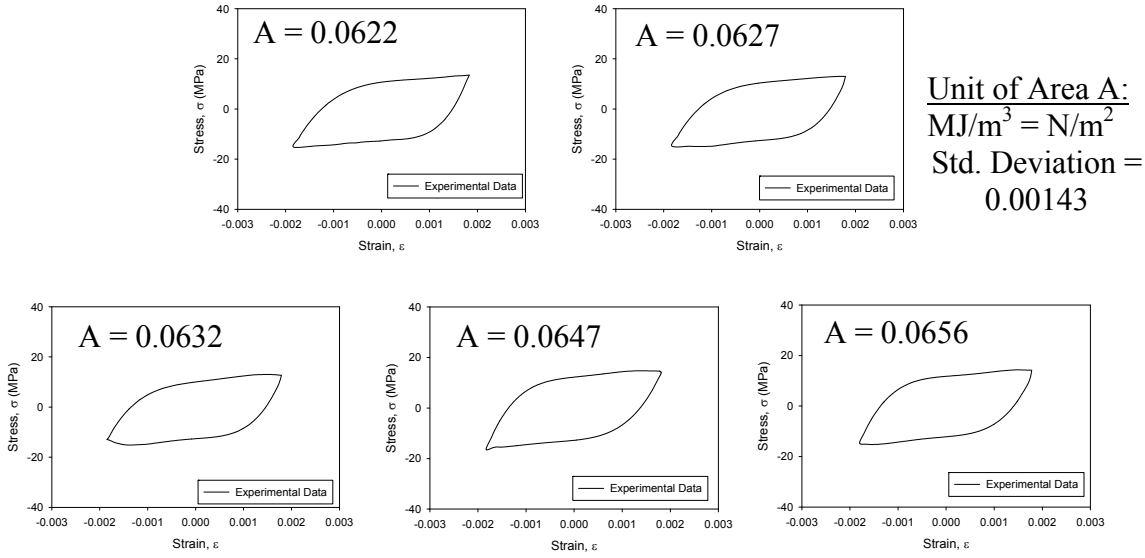

(b) 60 Days Aging at 125 C

Figure 5.6 Hysteresis Loops for Cyclic Stress-Strain Testing of SAC105 (Strain Controlled, WQ Samples, 10th Cycle)

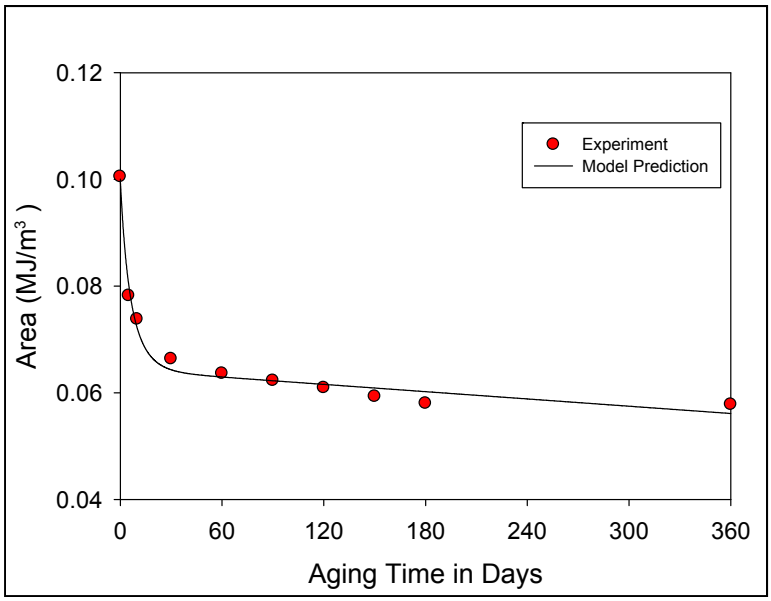

$r^2 = 0.996$

Empirical Model:

$$A = \frac{k_1}{1 + k_2 e^{-k_3 t}} + k_4 t$$

Material Constants:

$k_1 = 0.0675$
$k_2 = -0.3265$
$k_3 = 0.1521$
$k_4 = -5.5022 \times 10^{-5}$

Figure 5.7 Variation of the Hysteresis Loop Area with Aging Time (SAC105, Strain Controlled, WQ Samples)

The data in Figure 5.7 illustrate a smooth reduction of the hysteresis loop size with aging. The data points were well fit with an empirical model that includes exponential and linear terms:

$$A = \frac{k_1}{1 + k_2 e^{-k_3 t}} + k_4 t \qquad (5.1)$$

where A denotes the area of hysteresis loop, and k_1, k_2, k_3 and k_4 are material constants. It is observed that the most dramatic changes in the hysteresis loop area occur within the first 20-30 days of aging. The rate of change of the area with aging time then becomes much smaller and the loop size decreases linearly with long aging times (the slope is constant k_4 in Eq. (5.1)).

The reduction of the loop size with aging suggests that damage accumulation is mitigated with aging. However, this trend is mainly due to the fact that there are large drops in yield stress and ultimate strength of the solder material with aging (see Figure

5.8). These changes reduce the height of the hysteresis loop. Since the cyclic testing was performed using a fixed set of strain limits, the hysteresis loop width does not vary during cycling. Thus, the loop area must decrease because of the material strength reductions associated with aging.

Morrow [36] suggested that on the microscopic level, cyclic plastic strain is related to the movement of dislocations and the cyclic stress is related to the resistance to their motion. Repeated stress without accompanying plastic strain (no movement of dislocations) will not cause fatigue damage nor would repeated slip without repeated stress (no resistance to dislocation movement). Both are needed. Stress and plastic strain are required resulting in the dissipation of mechanical energy (a hysteresis loop exists). Thus, the plastic strain energy per cycle may be regarded as a composite measure of the amount of fatigue damage per cycle, and the fatigue resistance of a material may be characterized in terms of its capacity to absorb and dissipate plastic strain energy.

From the theory, it is evident that for a particular strain controlled cyclic test, the movement of dislocations does not change significantly as the plastic strain range increases slowly while aging progresses (see Figure 5.9). However, the stress, which is the height of a hysteresis loop, decreases significantly as resistance to dislocation movement decreases due to aging. Decreasing resistance of dislocation movement is the clear indication of microstructural damage occurred during aging. Therefore, for strain controlled cyclic tests, the area of hysteresis loop decreases because of damage accumulation and material strength reductions associated with aging.

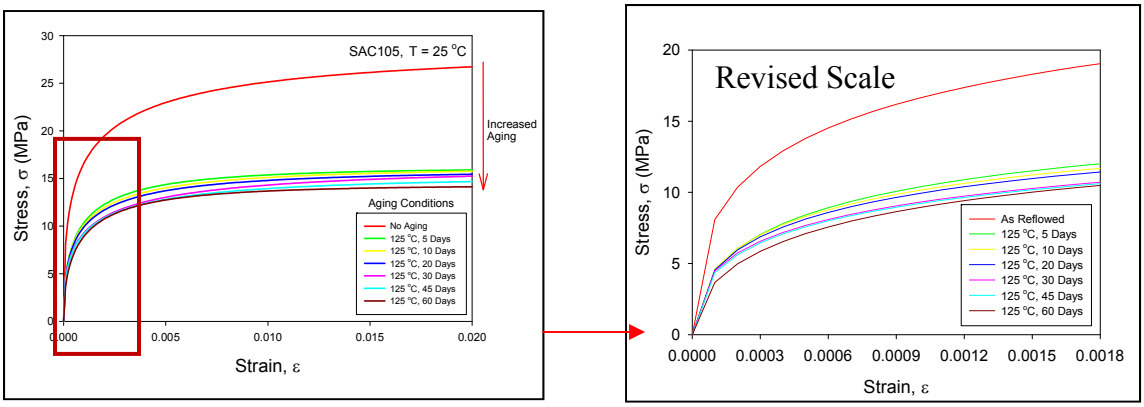

Figure 5.8 Reduction of Solder Material Strength Due to Aging (SAC105, RF)

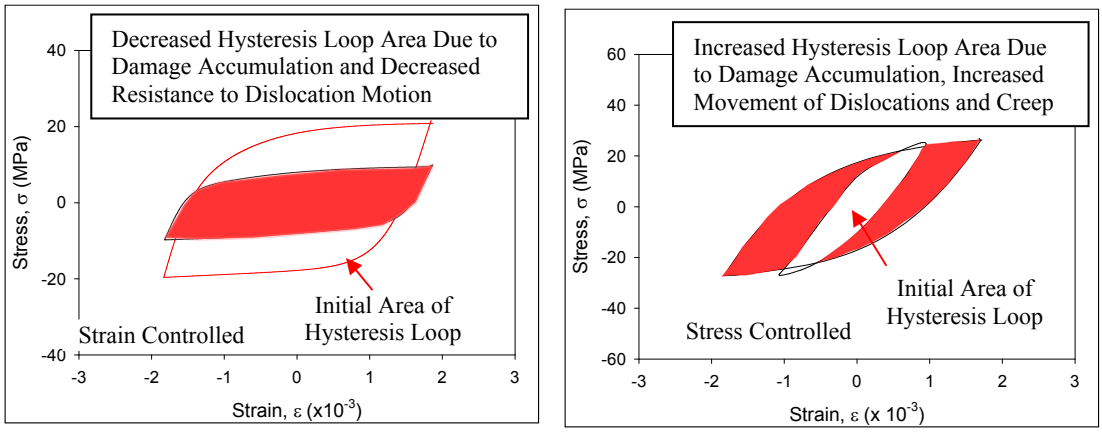

Figure 5.9 Evolution of Hysteresis Loop Due to Damage Accumulation in the Material for both Stress and Strain Controlled Cyclic Tests

Analogous cyclic testing results for SAC105 samples prepared with the RF solidification profile are shown in Figure 5.10. Experiments have been performed for up to 360 days of aging. Each curve in Figure 5.10 is again one of the five tests performed for a particular aging duration. Results for the other 4 samples were remarkably similar, and the data showed a high level of consistency and repeatability from sample to sample. Similar to the WQ samples, it is observed that the hysteresis loops of the RF samples rotate and become smaller in height as aging progresses. A plot of the evolution of hysteresis loop area with aging time is shown in Figure 5.11. In this graph, each data point represents the average value of the 5 tests performed for a particular aging duration, and the empirical model in Eq. (5.1) was used to fit the data.

Figures 5.7 and 5.11 for the WQ and RF samples show very similar trends. The two plots are directly compared in Figure 5.12. It is observed that the initial microstructures are important in determining the vertical and relative positions of the curves for all aging times. However, the reductions in areas follow similar trends for the drastically different initial microstructures. Initial microstructures of reflowed and water quenched SAC105 solder samples have been previously investigated by Zhang [146]. A relatively fine phase structure was formed in the water quenched specimens after solidification, whereas coarser structure was observed in the reflowed specimens. The mechanical behavior in cyclic loading corresponded with the microstructure, and the quickly cooled WQ specimens exhibited higher strength than slowly cooled RF specimens, due to their finer grain size and the interaction of dislocations with Ag_3Sn particles.

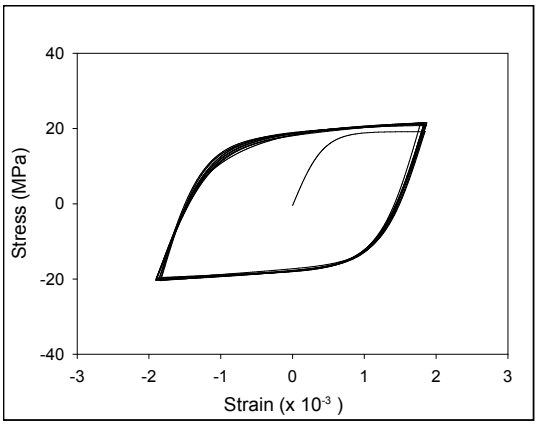

(a) No Aging

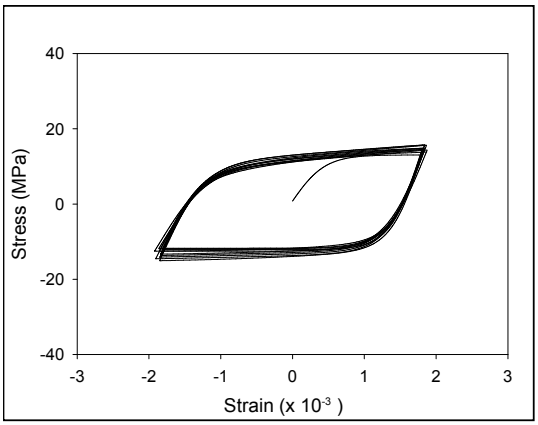

(b) 5 Days Aging

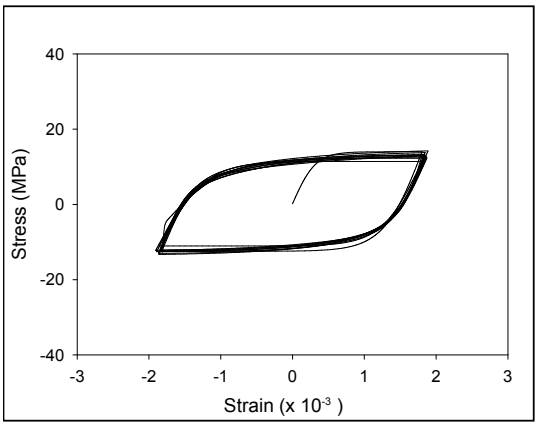

(c) 10 Days Aging

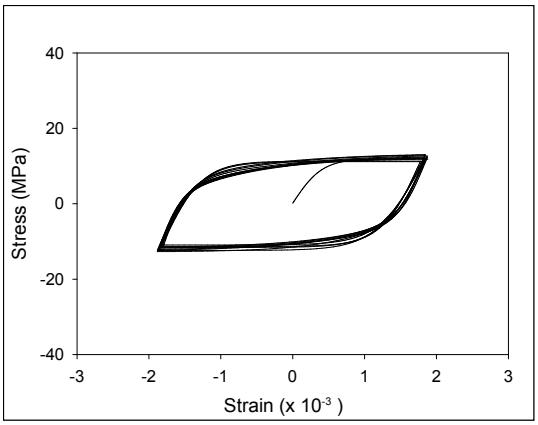

(d) 20 Days Aging

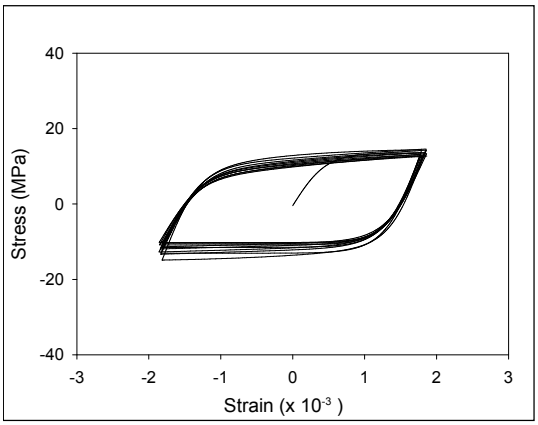

(e) 30 Days Aging

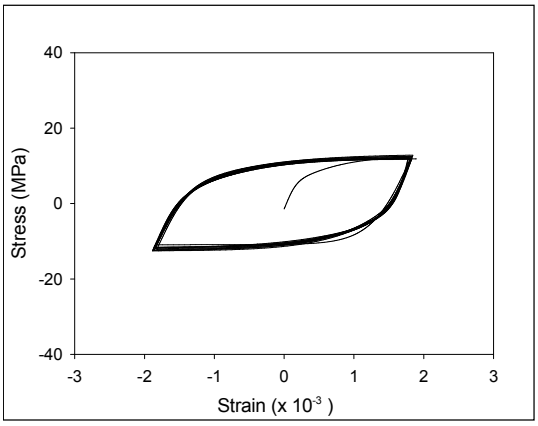

(f) 60 Days Aging

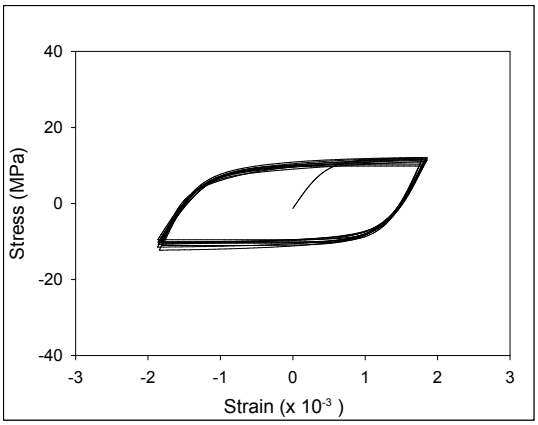

(g) 120 Days Aging

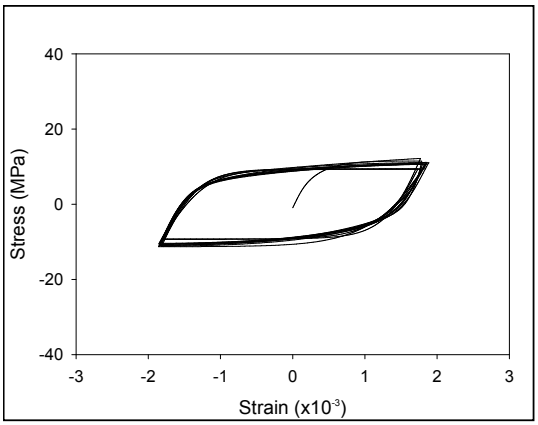

(h) 180 Days Aging

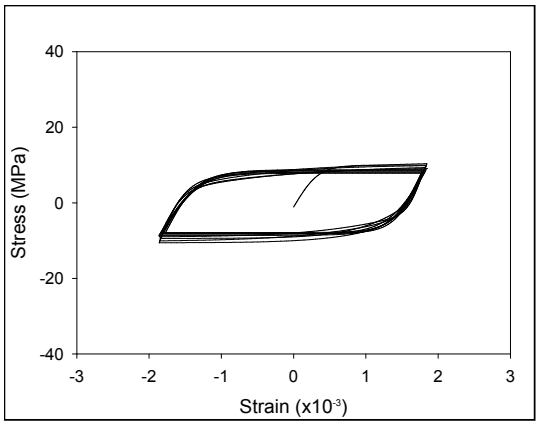

(j) 270 Days Aging

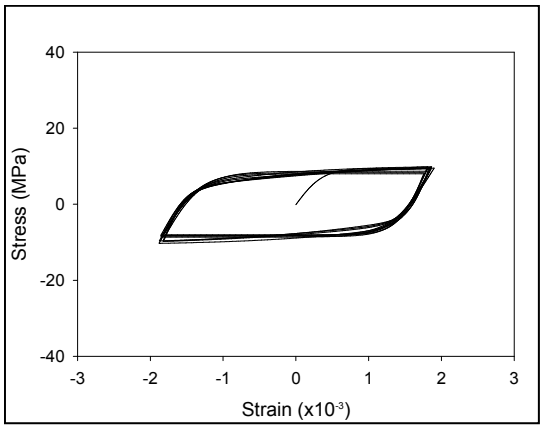

(i) 360 Days Aging

Figure 5.10 Hysteresis Loops for Cyclic Stress-Strain Testing
of SAC105 (Strain Controlled, RF Samples)
Aging for 0-12 Months at 125 C

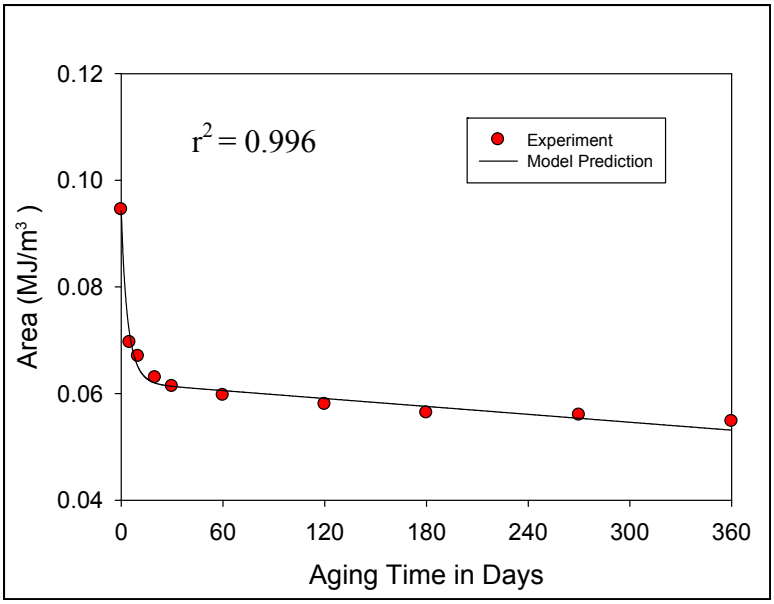

Model:

$$A = \frac{k_1}{1 + k_2 e^{-k_3 t}} + k_4 t$$

Material Constants:

$k_1 = 0.0636$
$k_2 = -0.3269$
$k_3 = 0.2305$
$k_4 = -5.0100 \times 10^{-5}$

Figure 5.11 Variation of the Hysteresis Loop Area with Aging Time (SAC105, Strain Controlled, RF Samples)

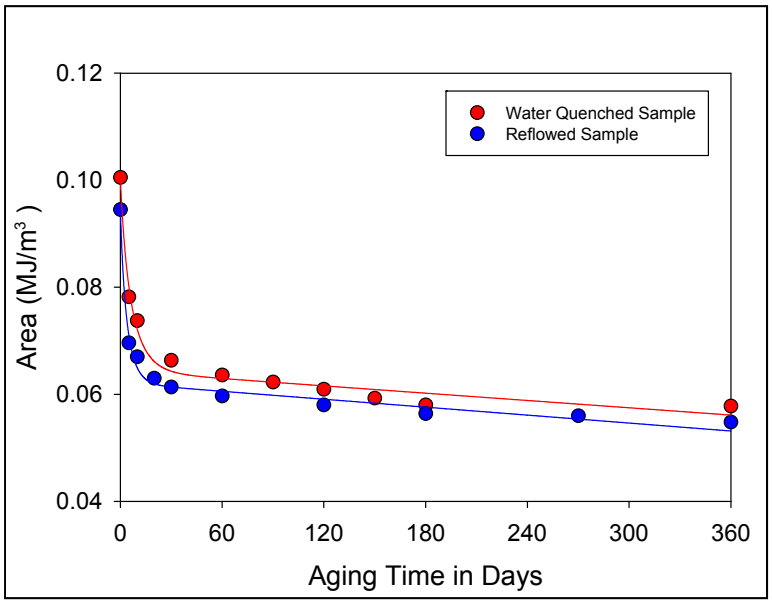

Figure 5.12 Comparison of Hysteresis Aging Behaviors of Water Quenched and Reflowed Samples (SAC105, Strain Controlled Cycling)

5.5 Effects of Aging for Stress Controlled Cyclic Testing

Stress controlled cyclic testing has also been performed on SAC105 samples (RF) subjected to aging at 125 C. Similar to the strain controlled cyclic experiments discussed above, the samples were subjected to aging at 125 C for various durations including 0, 5, 10, 20, 30, 60, 90, 120, 150, 180, 270 and 360 days (0-12 months). Again, there were 5 specimens in each leg of the test matrix, which were defined by the sample cooling profile (RF) and aging time (10 different durations). The stress controlled testing was performed with stress limits of ±10 MPa, and the testing temperature was 25 C. Figure 5.13 illustrates example plots of the cyclic stress-strain behavior for RF samples subjected to the various aging times. Each plot contains one of the five test results obtained for a particular aging duration. Results for the other 4 samples were remarkably similar, and the data showed a high level of consistency and repeatability from sample to sample. Unlike the strain-controlled testing, the hysteresis loops tend to shift slightly from cycle to cycle, so that the loops were not perfectly closed. An algorithm was developed to define the area of the loop and to calculate the loop area.

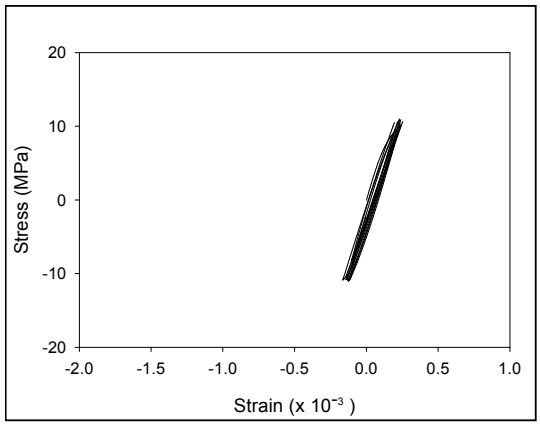

(a) No Aging

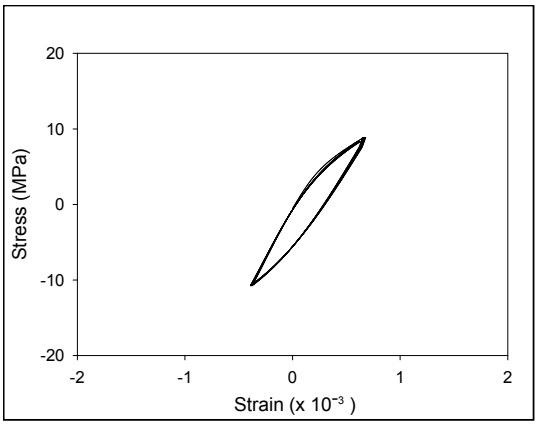

(b) 5 Days Aging

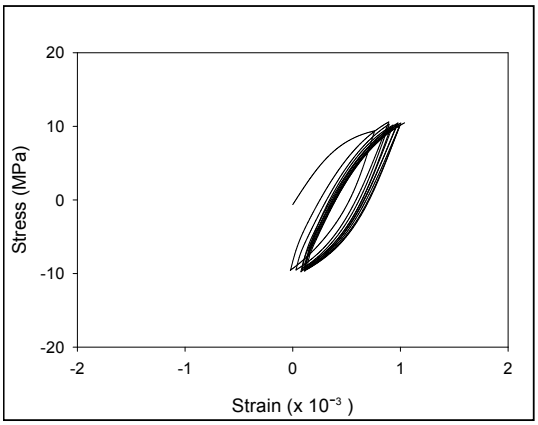

(c) 10 Days Aging

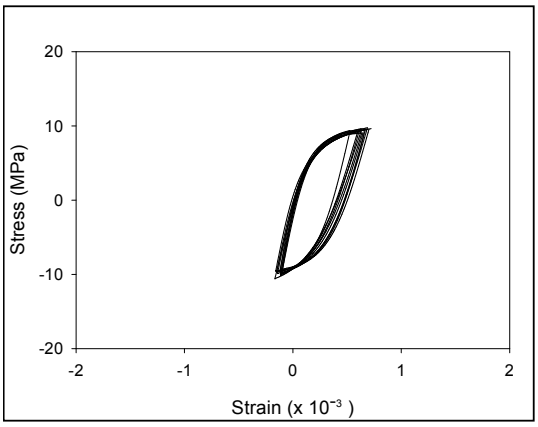

(d) 20 Days Aging

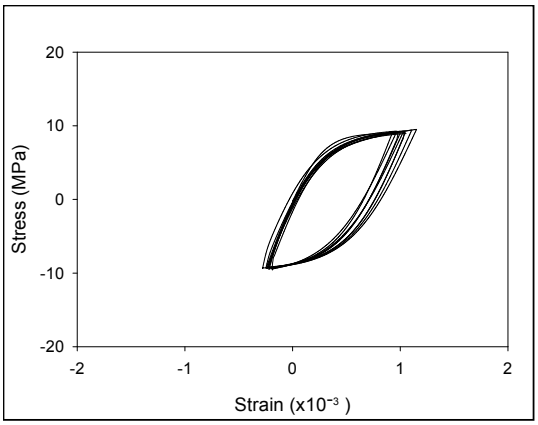

(e) 30 Days Aging

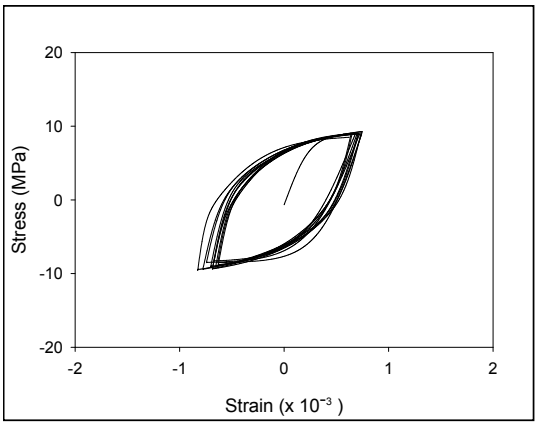

(f) 60 Days Aging

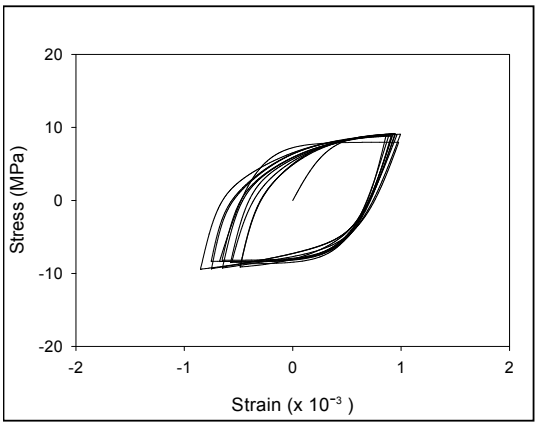

(g) 120 Days Aging

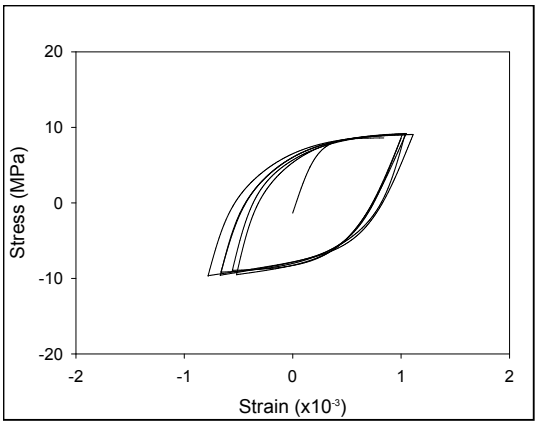

(h) 180 Days Aging

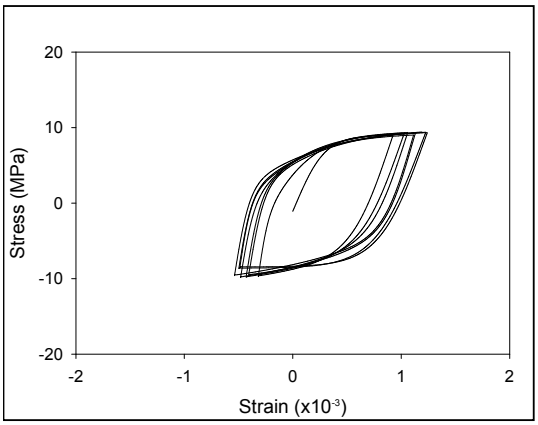

(i) 270 Days Aging

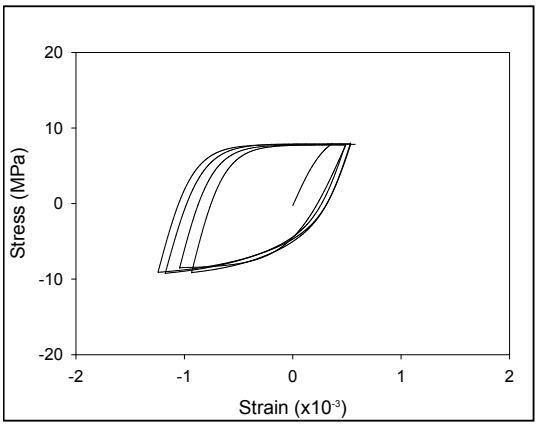

(j) 360 Days Aging

Figure 5.13 Hysteresis Loops for Cyclic Stress-Strain Testing
of SAC105 (Stress Controlled, RF Samples)
Aging for 0-12 Months at 125 C

From the results, it is clear that the loops become wider and larger in area as the aging time increases. A plot of the evolution of hysteresis loop area with aging time is shown in Figure 5.14. In this graph, each data point represents the average value of the 5 tests performed for a particular aging duration. The data illustrate a smooth increase in the hysteresis loop size with aging. The data points were well fit with an empirical five parameter modified Weibull model:

$$A = k_0 + k_1 t - k_2 e^{-k_3 t^{k_4}} \tag{5.2}$$

where A denotes the area of hysteresis loop, and k_1, k_2, k_3, k_4 and k_5 are material constants. Again, rapid changes in the hysteresis loop area occur within the first 20-30 days of aging. The rate of change of the area with aging time then becomes much smaller and the loop size increases linearly with long aging times (the slope is constant k_1 in Eq. (5.2)).

The increase in the hysteresis loop area with aging means the energy dissipation per cycle is also increasing with aging. Thus, damage accumulation is accelerated with aging during stress controlled cycling tests. This trend occurs due to the fact that there are large drops in the yield stress and ultimate strength of the solder material with aging (see Figure 5.15). Since the height of the hysteresis loop is fixed in size (due to the stress limit controlled nature of the experiments), the width will increase due to the reduction in material stiffness and strength. In accelerated life testing of assemblies, solder joints are subjected to thermal cycling that causes stress-strain cycling of the solder material. It is expected that the cycling conditions in this case are somewhere in between pure strain limit controlled and pure stress limit controlled cycling.

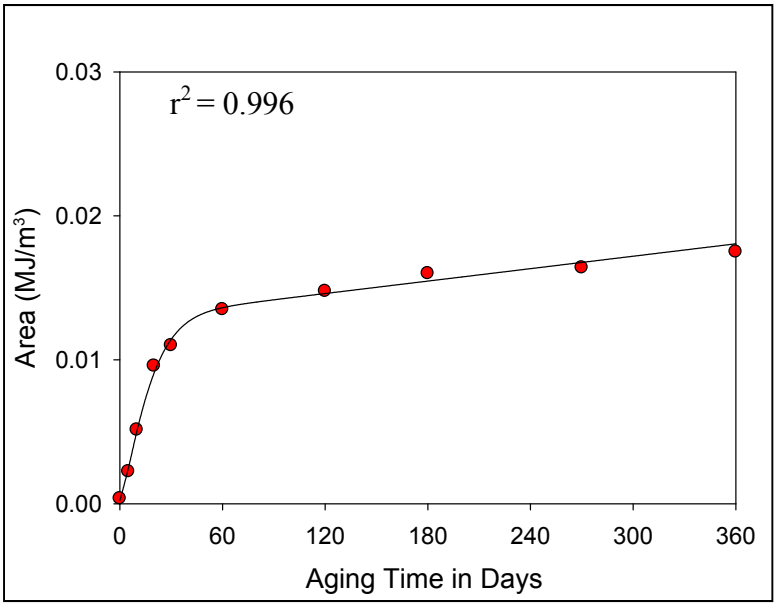

Model:

$$A = k_0 + k_1 t - k_2 e^{-k_3 t^{k_4}}$$

Material Constants:

$k_0 = 0.0129$
$k_1 = 1.4298 \times 10^{-5}$
$k_2 = 0.0127$
$k_3 = 0.0241$
$k_4 = 1.2854$

Figure 5.14 Variation of the Hysteresis Loop Area with Aging Time (SAC105, Stress Controlled, RF Samples)

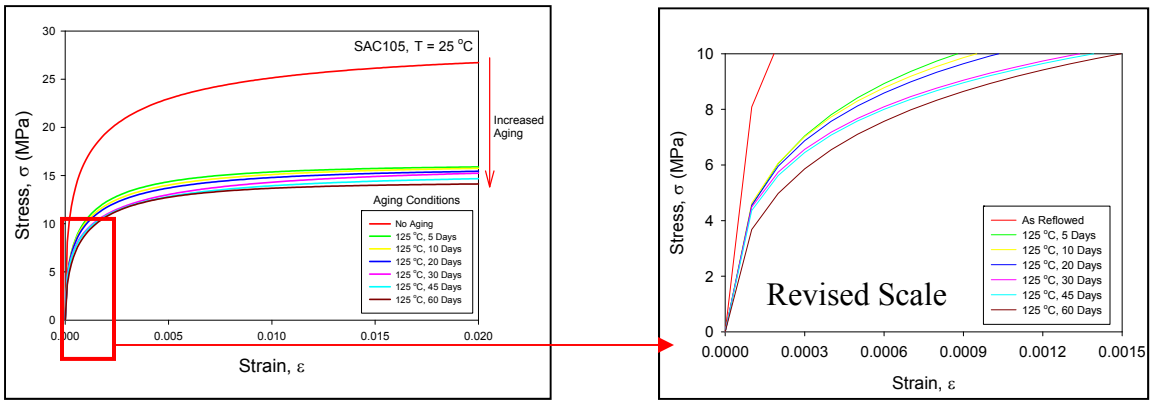

Figure 5.15 Increase of Plastic Strain Due to Aging (SAC105, RF)

According to Morrow's theory [36], cyclic plastic strain is related to the dislocation movement on the microscopic level and cyclic stress is related to the resistance to dislocation motion. Therefore, it is noticeable that the plastic strain range increases during aging for stress limit controlled cycling (see Figure 5.9), as movements of dislocations increase significantly. Increasing dislocation movements lead to microstructural damage accumulation, and voids form along grain boundaries. As shown in Figure 5.16, voids are evident between two adjacent sub-grain boundaries in an aged sample during cyclic loading. Therefore, it can be concluded that for stress controlled cyclic testing, the area of the hysteresis loops increase due to aging induced microstructural damage accumulation, which is related to increasing dislocation movements.

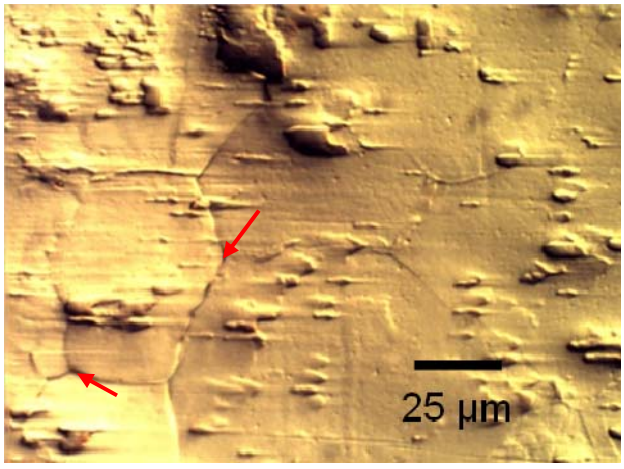

Figure 5.16 Optical Microscopic Image of Void Formation along Sub-Grain Boundaries in an Aged Sample (SAC105, RF, Aging for 210 Days at 125 C)

5.6 Comparisons of Hysteresis Loops for Different SAC Alloys

In previous studies [53-54, 40, 148], it has been demonstrated that that lowering the silver content of a SAC alloy leads to decreases in stiffness and strength, and increases in the creep rate. In addition, lower silver content SAC alloys were more susceptible to aging induced degradations of the effective elastic modulus, yield strength, ultimate tensile strength, and steady state creep rate. In the present study, an initial investigation has been made on the effect of silver content on the hysteresis loop area for SAC alloys subjected to strain limit controlled cyclic loading (no aging). Tests were performed on four different SAC alloys: SAC105, SAC205, SAC305, and SAC405; with 1%, 2%, 3%, and 4% silver in their composition, respectively. All samples were formed using the WQ solidification profile, and there were 5 specimens tested for each material. The strain controlled testing was performed with strain limits of ±0.0018 and a strain rate of 0.0001 sec^{-1}, and the testing temperature was 25 C.

Figure 5.17 illustrates example plots of the cyclic stress-strain behavior for the SACN05 samples (no aging). A plot of the variation of the average hysteresis loop size with alloy composition is shown in Figure 5.18. It is observed that hysteresis loop area increases when the silver content of the alloy decreases, so that lower silver content alloys experience increased energy dissipation and damage accumulation when subjected to similar cycling conditions (same strain limits). This was expected because the low silver content alloys have increased nonlinearity (plasticity) in their regular (non cyclic) stress-strain curves. It is also noticeable that cyclic stress also decreases in lower silver content SAC alloys. This can be explained based on Morrow's theory [36], where increasing plastic strain is related to increasing movement of dislocations and decreasing

cyclic stress is related to decreasing resistance to dislocation motions. Higher movement of dislocations and lower resistance to dislocation motion also imply lower fatigue resistance. Therefore, low silver content SAC (e.g. SAC105) alloys have lower fatigue resistance, and by increasing silver content better fatigue properties can be attained. Similar experimental results were also reported by Kariya, et al. [149].

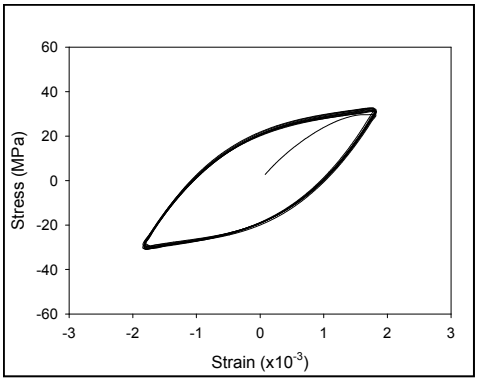

(a) SAC105

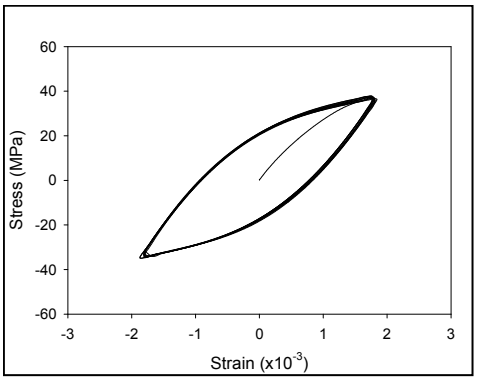

(b) SAC205

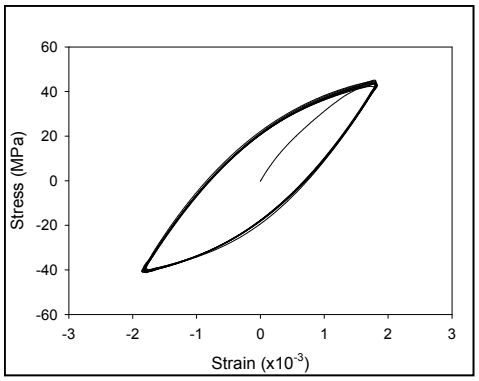

(d) SAC305

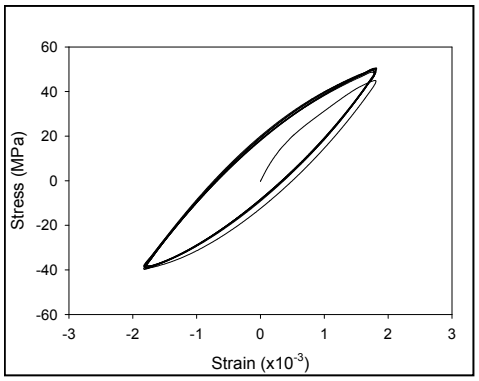

(c) SAC405

Figure 5.17 Cyclic Stress-Strain Curves for SACN05 Lead Free Solders (Strain Controlled Cyclic Testing)

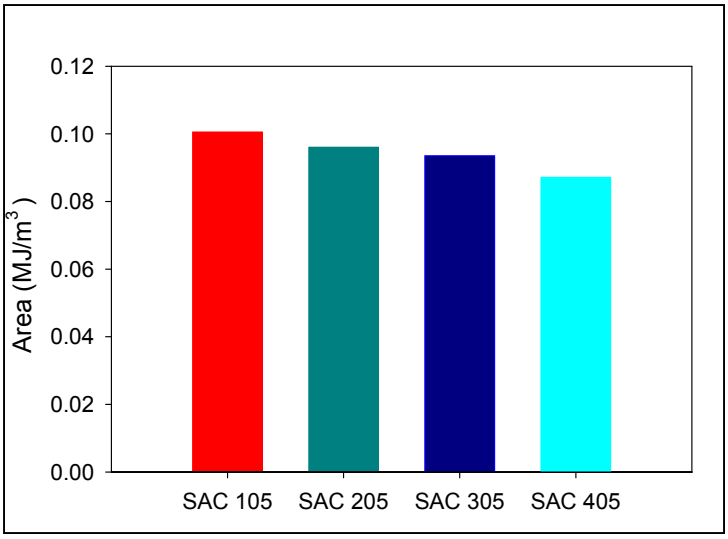

Figure 5.18 Comparison of Hysteresis Loop Areas for SACN05 Lead Free Solder Alloys

5.7 Effects of Testing Temperature on Hysteresis Loop Size

A limited study on the effect of testing temperature on the hysteresis loop size has been performed for SAC405 solder (RF, no aging). The samples were subjected to stress limit controlled cycling with stress limits of ±25 MPa, and testing was performed at 4 different temperatures: 25, 50, 75 and 100 C. Hysteresis loops for the 10^{th} cycle for each testing temperature are shown in Figure 5.19. A summary of the results are shown in Figure 5.20, where the average hysteresis loop area is plotted vs. testing temperature. For higher testing temperature, plasticity increases in the material and the plastic strain range increases. Therefore, the width of hysteresis loop increases. As expected, the loop area is strongly dependent on temperature, and higher temperatures lead to increased damage accumulation per cycling in the solder alloys.

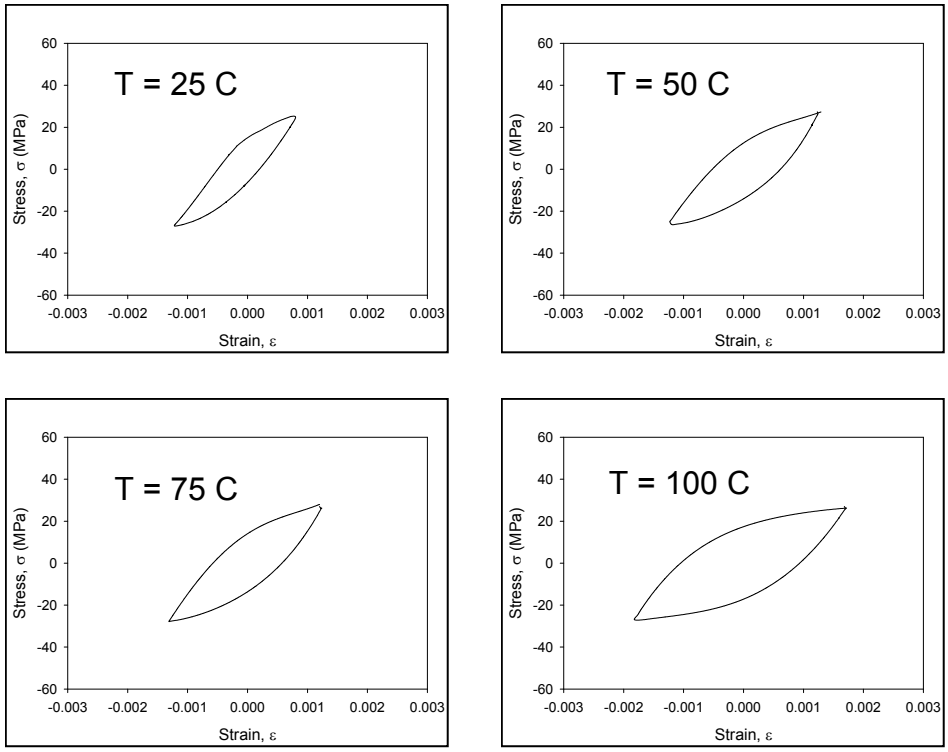

Figure 5.19 Evolution of Hysteresis Loop Size at Different Testing Temperatures for SAC405 Solder Alloy (Stress Controlled Cyclic Tests)

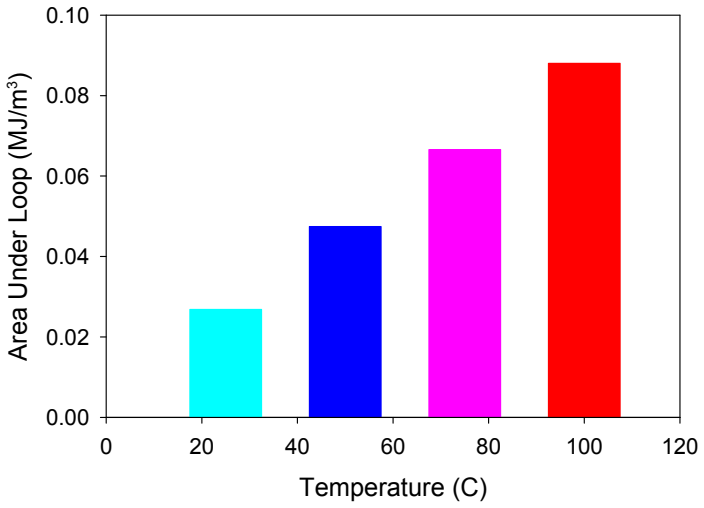

Figure 5.20 Hysteresis Loop Areas for SAC405 at Different Testing Temperatures

The opposite trend was observed for strain limit controlled cyclic testing at different test temperatures. The samples were subjected to strain controlled cycling with strain limits of ±0.0015, and testing was performed at 4 different temperatures: 25, 50, 75 and 100 C. The hysteresis loops for each testing temperature are shown in Figure 5.21. In this case, the height of the hysteresis loops declined, leading to a decreasing loop area with temperature.

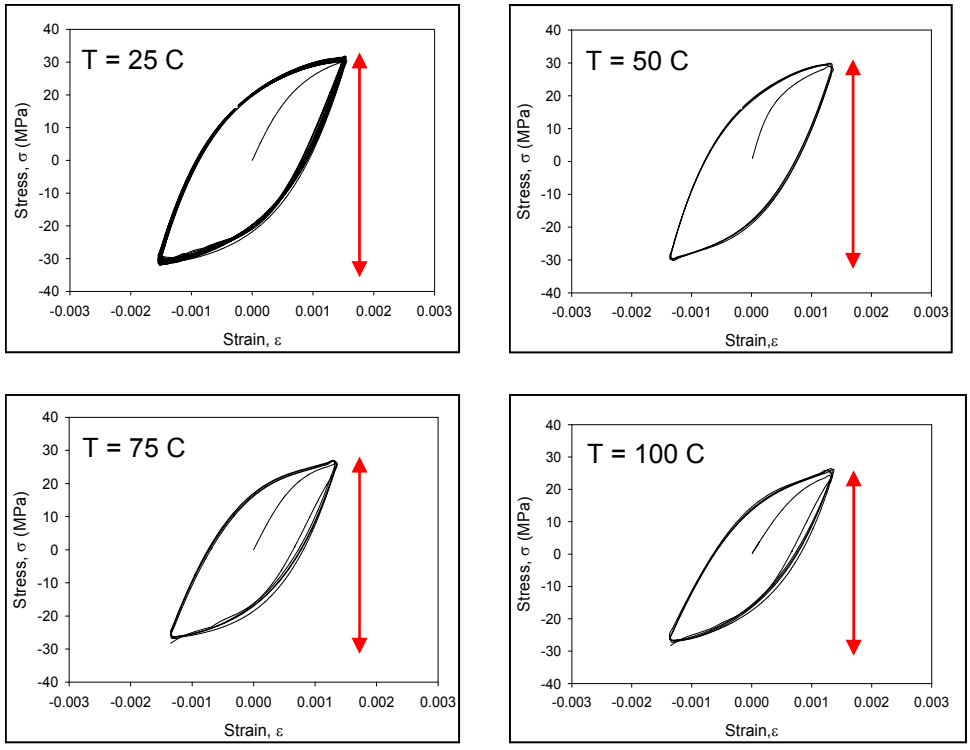

Figure 5.21 Evolution of Hysteresis Loop Size at Different Testing Temperatures for SAC405 Solder Alloy (Stress Controlled Cyclic Tests)

5.8 Summary and Discussion

In this chapter, the effects of several parameters (aging, temperature, strain/stress limits, and solder alloy composition) on the cyclic stress-strain behavior of lead free solders have been investigated. Uniaxial SAC lead free solder specimens were subjected to cyclic (tension/compression) mechanical loading. Samples were cyclically loaded under both strain limit control (constant positive and negative strain limits) and stress limit control (constant positive and negative stress limits). The hysteresis loop size (area) was calculated from the measured cyclic stress-strain curves for a given solder alloy and temperature. This area represents the strain energy density dissipated per cycle, which can be typically correlated to the damage accumulation in the solder material. Also plastic strain is related to movement of dislocations and the cyclic stress is related to resistance to dislocation motion.

SAC105 lead free solder specimens were subjected to both strain controlled and stress controlled cyclic loading. It was observed that the hysteresis loop area changes significantly with aging, and mathematical models have been found to fit the aging induced evolution. For strain controlled cyclic testing, the hysteresis loop size decreases with aging time, while for stress controlled cyclic testing the hysteresis loop size increases with aging time. These phenomena have been explained through comparison to the aging induced degradation of the yield stress and ultimate strength extracted from the standard (non-cyclic) stress-strain curves for SAC solders, and from Morrow's theory of dislocation movement and resistance to dislocation motion.

Preliminary studies have also been made on the effects of solder composition on the cyclic stress-strain behavior by testing four SAC alloys (SAC105, SAC205, SAC305,

SAC405) with varying silver content (1-4%) under strain controlled cycling. In addition, the effect of the testing temperature has also been studied by performing cyclic testing of SAC405 samples at four different temperatures (25, 50, 75, and 100 C). As expected, larger hysteresis loops were found for the lower silver content alloys under strain control, and for higher testing temperatures under stress control.

CHAPTER 6

EFFECTS OF AGING ON THE UNIAXIAL FATIGUE BEHAVIOR OF LEAD FREE SOLDER MATERIALS

6.1 Introduction

Thermally cycling induced solder joint fatigue is a common failure mode in electronic packaging. When subjected to temperature changes, stresses in electronic assemblies are typically developed due to the mismatches in the coefficients of thermal expansion (CTE) of the soldered components and the PCB as illustrated in Figure 6.1. Cyclic temperature changes, either due to external environment or power switching, can therefore lead to substantial alternating stresses and strains within the solder joints. Energy dissipation occurs during such cyclic loading due to yielding and occurrence of viscoplastic deformations, and the strain energy density dissipated per cycle can be calculated from the area of stress-strain hysteresis loops. The cycling eventually leads to micro cracks being formed within the solder material, followed by macro cracks which leads to damage progression and ultimately to fatigue failure. Aging of solder materials degrades their mechanical and creep properties, and is expected to exacerbate the rate of damage accumulation during cycling loading.

While the effects of aging on solder constitutive behavior (stress-strain and creep) have been recently examined in some detail, there have been no prior studies on the effects of aging on solder failure/fatigue behavior. In this chapter, the effects of aging on

the fatigue life of mechanically cycled lead free solders has been investigated. Uniaxial solder test specimens (SAC105 and SAC305) have been prepared and subjected to cyclic stress/strain loading to failure. Prior to testing, the specimens were aged (preconditioned) at 125 C for various aging times, and then the samples were subjected to strain limit controlled cyclic loading at room temperature (25 C). Various empirical failure criteria such as the Coffin-Manson model and the Morrow model have been used to fit the measured data, and the parameters in the models have been determined as a function of the aging conditions.

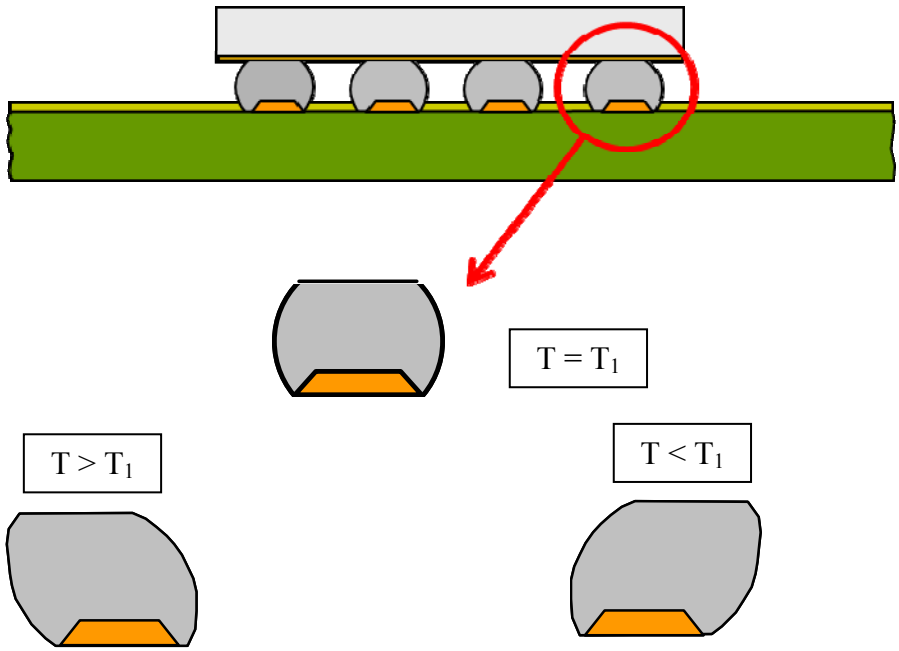

Figure 6.1 Depiction of Cyclic Loading in Solder Joints during Thermal Cycling

6.2 Fatigue Phenomena

Solder joints in electronic assemblies are often subjected to cyclic loadings due to CTE mismatches. The operational life span of an electronic product will typically

depend upon the solder joint fatigue life, defined as the number of cycles before fatigue failure occurs. When a material is subjected to high cyclic stress, which causes its structure to break down and finally fracture, the material undergoes a deformation process called fatigue. This phenomenon usually occurs at stress levels lower than the yield stress of the material. Fatigue is responsible for a large percentage of failures of engineering materials, and fatigue failure results from localized stress concentrations. The surface of materials contains microscopic regions, where the localized stress becomes much greater than the average stress acting over the cross section. As the increased stress is cycled, micro-cracks will initiate and lead to stress concentrations at crack tips or boundaries. Higher stresses consequently cause crack extensions into the material. As the process continues, the reduced cross-sectional area will no longer be able to withstand the applied load and fatigue fracture occurs.

Fatigue failure is sudden, catastrophic, and involves relatively little plastic deformation. When subjected to fatigue, ductile materials often behave as if they were brittle. The fatigue damage is cumulative, and the materials will not recover when load is removed. There are three stages for a fatigue failure to fully develop and occur [23]:

- Stage 1: Crack nucleation, where cracks initiate at the sites of stress concentration (micro-cracks, scratches, indents, interior corners, dislocation slip steps, etc.).
- Stage 2: Crack propagation occurs in two steps:
  - Step I: Initial slow propagation along crystal planes with high resolved shear stress. Cracks formed in this step feature flat surfaces.

- Step II: Faster propagation perpendicular to the applied stress. Cracks grow by repetitive blunting and sharpening process at the crack tips. Fractures have a rough surface.

- Stage 3: Ultimate failure, where cracks eventually reach critical dimensions and propagate very rapidly. It is notable that competition in mechanisms occurs during the process of fatigue crack growth [150]:

  (1) Intrinsic, crack growth promoting mechanism: cracks advancing ahead of the crack tip, including alternating crack-tip blunting and resharpening, etc.

  (2) Extrinsic, crack growth impeding mechanism: crack-tip shielding behind the tip, including crack closure and bridging, etc.

The American Society for Testing Materials (ASTM) [151] defines fatigue life by N_f, the number of cycles to fail at specified stress level. The length of a material's fatigue life depends on such factors as surface finish, load amplitude and direction, residual stress, grain size, internal defect distribution, notch sensitivity, geometry and size, as well as temperature and environment.

6.3 Fatigue Life Prediction

The grain structure in a metal is inherently unstable. The grains will often grow in size over time as the material reduces the internal energy of a fine-grain structure. This grain growth process is enhanced at elevated temperatures as well as during strain energy input from cycling loading. The grain growth is thus an indication of the accumulating fatigue damage. At grain boundaries, contaminants like oxide compounds are concentrated. As the grains grow, these contaminants are further concentrated at the

grain boundaries, further weakening them. After the consumption of about 25% of the fatigue life, micro-voids often form at the grain boundary interactions. These micro-voids grow into micro-cracks after about 40% of the fatigue life. The micro-cracks grow and coalesce into macro-cracks leading to total fracture [154].

The Coffin-Manson low-cycle fatigue equation [152] is perhaps the most well-known low cycle fatigue life model:

$$N_f^n \Delta\varepsilon_p = C \tag{6.1}$$

where, $\Delta\varepsilon_p$ is the cyclic plastic strain range, n is the fatigue exponent, and C is the fatigue ductility.

A similar equation has been proposed by Solomon [64] for low-cycle shear fatigue:

$$N_f^n \Delta\gamma_p = C \tag{6.2}$$

For solder joints, Coffin-Manson type relationships have often been used to estimate fatigue life in thermal cycling environments.

Another popular fatigue model for low cycle fatigue of metals is the strain-energy relationship of Morrow [153]:

$$N_f^m \Delta W = K \tag{6.3}$$

where, m is fatigue ductility coefficient, ΔW is the cyclic visco-plastic strain energy density (area of the cyclic hysteresis loop in the stress-strain diagram), and K is the fatigue ductility exponent.

The Englemaier-Wild solder creep-fatigue equation [154-163] relates the cyclic total strain energy, to the median cyclic fatigue life for both isothermal-mechanical and thermal cycling:

$$N_f(50\%) = \frac{1}{2}\left[\frac{2\varepsilon_f'}{\Delta D}\right]^{-\frac{1}{c}} \tag{6.4}$$

where ε_f' is the fatigue ductility coefficient, ΔD is the cyclic total strain energy, and c is the fatigue ductility exponent. If the cycles have sufficient half-cycle dwell times to result in complete stress-relaxation/creep, then $\Delta D = \Delta W$. Englemaier has suggested that the fatigue ductility exponent is a function of temperature and time:

$$c = -0.442 - 6\times10^{-4}\,\overline{T}_{SJ} + 1.74\times10^{-2}\ln\left(1+\frac{360}{t_D}\right) \tag{6.5}$$

where T_{SJ} is the mean cyclic solder joint temperature, and t_D is half-cycle dwell time in minutes. The half-cycle dwell time relates to the cyclic frequency and the shape of the cycles, and represents the time available for stress-relaxation/creep to take place.

Literature values of the fatigue ductility exponents of the plastic strain range based model (Coffin-Manson model) and plastic strain energy density based model (Morrow Model) are listed in the Table 6.1 and Table 6.2 for a number of Sn-rich lead free solder alloys as well as SnPb eutectic solder. Published fatigue exponents vary widely with alloy composition and testing conditions. For the Coffin-Manson model, the fatigue ductility exponent n ranges from 0.27 to 0.90, and for the Morrow model, the fatigue ductility exponent m ranges from 0.34 to 1.17. These ranges are much greater than the observed variations for ferrous alloys, where the fatigue ductility exponent is roughly equal to 0.6, and where the fatigue ductility correlates well with the tensile ductility [23].

Table 6.1 Fatigue Ductility Exponent of Plastic Strain Range Based Model(Coffin-Manson Model) from Different Sources

Source	Fatigue Ductility Exponent, n	Material
Anderson, et al.[97]	0.27	Sn-Ag-Bi
Anderson, et al.[97]	0.32	Sn-Ag
Anderson, et al.[97]	0.35	Sn-Pb
Sun, et al.[94]	0.35	Sn-Zn-Bi
Cortez, et al.[172]	0.37	63Sn-37Pb
Anderson, et al.[97]	0.42	SAC
Lee, et al.[98]	0.43	Sn-Cu
Kariya, et al.[173]	0.44	SAC
Lee, et al.[98]	0.57	Sn-Ag
Akay, et al.[165]	0.63	SAC
Wu, et al.[166]	0.68	SAC
Lee, et al.[98]	0.74	SAC
Lee, et al.[94]	0.87	Sn-Ag-Bi
Pang, et al.[174]	0.99	Sn-Cu
Kanchanomai, et al. [176]	1.14	Sn-Ag-Cu-Bi

Table 6.2 Fatigue Ductility Exponent of Plastic Strain Energy Based Model (Morrow Model) from Different Sources

Source	Fatigue Ductility Exponent m	Materials
Anderson, et al.[97]	0.34	Sn-Ag
Anderson, et al.[91]	0.37	Sn-Pb
Anderson, et al.[100]	0.42	SAC
Kanda, et al.[91]	0.49	SAC
Lau, et al.[100]	0.51	SAC
Akay, et al.[165]	0.63	SAC
Wu, et al.[166]	0.68	SAC
Shi, et al.[70]	0.70	Sn-Pb
Pang, et al.[101]	0.87	SAC0387
Kim, et al.[92]	0.88	SAC405
Ahmer, et al. [167]	1.00	SAC
Jung, et al.[168]	1.00	63Sn37Pb
Dudek, et al.[169]	1.00	SAC
Pang, et al.[170]	1.07	SAC at 25C
Chi, et al.[171]	1.10	SAC
Lee, et al.[98]	1.17	Sn3.5Ag7.5Bi

While some of the variations in fatigue exponent and fatigue ductility may be related to the effects of alloy microstructure and mechanical variables, considerable uncertainties have also arisen from lack of sufficient experimental data. For example, it is common to find that the Coffin-Manson parameters have been obtained from a line drawn through only a few (e.g. three) data points even though fatigue data are well known to have a larger scatter. In the low cycle regime, the errors can be quite significant. When the fatigue life curves from three different sources were compared for Sn-3.5Ag alloy, the divergence was quite large except for the region around the point of 1% strain amplitude [88]. Testing conditions (e.g. constant strain rate and constant frequency) and definition of failure criteria are also different for various sources.

6.4 Fatigue Test Matrix Description

Using specimens fabricated with the casting procedure described in Chapter 3, thermal aging effects and viscoplastic material behavior evolution under cyclic loading have been characterized for SAC105 (Sn-1.0Ag-0.5Cu) and SAC305 (Sn-3.0Ag-0.5Cu) lead free solders. These alloys are commonly used for solder balls in lead free BGAs, CSPs, and flip chip die, as well as for solder pastes used in SMT processes with other components. After solidification and cooling, the test specimens were subjected to various durations of aging at 125 C. For each set of aging conditions, several specimens were prepared and formed a group of test specimens for subsequent mechanical testing. The samples in each group were cooled to room temperature (25 C) after aging, and then they were subjected to cyclic loading under different strain-controlled conditions. The fatigue tests conducted in this work were at constant strain rate of 0.001 sec^{-1} and the failure criterion was defined as a 50% drop in the peak stress during cyclic loading.

Table 6.3 Fatigue Test Matrix (X = Completed)

Aging Time	SAC105	SAC305
0 Days	X	X
30 Days	X	X
120 Days	X	X
210 Days	X	X
300 Days	X	X
360 Days	X	X

6.5 Evolution of Hysteresis Loops during Cyclic Loading

Fatigue testing was performed using both SAC105 and SAC305 test specimens subjected to prior aging. After solidification, the samples were aged at 125 C for various durations up to 1 year as shown in the test matrix in Table 6.3. The 0-day aging specimens represented non-aged samples, which were tested within a few minutes after solidification. Strain limit controlled fatigue testing was performed with various strain limits ranging from ±0.0005 to ±0.006 (e.g. ±0.0015, ±0.0025, ±0.0035, ±0.0045, etc.). For each set of aging conditions and strain range, at least 5 samples were tested to failure. The cyclic stress-strain response and the number of cycles to failure were recorded for each test, and the average and standard deviation of the number cycles to failure were calculated for each set of aging conditions and strain range.

Figure 6.2 illustrates an example of typical hysteresis loops generated during a single fatigue test performed until specimen failure. In this plot, the hysteresis loops are shown on increments of 100 cycles (i.e. the cycles shown include N = 1, 100, 200, 300, etc.). It is evident that during the cyclic loading for many hundreds or thousands of cycles that the peak stress drops continuously due to damage accumulation. Eventually crack initiation occurs, followed by crack growth, and fracture.

The evolution of the peak stress with the number of cycles for a typical SAC fatigue test is shown in Figure 6.3. It is seen that stress initially drops rapidly due to damage accumulation and material softening. Then, a steady state region ensues where re-crystallization and grain growth can occur, and where micro-cracks and micro-voids form as shown in Figure 1.9. Eventually, the stress will begin to drop rapidly when macro-sized cracks initiate and crack growth progresses to final rupture of the material. In this work, the fatigue life (cycles to failure) was defined to be the point in the cyclic test where a 50% load drop occurred. Park and Lee [176] showed that there were abrupt increases in the resistance of BGA solder joints at 50% load drop during fatigue testing.

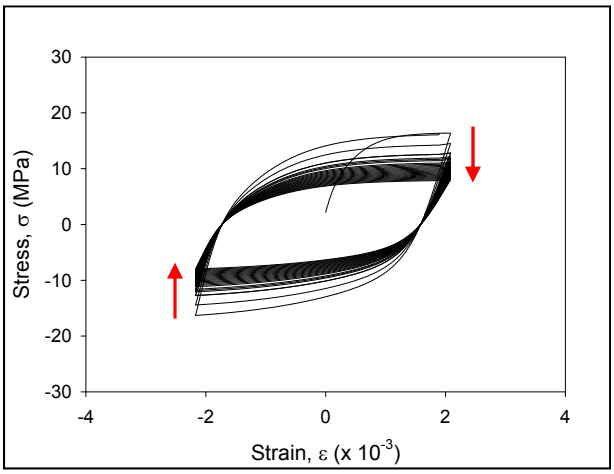

Figure 6.2 Hysteresis Loop Evolution during a Fatigue Test
(SAC105, Aged for 30 Days, Increments of One Hundred Cycles)

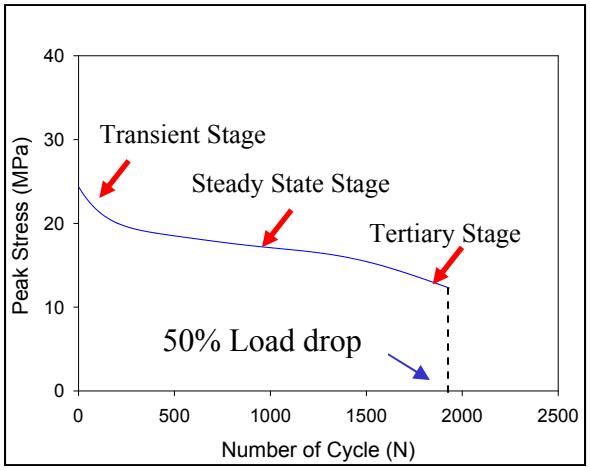

Figure 6.3 Typical Peak Stress Drop during a Fatigue Test

6.6 Effects of Aging on Fatigue Life

Figure 6.4 illustrates the recorded fatigue data (plastic strain range vs. number of cycles to failure) for SAC105 lead free solder samples subjected to different aging conditions (aging at 125 C for 0, 30, 120, 210, 300 and 360 days) prior to cyclic testing. Each data point represents an average of at least 5 fatigue tests for a particular set of aging/strain conditions, and the error bars indicated the standard deviations in the data. For each set of aging conditions, the $\Delta\varepsilon_p$ vs. N_f data demonstrated a nearly linear variation when graphed on a log-log scale. This suggests that the Coffin-Manson fatigue law [177-178] can accurately represent the data:

$$\begin{aligned} N_f^n \Delta\varepsilon_p &= C \\ \log\Delta\varepsilon_p &= \log C - n\log N_f \end{aligned} \tag{6.6}$$

where $\Delta\varepsilon_p$ is the inelastic strain range, N_f is the fatigue life (cycles to failure), n is the fatigue exponent, and C is the fatigue ductility. The inelastic strain range was calculated by subtracting the elastic strain from the total strain as indicated in the Figure 6.4. For each set of aging conditions, Eq. (6.6) has been regression fit to the data, and the colored straight lines in Figure 16 are the Coffin-Manson fatigue curves that result from the best fits to the data for the various aging conditions. The Coffin-Manson coefficients C and n calculated by least-squares regression analysis are tabulated in Table 6.4. From the plots in Figure 6.4, it can be seen that the Coffin-Manson curves/fits are nearly parallel. This is reflected by the small changes in coefficient n (see Table 6.4) that occur with aging.

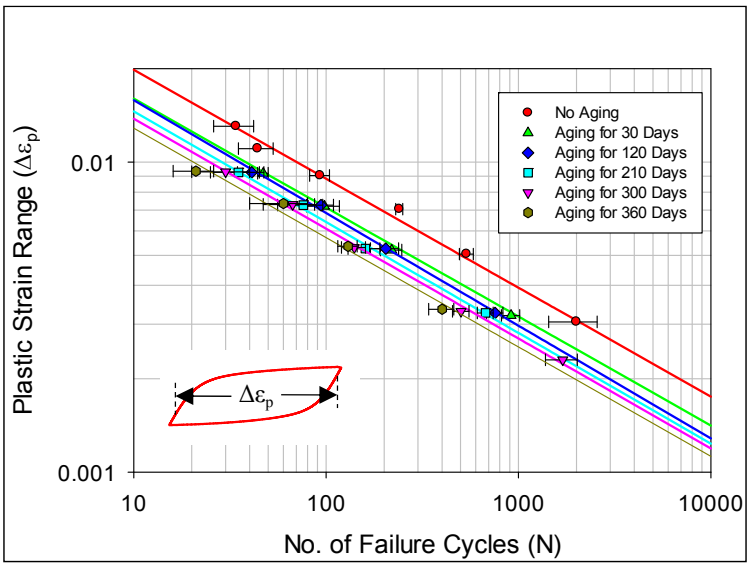

Figure 6.4 Fatigue Data (Plastic Strain Range vs. Cycles to Failure) for SAC105 Solder Subjected to Aging at 125 C

Table 6.4 Coffin-Manson Coefficients for SAC105 for Various Aging Conditions

Aging Conditions (Days)	Material Ductility Coefficient, C	Fatigue Exponent, n
0	0.04455	0.3514
30	0.03598	0.3515
120	0.03655	0.3636
210	0.03321	0.3575
300	0.03120	0.3545
360	0.02900	0.3529

The largest shift in the fatigue curves occurs in the first 30 days of aging. This is reflected by the relatively large (19.2%) change in coefficient C that occurs between no aging and 30 days of aging. As discussed subsequently in Chapter 9, transgranular cracking was the primary damage mode occurring in the non-aged SAC solder samples subjected to cyclic loading at room temperature. The fine grain sizes in the non-aged sample offered the best resistance to crack initiation. The large number of grain boundaries acted as crack stoppers or deflectors, thus reducing fatigue crack growth rates. With aging, there is significant micro-structural evolution and grain size coarsening. These effects promote more intergranular crack propagation (see Chapter 9), and contribute to the reduction in the fatigue life with aging. Crack propagation rates at grain boundaries are faster than those within grains due to prior microstructural damage and dislocation in the grain boundaries during aging. These observations are similar to those made by Kariya, et al. [40], who measured the fatigue life of SAC solders at room temperature and elevated temperature (100 C).

The fatigue data in Figure 6.4 has been recast to be in terms of the strain energy density (ΔW) dissipated per cycle, and the results are shown in Figure 6.5. The value of ΔW for each fatigue test was calculated from the area of the first cycle hysteresis loop. An alternative method to calculate ΔW calculation is to consider the area of the hysteresis loop in the final cycle just prior to failure. In that case, value of ΔW for each data point will be smaller. As before, each data point in Figure 6.5 represents the average of the fatigue tests for the particular set of aging/strain conditions, and the error bars indicated the standard deviations in the data. For each set of aging conditions, the recast ΔW vs. N_f data also demonstrated a nearly linear variation when graphed on a log-log scale. This

suggests that the Morrow energy-based fatigue law [153] can accurately represent the data:

$$\begin{aligned} N_f^m \Delta W &= K \\ \log \Delta W &= \log K - m \log N_f \end{aligned} \tag{6.7}$$

where m is the fatigue exponent, and K is the material ductility coefficient. For each set of aging conditions, Eq. (6.7) has been regression fit to the data, and the colored straight lines in Figure 6.5 are the Morrow model fatigue curves that result from the best fits to the data for the various aging conditions. The coefficients K and m calculated by least-square regression analysis are tabulated in Table 6.5.

Similar to the Coffin-Manson model prediction, it can be seen that the Morrow model curves/fits are nearly parallel. This is reflected by the small changes in coefficient m (see Table 6.5) that occur with aging. The largest shift in the fatigue curves again occurred in the first 30 days of aging. This is reflected by the relatively large (58.8%) change in coefficient K that occurs between no aging and 30 days of aging. As shown in Figure 6.6 and 6.7, fatigue life drops when the hysteresis loop size increases at a particular aging condition. These results agree with intuition, which says that increasing plastic work leads to decreased fatigue life. Such results are true for any particular fixed aging condition (microstructure). However, one cannot easily compare fatigue results for a given solder when several aging conditions are present. In this case, several microstructures exist for the same material, and our intuition must be adjusted.

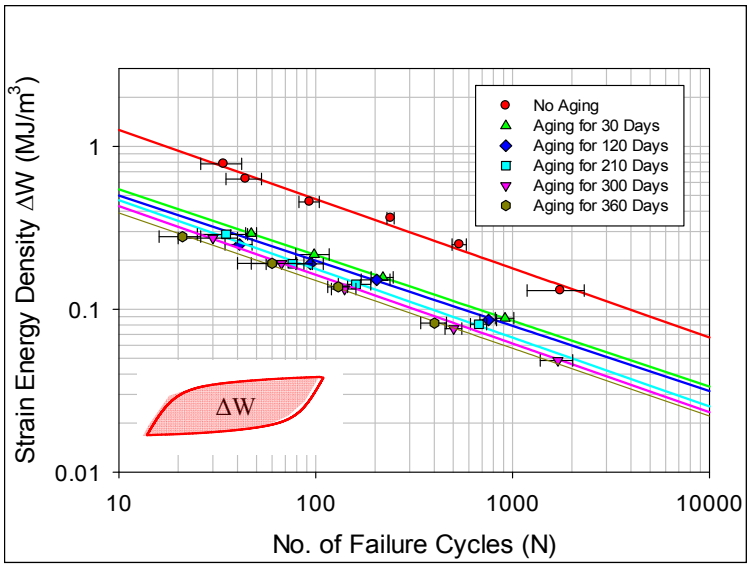

Figure 6.5 Fatigue Data (Energy Dissipation vs. Cycles to Failure) for SAC105 Solder Subjected to Aging at 125 C

Table 6.5 Morrow Model Coefficients for SAC105 for Various Aging Conditions

Aging Conditions (Days)	Material Ductility Coefficient, K	Fatigue Exponent, m
0	3.3510	0.4246
30	1.3816	0.4038
120	1.2534	0.4000
210	1.2370	0.4222
300	1.1347	0.4218
360	1.0162	0.4156

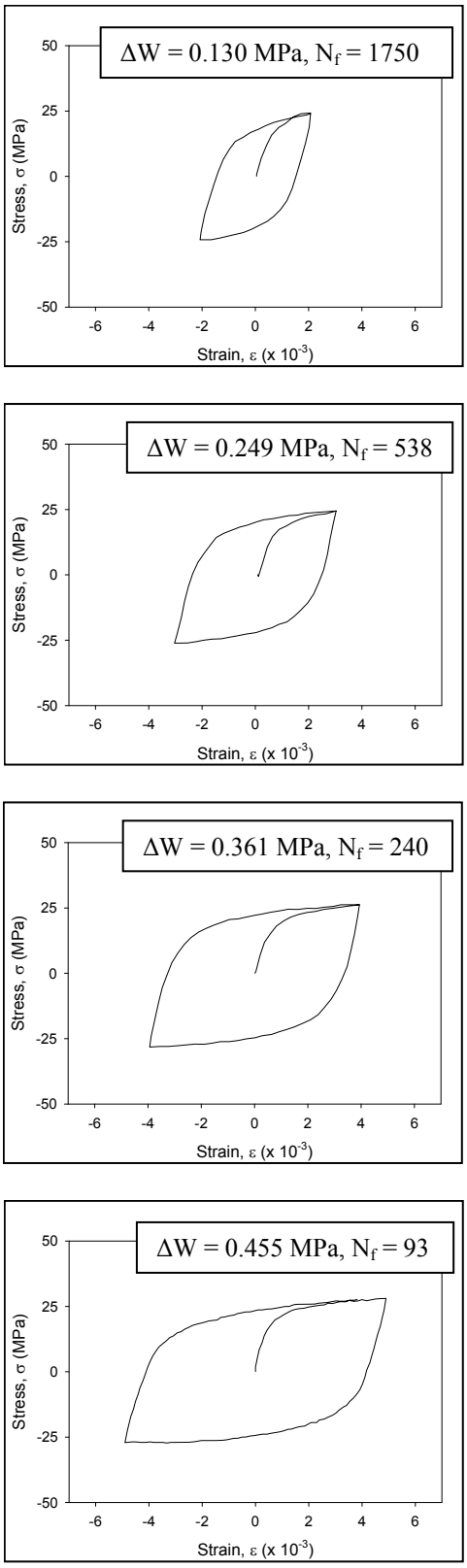

Figure 6.6 Cyclic Curves for Non-Aged Samples with Different ΔW (SAC105)

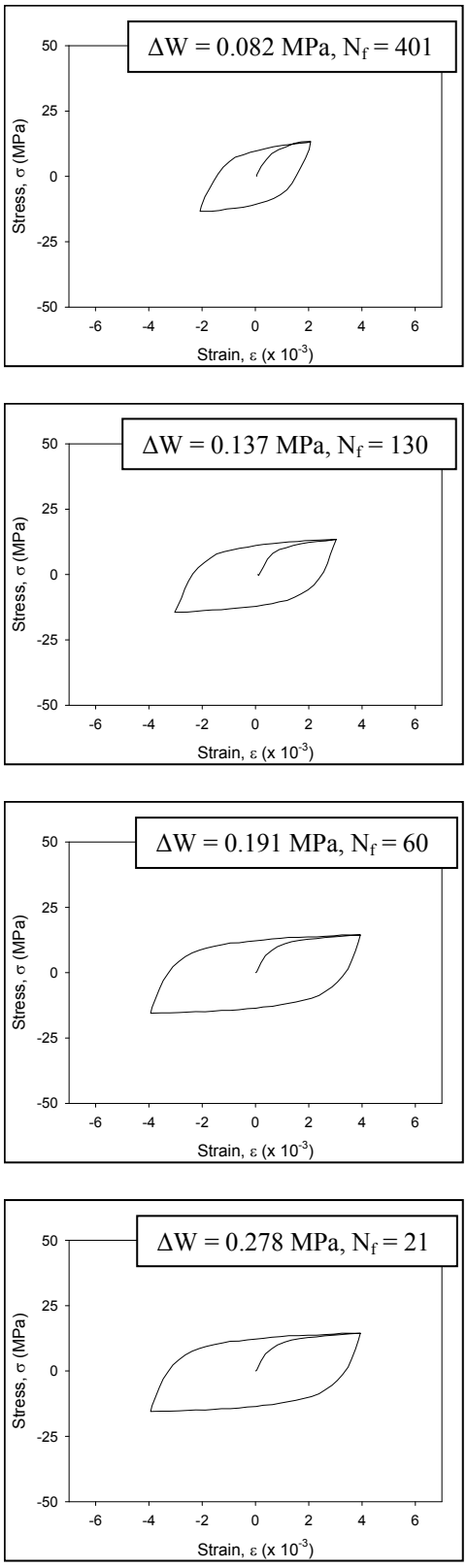

Figure 6.7 Cyclic Curves for Aged Samples with Different ΔW
(SAC105, Aging for 360 Days)

As mentioned previously, the value of ΔW used for each data point in the fatigue plots was found from the area of the first cycle during mechanical cycling. In actuality, the value of ΔW evolves dramatically during each fatigue test. This is shown pictorially in Figure 6.8 and quantitatively in Figure 6.9. For any given test, the value of ΔW for the first cycle represents the largest value during the experiment. The hysteresis loop size also changes with aging as discussed in Chapter 5 and shown in Figure 6.10. In this case, the first cycle hysteresis loop has been plotted for each aging condition.

Figures 6.11 contains the analogous fatigue data for SAC305 along with the Coffin-Manson fatigue curves, and Table 6.6 contains the calculated Coffin-Manson coefficients C and n for various aging conditions. Likewise, the SAC305 fatigue data in terms of the strain energy density (ΔW) dissipated per cycle are shown in Figure 6.12, while Table 6.7 contains the calculated Morrow model coefficients K and m for the various aging conditions. The fatigue curves again show a progression with duration of aging, with the largest changes occurring with the first 30 days of aging. In addition, the fatigue curves are nearly parallel for the various aging conditions (m and n are nearly independent of aging).

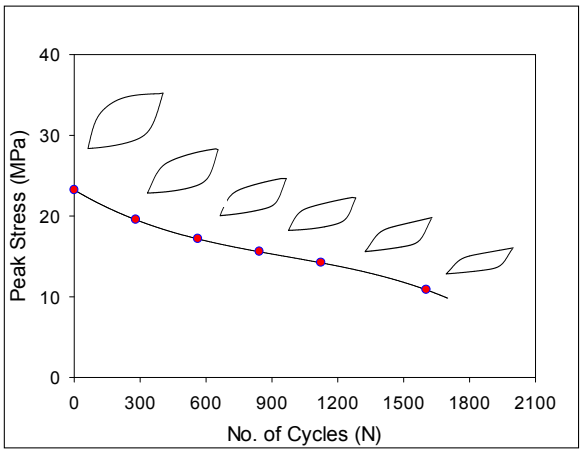

Figure 6.8 Evolution of Hysteresis Loop Shape with Number of Cycles during a Single Fatigue Test (Δε = 0.004, No Aging, SAC105)

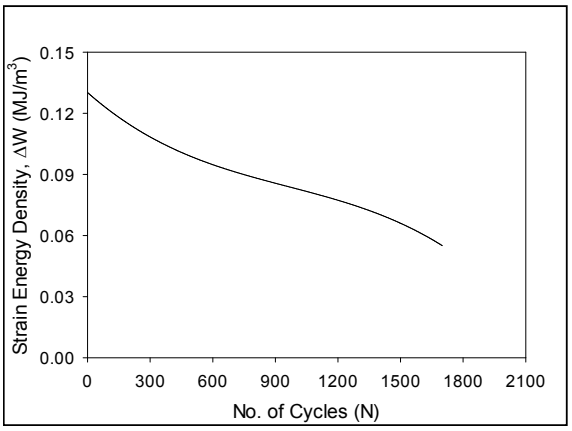

Figure 6.9 Evolution of Hysteresis Loop Area with Number of Cycles during a Single Fatigue Test (Δε = 0.004, No Aging, SAC105)

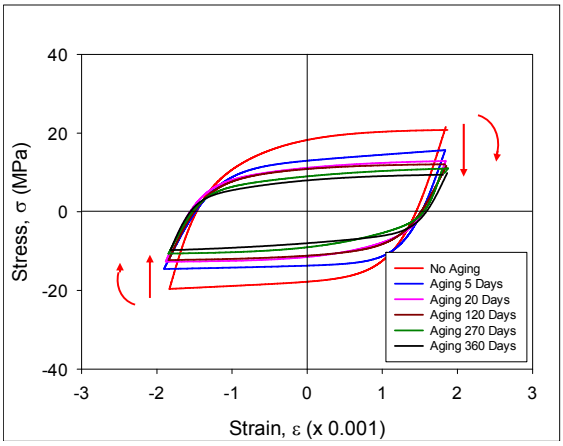

Figure 6.10 First Cycle Hysteresis Loops for Cyclic Stress-Strain Testing of SAC105 (Strain Controlled, Aging for 0-12 Months at 125 C)

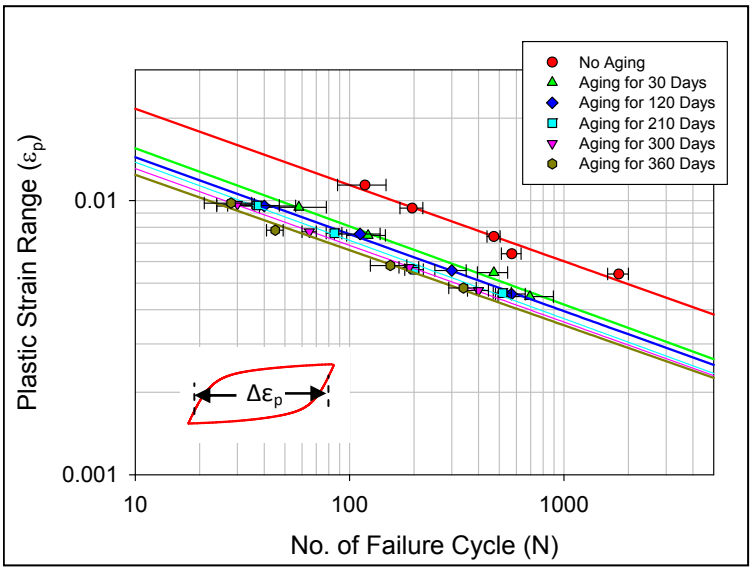

Figure 6.11 Fatigue Data (Plastic Strain Range vs. Cycles to Failure) for SAC305 Solder Subjected to Aging at 125 C

Table 6.6 Coffin-Manson Coefficients for SAC305 for Various Aging Conditions

Aging Conditions (Days)	Material Ductility Coefficient, C	Fatigue Exponent, n
0	0.04106	0.2782
30	0.02994	0.2850
120	0.02752	0.2809
210	0.02670	0.2856
300	0.02490	0.2799
360	0.02340	0.2743

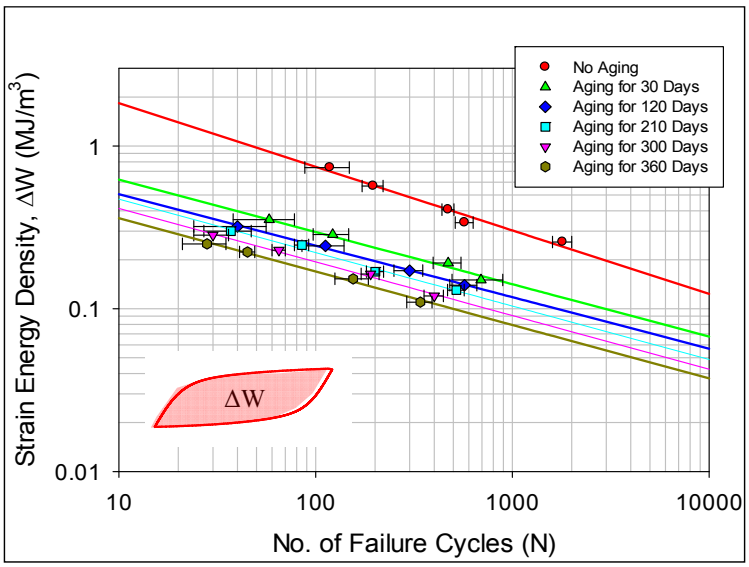

Figure 6.12 Fatigue Data (Plastic Strain Range vs. Cycles to Failure) for SAC305 Solder Subjected to Aging at 125 C

Table 6.7 Morrow Model Coefficients for SAC305 for Various Aging Conditions

Aging Conditions (Days)	Material Ductility Coefficient, C	Fatigue Exponent, m
0	4.5040	0.3906
30	1.3028	0.3214
120	1.0490	0.3165
210	1.0055	0.3286
300	0.8828	0.3292
360	0.7674	0.3282

6.7 Effects of Silver Content on Fatigue Life of Lead-free Solder

The slopes of the fatigue curves in Figures 6.4, 6.5, 6.11 and 6.12 are nearly constant for each SAC alloy taken individually. However, they are different for the 2 alloy systems. For example, Figures 6.13 and 6.14 show the Coffin-Manson and Morrow model fatigue curves for no aging for both SAC105 and SAC305. The convergence of the curves for very high strain levels is clearly evident. It is also noticeable (see Tables 6.4, 6.5, 6.6, and 6.7) that the fatigue ductility exponents (m and n) of SAC305 are lower than those for SAC105 for both plastic strain range (Coffin-Manson) and strain energy density (Morrow) based models. Low fatigue ductility exponents are necessary to have necessary to have excellent fatigue endurance as reported by Kariya, et al. [149, 179]. Also, good strength and good ductility are required for solder alloys that will undergo low cycle fatigue.

SAC305 alloy has good low cycle fatigue resistance, since the strength and the ductility of the alloy are well balanced. From the Coffin-Manson fits, it is evident that the SAC105 alloy has high ductility, which results in good fatigue performance in the high strain regime. The cycle strain hardening exponent (inverse function of the fatigue ductility exponent) of SAC105 is much lower than that for SAC305, which leads to somewhat poor fatigue resistance in the low strain regime. Similar experimental results were also reported by Kariya, et al. [149], where it was concluded that low silver content alloys were unsuitable candidates for lead-free solder bumps.

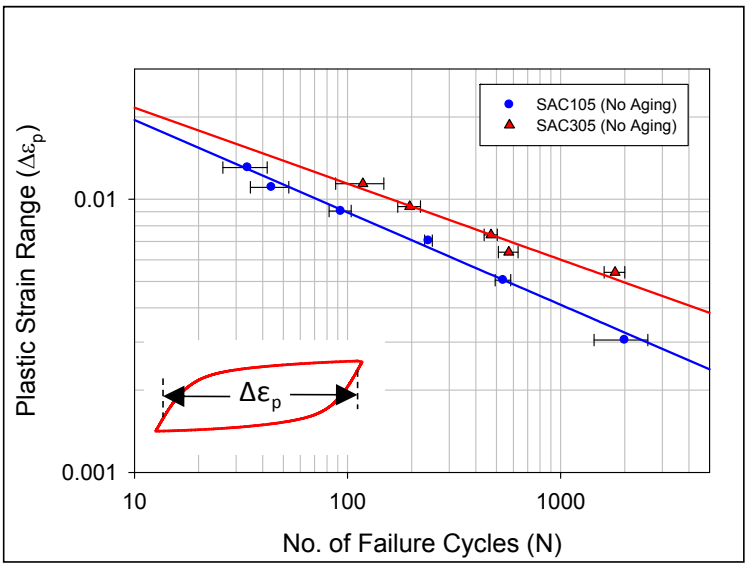

Figure 6.13 Fatigue Data (Plastic Strain Range vs. Cycles to Failure) for SAC105 and SAC305 Solders (No Aging)

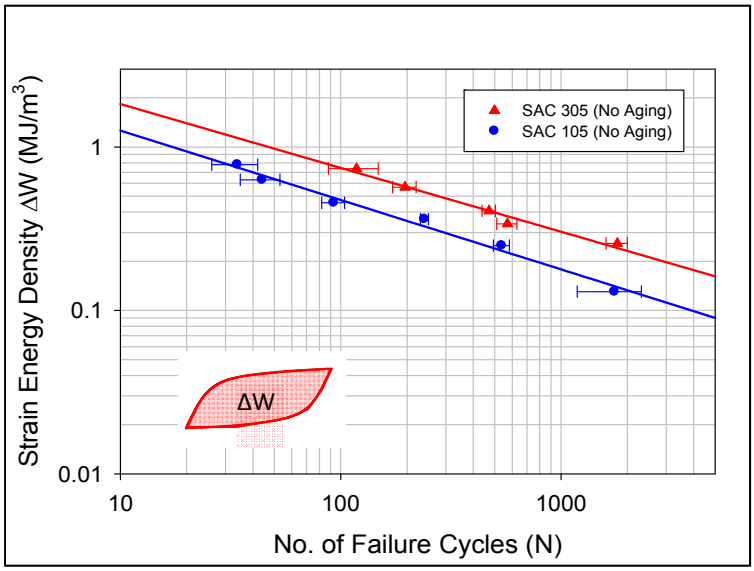

Figure 6.14 Fatigue Data (Strain Energy Density vs. Cycles to Failure) for SAC105 and SAC305 Solders (No Aging)

The microstructures of SACN05 solder alloys consist of a β-Sn matrix with a dispersed system of Ag_3Sn and Cu_6Sn_5 intermetallic compounds. The size of the dispersoids vary from submicron to several microns for all alloys, which is a common feature of the alloys reported [180]. The volume fraction of the dispersoids in the microstructure increases with increasing silver content. In the microstructure of SAC105, there were relatively large Sn dendrites and the Ag_3Sn dispersoids appeared sparsely within the matrix. For SAC305, the Ag_3Sn intermetallic compound formed a network structure around the Sn dendrites, and the Ag_3Sn intermetallic compounds were finely dispersed within the matrix. The interparticle distance for SAC305 was smaller than that in SAC105. It has been reported that Sn-Ag-Cu solder alloys have a dispersion or precipitation strengthening mechanism [181]. Thus, the dispersion morphology of the Ag_3Sn intermetallics strongly affects the mechanical properties of the alloys tested. Namely, if the microstructure of an alloy has finely dispersed Ag_3Sn particles, the alloy and Sn grains may exhibit high strength because of the Orowan effect. Moreover, if coarsening of an alloy is inhibited because of the finely dispersed Ag_3Sn particles, good fatigue resistance can be expected as a result of increasing resistance to dislocation movement in the material. The Ag_3Sn dispersoids were more finely dispersed in the microstructure of SAC305 which led to a good fatigue resistance relative to SAC105. The phenomenon was also reported by Terashima, et al. [182].

6.8 Effects of Solidification Temperature Profile on the Fatigue Life

A comparative study has been carried out for two different solder solidification cooling rates, namely water quenching (WQ) and reflow (RF) cooling as discussed in Chapter 3. Water quenching is considered an extremely fast cooling solidification process, while a reflow process is relatively slow in comparison. Initial microstructures of the specimens are highly dependent on the cooling rate during solidification. A relatively fine phase structure was formed in the water quenched specimens after solidification, whereas a coarser structure was observed in the reflowed specimens. Mechanical behavior corresponds with the microstructure, and for SAC solder, quickly cooled specimens exhibit higher strength than slow-cooled specimens due to finer grain size and the interaction of dislocations with Ag_3Sn particles [146]. In addition, the microstructure of reflowed SAC105 and SAC305 samples exhibit relatively more Cu_6Sn_5 IMC particles with wider area of binary eutectic at the Sn boundaries [183]. Therefore, in general, fine microstructure results in good mechanical strength and good ductility for an alloy and such mechanical properties are preferred to enhance the fatigue performance.

A similar study was carried out for SAC387 solder considering air cooling and water quenching solidification processes by Kim, et al. [184]. They reported that the fatigue life was about 14.5% lower for the air cooled specimens. Conversely, Abtew, et al. [183] concluded that the cooling rate had little effect on the fatigue life of SAC solder joints.

Figures 6.15 and 6.16 show comparisons of the isothermal fatigue curves for water quenched and reflowed samples of SAC105 solder based on plastic strain range

and strain energy density. Analogous results for SAC305 are shown in Figures 6.17 and 6.18. From the plastic strain range based fatigue model prediction (Coffin-Manson model), it is clearly observed that fatigue life of the water quenched SAC105 samples was about 20% (17% in case of SAC305) higher than reflowed samples (see Figures 6.15 and 6.17). About 30% (29% in case of SAC305) higher fatigue life was found for the water quenched SAC105 samples relative to the reflowed samples using the strain energy density based fatigue model prediction (see Figures 6.16 and 6.18). The slopes of the fatigue curves for the SAC105 and SAC305 solders were nearly constant (fatigue ductility exponents n and m) for each solidification profile (see Tables 6.8-6.11). Therefore, the percentage of degradation in the fatigue life can be calculated from fatigue coefficients C and K.

By using Eq. (6.6) and the assumptions of a fixed strain range and constant n, the following expression can be obtained for the differences in the fatigue lifetimes of the WQ and RF specimens:

$$\left[\frac{N_{WQ}-N_{RF}}{N_{WQ}}\right]\times 100=\left[\frac{\sqrt[n]{C_{WQ}}-\sqrt[n]{C_{RF}}}{\sqrt[n]{C_{WQ}}}\right]\times 100 \tag{6.8}$$

A similar expression can be obtained from the Morrow model in Eq. (6.7) for the assumptions of fixed ΔW and constant m:

$$\left[\frac{N_{WQ}-N_{RF}}{N_{WQ}}\right]\times 100=\left[\frac{\sqrt[m]{K_{WQ}}-\sqrt[m]{K_{RF}}}{\sqrt[m]{K_{WQ}}}\right]\times 100 \tag{6.9}$$

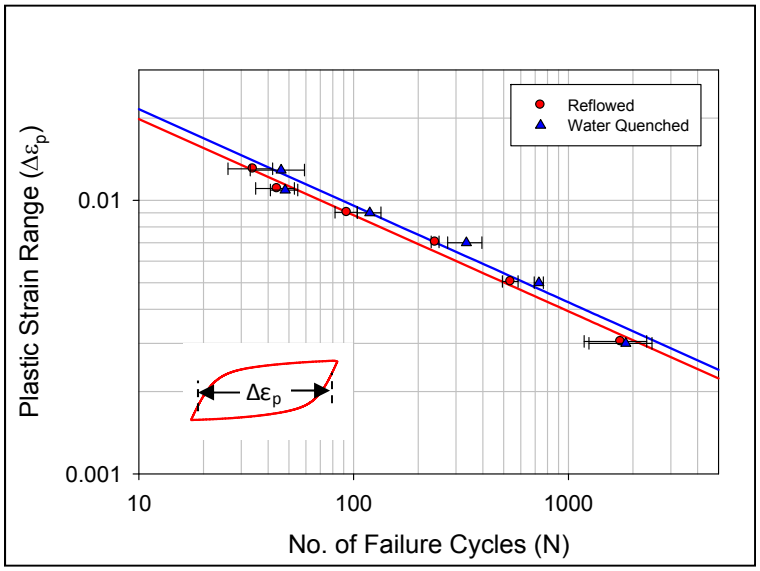

Figure 6.15 Comparison of Fatigue Life for Water Quenched and Reflowed SAC105 Samples (No Aging) Based on Plastic Strain Range

Table 6.8 Coffin-Manson Model Coefficients and Number of Failure Cycles for SAC105 (No Aging)

Solidification Type	Material Ductility Coefficient, C	Fatigue Exponent, n
Reflowed	0.04455	0.3514
Water Quenched	0.03598	0.3515

Plastic Strain Range	No. of Failure Cycles (WQ)	No. Failure Cycles (RF)
0.011268	63	50
0.006400	312	250
0.004915	659	530
0.003815	1351	1090
0.003082	2471	2000

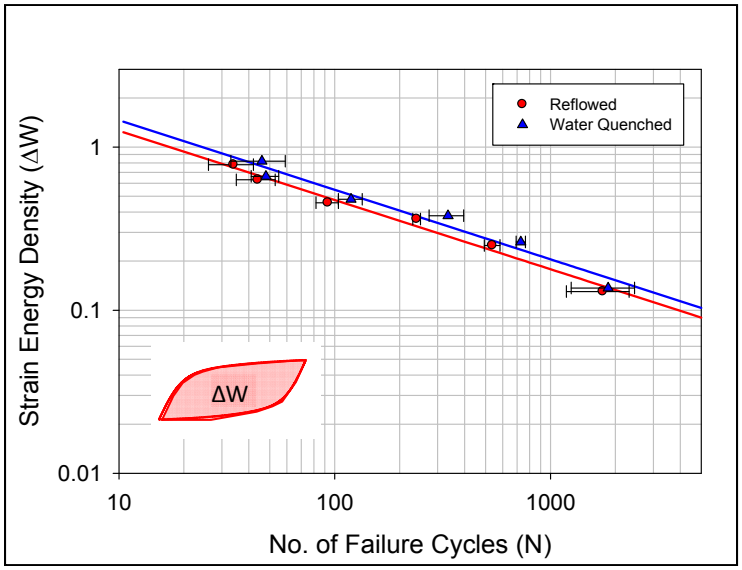

Figure 6.16 Comparison of Fatigue Life for Water Quenched and Reflowed SAC105 Samples (No Aging) Based on Strain Energy Density

Table 6.9 Morrow Model Coefficients and Number of Failure Cycles for SAC105 (No Aging)

Solidification Type	Material Coefficient, K	Fatigue Exponent, m
Reflowed	4.5040	0.3906
Water Quenched	5.2215	0.3956

Strain Energy Density	No. of Failure Cycles (WQ)	No. Failure Cycles (RF)
1.83231	14	10
0.63421	206	151
0.32552	1113	834
0.21909	3029	2299
0.17422	5405	4133

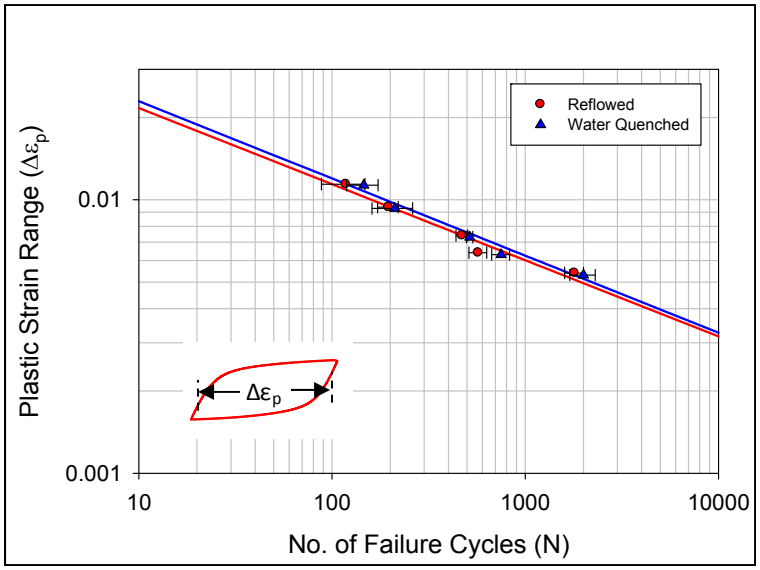

Figure 6.17 Comparison of Fatigue Life for Water Quenched and Reflowed SAC305 Samples (No Aging) Based on Plastic Strain Range

Table 6.10 Coffin-Manson Model Coefficients and Number of Failure Cycles for SAC305 (No Aging)

Solidification Type	Material Ductility Coefficient, C	Fatigue Exponent, n
Reflowed	0.04106	0.2782
Water Quenched	0.04390	0.2822

Plastic Strain Range	No. of Failure Cycles (WQ)	No. Failure Cycles (RF)
0.02164	12	10
0.01127	124	104
0.00640	919	797
0.00492	2343	2059
0.00382	5750	5120
0.00308	12243	11022

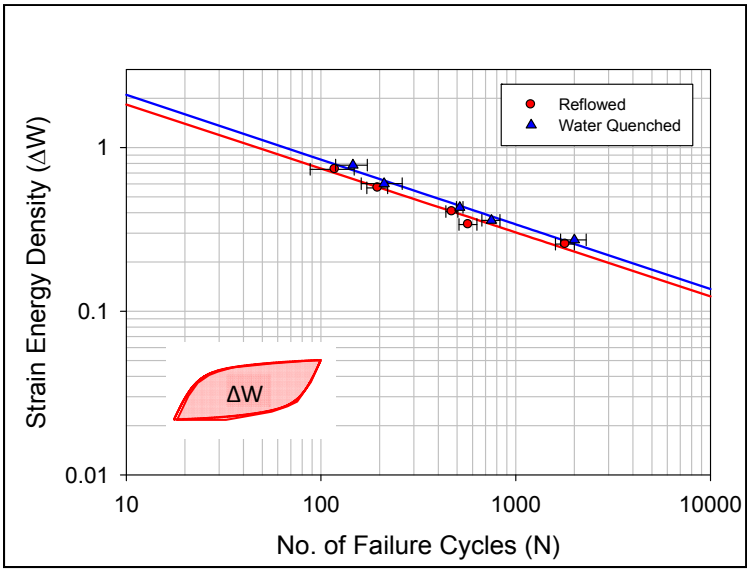

Figure 6.18 Comparison of Fatigue Life for Water Quenched and Reflowed SAC305 Samples (No Aging) Based on Strain Energy Density

Table 6.11 Morrow Model Coefficients and Number of Failure Cycles For SAC305 (No Aging)

Solidification Type	Material Coefficient, K	Fatigue Exponent, m
Reflowed	4.5040	0.3906
Water Quenched	5.2215	0.3956

Strain Energy Density	No. of Failure Cycles (WQ)	No. Failure Cycles (RF)
1.83231	14	10
0.63421	206	151
0.32552	1113	834
0.21909	3029	2299
0.17422	5405	4133

6.9 Reduction of the Fatigue Life of SAC Solder for Long-term Aging

Figure 6.19 shows the fatigue curves for no aging and long term aging (Aging for 360 days) for reflowed SAC105 and SAC305 solders using the Coffin-Manson model. Although the convergence of the curves for very low strain levels is clearly evident, SAC305 exhibits higher fatigue endurance than SAC105 at all strain levels for a given solidification profile (microstructure). However, the fatigue resistance of highly aged SAC305 solder is lower than that for non-aged SAC105 solder. Analogous results for the Morrow model fatigue curves are shown in Figure 6.20. Again, the fatigue resistance of highly aged SAC305 solder is lower than that for non-aged SAC105 solder.

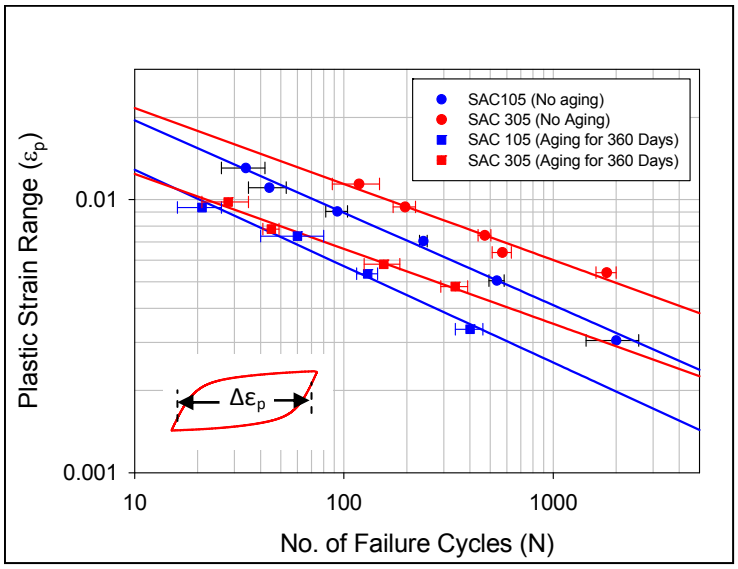

Figure 6.19 Fatigue Data (Plastic Strain Range vs. Cycles to Failure) for SAC105 and SAC305 Solders

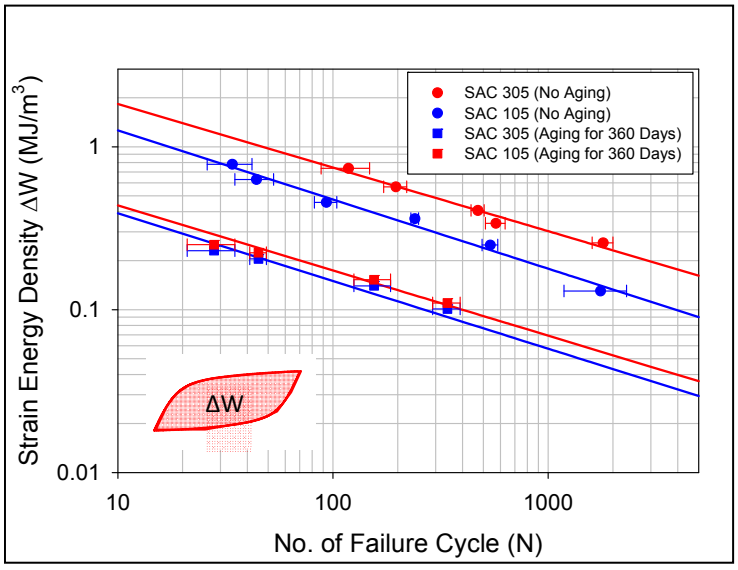

Figure 6.20 Fatigue Data (Strain Energy Density vs. Cycles to Failure) for SAC105 and SAC305 Solders

6.10 Summary and Discussion

In this chapter, the effects of aging on the fatigue behavior of lead free solders were investigated. Uniaxial SAC105 and SAC305 lead free solder specimens were subjected to cyclic (tension/compression) mechanical loading under strain limit control (constant positive and negative strain limits). The hysteresis loop size (area) was calculated from the measured cyclic stress-strain curves for a given solder alloy and temperature. This area represents the strain energy density dissipated per cycle, which can be typically correlated to the damage accumulation in the solder material.

For both alloys, the fatigue data expressed as plastic strain change vs. cycles to failure demonstrated a nearly linear variation for all aging conditions when graphed on a log-log scale. This suggests that the Coffin-Manson fatigue law can accurately represent the data for the various aging conditions, and the largest shift in the fatigue curves occurred in the first 30 days of aging. While the slopes of the fatigue curves were nearly constant for each SAC alloy taken individually, they were different for SAC105 and SAC305. A clear progression of the fatigue curves was observed with longer aging times prior to mechanical cycling. The fatigue data was also recast in terms of the energy dissipated per cycle (ΔW) in the first cycle hysteresis loop. The fatigue curves in this case were found to be well fit by the Morrow energy-based fatigue law for all aging conditions. Effects of the solidification cooling profile and of silver content on the fatigue behavior of the SAC alloys were also discussed. Higher silver content SAC305 alloy exhibited excellent fatigue resistance for both non-aged and aged conditions.

CHAPTER 7

SHEAR SPECIMEN PREPARATION AND DEVELOPMENT OF EXPERIMENTAL TEST SYSTEM

7.1 Introduction

In this chapter, a shear specimen design and associated testing preparation technique are presented. The developed sample configuration is based on an Iosipescu-type specimen design. The micro-scale shear specimens can be fabricated without further modification and machining. Several different shear testing techniques have used for solder joints including the Iosipescu technique [83-84, 185-188], ring-and-plug shear [189-190], single lap-shear [191-193], double lap shear [194], and solder ball shear [195]. Although none of these techniques provide a uniform pure state of shear stress in the test sample, the Iosipescu method has been popular due to its widespread use for shear testing of fiber-reinforced composite materials. Zhang, et. al [83-84, 187] have used an Iosipescu-type specimen to perform cyclic testing and creep testing of solders in shear. The uniformity of the shear stress/strain state in the utilized test samples has been explored by Mukherjee and Dasgupta [188]. In this chapter, a similar modified lap shear technique has been developed using an Iosipescu-type shear specimen. Finite element analysis has been used to establish that the developed method provides a good approximation to pure shear loading. A shear specimen loading fixture

has also been designed and constructed to perform shear cyclic stress-strain tests and shear fatigue tests. A load train calibration procedure was established for the developed system, and the results are also presented in this chapter.

7.2 Shear Specimen Design

Due to differences in the coefficients of thermal expansion in the materials making up electronic assemblies, solder joints are often subjected to cyclic shear deformations during thermal cycling. Since the dominant mode of failure in most solder interconnects is shear, it is important to perform shear cyclic stress-strain and fatigue testing of solder alloys (in addition to the tension/compression cyclic testing discussed in previous chapters). It is desirable that the utilized shear test specimens should be fabricated with a solidification profile similar to the assembly reflow process, so that the specimen microstructures are similar to those in actual solder joints.

Miniature solder shear specimens can have a single joint (single-lap shear), or two joints (double-lap shear), or have multiple joints (arrayed-lap shear; solder ball array). Iosipescu [196] has designed a specimen for single in-plane shear of metals or composites utilizing a notched beam type sample, which is loaded so as to produce a zero bending moment across the notch or test section. A typical Iosipescu specimen is shown in Figure 7.1.

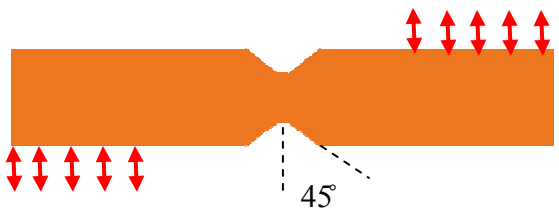

Figure 7.1 Typical Configuration of Iosipescu Shear Specimen

Kwon, et al. [197] have developed a solder Iosipescu specimen based on a micro-lap shear design [198]. They have used a nominal joint height of 300 μm to simulate the geometric and loading constraints present in a solder bump. In addition, Kariya, et al. [199] investigated the influence of the joint size on low cycle fatigue characteristics of SAC solders by using a miniature of shear specimens fabricated using solder balls having various diameters including 500 μm, 300 μm, 240 μm, 200 μm, 150 μm, and 100 μm. Lee, et al. [200] studied the effects of Sb addition on the shear strength and fracture behavior of Sn-Ag based solders using a single ball shear specimen having a diameter of roughly 1.7 μm. Andersson, et al. [201] used hourglass shaped solder joints with an average height of 0.4 mm and average diameter of 1.5 mm. Darveaux and Banerji [202] have fabricated double lap shear specimens employing a 3 x 3 solder ball array. In their investigation, they used various solder joint heights from 0.004 to 0.016 inches. The effects of solder-ball shape and height as well as chip size on the fatigue life of Sn-Pb eutectic solder balls in a soldered BGA component were investigated by Liang, et al. [203] (see Figure 7.2).

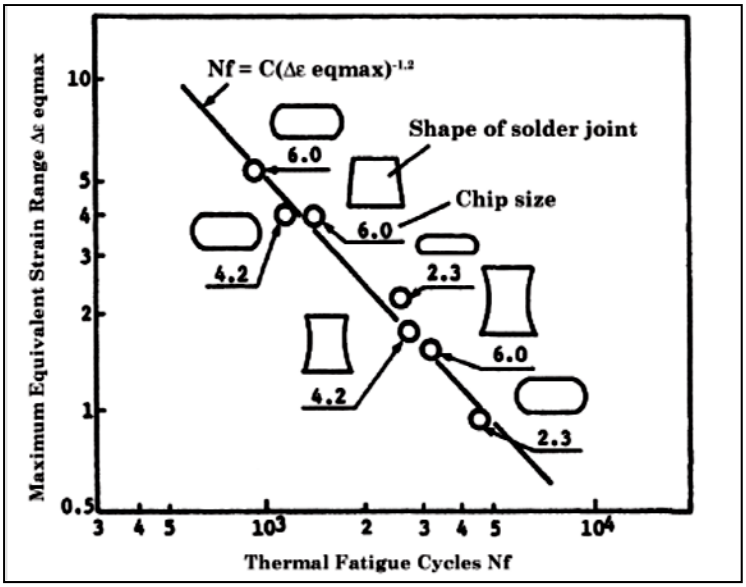

Figure 7.2 Effects of BGA Ball Geometry and Chip Size on Fatigue Life of Sn-Pb Eutectic Solder Balls [203]

7.3 Finite Element Analysis of Shear Specimens

In this work, finite element modeling was used to study the stress and strain distributions in solder ball and Iosipescu lap shear specimens. The results are now discussed.

7.3.1 Ball Shear Specimen

A finite element model of a ball shear test sample is shown in Figure 7.3. The solder ball assembly consisted of a 3 x 3 array of solder balls that were solidified to pads on a BT substrate and PCB. The solder balls were 1 mm in diameter, and had a pitch of 2 mm (see Figure 7.4). The whole solder ball assembly was held and loaded by a pair of stainless steel grips as shown in Figure 7.3. Three-Dimensional brick elements were used for the solder balls and assembly as shown in Figure 7.5. For boundary conditions, it was assumed that one end of fixture was fixed, and that a uniaxial load was applied to the other end of the fixture. The stainless steel, copper, BT substrate, and PCB materials

were all modeled as linear elastic, while the solder balls (SAC105) were modeled as a viscoplastic (Anand Model) as shown in Figure 7.6.

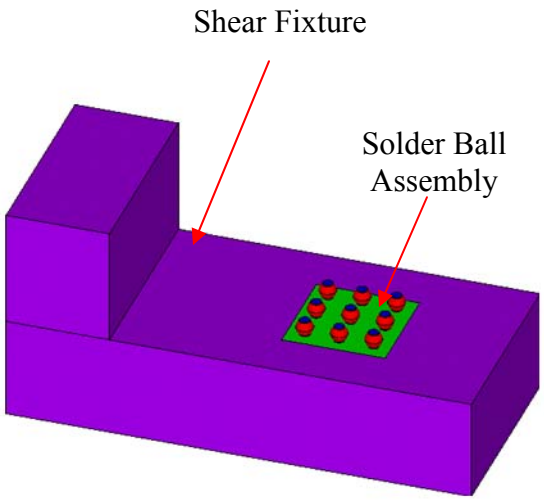

(a) Gripping Solder Ball Assembly into Shear Fixture

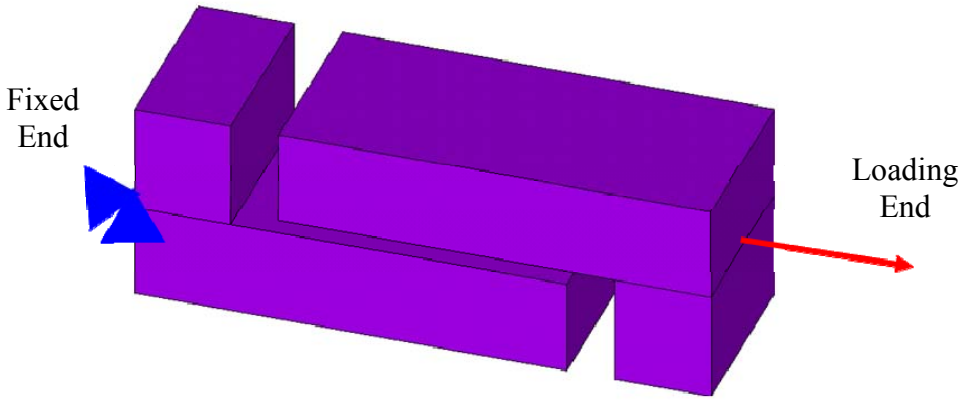

(b) Boundary Conditions

Figure 7.3 Finite Element Modeling of Solder Ball Shear Test Assembly

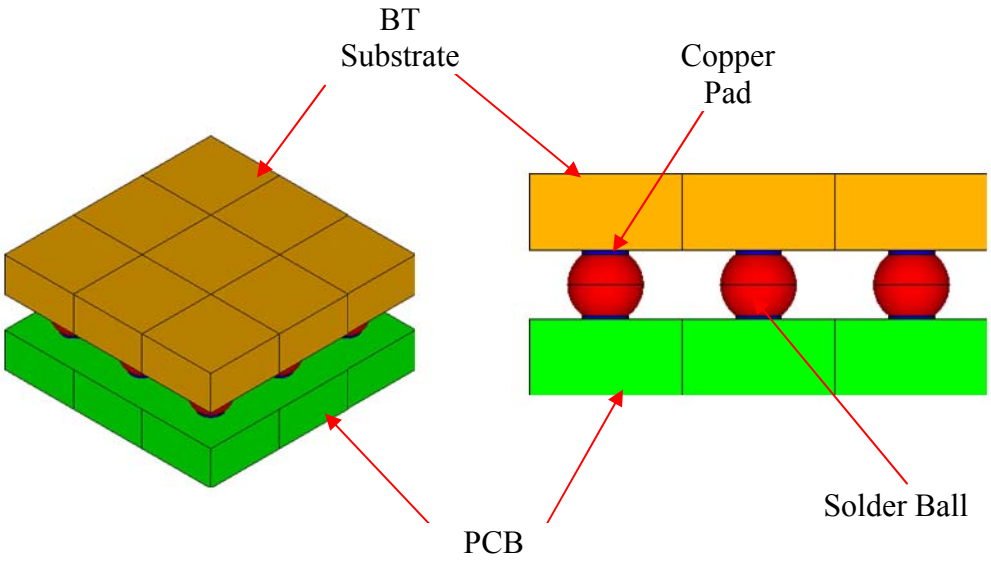

Figure 7.4 Solder Ball Assembly

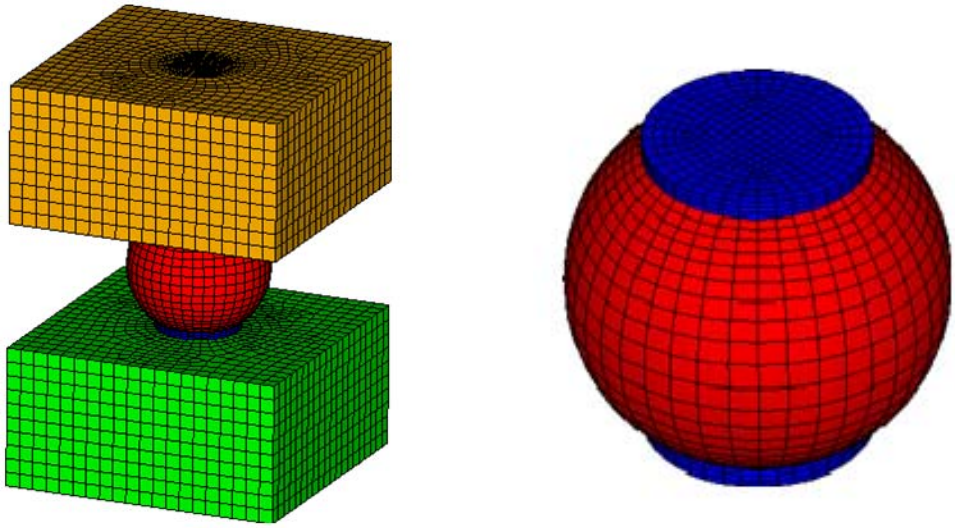

Figure 7.5 Finite Element Mesh Near a Solder ball

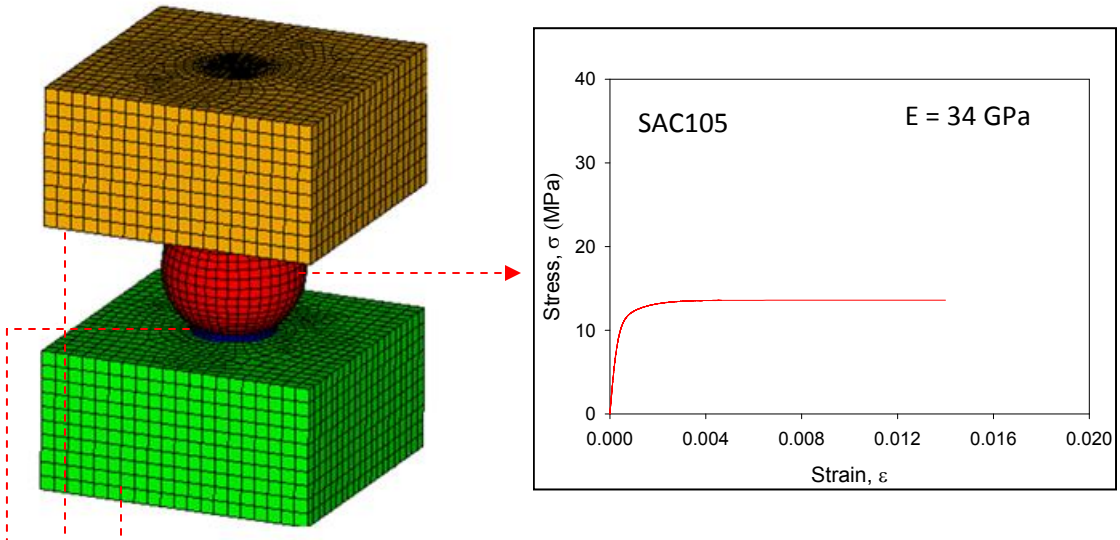

Material	Elastic Modulus (GPa)	Poisson's Ratio
PCB Board (FR-4)	17.3	0.3
BT Substrate	17.3	0.3
Copper Pad	117.0	0.3
Stainless Steel	209.0	0.3

Figure 7.6 Material Properties of Solder Ball Assembly Model

An ANSYS finite element model was created to simulate the stresses and strains in the loaded solder joints. SOLID95 brick elements were used for the 3D finite element meshing as shown in Figure 7.5. Convergence testing (element dependency test) confirmed that a sufficient number of elements had been used to get accurate results. Figure 7.7 shows the three-dimensional shear stress τ_{xy} distribution within solder balls for a typical loading level. It was observed that the shear stress τ_{xy} was not uniform throughout the solder balls. In addition, the six stress component and strain component distributions for the center ball are shown in Figures 7.8 and 7.9. It is clear that the other stress and strain components are not negligible, and often exceed the values of τ_{xy} and

γ_{xy}. Thus, the state of loading is not pure shear, and this approach is not suitable for measuring pure shear properties of solder alloys.

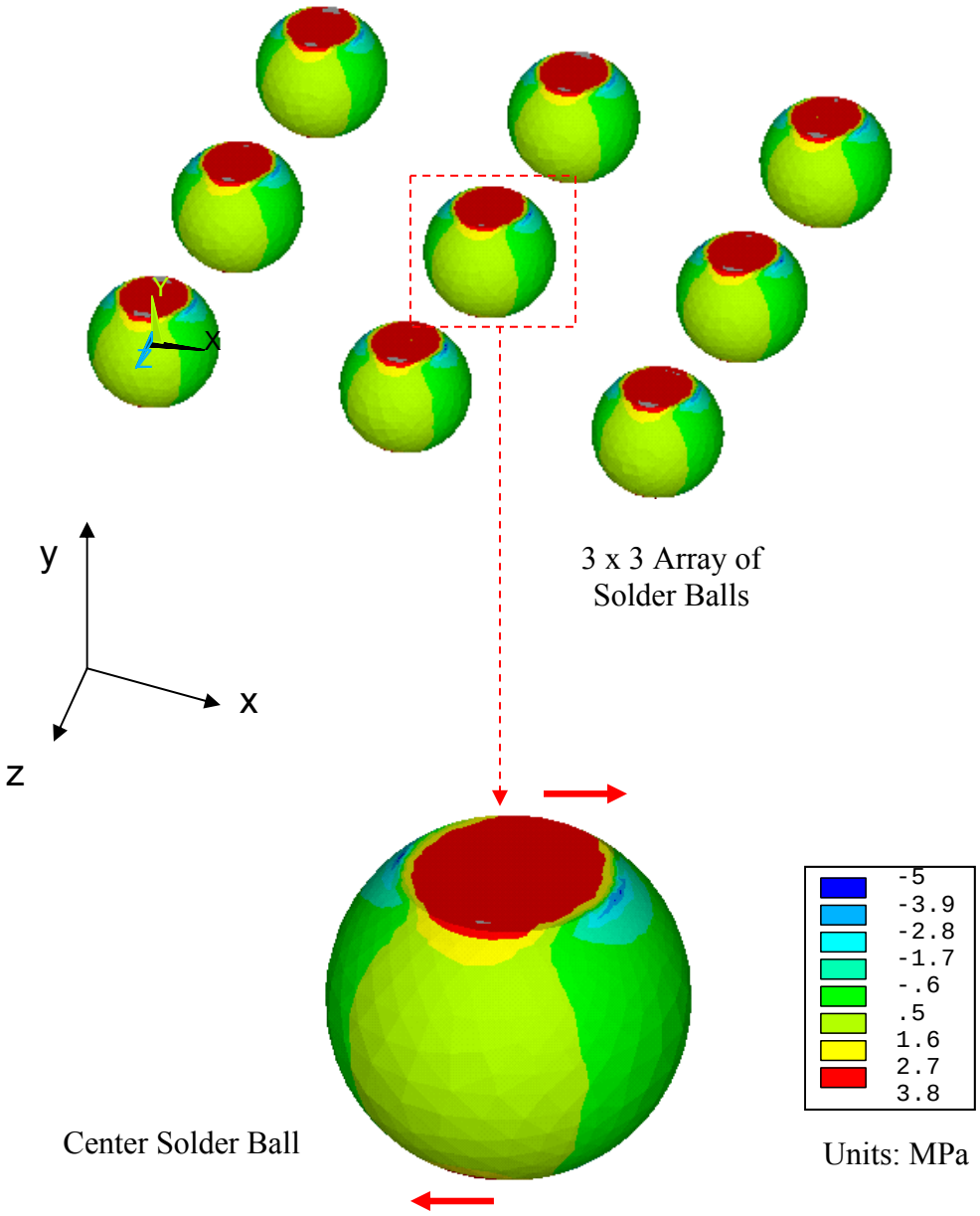

Figure 7.7 Shear Stress τ_{xy} Distribution in the Solder Balls

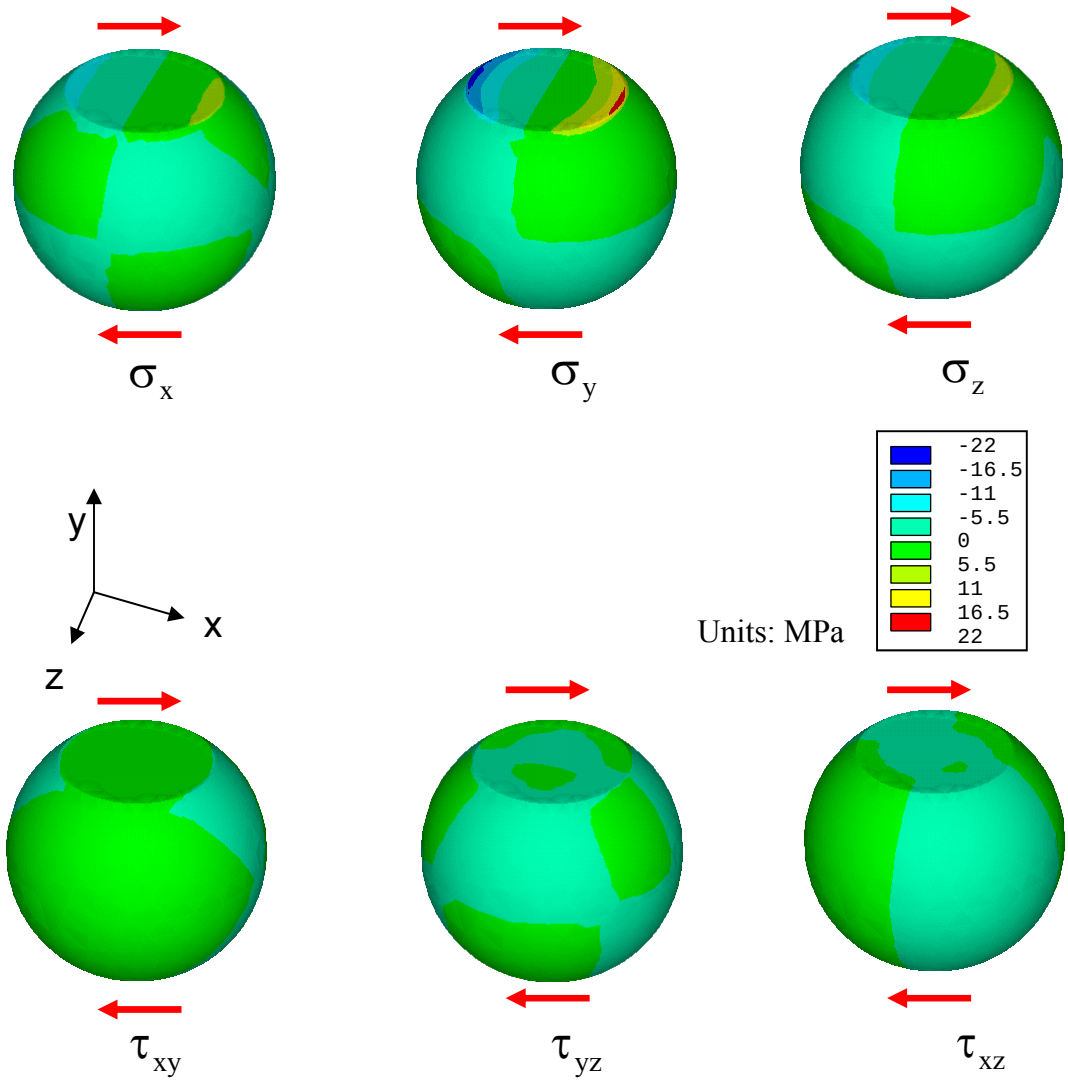

Figure 7.8 Normal and Shear Stress Distributions for the Center Solder Ball

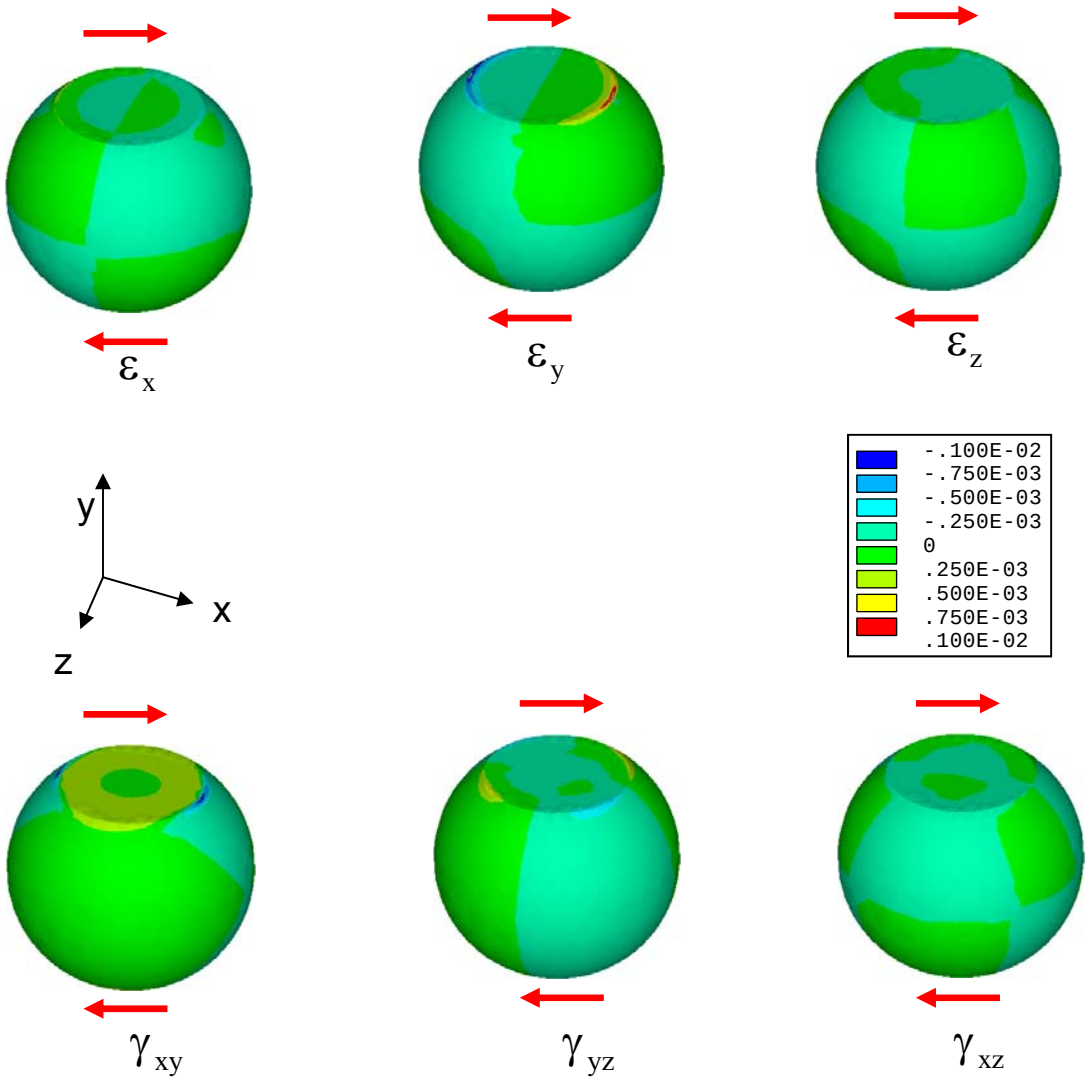

Figure 7.9 Normal and Shear Strain Distributions for the Center Solder Ball

7.3.2 Lap Shear Specimen (Iosipescu Shear Specimen)

The shear test sample developed in this work is shown in Figure 7.10. It consists of a 3 x 3 x 0.25 mm solder layer that is solidified between two copper end pieces that are angled to form an Iosipescu-type test assembly. The copper/solder Iosipescu specimen assemblies are held and loaded by a pair of stainless steel grips as shown in Figure 7.10. This approach creates a modified lap shear type loading of the solder layer, where the Iosipescu design in the copper end pieces helps to provide a more uniform state of shear. An ANSYS finite element model (see Figure 7.11) was created to simulate the stresses and strains in the loaded solder layer. For boundary conditions, it was assumed that one end of fixture was fixed, and that a uniaxial load was applied to the other end of the fixture. The stainless steel and copper portions of the fixture were modeled as linear elastic materials, while the solder layer (SAC105) was modeled as a viscoplastic material (Anand Model) as shown previously in Figure 7.6.

Figures 7.12 to 7.14 show the three-dimensional stress and strain distributions within solder layer for a typical loading level and a solder layer thickness if 0.25 mm. It is observed that the shear stress τ_{xy} is quite uniform throughout the solder layer and much bigger than the 5 other normal and shear stress components, which are nearly zero everywhere. Similarly, the corresponding shear strain γ_{xy} is uniformly distributed throughout the solder layer and much bigger than other normal and shear strains. Figure 7.13 illustrates the uniformity of shear stress τ_{xy} distribution within the solder layer. The variations of the shear stress τ_{xy} along lines A-B and P-Q are also plotted. It is clearly evident that the groove geometry of the Iosipescu shear specimen helps to maintain a nearly uniform distribution of shear stress in the solder material.

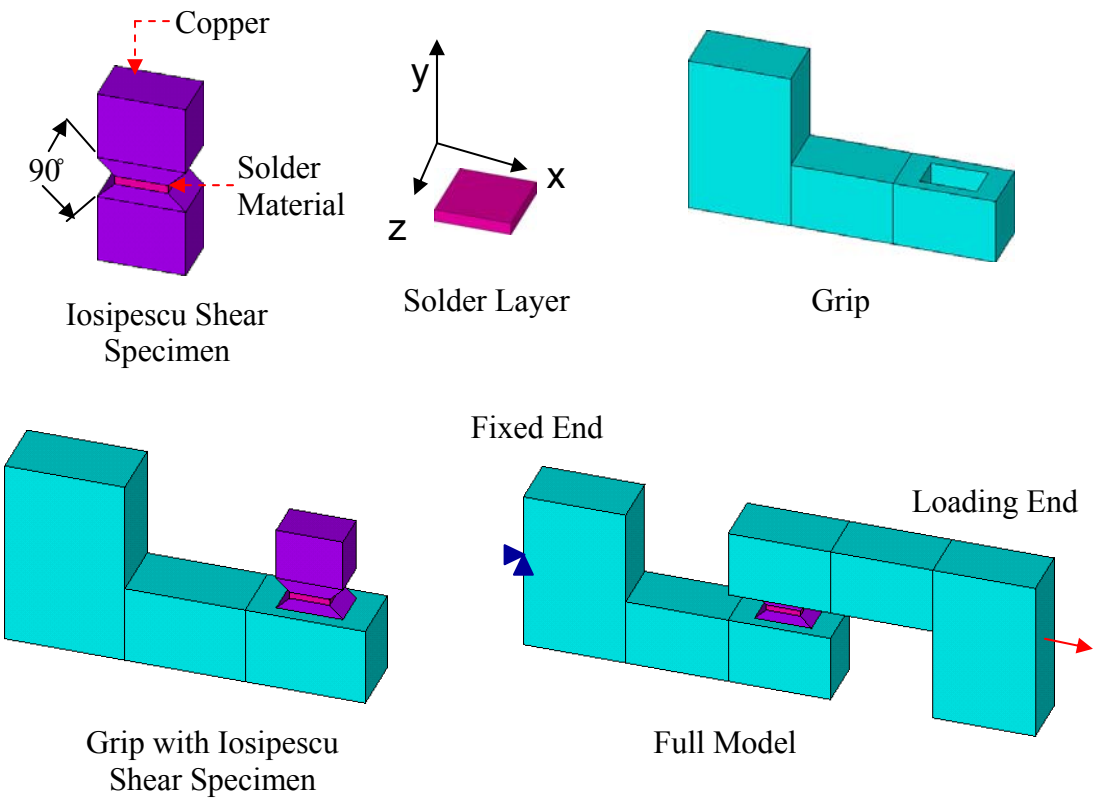

Figure 7.10 Iosipescu Shear Test Specimen Assembly and Loading Fixture

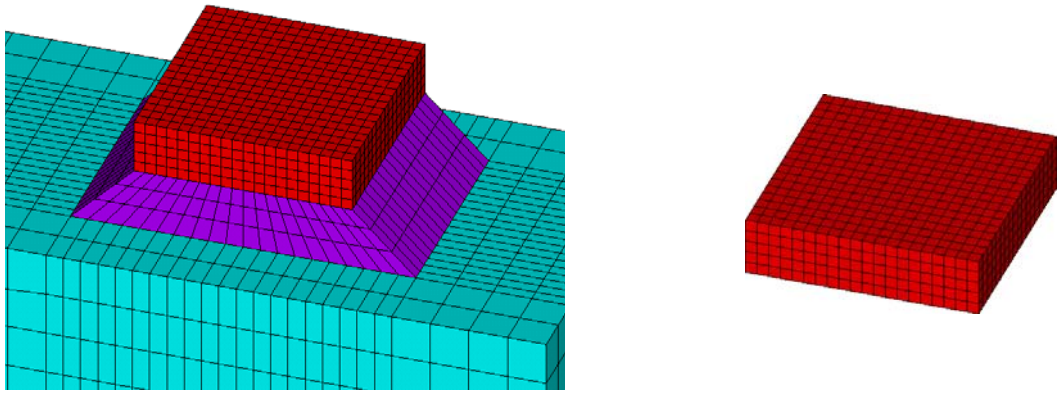

Figure 7.11 Finite Element Meshing near Solder Layer (SOLID95 Brick Element)

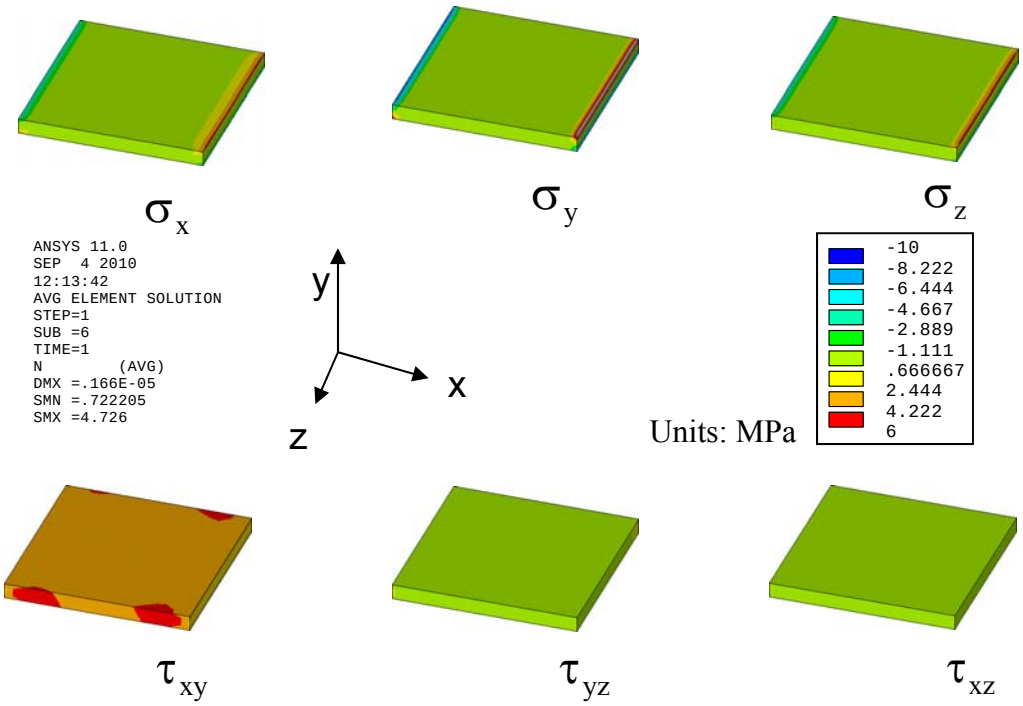

Figure 7.12 Normal and Shear Stress Distributions within the Solder Layer in the Iosipescu Assembly

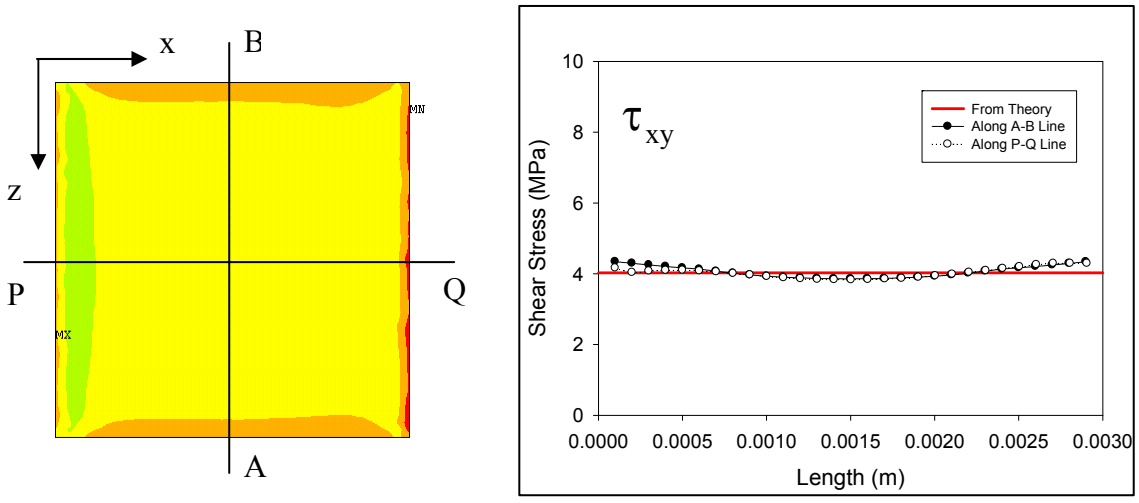

Figure 7.13 Uniformity of the Shear Stress Distribution within the Solder Layer in the Iosipescu Assembly

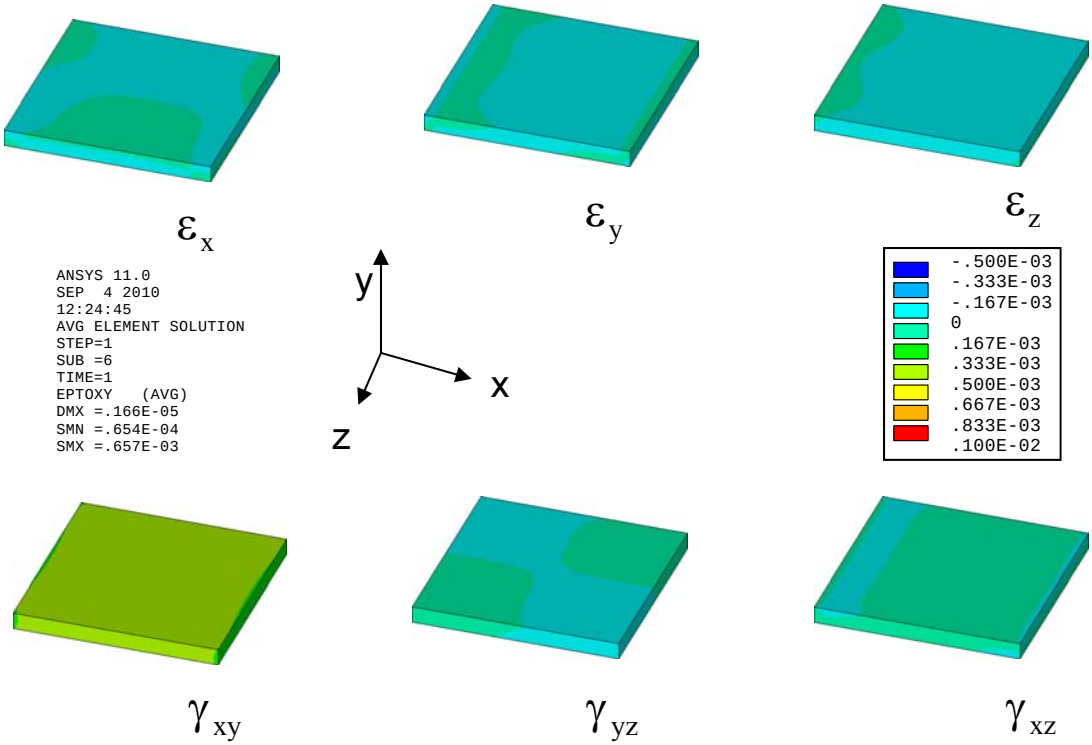

Figure 7.14 Normal and Shear Stress Distributions within the Solder Layer in the Iosipescu Assembly

The 3 normal stresses in Figure 7.12 illustrate stress concentrations near the edges of the specimen. The levels of these stress concentrations are dependent on the thickness of the solder layer. Lee and Kim [204] investigated the effects of the thickness of the shear specimen on fatigue life assessment. They studied four different types of solder bumps having different thickness and shapes (see Figure 7.15). They also reported that the solder volume applied to each solder pad is needed to be constant to ensure good test specimens. In addition to a layer thickness of 0.25 mm, finite element analyses were also carried out for three other solder layer thicknesses as shown in Figure 7.16. The main reason for this study was to determine the optimum solder layer thickness to reduce stress concentrations near the edges of the specimen. Figures 7.17, 7.18, and 7.19 show the

normal and shear stress and strain distributions within solder layers having thicknesses of 0.75 mm, 0.5 mm, and 0.125 mm respectively. As shown in Figure 7.20, finite element analysis has shown that decreasing the solder layer thickness helps to reduce the normal stress concentration factor in the solder layer. Henshall, et al. [205] measured the typical diameter of a BGA solder joint as 0.46 mm whereas, Darvaeux [202] considered the height of BGA solder balls in the range of 0.1 to 0.5 mm. Tamin, et al. [206] considered BGA solder balls with a height of 0.6 mm. Therefore, a layer thickness of 0.25 mm was chosen in this work to represent an appropriate average height of typical BGA solder balls.

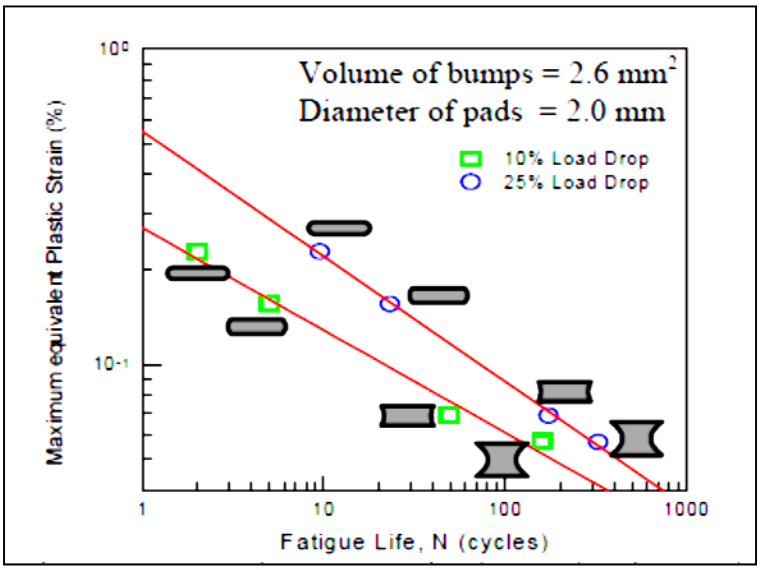

Figure 7.15 Effects of Thickness and Size of Solder Bump on Fatigue Life [204]

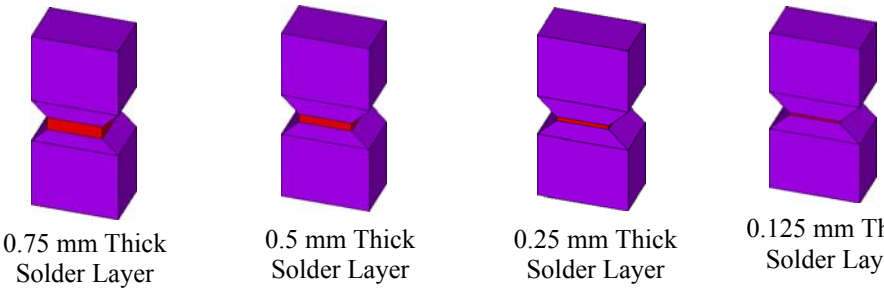

Figure 7.16 Iosipescu Shear Specimen with Solder Layer having Different Thicknesses

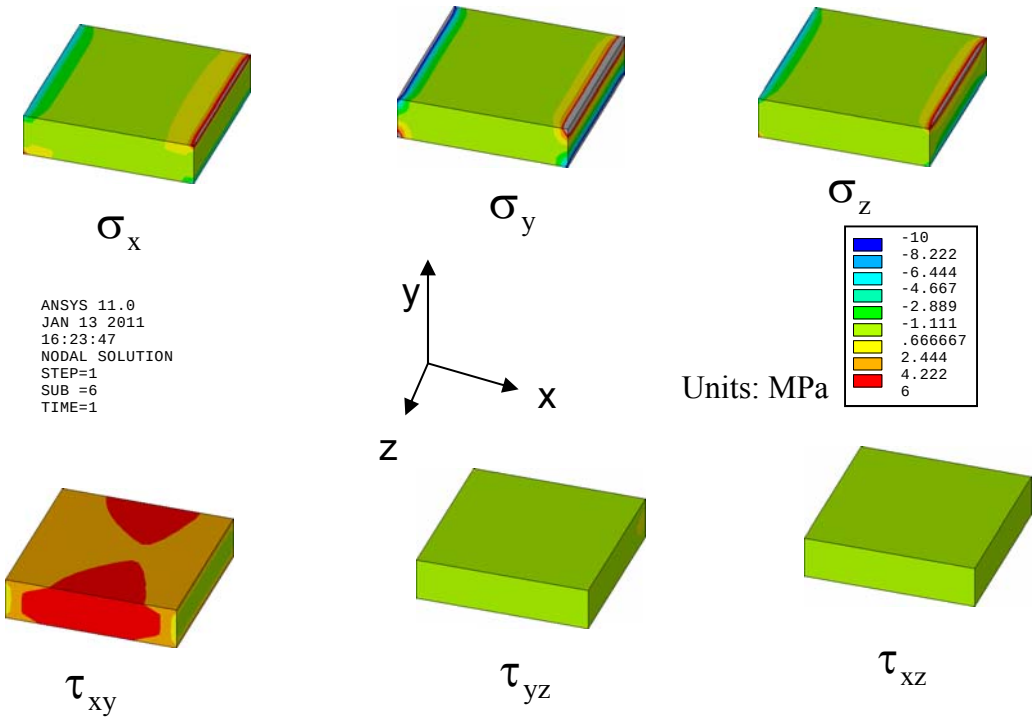

Figure 7.17 Stress Distributions within a Solder Layer of Thickness 0.75 mm

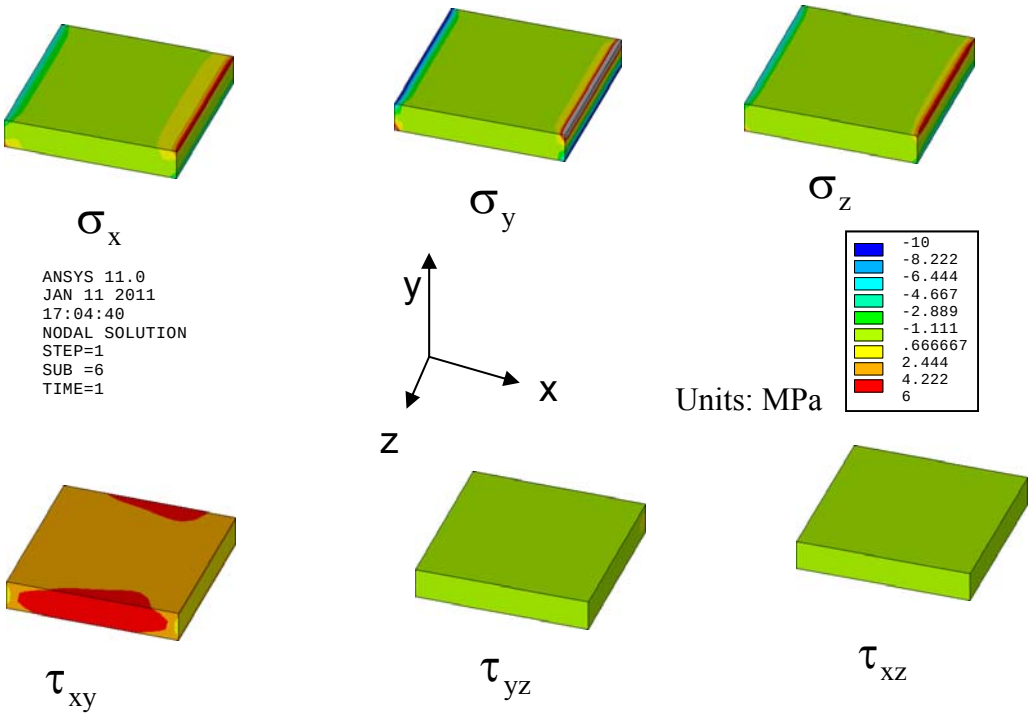

Figure 7.18 Stress Distributions within a Solder Layer of Thickness 0.50 mm

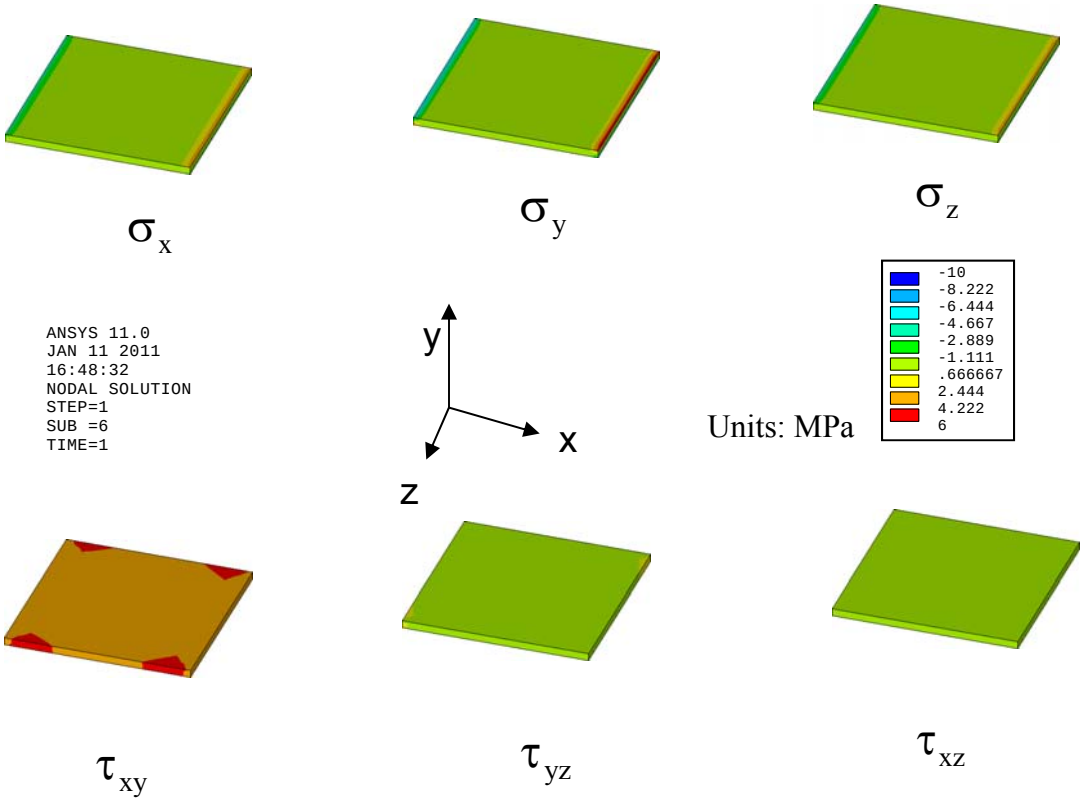

Figure 7.19 Stress Distributions within a Solder Layer of Thickness 0.125 mm

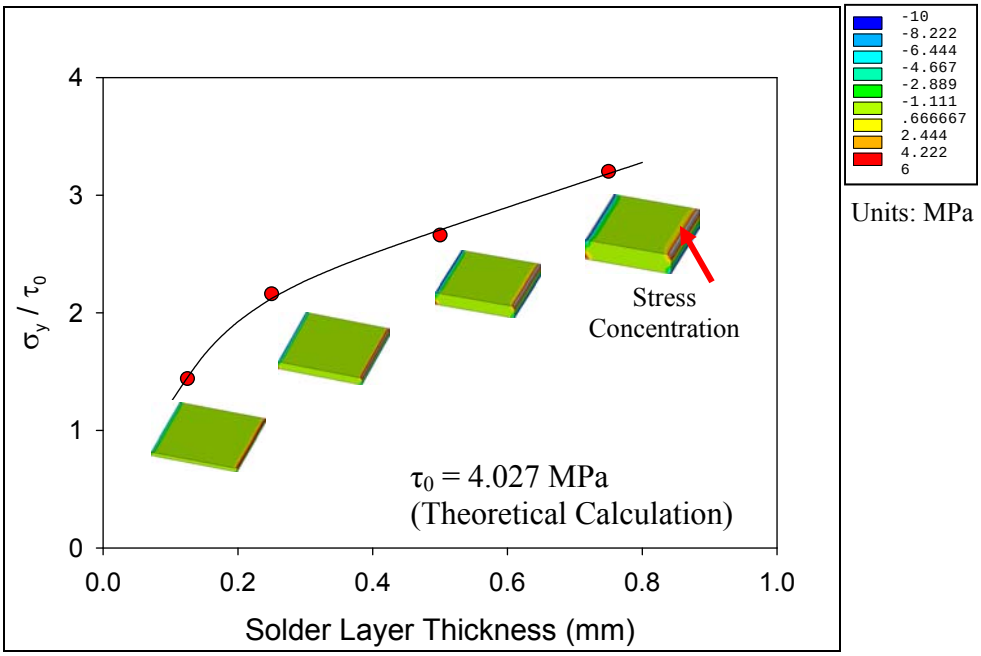

Figure 7.20 Stress Concentration at the Side of the Solder Layer for Different Layer Thicknesses

The Iosipescu shear specimen geometry (modified lap shear) differs from a simple lap shear specimen by adding the 45° grooves (see Figure 7.21). This modification helps to provide a more uniform state of shear and also to reduce stress concentrations at the edges. A comparative study was also done with finite element analysis on both the simple lap shear and the Iosipescu shear for solder layers. The results showed that the stress concentration at the edge of solder can be reduced with the help of Iosipescu type geometry as shown in Figure 7.22.

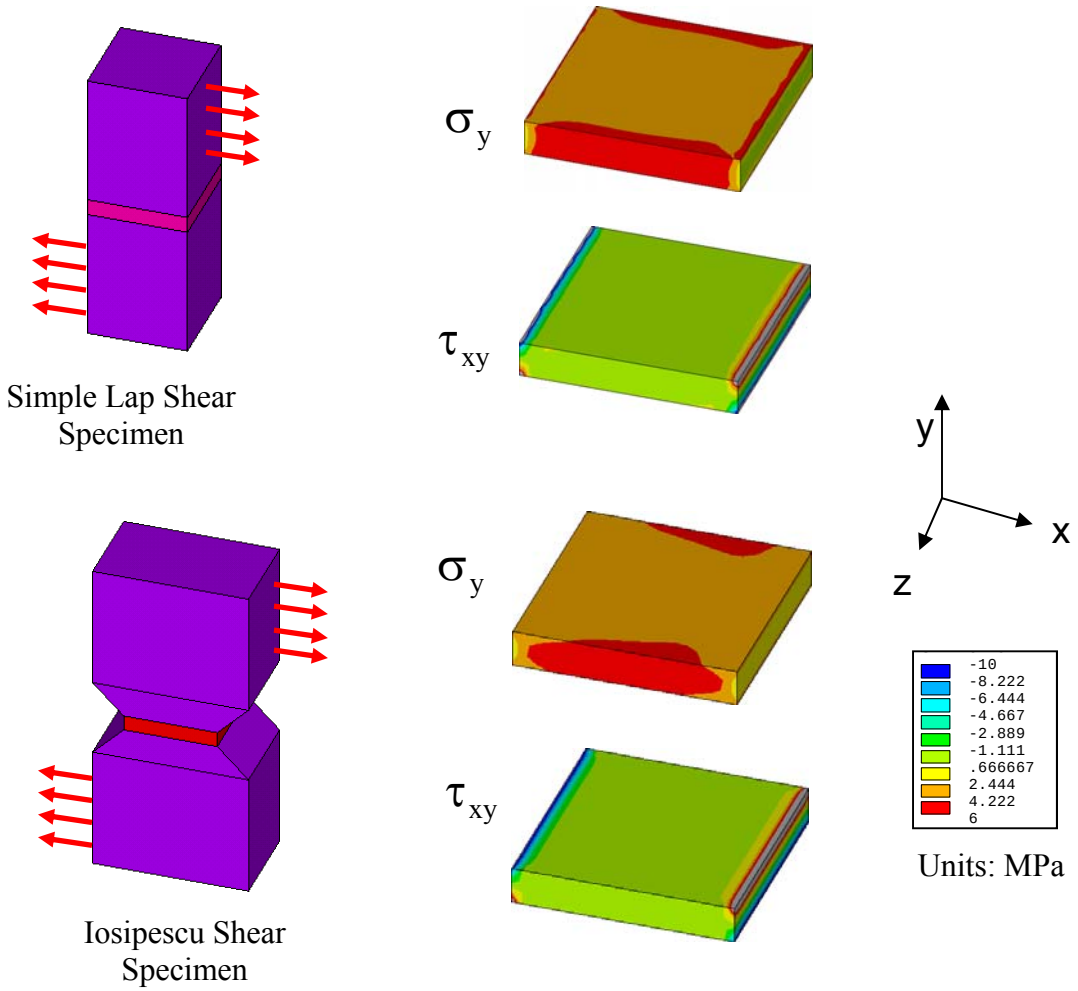

Figure 7.21 Comparison between Simple Lap Shear Specimen and Iosipescu Shear Specimen (Layer Thickness = 0.50 mm)

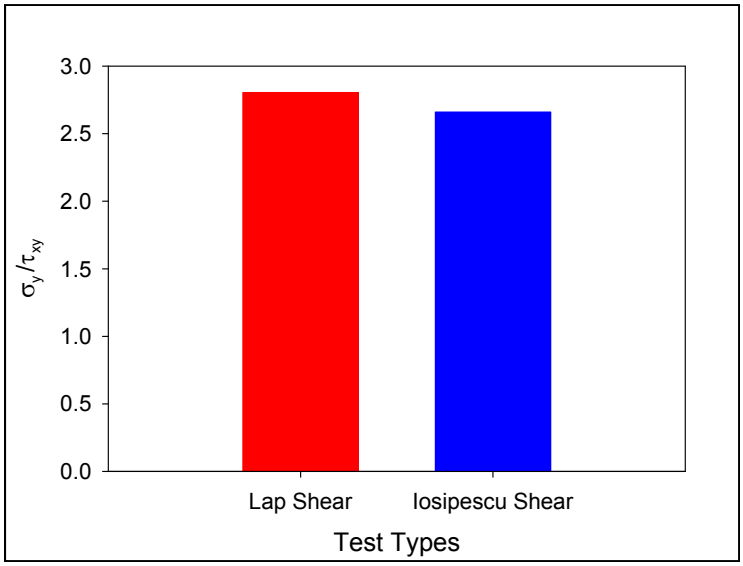

Figure 7.22 Stress Concentrations for Simple Lap Shear Specimen and Iosipescu Shear Specimen (Layer Thickness = 0.50 mm)

7.4 Design and Development of a Mold Assembly for Specimen Preparation

An aluminum mold was designed for preparation of Iosipescu shear specimen assemblies for SAC105 solder material. As shown in Figure 7.23, the mold consisted of three parts: upper plate, base plate, and spring-loaded lid. The upper plate contained three slots. Each slot was 5 mm wide and held one specimen, so that three specimens could be prepared simultaneously. The base plate was attached to the upper plate by four 8-32 (standard screw size) screws. A spring-loaded lid was also used so that the solder perform was maintained under a small pressure during solidification. The spring-loaded lid was attached through two 5-40 screws as shown in Figure 7.23.

During assembly, the two copper end pieces were placed into the aluminum mold with the wedge shaped ends facing each other. The mold was sized so that there was a nominal 0.25 mm clearance between the copper pieces, which was just big enough to fit a thin solder layer preform. Thermal expansion coefficient (CTE) of aluminum is 22.2 x

10^{-6}/C and that of copper is 16.6 x 10^{-6}/C [207]. Therefore, mismatch of the thermal expansion coefficients was assumed negligible during the solder reflow process.

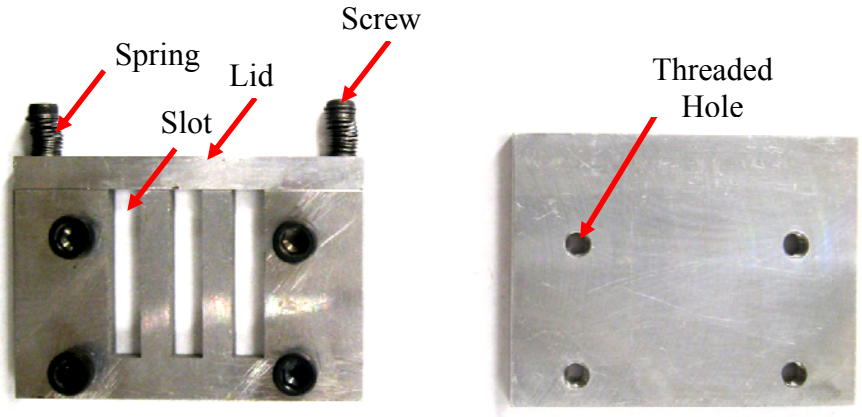

Spring Loaded Lid and Upper Plate

Base Plate

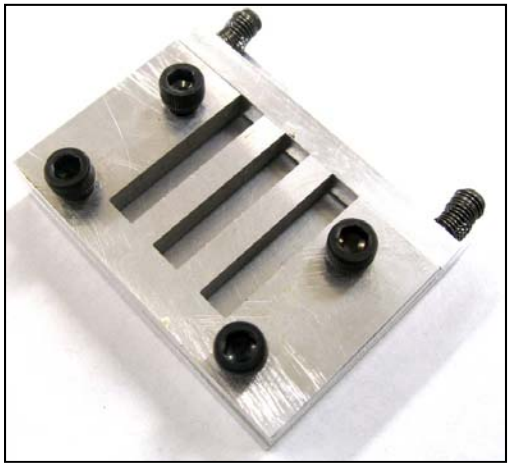

Full Assembly

Figure 7.23 Mold Assembly for Iosipescu Shear Specimens

7.5 Procedure for Iosipescu Shear Sample Preparation

The twin imperatives in preparing quality Iosipescu test specimens for shear testing were cleanliness of surfaces to be soldered, and precise alignment of the two copper platens that are joined together to the thin solder specimen. Good wetting of the solder to the copper requires all of the surfaces to be clean and free of all forms of contamination. Using well-alignment specimens, free of non-linearity, non-planarity and twist, provided specimen symmetry and reduced the stresses that arise from installing the specimen into the test fixture. This, in turn, simplifies the stress fields throughout the solder joint during testing, thereby producing more uniform test data [208]. A quick and repeatable method has been developed in the present work to prepare shear specimen for the testing.

A complete Iosipescu shear specimen assembly as used in this work is shown in Figure 7.24. The copper end pieces are 13 x 5 x 3 mm, with 45º angular cuts. They are joined together by the 3 x 3 x 0.25 mm solder layer to be tested. As discussed above, the angled cuts in the copper pieces help reduce the effects of stress concentrations, and establish a fairly uniform shear stress distribution throughout the solder layer. The steps for specimen assembly preparation are shown in Figure 7.25 and are summarized below.

Figure 7.24 Iosipescu Shear Specimen

7.5.1 Surface Polishing

Good wetting of the solder to copper requires all of the surfaces to be clean and free of all forms of contamination. Before assembly, each copper part is placed in a holding fixture and polished using multiple grades of waterproof metallographic sandpaper (600 and 1200 grit), a 0.3 μm diamond paste, and a 0.05 μm colloidal silica suspension. The holding fixture was designed so that the copper pair surfaces are flat and parallel with each other.

7.5.2 Surface Cleaning

Even after polishing the copper surfaces, further cleaning is needed to remove silicon carbide particles left behind by the sandpaper. The copper surface was next cleaned with acetone and isopropyl alcohol.

7.5.3 RMA Flux

A drop of RMA flux was placed over the polished and cleaned copper surfaces by a dispenser. A micro-brush was used to spread the RMA flux uniformly over the copper surfaces. RMA flux was used to reduce oxidation and increase wettability of the solder to the copper surfaces.

7.5.4 Placing Materials in the Mold Assembly

During assembly, the two copper end pieces were placed into the aluminum mold with the wedge shaped ends facing each other. The mold was sized so that there was a nominal 0.25 mm clearance between the copper pieces, which was just big enough for the thin solder layer perform (3 mm x 3mm x 0.25 mm in size) to fit. A spring-loaded lid

was also used so that the solder perform was maintained under a small pressure during solidification.

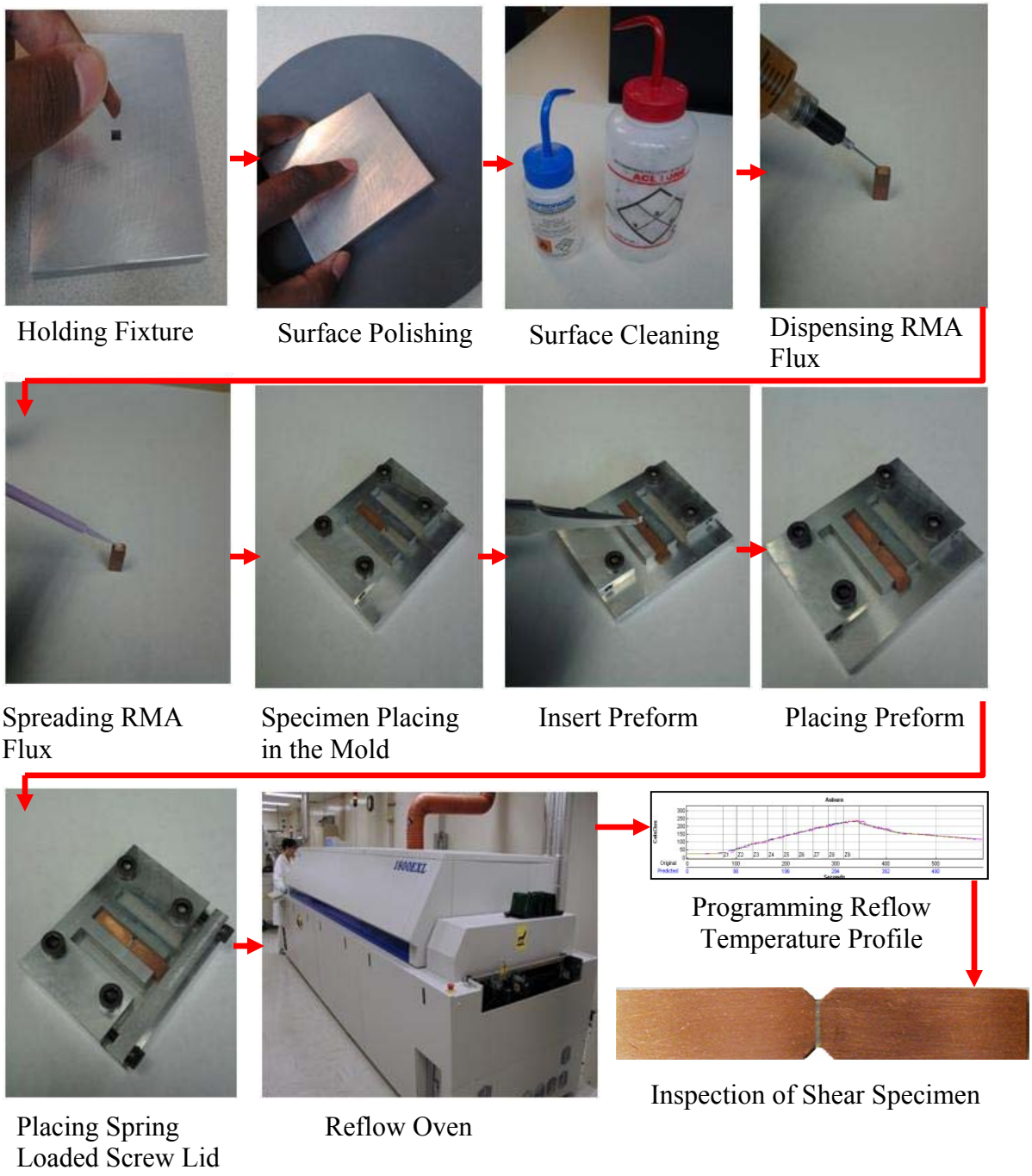

Figure 7.25 Flow Chart for Preparing Iosipescu Shear Specimen Assemblies

7.5.5 Reflow Soldering

The whole mold assembly was sent through a reflow oven consisting of 9 zones (see Figure 7.26) to melt the solder preform between the copper end pieces in the mold, and subject it to a desired temperature profile. Thermocouples were attached to the aluminum mold and monitored continuously using a radio-frequency temperature profiling system to ensure that the samples were formed using the desired temperature profile (similar to actual solder joints). Figure 7.27 illustrates the reflow temperature profile used in this work for SAC105 Iosipescu shear specimen assemblies.

Figure 7.26 Heller 1800EXL Reflow Oven

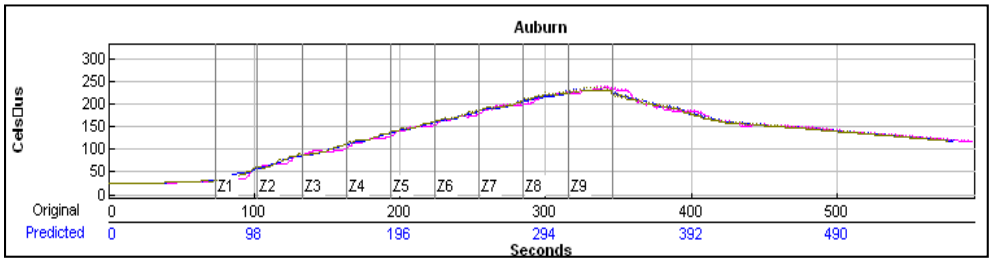

Figure 7.27 Reflow Profile for Iosipescu Shear Specimen Assemblies

7.5.6 Inspection and Measurement of Joint Dimension

The specimens were inspected in an optical microscope for defects such as cracks or surface voids and photographed for documentation purposes. Actual joint dimensions were measured using a digital micrometer and an optical microscope. There were a few key issues during specimen preparation, which if ignored could have resulted in poor specimen quality. Those errors are separated by four major categories as shown in Figure 7.28:

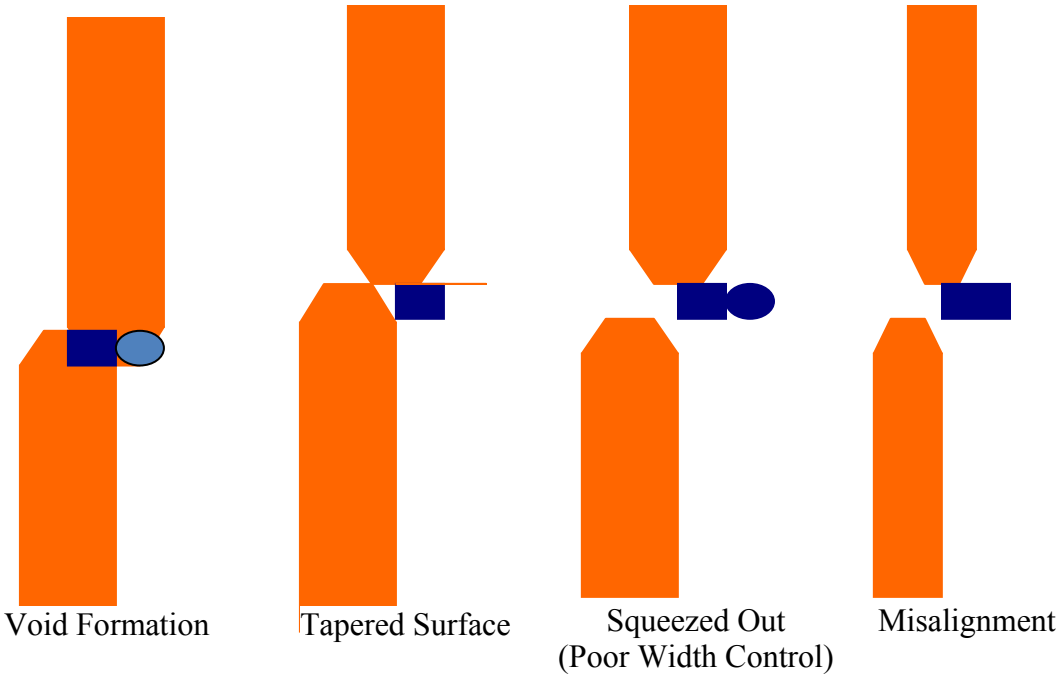

Figure 7.28 Defects during Shear Sample Preparation

Good quality specimens were selected using visual inspection by optical microscopy. Good alignment, uniform thickness of solder layer, and lack of voids were the major qualifications for selection of a good quality sample. Figure 7.29 shows an SEM image of a good Iosipescu shear specimen assembly having uniform thickness. The optical microscope used for inspection is shown in Figure 7.30.

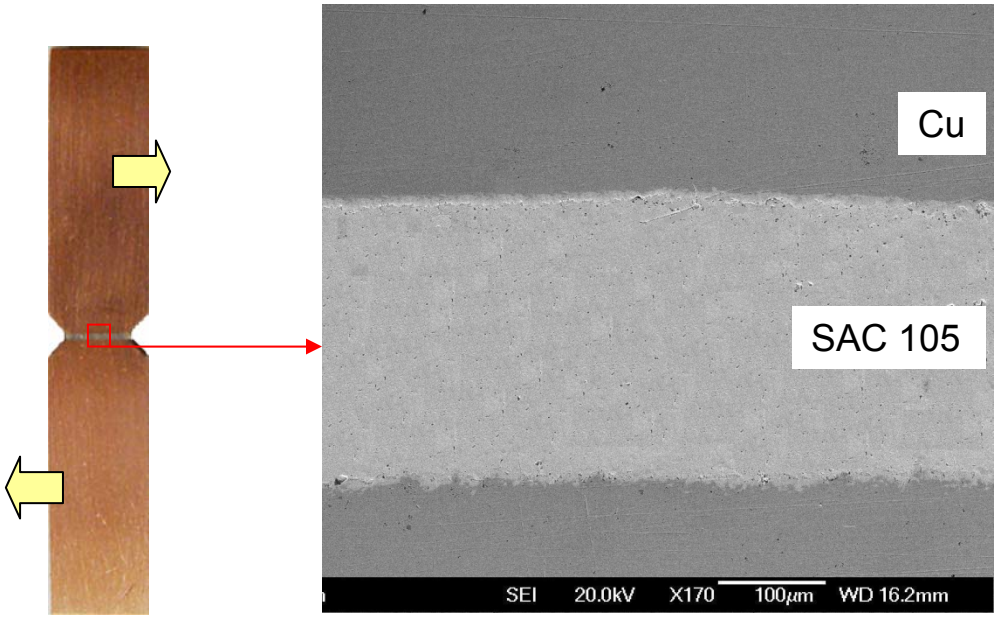

Figure 7.29 Good Quality Iosipescu Shear Specimen Assembly
and Corresponding SEM Image

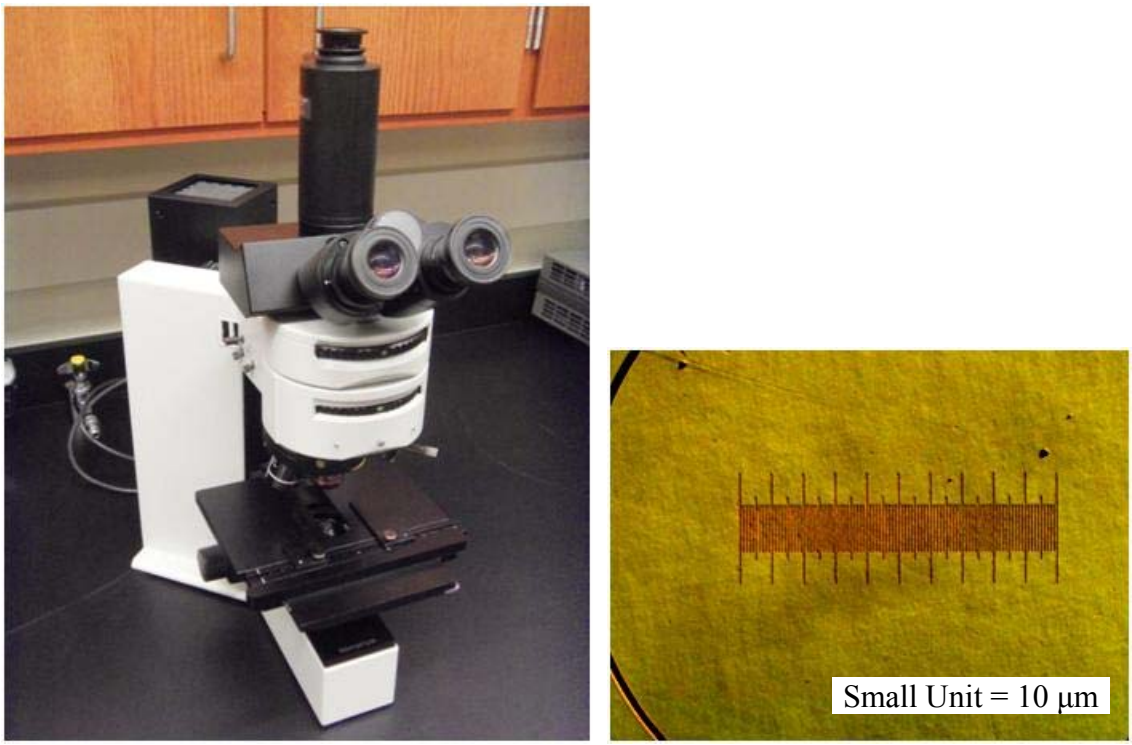

Figure 7.30 Olympus BX60 Optical Microscope and Measuring Scale

7.6 Mechanical Testing System

Similar to the uniaxial tension/compression testing described previously in Chapter 3, the microtester system and newly designed grips shown in Figure 7.31 were used to test the Iosipescu shear samples in this study.

The grips are consisted of two parts: moving part and static part, and were attached to the microtester cross-heads through screws. An alignment guide was used to ensure alignment of the solder layer along the centerline of the microtester system. The initial design of the grips is shown in Figure 7.31. This design was further modified by alignment rigidity screws on the top of both grips. The upper screw and side screw were used to provide additional clamping of the shear specimen copper pieces as shown in Figure 7.32.

During testing, shear forces and displacements were measured. The shear stress and shear strain were calculated from the applied shear force and measured cross-head displacement using

$$\tau = \frac{F}{A} \qquad \gamma = \frac{\delta_{solder}}{h} \tag{7.1}$$

where τ is the shear stress, γ is the engineering shear strain, F is the measured shear force, A is the original cross-sectional area (3 x 3 mm), δ_{solder} is the measured solder layer deformation, and h is the solder layer thickness. The actual thickness of each solder layer was measured by an optical microscope as described in the previous section.

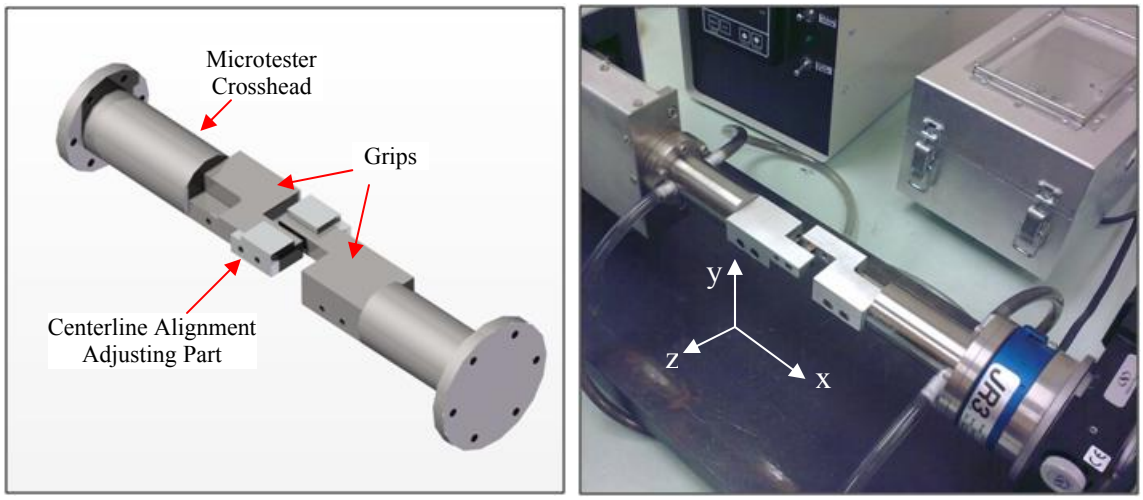

Figure 7.31 Design and Development of Testing System for
Iosipescu Shear Specimen Assemblies

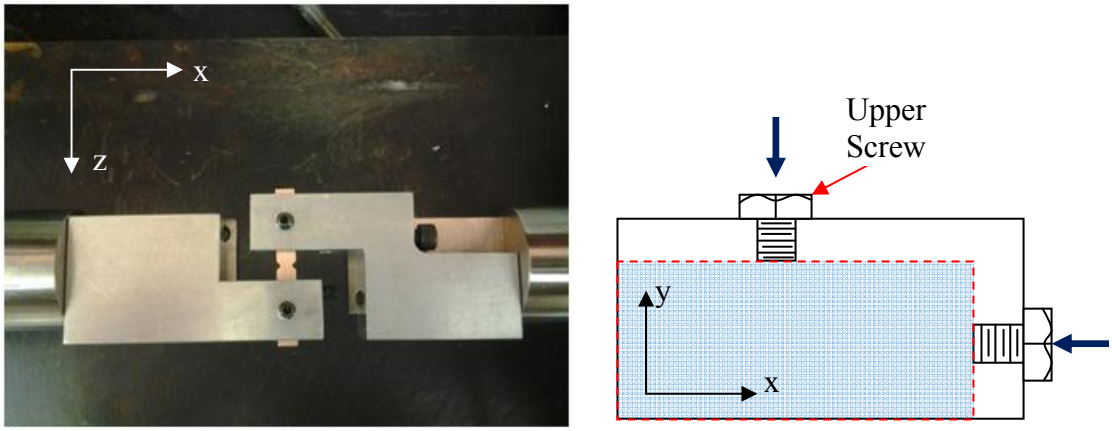

Figure 7.32 Modified Design for Specimen Grips (Two-Point Holding)

7.7 Load Train Calibration

The shear lap tests were performed using a uniaxial testing machine and the measured uniaxial displacements were converted to shear displacements. The total displacement captured by the actuator of the microtester includes displacements of other deformable bodies in the system (e.g. the grips), and they must be compensated for to obtain the true

deformations of the solder layer. This compensation should include the machine compliance, grip compliance, and copper end piece compliance.

A technique was developed for load train calibration. A solid copper Iosipescu shear specimen (see Figure 7.33), having no solder layer was used to calculate the load train stiffness. A mathematical relationship [187] for the total measured displacement is:

$$\delta = \delta_{machine} + \delta_{grip} + \delta_{cu} + \delta_{Solder} \tag{7.2}$$

As shown in Figure 7.34 the machine, grip, and copper system can be regarded as a spring equivalent system (linear elastic material) as the system is much stiffer than solder material. Therefore, displacement of the system can be determined from spring displacement equation, and Eq. (7.2) can be re-written as:

$$\delta_{Solder} = \delta - \left(\delta_{machine} + \delta_{grip} + \delta_{cu}\right) = \delta - \frac{F}{k_m} \tag{7.3}$$

$$\delta_{machine} + \delta_{grip} + \delta_{cu} = \frac{F}{k_m}$$

where k_m is the equivalent spring stiffness that can be regarded as the "load train stiffness".

Figure 7.33 Iosipescu Shear Specimen having no Solder Layer

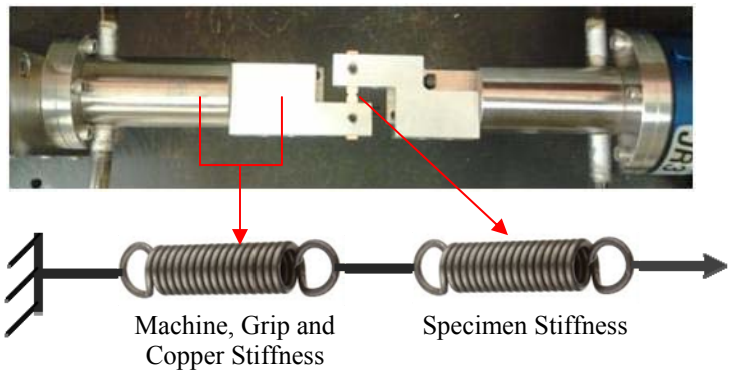

Figure 7.34 Load Train Equivalent System

The solid Iosipescu shear specimen (as shown in Figure 7.33) was gripped into the fixture attached to the microtester crossheads and a monotonically increasing load was applied. The displacements were measured, and represented only the load train deformations as no solder layer was present. The recorded force-displacement curve is plotted in Figure 7.35. It is noticeable that the displacement varied linearly with force, and the load train stiffness k_m was determined by finding the slope of the load-displacement curve.

In Figure 7.36, shear stress-strain curves are illustrated before and after compensation for the load train compliance. From the initial slope of the shear stress-strain curve, the effective shear modulus was determined to be E = 11 GPa (No Aging, RT) for SAC105 solder material after adjustment for the load train compliance. The shear modulus can be determined from available data in the literature [147], and those values are fairly close to the measured shear modulus in the present work.

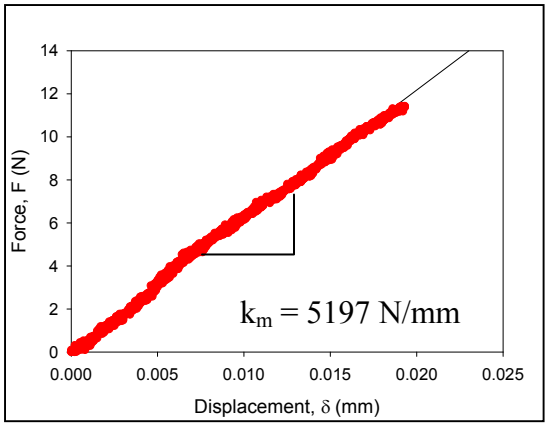

Figure 7.35 Load Train Stiffness Measurement

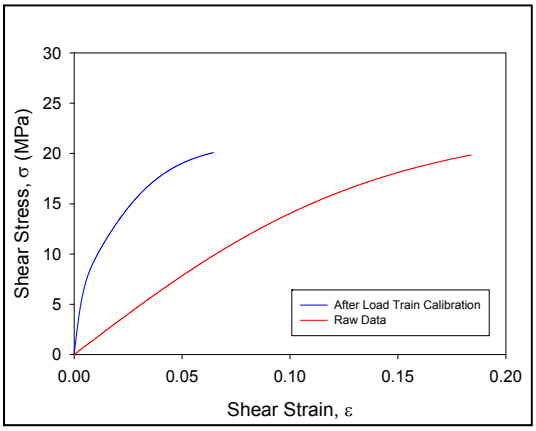

Figure 7.36 Shear Stress-Strain Curve Before and After Adjustments for Load Train Compliance

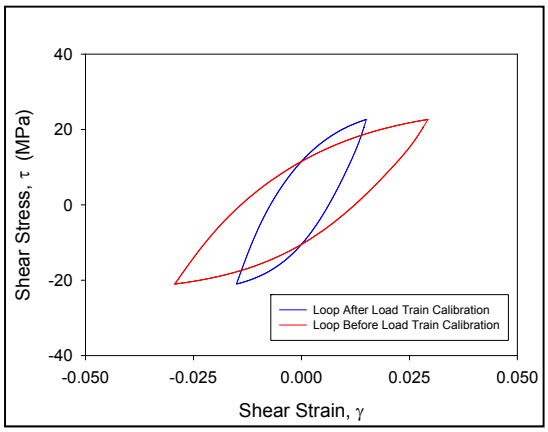

Figure 7.37 Shear Hysteresis Loops Before and After Adjustments for Load Train Compliance

Figure 7.37 illustrates the hysteresis loops generated during cyclic loading before and after adjustments for load train compliance. It is obvious that the actual strain range was smaller than the unadjusted (measured) strain range. Therefore, the actual area of the shear hysteresis loop is smaller than the unadjusted (measured) area.

7.8 Shear Cyclic Stress-Strain Data Processing

A four-parameter hyperbolic tangent model was again used to represent cyclic shear stress strain data for solder.

$$\tau = D_1 \tanh(D_2\gamma) + D_3 \tanh(D_4\gamma) \tag{7.4}$$

where D_1, D_2, D_3 and D_4 are material constants to be determined through regression fitting of the model to the experimental data. Typical measured cyclic shear stress-strain curves and hysteresis loops for a SAC105 Iosipescu specimen assembly are shown in Figure 7.38. A similar procedure was used to calculate the area of the shear hysteresis loop as described previously in Chapter 4 for uniaxial tension/compression tests.

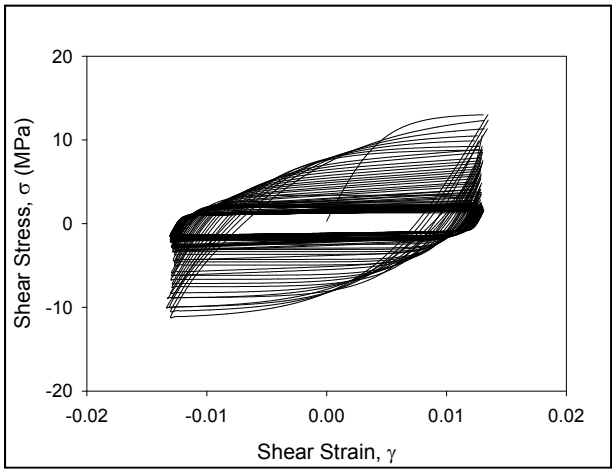

Figure 7.38 Typical Shear Cyclic Stress-Strain Test Results
for SAC105 Solder (Strain Limit Controlled)

7.9 Summary and Discussion

A comparative study was performed using finite element analysis to study solder ball shear, simple lap shear, and Iosipescu shear. It has been established that solder ball shear tests are not suitable for measuring mechanical behavior since the stress and strain states are not uniform. It is evident that the Iosipescu design using copper end pieces helps to provide a more uniform state of shear in the thin solder layer being tested. Finite element analysis has shown that decreasing the solder layer thickness helps to reduce stress concentrations in the solder layer.

A quick and repeatable method was developed to prepare Iosipescu shear specimen assemblies. During assembly, the two copper end pieces were placed into an aluminum mold with the wedge shaped ends facing each other. The mold was sized so that there is a nominal 0.25 mm clearance between the copper pieces, which is just big enough for a thin solder layer preform to fit. A spring-loaded lid was also used so that the solder perform was maintained under a small pressure during solidification. The whole mold assembly was sent through a reflow oven to melt the solder preform between the copper end pieces in the mold, and subject it to a desired temperature profile.

Shear fixtures were also designed and manufactured to grip the Iosipescu shear specimen in a testing machine. A procedure was developed for load train calibration and to adjust the shear displacement data for load train compliance. A four-parameter hyperbolic tangent model was again used to represent the cyclic shear stress strain data for solder.

CHAPTER 8

EFFECTS OF AGING ON SHEAR CYCLIC STRESS-STRAIN AND FATIGUE BEHAVIOR OF LEAD FREE SOLDERS

8.1 Introduction

In this chapter, the effects of aging on the shear cyclic stress-strain and fatigue behaviors of SAC105 lead free solder have been investigated under strain controlled cyclic loading. Shear test specimens were constructed using the Iosipescu approach discussed in the previous chapter. Comparisons have also been made between shear and uniaxial tension/compression fatigue data.

8.2 Test Matrix Description

Using the Iosipescu shear specimen assemblies fabricated with the procedure described in Chapter 7, the effects of isothermal aging on the shear cyclic stress-strain curve and hysteresis loop evolution have been characterized. The solder alloy investigated was again SAC105. The specimens were subjected to various durations of aging at 125 C as illustrated in the test matrix shown in Table 8.1. The samples in each group were cooled to room temperature (25 C) after aging, and then they were subjected to cycling mechanical loading under a set of fixed strain limit controlled conditions.

Table 8.1 Aging Test Matrix for Iosipescu Shear Specimens (X = Completed)

Aging Time (Days)	Reflowed Cooling Profile
0	X
5	X
15	X
30	X
60	X
90	X

8.3 Effects of Aging on Shear Cyclic Stress Strain Behavior

Strain controlled cyclic testing has been performed on a SAC105 Iosipescu samples subjected to aging prior to testing. The samples were reflowed and then aged at 125 C for various durations including 0, 5, 15, 30, 60 and 90 days (0-3 months). The 0-day aging specimens represented non-aged samples, and were tested within a few minutes after the reflow process. The strain controlled testing was performed with shear strain limits of ±0.008, and the testing temperature was 25 C. The strain rate was maintained at 0.0001 sec^{-1} for this study.

Figure 8.1 illustrates example plots of the shear cyclic stress-strain behavior for shear specimens subjected to different aging times. Several tests are performed for each aging condition and only one example of the test results for each condition is shown in Figure 8.1. Similar to the strain-controlled uniaxial cyclic tests, it was observed that the hysteresis loops rotate and become smaller in height as aging progresses. This results in a decrease in loop size with aging due to decreasing cyclic stress, which causes reduction of the height of the hysteresis loop. The hysteresis loops for the 10^{th} cycle at each aging condition are superimposed in the plot in Figure 8.2, further illustrating the hysteresis loop evolution.

The reduction of the loop size with aging suggests that damage accumulation is mitigated with aging. However, this trend is mainly due to the fact that there are large drops in yield stress and ultimate strength of the solder material with aging. These changes reduce the height of the hysteresis loop. Since the cyclic testing was performed using a fixed set of strain limits, the hysteresis loop width does not vary significantly. Thus, the area must decrease because of the material strength reductions associated with aging.

Morrow [36] suggested that on the microscopic level, cyclic plastic strain is related to the movement of dislocations and the cyclic stress is related to the resistance to their motion. From this theory, it is evident that for a particular strain limit controlled cyclic test, the movement of dislocations does not change significantly since the plastic strain range remains nearly constant. However, the stress, which is the height of a hysteresis loop, decreases significantly as resistance to dislocation movement decreases due to aging. Decreasing resistance of dislocation movement is the clear indication of microstructural damage occurred during aging. Therefore, for strain limit controlled cyclic testing, the area of hysteresis loop decreases because of damage accumulation and material strength reductions associated with aging.

A plot of the evolution of shear hysteresis loop area with aging time is shown in Figure 8.3. In this graph, each data point represents the average value of loop area of 10^{th} cycle for a particular aging duration. The area of hysteresis loop denotes the energy density (volumetric) dissipated per cycle, and is related to the damage accumulated per cycle. The units are in J/m^3 (energy per unit volume). It is seen that area of shear

hysteresis loop decreases with aging time. The empirical model in Eq. 8.1 was again used to fit the data points.

$$A = \frac{k_1}{1 + k_2 e^{-k_3 t}} + k_4 t \tag{8.1}$$

Reduction of shear the hysteresis loop size is mainly due to the large drop of the shear strength of the solder material with aging. This change reduces the height of the hysteresis loop. Since the strain controlled cyclic tests were performed using fixed strain limits, the width of the hysteresis loop stays constant and area of loop obviously decreases.

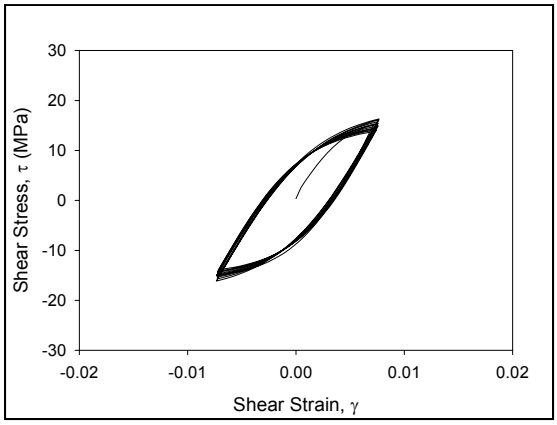

(a) No Aging

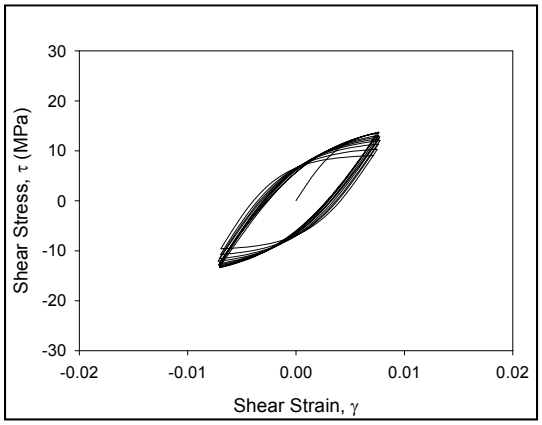

(b) 5 Days Aging

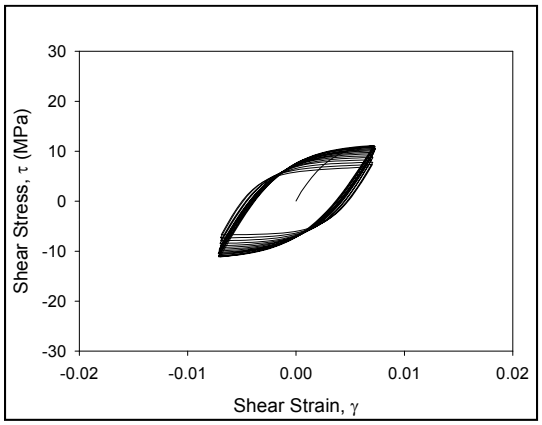

(c) 15 Days Aging

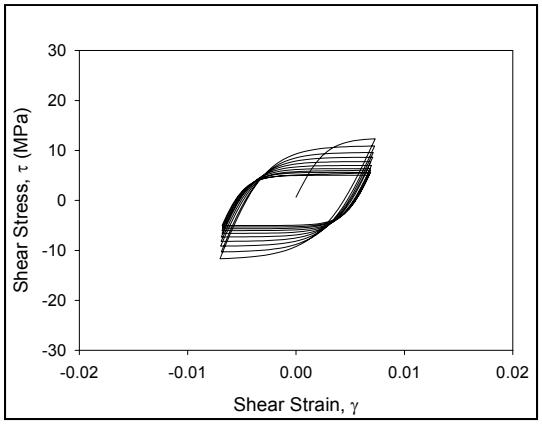

(d) 30 Days Aging

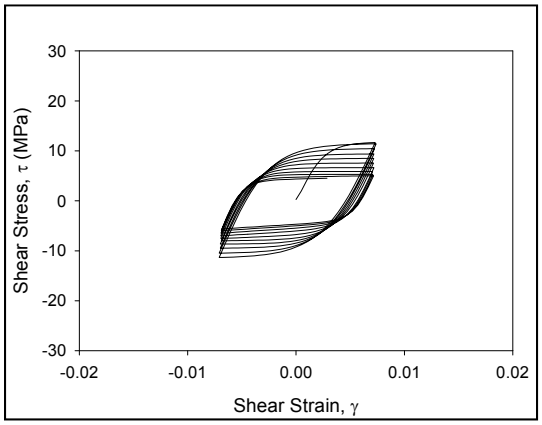

(e) 60 Days Aging

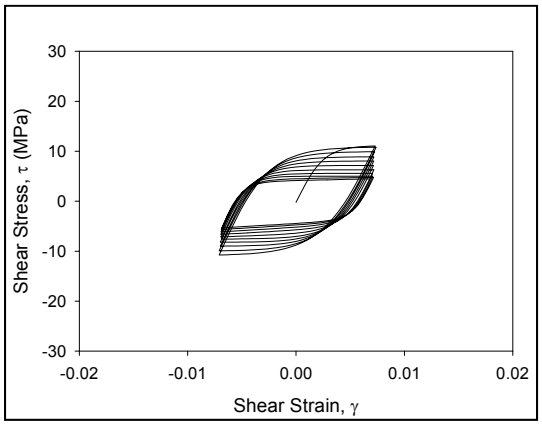

(f) 90 Days Aging

Figure 8.1 Hysteresis Loops for Cyclic Shear Stress-Strain Testing of SAC105 Solder (Strain Limit Controlled)

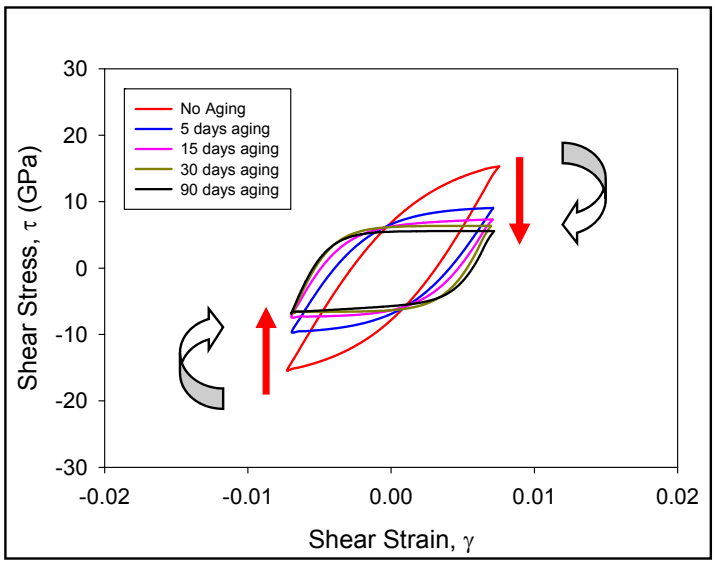

Figure 8.2 Evolution of the Shear Hysteresis Loop Area of the 10^{th} cycle with Aging Time (SAC105, Strain Controlled, RF Samples)

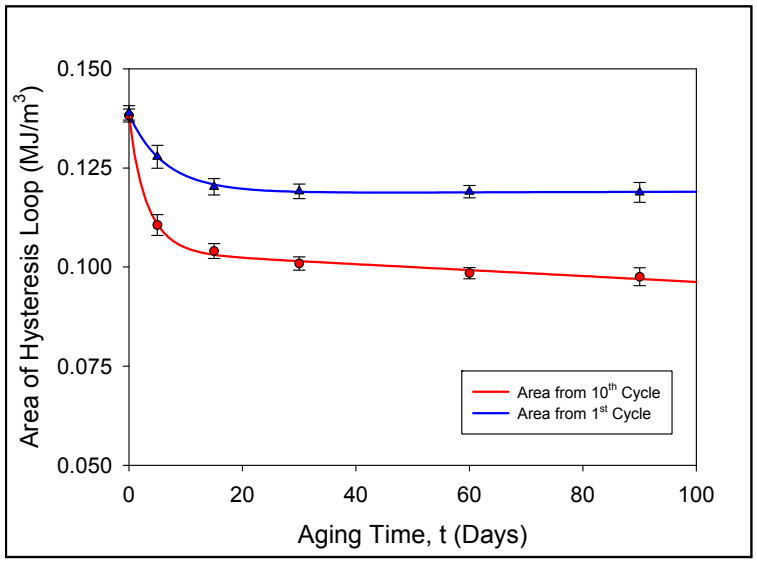

Figure 8.3 Variation of the Shear Hysteresis Loop Area with Aging Time (SAC105, Strain Controlled, RF Samples)

8.4 Effects of Aging on the Shear Fatigue Behavior

Fatigue testing was performed using the Iosipescu shear specimen assemblies to various conditions of prior aging. After solidification, the SAC105 samples were aged at 125 C for various durations up to 1 year. The samples in each group were cooled to room temperature (25 C) after aging. The 0-day aging specimens represented non-aged samples, which were tested within a few minutes after solidification. Strain limit controlled fatigue testing was performed with various strain limits. For each set of aging conditions and strain range, at least 5 samples were tested to failure. The cyclic stress-strain response and the number of cycles to failure were recorded for each test, and the average and standard deviation of the number cycles to failure were calculated for each set of aging conditions and strain range. The strain rate was maintained as 0.001 sec^{-1} during the shear fatigue tests.

Figure 8.4 illustrates an example of the typical hysteresis loops generated during a single fatigue test performed until specimen failure. It is evident that during the cyclic loading that the peak stress drops continuously due to damage accumulation. Eventually crack initiation occurs, followed by crack growth, and fracture. In this work, the fatigue life (cycles to failure) was defined to be the point in the cyclic test where a 50% load drop occurred.

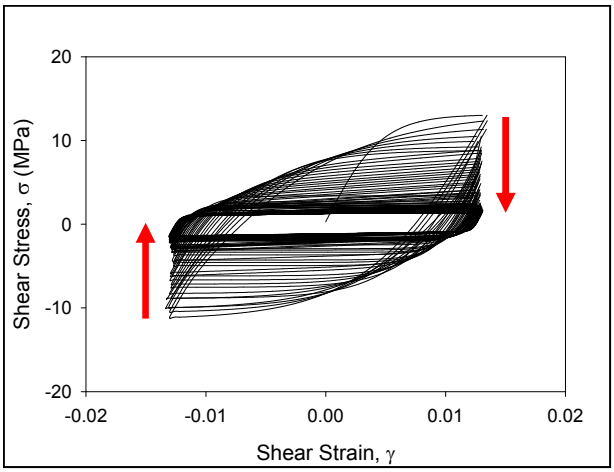

Figure 8.4 Hysteresis Loop Evolution During a Shear Fatigue Test

Figure 8.5 illustrates the recorded shear fatigue data (shear plastic strain range vs. number of cycles to failure) for SAC105 lead free solder specimens subjected to different aging conditions (aging at 125 C for 0, 30, 120, and 300 days) prior to cyclic testing. Each data point represents an average of at least 5 fatigue tests for a particular set of aging/strain conditions, and the error bars indicated the standard deviations in the data. For each set of aging conditions, the $\Delta\gamma_p$ vs. N_f data demonstrated a nearly linear variation when graphed on a log-log scale. This suggests that the Coffin-Manson fatigue law [177-178] can accurately represent the shear test:

$$\begin{aligned} N_f^{\alpha}\Delta\gamma_p &= \theta \\ \log\Delta\gamma_p &= \log\theta - \alpha\log N_f \end{aligned} \tag{8.2}$$

where $\Delta\gamma_p$ is the inelastic shear strain range, N_f is the fatigue life (cycles to failure), α is the fatigue exponent, and θ is the fatigue ductility.

For each set of aging conditions, Eq. (8.2) has been regression fit to the data, and the colored straight lines in Figure 8.5 are the Coffin-Manson fatigue curves that result from the best fits to the data for the various aging conditions. The Coffin-Manson coefficients θ and α calculated by least-squares regression analysis are tabulated in Table

8.2. From the plots in Figure 8.5, it can be seen that the Coffin-Manson curves/fits are nearly parallel. This is reflected by the small changes in coefficient α (see Table 8.2) that occur with aging. The largest shift in the fatigue curves occurs in the first 30 days of aging. This is reflected by the relatively large (52.3%) change in coefficient θ that occurs between no aging and 30 days of aging.

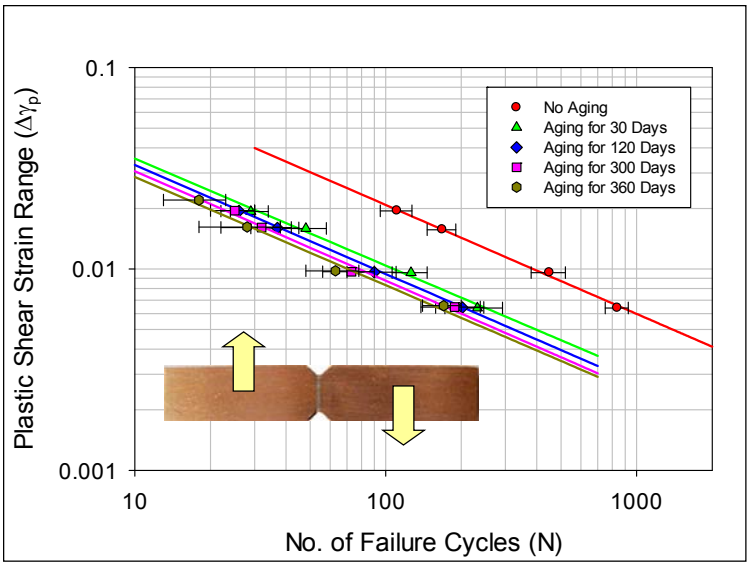

Figure 8.5 Shear Fatigue Data (Plastic Shear Strain Range vs. Cycles to Failure) for SAC105 Solder Subjected to Aging at 125 C

Table 8.2 Coffin-Manson Coefficients for SAC105 for Various Aging Conditions

Aging Conditions (Days)	Material Ductility Coefficient, θ	Fatigue Exponent, α
0	0.2516	0.5413
30	0.1200	0.5310
120	0.1144	0.5415
300	0.1073	0.5444
360	0.0988	0.5379

The fatigue data in Figure 8.5 has been recast to be in terms of the shear strain energy density (ΔW) dissipated per cycle, and the results are shown in Figure 8.6. The value of ΔW for each fatigue test was calculated from the area of the first cycle shear hysteresis loop. As before, each data point represents the average of the fatigue tests for the particular set of aging/strain conditions, and the error bars indicated the standard deviations in the data. For each set of aging conditions, the recast ΔW vs. N_f data also demonstrated a nearly linear variation when graphed on a log-log scale. This suggests that the Morrow energy-based fatigue law [153] can accurately represent the data:

$$\begin{aligned} N_f^{\beta}\Delta W &= \varphi \\ \log \Delta W &= \log \varphi - \beta \log N_f \end{aligned} \tag{8.3}$$

where β is the fatigue exponent, and φ is the material ductility coefficient. For each set of aging conditions, Eq. (8.3) has been regression fit to the data, and the colored straight lines in Figure 8.6 are the Morrow model fatigue curves that result from the best fits to the data for the various aging conditions. The coefficients φ and β calculated by least-square regression analysis are tabulated in Table 8.3.

Similar to Coffin-Manson model prediction, it can be seen that the Morrow model curves/fits are nearly parallel. This is reflected by the small changes in coefficient m (see Table 8.3) that occur with aging. The largest shift in the fatigue curves again occurred in the first 30 days of aging. This is reflected by the relatively large (63.8%) change in coefficient φ that occurs between no aging and 30 days of aging. As mentioned previously, the value of ΔW used for each data point in the fatigue plots was found from the area of the first cycle during mechanical cycling. In actuality, the value of ΔW evolves dramatically during each fatigue test.

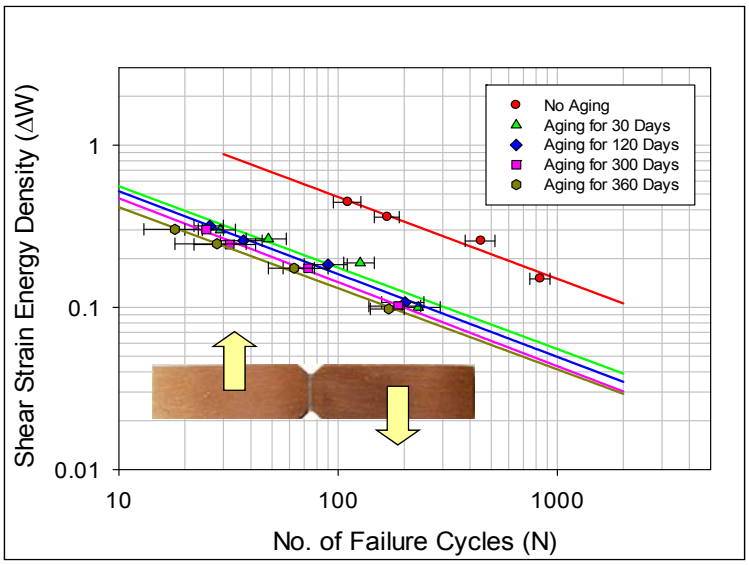

Figure 8.6 Shear Fatigue Data (Energy Dissipation vs. Cycles to Failure) for SAC105 Solder Subjected to Aging at 125 C

Table 8.3 Morrow Model Coefficients for SAC105 for Various Aging Conditions

Aging Conditions (Days)	Material Ductility Coefficient, φ	Fatigue Exponent, β
0	4.896	0.5047
30	1.769	0.5017
120	1.683	0.5175
300	1.547	0.5175
360	1.310	0.5000

Figure 8.7 shows the peak shear stress evolution during cyclic loading for different aging conditions. It is seen that the peak stress drop-off was quite gradual for the no aging condition ($\Delta\gamma_p$ = 0.0096). As aging progressed, the peak shear stress drop-off was highly accelerated because of higher fatigue damage accumulation and earlier onset of fatigue cracking. For short term aging (aging for 30 days), the peak stress was initially stable, followed by a rapid drop. For long term aging (aging for 360 days), the rapid drop of the peak stress is occurred immediately due to high aging-induced accumulation in the microstructure prior to testing.

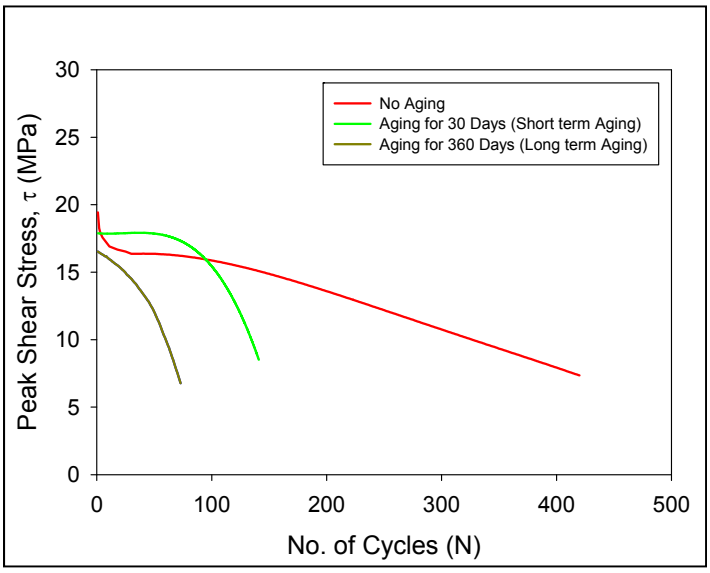

Figure 8.7 Variation of Peak Shear Stress with Cycling for SAC105 Subjected to Shear

8.5 Equivalency Between Uniaxial and Shear Fatigue Data

In this section, a comparison of the low-cycle fatigue results for uniaxial tension/compression and shear testing has been made by converting all data to be in terms of the von Mises plastic equivalent strains, and then plotting them on the same graph. The

procedure for converted uniaxial and pure shear strains to plastic equivalent strains is now discussed.

The von Mises equivalent stress σ_{VM} can be expressed as,

$$\sigma_{eq} = \sigma_{VM} = \left(\frac{1}{2} \left[(\sigma_1 - \sigma_2)^2 + (\sigma_1 - \sigma_3)^2 + (\sigma_2 - \sigma_3)^2 \right] \right)^{\frac{1}{2}} \tag{8.4}$$

where σ_1, σ_2, σ_3 are the principal stresses. For linear elastic materials, the stress-strain relationships in the principal coordinate system can be expressed as:

$$\begin{aligned} \sigma_1 &= \frac{E}{(1+\nu)(1-2\nu)} \left[(1-\nu)\varepsilon_1 + \nu\varepsilon_2 + \nu\varepsilon_3 \right] \\ \sigma_2 &= \frac{E}{(1+\nu)(1-2\nu)} \left[(1-\nu)\varepsilon_2 + \nu\varepsilon_1 + \nu\varepsilon_3 \right] \\ \sigma_3 &= \frac{E}{(1+\nu)(1-2\nu)} \left[(1-\nu)\varepsilon_3 + \nu\varepsilon_1 + \nu\varepsilon_2 \right] \end{aligned} \tag{8.5}$$

where ε_1, ε_2, and ε_3 are the principal strains, E is the elastic modulus, and ν is the Poisson's ratio. Combining Eq. (8.5) and Eq. (8.4), the von Mises equivalent stress can be expressed as:

$$\sigma_{eq} = \sigma_{VM} = \frac{E}{1+\nu} \left(\frac{1}{2} \left[(\varepsilon_1 - \varepsilon_2)^2 + (\varepsilon_1 - \varepsilon_3)^2 + (\varepsilon_2 - \varepsilon_3)^2 \right] \right)^{\frac{1}{2}} \tag{8.6}$$

von Mises equivalent strain can be defined as,

$$\varepsilon_{eq} = \frac{\sigma_{eq}}{E} \tag{8.7}$$

By putting Eq. (8.7) into Eq. (8.6) this expression becomes:

$$\varepsilon_{eq} = \frac{1}{1+\nu} \left(\frac{1}{2} \left[(\varepsilon_1 - \varepsilon_2)^2 + (\varepsilon_1 - \varepsilon_3)^2 + (\varepsilon_2 - \varepsilon_3)^2 \right] \right)^{\frac{1}{2}} \tag{8.8}$$

For perfectly plastic behavior, the Poisson's ratio is set to a value of 0.5 [222-223]. With this assumption, Eq. (8.8) simplifies to:

The Eq. (8.8) is reduced to,

$$\varepsilon_{eq} = \frac{\sqrt{2}}{3}\left[(\varepsilon_1 - \varepsilon_2)^2 + (\varepsilon_1 - \varepsilon_3)^2 + (\varepsilon_2 - \varepsilon_3)^2\right]^{\frac{1}{2}} \tag{8.9}$$

This quantity is often referred to as the von Mises plastic equivalent strain.

For the case of uniaxial/compression testing, the principal stresses are $\sigma_1 = \sigma$, $\sigma_2 = \sigma_3 = 0$; and the strains are $\varepsilon_1 = \varepsilon$, $\varepsilon_1 = \varepsilon_2 = -\nu\varepsilon = -0.5\varepsilon$

Eqs. (8.4) and (8.8) then becomes:

$$\sigma_{eq} = \sigma \tag{8.10}$$

$$\varepsilon_{eq} = \varepsilon \tag{8.11}$$

where σ is the applied uniaxial stress, and ε is the uniaxial strain in the specimen.

For the case of pure shear testing, the principal stresses are $\sigma_1 = \tau$, $\sigma_2 = -\tau$, and $\sigma_3 = 0$; and the principal strains are $\varepsilon_1 = \gamma/2$, $\varepsilon_2 = \gamma/2$, and $\varepsilon_3 = 0$. Eqs. (8.4) and (8.9) then become:

$$\sigma_{eq} = \sqrt{3}\,\tau \tag{8.12}$$

$$\varepsilon_{eq} = \frac{\gamma}{\sqrt{3}} \tag{8.13}$$

where τ is the applied shear stress, and γ is the shear strain in the specimen.

Using the relationships in Eqs. (8.11) and (8.13), the plastic strain range vs. cycles to failure fatigue data in Figure 6.4 (uniaxial tension/compression) and Figure 8.5 (shear) have been recast in terms of the von Mises equivalent plastic strains. The combined results are shown in Figure 8.8 for the various aging conditions. In this plot, the different colors again represent different aging conditions. Both uniaxial and shear test data are

included, and different symbols are used to differentiate the data coming from uniaxial and shear tests. It can be seen that the mixed uniaxial/shear data for each aging condition demonstrate a fairly linear variation when graphed on a log-log scale, and the regression coefficients are listed in Table 8.4. This suggests that the Coffin-Manson type relationship in Eq. (6.6) is applicable for general strain states if the equivalent plastic strain is used.

Similarly, the energy dissipation fatigue data in Figure 6.5 (uniaxial tension/compression) and Figure 8.6 (shear) have been recast in terms of hysteresis loops calculated from plots of equivalent stress vs. equivalent plastic strain found using the relationships in Eqs. (8.10-8.13). The combined results are shown in Figure 29 for the various aging conditions. In this plot, the different colors again represent different aging conditions. Both uniaxial and shear test data are included, and different symbols are used to differentiate the data coming from uniaxial and shear tests. It can be seen that the mixed uniaxial/shear data for each aging condition demonstrate a fairly linear variation when graphed on a log-log scale and the regression coefficients are listed in Table 8.5. This suggests that the Morrow type relationship in Eq. (6.7) is applicable for general stress and strain states if the energy dissipation is calculated from the equivalent stress and equivalent plastic strain.

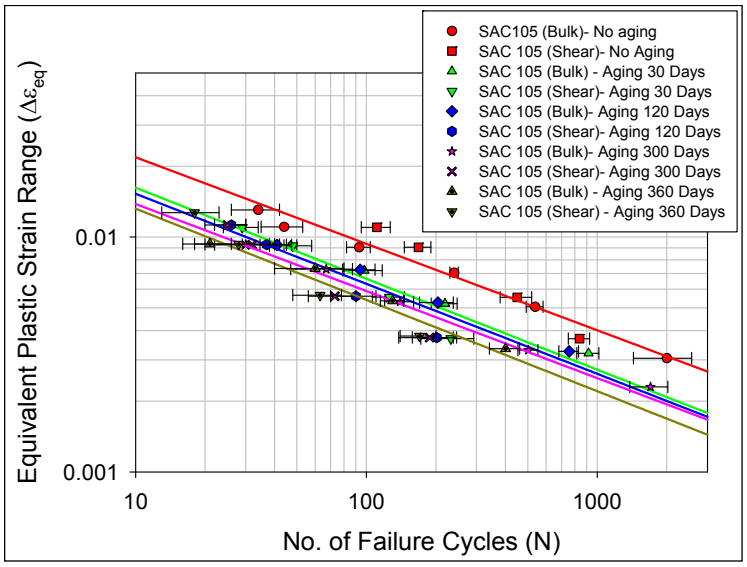

Figure 8.8 Fatigue Life Curves (Equivalent Plastic Strain Range vs. Cycles to Failure) Including Uniaxial and Shear Data

Table 8.4 Coffin-Manson Coefficients for SAC105 for Various Aging Conditions

Aging Conditions (Days)	Material Ductility Coefficient, C	Fatigue Exponent, n
0	0.0510	0.3681
30	0.0395	0.3872
120	0.0369	0.3892
300	0.0325	0.3706
360	0.0323	0.3887

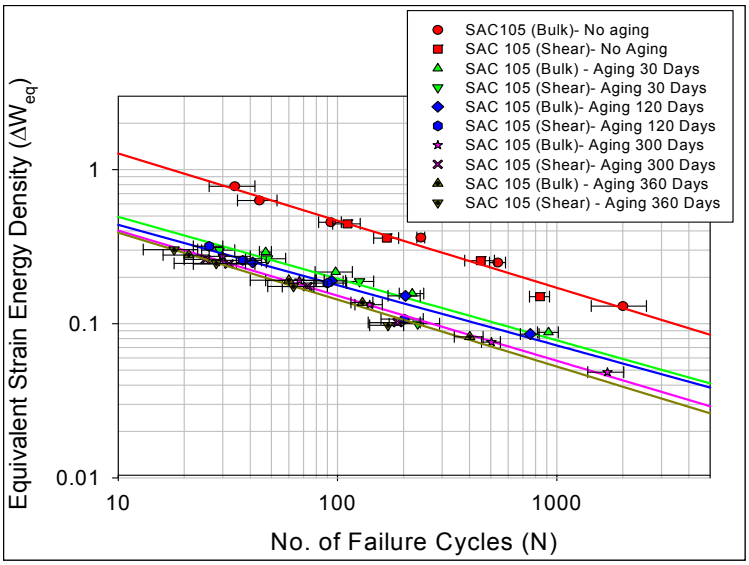

Figure 8.9 Fatigue Life Curves (Energy Dissipation vs. Cycles to Failure) Including Uniaxial and Shear Data

Table 8.5 Morrow Model Coefficients for SAC105 for Various Aging Conditions

Aging Conditions (Days)	Material Ductility Coefficient, K	Fatigue Exponent, m
0	3.475	0.4359
30	1.243	0.4010
120	1.077	0.3909
300	1.063	0.4223
360	1.059	0.4342

8.6 Summary and Discussion

In this chapter, the effects of aging on the cyclic shear stress-strain behavior of lead free solders were investigated. Iosipescu shear specimen assemblies for SAC105 solder were subjected to mechanical cyclic loading. It was observed that the shear hysteresis loop area changes significantly with aging, and mathematical models have been found to fit the aging induced evolution. For strain limit controlled cyclic testing, the shear hysteresis loop size decreases with aging time. These phenomena have been explained through comparison to the aging induced degradation of the yield stress and ultimate shear strength as well as through microstructural damage accumulation.

The fatigue data expressed as plastic shear strain change vs. cycles to failure demonstrated a nearly linear variation for all aging conditions when graphed on a log-log scale. This suggests that the Coffin-Manson fatigue law can accurately represent the data for the various aging conditions, and the largest shift in the fatigue curves occurred in the first 30 days of aging. A clear progression of the fatigue curves was observed with longer aging times prior to mechanical cycling. The fatigue data was also recast in terms of the energy dissipated per cycle (ΔW) in the first cycle shear hysteresis loop. The fatigue curves in this case were found to be well fit by the Morrow energy-based fatigue law for all aging conditions.

A comparison of the low-cycle fatigue results for uniaxial tension/compression and shear testing was made by recasting the data in terms of von Mises equivalent stresses and strains. With this approach, it has been shown that uniaxial fatigue data and the shear fatigue data for SAC105 were in good agreement.

CHAPTER 9

MICROSTRUCTURE BASED FATIGUE MODEL INCLUDING AGING EFFECTS

9.1 Introduction

Solder fatigue failure criteria prediction has been one of the important issues for the electronic packaging industry to estimate the package reliability. The next generation electronic components features extremely small package sizes with large numbers of connections. The trends in chip packaging have changed from leaded through hole mounted devices to leaded surface mount devices and on to leadless solder ball arrays, which have recently been the focus of concern due to their fine pitch size. This becomes challenge for engineers and scientists where at the forefront of this issue is solder joint reliability. Successful prediction of solder fatigue failure will depend on the ability of accurately model the solder joint.

Early solder joint fatigue models were developed based on experimental thermal cycling tests. Most of the fatigue models require stress-strain data in order to predict service life. Early fatigue data was collected experimentally using strain gages. However, with the decreasing size of the solder joint, experimental collection of stress-strain data is becoming increasingly difficult, and Finite Element Analysis (FEA) is becoming the more practical route for obtaining stress and strain distribution. Rapid

thermal cycling of actual parts is still necessary for verifying the fatigue life predictions. The necessity of fatigue model of solder material has also recognized by other investigators. As a result several solder joint fatigue models have been proposed. However, the assumptions and applicability of these models vary, including the manner in which the physical and metallurgical aspects of fatigue are taken into account.

Solder joints in electronic assemblies are typically subjected to thermal cycling, either in actual application or in accelerated life testing used for qualification. Mismatches in the thermal expansion coefficients of the assembly materials cause the solder joints to be subjected to cyclic (positive and negative) mechanical strains and stresses. This cyclic loading leads to thermomechanical fatigue damage that involves damage accumulation, crack initiation, crack propagation, and failure. In addition, the microstructure, mechanical response, and failure behavior of lead free solder joints in electronic assemblies are constantly evolving when exposed to isothermal aging and/or thermal cycling environments. While the effects of aging on solder constitutive behavior (stress-strain and creep) have been examined in some detail, there have been no prior studies on the effects of aging on solder failure and fatigue behavior. Aging leads to both grain and phase coarsening, and can cause recrystallization at Sn grain boundaries. Such changes are closely tied to the damage that occurs during mechanical cyclic loading.

Most of the fatigue models available in the literature are empirical, and microstructurally adaptive fatigue models are rare in the literature. In this chapter, Coffin-Manson and Morrow models have been modified by including a microstructurally adaptive shift function with aging effects incorporated by considering grain/sub-grain coarsening and phase growth.

9.2 Review of Available Fatigue Models

The models proposed for predicting the fatigue life of solder materials can be divided into five major categories, based on the fundamental mechanism viewed as being responsible for including damage. These five categories are (i) stress-based, (ii) plastic strain-based, (iii) creep strain-based, (iv) energy-based, (v) damage accumulation based. Example criteria are tabulated in Table 9.1, along with the researchers who originally proposed or applied these models. These 14 models are summarized and arranged by model class in Table 9.2.

Table 9.1 Fatigue Models and Classification

No.	Fatigue Model	Equation Nos.	Strain		Energy	Damage	Other
			Plastic	Creep			
1	Coffin-Manson	2	x				
2	Total Strain	3	x				
3	Solomon	4	x				
4	Englemaier	5	x				
5	Miner	6,7	x	x			
6	Knecht and Fox	8		x			
7	Syed	9		x	x		
8	Akay	10			x		
9	Liang	11			x		
10	Heinrich	12, 13			x		
11	Pan	17			x		
12	Darveaux	14			x	x	
13	Stolkarts	18				x	
14	Norris and Landzberg	19					x

Table 9.2 Summary of Solder Fatigue Models

No.	Fatigue Model	Model Class	Applicable Packages	Required Parameters	Coverage	Parameters
1	Coffin-Manson	Plastic Strain	All	Plastic Strain	Low Cyclic Fatigue	Fatigue Ductility Coefficient, Fatigue Strength Exponent
2	Total Strain	Plastic Strain+Elastic Strain	All	Strain Range	High and Low Cycle Fatigue	Fatigue Ductility Coefficient, Fatigue Strength Exponent and Fatigue Ductility Exponent
3	Solomon	Plastic Shear Strain	All	Plastic Shear Strain	Low Cycle Fatigue	Inverse Fatigue Ductility Coefficient, Constant
4	Englemaier	Total Strain	Leaded and Leadless, TSOP	Total Shear Strain	Low Cycle Fatigue	Mean Cyclic Solder Joint Temperature, Cyclic Frequency
5	Miner	Superposition (Plastic and Creep)	PQFP, FCOB	Plastic Failure and Creep Failure	Plastic Shear and Matrix Creep	Plastic Failure, Creep Failure
6	Knecht and Fox	Matrix Creep	ALL	Matrix Creep Shear Strain	Matrix Creep Only	Constant, c
7	Syed	Accumulation of Creep Strain Energy	PBGA, SMD, NSMD	GBS Energy and MC Energy	Implies Full Coverage	Accumulated Matrix Creep/Cycle and Creep Strain/Cycle
8	Dasgupta	Total Strain Energy	LLCC, TSOP	Energy	Joint Geometry Accounted For	Total Strain Energy Density
9	Liang	Stress/strain Energy Density Based	BGA and Leadless Joints	Energy	Constants From Isothermal Low Cycle Fatigue Tests	Temperature Dependent Material Constants
10	Heinrich	Energy Density Based	BGA	Energy	Hysteresis Curve	Viscoplastic Strain Energy/Cycle
11	Darveaux	Energy Density Based	Leadless, PBGA	Damage and Energy	Hysteresis Curve	Total Possible Crack Length, Crack Growth, Crack Initiation
12	Pan	Energy Density Based	LCCC	Strain Energy Density and Plastic Energy Density	Hysteresis Curve	Strain Energy Density, Plastic Strain Creep Energy Density/Cycle, Creep Strain Energy/Cycle
13	Stolkarts	Damage Accumulation	ALL	Damage	Hysteresis Curve and Damage Evolution	Damage Parameter, Material Constant
14	Norris and Landzberg	Temperature and Frequency	ALL	Temperature Frequency	Test Condition versus Use Conditions	Temeprature, Isothermal Fatigue Ratio

9.2.1 Plastic Strain Fatigue Models

The Coffin-Manson low-cycle fatigue equation [152] is perhaps the most well known of the fatigue life relationship:

$$N_f^n \Delta\varepsilon_p = C \tag{9.1}$$

where $\Delta\varepsilon_p$ is cyclic plastic strain range.

Similar equation has been proposed by Solomon [219] for low-cycle shear fatigue as:

$$N_f^n \Delta\gamma_p = C \tag{9.2}$$

Because the Coffin-Manson equation considers only plastic deformations, it is commonly combined with Basquin's equation to account for elastic deformation as well. The resulting equation is known as the total strain equation, and is shown in Eq. (9.3) [33].

$$\frac{\Delta\varepsilon}{2} = \frac{\sigma_f'}{E}(2N_f)^b + \varepsilon_f'(2N_f)^c \tag{9.3}$$

where $\Delta\varepsilon$ is the strain range, σ_f' is the fatigue strength coefficient, E is the elastic modulus, ε_f' is the fatigue ductility, b is the fatigue strength exponent, and c is the fatigue ductility exponent.

By applying Miner's Linear superposition principal, both plastic and creep strain can be accounted for in a strain-based fatigue mode. This model combines the Solomon fatigue model with Knecht and Fox creep model, and is shown in Eq. (9.4) [222],

$$\frac{1}{N_f} = \frac{1}{N_p} + \frac{1}{N_c} \tag{9.4}$$

N_p refers to the number of cycles to failure due to plastic fatigue and is obtained directly from Solomon's fatigue model. N_c refers to the number of cycles to failure due to creep fatigue and is obtained from Knecht and Fox's creep fatigue model. This fatigue model is similar to a full method reported by Lau, et al. [33] as Strain Range Partitioning (SRP). In SRP, a typical hysteresis loop can be separated into four components: the plastic strain in tension and compression (PP), the creep strain in tension and compression (CC), the creep strain intension-plastic strain in compression (CP) and the plastic strain in tension-creep strain incompression (PC). SRP equation is shown in Eq. (9.5):

$$\frac{1}{N_f} = \frac{F_{pp}}{N_{pp}} + \frac{F_{cc}}{N_{cc}} + \frac{F_{cp}}{N_{cp}} + \frac{F_{pc}}{N_{pc}} \tag{9.5}$$

9.2.2 Creep Strain Fatigue Models

Knecht and Fox [223] have proposed a simple matrix creep fatigue model relating the solder microstructure and matrix creep shear strain range as shown in Eq. (9.6).

$$N_f = \frac{C}{\Delta\gamma_{mc}} \tag{9.6}$$

where, N_f is the number of failure cycle, C is the constant which is dependent on failure criteria and solder microstructure and $\Delta\gamma_{mc}$ is the strain range due to matrix creep.

Syed [224-226] proposed a fatigue model considering creep mechanism, grain boundary sliding incorporated with matrix creep. In this model, creep strain is partitioned into two parts as shown in Eq. (9.7) [228].

$$N_f = \frac{1}{0.022D_{gbs} + 0.063D_{mc}} \tag{9.7}$$

where D_{gbs} and D_{mc} are the accumulated equivalent creep strain per cycle for grain boundary sliding and the matrix creep, respectively.

9.2.3 Energy-based Fatigue Models

It has been experimentally shown [154-158] that the fatigue life of surface mount solder joints can be described by a power law of some damage terms or descriptors, similar to the fatigue of the more typical engineering metals. Therefore, the most general fatigue life relationship is the strain-energy relationship of Morrow [153]:

$$N_f^m \Delta W = K \tag{9.10}$$

where m is fatigue ductility coefficient, ΔW is the cyclic visco-plastic strain energy, which simply is calculated from the area of the cyclic hysteresis loop in the stress-strain diagram, and K is the fatigue ductility exponent.

Gustafasson [227] has reported another energy based fatigue model, based on findings from Darveaux, as depicted in Eq. (9.11):

$$N_{\alpha w} = N_{0s} + \frac{a - \left(N_{0s} - N_{0p}\right)\frac{da_p}{dN}}{\frac{da_s}{dN} + \frac{da_p}{dN}} \tag{9.11}$$

Where, N_{0s}, N_{0p} are the primary and secondary crack initiation energy based terms, respectively. The Darveaux fatigue model (as shown in Eq. 9.11) is an example of an energy-based fatigue model that incorporates crack propagation. The crack propagation terms, da/dN, are dependent on the corresponding values of ΔW [227]:

$$\frac{da}{dN} = 3.49 \times 10^{-7} \Delta W^{1.13} \tag{9.12}$$

Pan [228] reports a strain-energy based fatigue model called Critical Accumulated Strain Energy or CASE. This fatigue model is shown in Eq. (9.13):

$$C = N_f^* \left(a\dot{E}_p + b\dot{E}_c\right) \tag{9.13}$$

where C is the critical strain energy density, and the creep and plastic energies E_c and E_p are calculated by finite element analysis.

9.2.4 Damage Fatigue Models

Stolkarts [229] has reported successful application of this model over a damage-free model. Eq. (9.14) depicts the equation used by Stolkarts in calculating the number of cycles to failure, N_f.

$$N_f = \frac{1-(1-d_f)^{k-1}}{(k+1)L} \tag{9.14}$$

where d_f is the amount of damage at failure and is taken as 0.5 for solders. K is defined as a material constant and given a value of 2. L is defined as, $L = \int f dt$ where, f is the initial rate of damage of remaining undamaged material in the representative volume of remaining element.

9.3 Microstructural Damage Evolution

As shown in a typical micrograph of a ternary Sn-Ag-Cu (SAC105) solder alloy (Figure 9.1(a)), the microstructure of SAC solders consists of primary β-Sn dendrites, and a honeycomb structure of uniformly dispersed fine precipitates over the β-Sn matrix throughout the bulk solder material. The typical microstructure of the SAC alloys consists of primary dendrites of β-Sn surrounded by a eutectic micro-constituent comprising Ag_3Sn and Cu_6Sn_5 intermetallic particles.

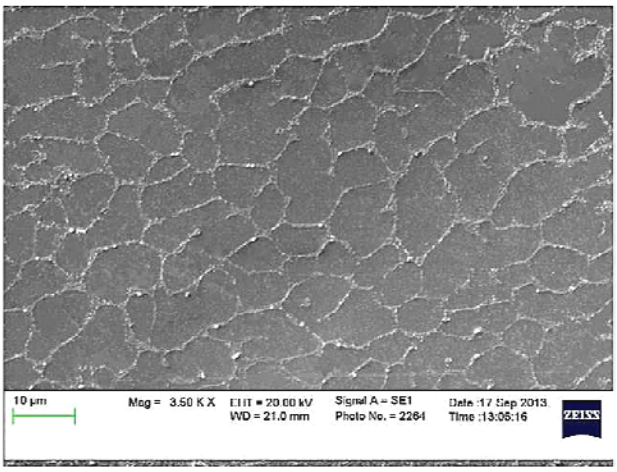

(a) Initial Microstructure

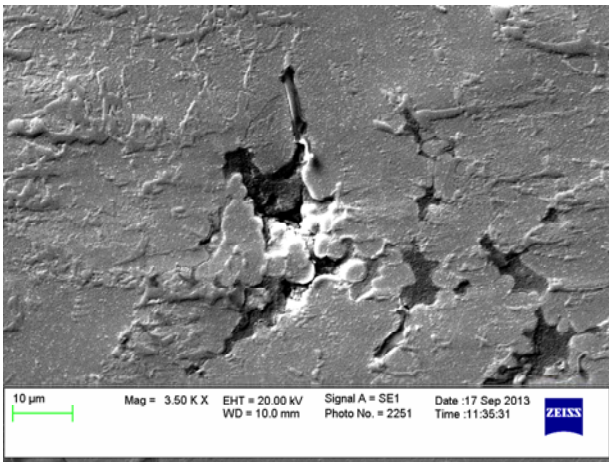

(b) After 30% of Cyclic Stress Drop

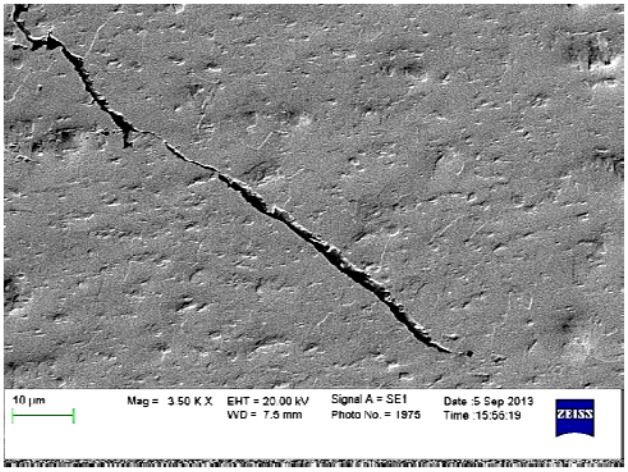

(c) After 50% of Cyclic Stress Drop

Figure 9.1 Microstrutural Damage Evolution for SAC105 (No Aging)

The fatigue and reliability behavior of solder joints are also affected by the grain structure of solder materials, which is inherently unstable. The grains will grow in size over time as the grain structure reduces the internal energy of a fine-grained structure. A nonequilibrious microstructure will change to an energetically more favorable morphology over time. During fatigue testing, the grain growth process can also be an indication of the accumulation of fatigue damage. Highly strained zones will become coarsened, and it is normally at these sites that crack initiation and propagation takes place [230]. As the grains grow there is a concentration of contaminants at the grain boundaries, weakening them. After a certain time, microvoids can be found at the grain boundary intersections. They may grow into microfissures, which in turn will grow into cracks and eventually lead to total fracture. As illustrated in Figure 9.1(b), at 30% drop of peak cyclic stress of hysteresis loop during cyclic loading, microvoids were formed which grew into microcracks. After 50% of peak cyclic stress drop, micro-cracks grew and coalesced into macro-cracks which led to total fracture as shown in Figure 9(c).

The basic microstructure of the SAC105 alloys consists of β-Sn dendrites and eutectic micro-constituents. As aging took place, the microstructure of solder material started to evolve: the IMC particles conglomerated and grew coarser, and the β-Sn dendrites grew larger with increased aging. Fewer and bigger IMCs are observed in the samples subjected to high temperature aging (125C for 210 days) for SAC105 at high magnification (3500x) as shown in Figure 9.2(a). Microfissure was formed at the sub-grain boundary intersections after 30% of peak cyclic stress drop (see Figure 9.2(b)). The Figure illustrates 9.2(c) that the microfussure grew into crack and crack initiated at 50%

of peak cyclic stress drop. It was also observed that crack propagates along the sub-grain boundaries as shown in Figure 9.2(c).

Figure 9.3 illustrates transgranular cracking through many small recrystallized grains. It was observed in Chapter 5 that strain energy density decreases as aging progresses for lead-free solder alloy. As the recrystallization requires a high strain energy accumulation, the result suggests that the strain energy due to cyclic deformation in non-aged sample is much higher than that in aged sample. A detailed examination of the recrystallization microstructure as shown in Figures 9.3 and 9.1(a) found that the densely distributed small Ag_3Sn particles in honey comb shaped microstructure (see Figure 9.1(a)) coalesced into larger ones during isothermal fatigue and then Ag_3Sn IMC became sparsely distributed gradually in recrystallized region (see Figure 9.3). The sparse distribution of the IMC particles leads to the weakening of the recrystallized microstructure. Due to low strength of the recrystallized microstructure without original densely distributed IMCs, the cracks tend to propagate transgranularly especially when the stress state, orientation and geometry of the grains are not in favor of cracking along grain boundaries. Occasionally, the cracks may be found propagating intergranularly when the recrystallized grain size is small. Similar phenomena are also reported by Chen, et al. [231] in their investigation on localized recystallization and cracking behavior of lead-free solder material under cyclic loading.

Figure 9.4 illustrates the intergrannular cracking in few irregularly shaped recrystallized grains. As the recrystallization requires a high strain energy accumulation, the result suggests that the strain energy due to cyclic deformation in non-aged sample is much higher than that in aged sample. The grain boundary sliding is the main mechanism

for cracking along the grain boundaries, and the decohesions of the grain boundaries were frequently observed. It can be assumed that the cracking along the recystallized grain boundaries needs less energy than transgranular cracking [232]. Although the intergranular cracking is not always an energy-saving mode for Sn alloy, and the cracking path is determined jointly by many factors, such as grain orientation and size, stress status, and IMC distribution. The combination of the stress concentration, sparsely distributed IMCs and prior weakened in grain boundaries during aging makes the crack initiation and propagation intergranularly in the recrystallized region.

It is clearly evident in Figure 9.5(a)-(b) that two different crack propagation modes exist in non-aged and aged samples. In non-aged sample, the crack propagation mode is mostly trangranular. Intergranular crack propagation mode is evident in aged samples. A zoomed view of a fractured surface has been depicted in Figure 9.6 for a non-aged sample.

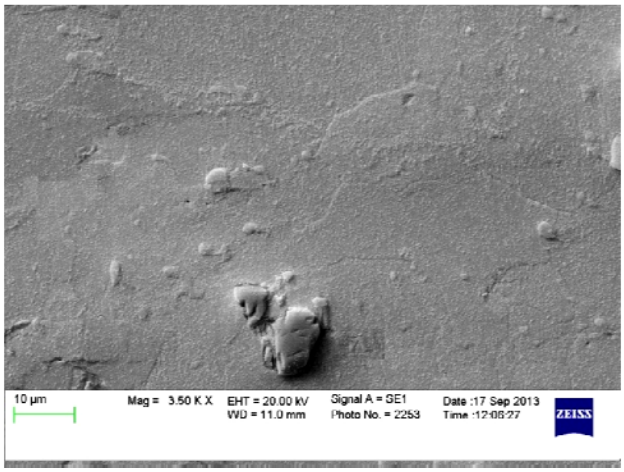

(a) Initial Microstructure

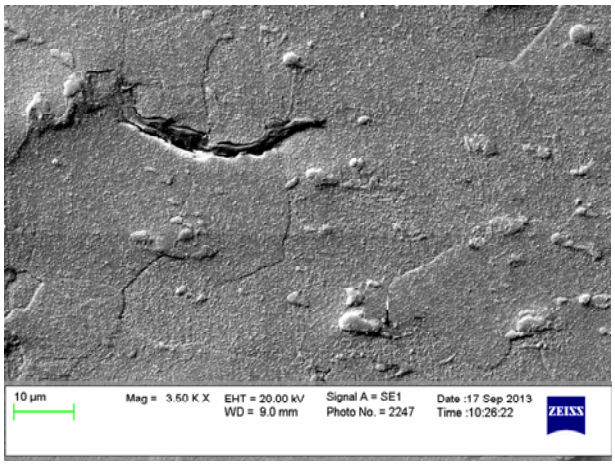

(a) After 30% of Cyclic Stress Drop

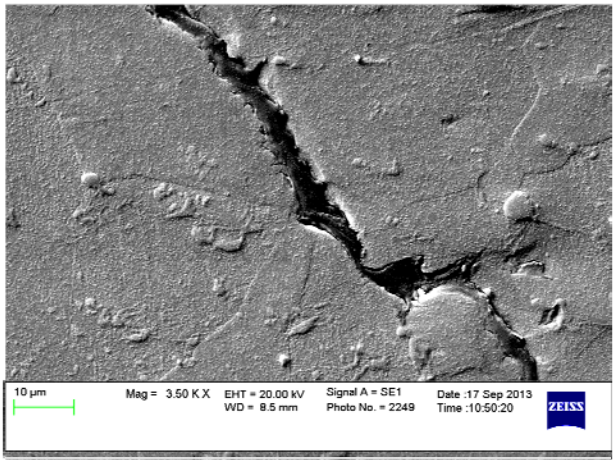

(b) After 50% of Cyclic Stress Drop

Figure 9.2 Microstrutural Damage Evolution for SAC105
(210 Days Aging at 125 C)

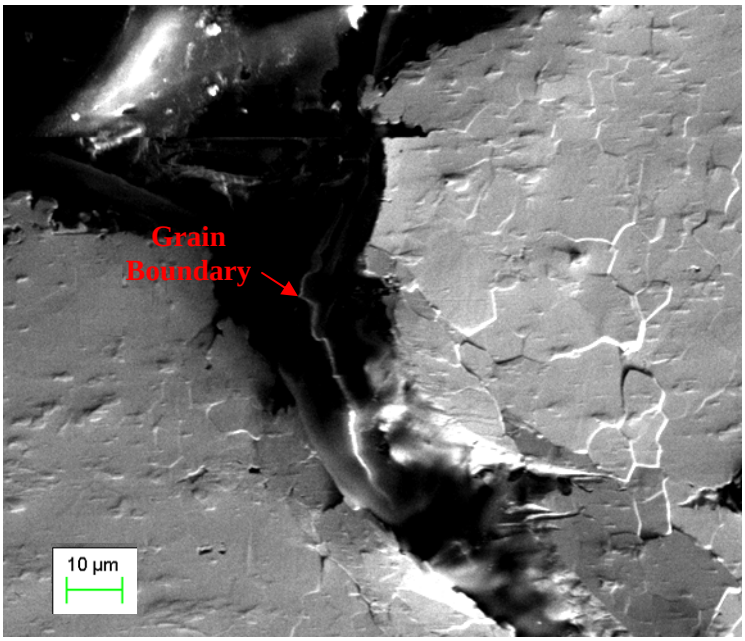

Figure 9.3 Transgranular Cracking Through Many Small Recrystallized Grains (No Aging, SAC105)

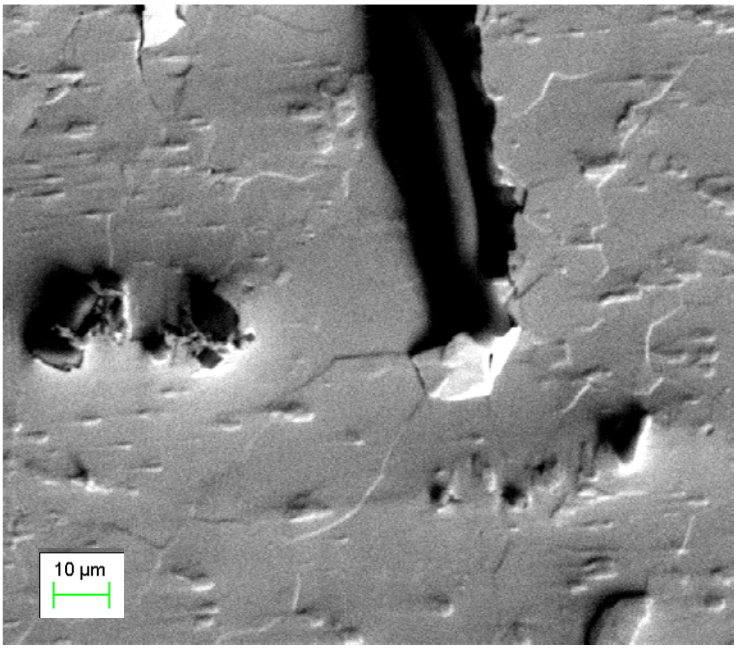

Figure 9.4 Intergranular Cracking Through Few Large Recrystallized Grains (210 Days Aging, SAC105)

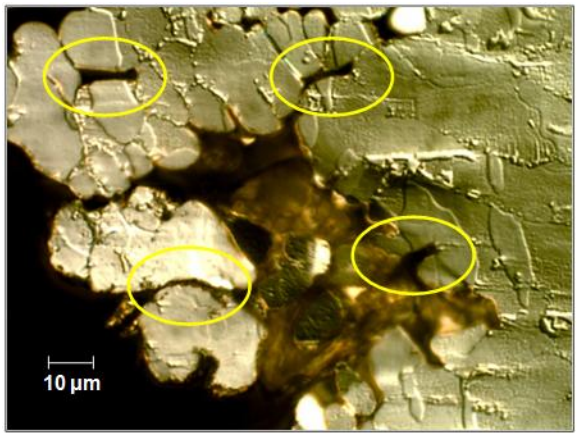

(a) Transgranular Cracking for Non-aged Sample

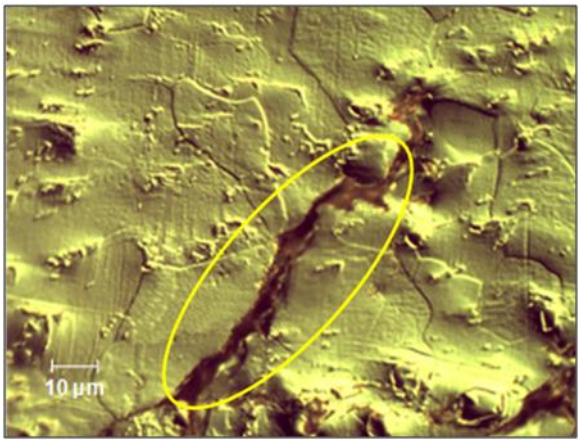

(b) Intergranular Cracking for Aged Sample

Figure 9.5 Optical Microscopic Images on Crack Propagation Modes for SAC105 Solder Alloy

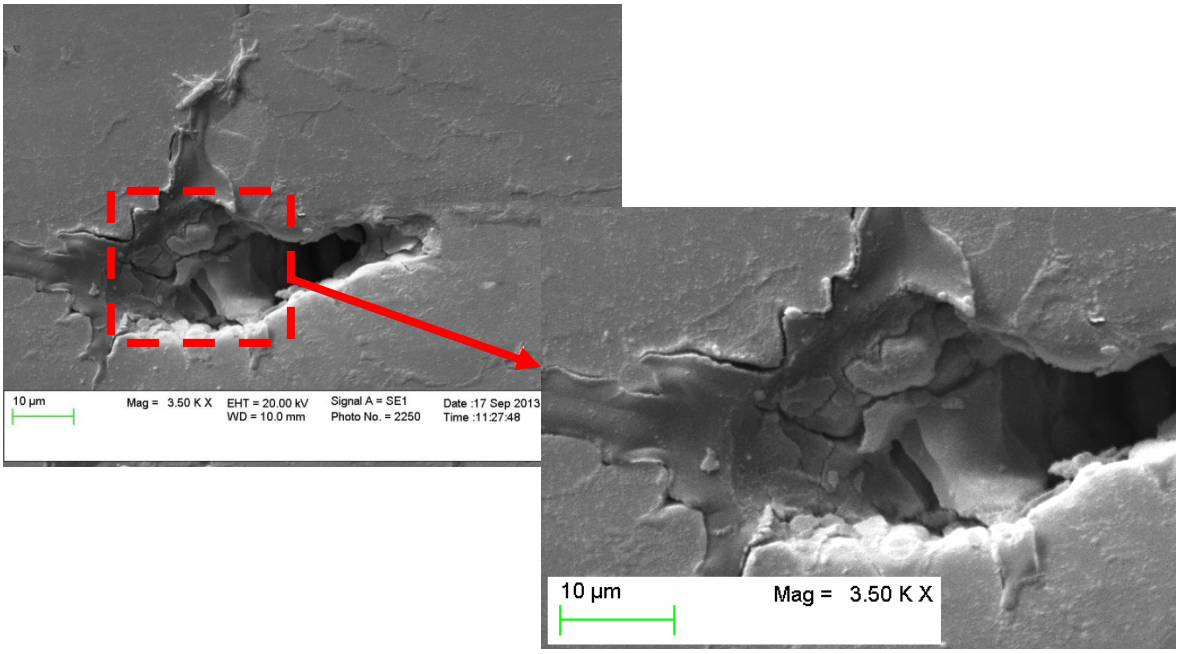

Figure 9.6 Fractured Surface of SAC105 (No Aging Condition)

9.4 Microstructural Adaptive Fatigue Model

In the literature, some modifications of Coffin-Manson model and Morrow model are available. The influence of frequency can be described in terms of a modified Coffin-Manson law [219]:

$$\left(N_f \nu^{K-1}\right)^n \Delta\varepsilon_p = C \tag{9.15}$$

A temperature dependent fatigue model was proposed by Shi et al. [81] after further modification of frequency dependent fatigue model:

$$\left(N_f \nu^{K-1}\right)^n \frac{W_p}{2\sigma_f} = C \tag{9.16}$$

where σ_f is the flow stress. The parameter σ_f can be used to reduce effectively the influence of temperature on the value of C.

In the present work, it is attempted to modify both the Coffin-Manson and Morrow fatigue models to include aging effects. A microstructural adaptive shift factor is incorporated into the models based on microstructural damage evolution occurring with aging.

9.4.1 Aging Induced Fatigue Model

Coffin-Manson model is modified by incorporating shift factor in the model. The modified model can be written as,

$$\left(N_t a\right)^n \Delta\varepsilon_p = C \tag{9.17}$$

Where, N_t is number of failure cycle at aging time t, a is the shift factor, n is the fatigue exponent and C is the fatigue ductility coefficient. The shift factor can be written as,

$$a = \frac{N_0}{N_t} \tag{9.18}$$

where N_0 is the number of failure cycle at no aging condition. Essentially, a is a function of microstructural damage accumulation due to aging temperature, aging time, strain rate during fatigue loading etc. Derivation of shift function is presented in the next section.

9.4.2 Derivation of Shift Function

Effects of aging on fatigue involve static phase and grain/sub-grain coarsening during static annealing and dynamic grain/sub-grain coarsening due to plastic deformation. Therefore, derivation of shift function is divided into two following parts: (1) Grain/Sub-grain coarsening during static annealing (2) Grain/Sub-grain coarsening during plastic deformation.

9.4.3 Grain/Sub-grain Coarsening during Static Annealing [233]

The physical process of the microstructure coarsening with releasing excess energy in a two-phase alloy is due to high dissolving of fine grains whose surface-to-volume ratio is large. This process is similar to the theoretically well-studied growth of the matrix. The matrix grain growth rate was ascertained [234, 235] to be controlled by the particle coarsening rate. When α-matrix contains the β-phase particles with radius $\bar{r}$, the equilibrium concentration of solute atoms in the matrix increases according to the Gibbs-Thomson equation [235]

$$C(\bar{r}) = C_0\left(1 + \frac{2\gamma\Omega}{RT\bar{r}}\right) \tag{9.19}$$

Where, C_0 is the solute concentration in equilibrium with an infinitely large particle, γ is the interfacial free energy per unit area of the particle-matrix interfaces, Ω is the molar volume of the particles.

The process of the particle growth induced by volume diffusion was theoretically analyzed in [236-237]. It was revealed that variation of the average particle radius with time is,

$$\bar{r}_t^3 - \bar{r}_0^3 = B_1 \frac{\gamma\Omega C_0 D_\upsilon}{RT} t \tag{9.20}$$

Here D_υ is the coefficient of solute diffusion in the matrix, B_1 is the parameter depending on the volume fraction of particles, φ. i.e. $B_1 = 16$ if $\varphi = 0.5$. If the particles lie at the grain boundaries and their coarsening is controlled by grain-boundary solute diffusion, the temporal dependence of particle radius is given by [238-239],

$$\bar{r}_t^4 - \bar{r}_0^4 = B_2 \frac{\delta\gamma\Omega C_0^{g.b.} D_{g.b.}}{RT} t \tag{9.21}$$

where $D_{g.b.}$ is the coefficient of solute diffusion in the grain boundary, $C_0^{g.b.}$ is the equilibrium solute concentration near the grain boundaries in the absence of particles, δ is the boundary width; B_2 is the parameter depending on particle geometry and φ. After making certain assumptions, the Eq. (9.21) becomes in the following form,

$$\bar{d}_t^4 - \bar{d}_0^4 = Ae^{-\frac{Q}{RT}}t \tag{9.22}$$

where t is aging time, T is aging temperature, R is Boltzmann constant, Q is activation energy.

The Eq. (9.22) can be written in following form,

$$\bar{d}_t^4 = \bar{d}_0^4 + Ae^{-\frac{Q}{RT}}t \tag{9.23}$$

Here, d_t is static coarsened grain size and d_0 is the initial grain size.

9.4.4 Grain/Sub-Grain Coarsening during Plastic Deformation [233]

It is assumed that the strain-enhanced diffusion coefficients will increase linearly with strain rate. They obey an empirical relation of the form,

$$\frac{D^{\dot{\varepsilon}}}{D^0} = 1 + G\dot{\varepsilon} \tag{9.24}$$

Where, D^0 and $D^{\dot{\varepsilon}}$ are the diffusion coefficients in an undeformed alloy and in an alloy deformed at the rate of $\dot{\varepsilon}$, respectively and G is a parameter whose value tends to increase as the temperature decreases. It is also assumed that diffusion takes place by a vacancy mechanism and the increase of diffusion coefficients is due to the appearance of the excess concentration of vacancies during deformation.

Assuming that the rate of production of excess vacancies is proportional to the strain rate and that the rate of their annihilation is proportional to their concentration, n_c, it can be obtained as,

$$\dot{n}_c = K_1\dot{\varepsilon} - \frac{n_c}{\tau_c} \tag{9.25}$$

Here, τ_c is the relaxation time of excess vacancies, K_1 is the proportionality factor, Integrating Eq. (9.25) it can be obtained,

$$n_c = K_1\tau_c\dot{\varepsilon}\left[1 - e^{-\frac{t}{\tau_c}}\right] \tag{9.26}$$

If n_υ is the thermally equilibrium concentration of vacancies at the boundary, then the coefficient of solute diffusion in a strained alloy is

$$D^{\dot{c}}_{g.b.} = K_2\left(n_\upsilon + n_c\right)$$

where K_2 is proportionality constant.

The grain growth rate for the case when the process is controlled by diffusion along boundaries is obtained from Eq. (9.21),

$$\frac{d\bar{r}}{dt} = B_2\frac{\delta\gamma\Omega C_0^{g.b.}D^{\dot{c}}_{g.b.}}{4RT\bar{r}^3} = K_2K_3\frac{n_\upsilon + n_c}{4\bar{r}^3} \tag{9.27}$$

Here,

$$K_3 = B_2\frac{\delta\gamma\Omega C_0^{g.b.}}{RT}$$

Integrating Eq. (9.27) with regard for Eq. (9.21), (9.26) and $\bar{d} = 2\bar{r}$ it can be obtained,

$$\bar{d}^4 = \bar{d}_t^4 + K_4\dot{\varepsilon}\left[t - \tau_c + \tau_c e^{-\frac{t}{\tau_c}}\right] \tag{9.28}$$

where

$K_4 = B_2 \frac{K\delta\gamma_i\Omega C_0}{RT} = 16K_1K_2K_3\tau_c$ and d_t can be determined from Eq. (9.23)

Using binomial theorem and neglecting higher order term the Eq. (9.28) can be expressed as,

$$d = d_0 + \frac{A}{4d_0^3} e^{-\frac{Q}{RT}} t + \frac{K_4}{4d_0^3}\dot{\varepsilon}\left[t - \tau_c + \tau_c e^{-\frac{t}{\tau_c}} \right] \tag{9.29}$$

Again,

$$J_1 = \frac{A}{4d_0^3} e^{-\frac{Q}{RT}}$$

$$J_2 = \frac{K_4\dot{\varepsilon}}{4d_0^3} = B_2 \frac{K_p\delta\gamma_i\Omega C_0\dot{\varepsilon}}{4d_0^3 RT}$$

The terms are: d_0 = Initial grain diameter, B_2 = Geometric constant, γ_i = Interfacial energy between phase boundaries, Ω = Molar volume of the second phase, C_0 = Equilibrium solute concentration at grain boundaries, δ = Grain boundary width, T = Aging temperature, t = Aging time, K_p = Proportional constant, t_c = Relaxation time, $\dot{\varepsilon}$ = Strain rate.

Superposition of grain growth during static annealing and plastic deformation is applied in Eq. (9.29) as it can be supposed that the grain growth during plastic deformation is the result of simultaneous action of both static annealing and deformation [233]. It is also evident that relative contribution of static and of deformation to grain growth does not depend on strain at a given strain rate while the strain rate is less than or equal to 10^{-3} (1/sec) [233]. It is also reported that the grain growth in the alloy during plastic deformation is controlled by the same processes as those during static annealing,

and the enhancement of the grain growth is due to production during deformation of excess concentration of vacancies, leading to an increased grain-boundary diffusivity of solute atoms [233]. Under this supposition, the derived theoretical equation (Eq. 9.29) is valid.

The Eq. (9.29) can be written as,

$$\begin{aligned} d &= d_0 + J_1 t + J_2 \left[t - \tau_c + \tau_c e^{-\frac{t}{\tau_c}} \right] \\ \Rightarrow d &= d_0 + J_1 t + J_2 t - J_2 \tau_c + J_2 \tau_c e^{-\frac{t}{\tau_c}} \\ \Rightarrow d &= (d_0 - J_2 \tau_c) + (J_1 t + J_2 t) + J_2 \tau_c e^{-\frac{t}{\tau_c}} \\ \Rightarrow d &= d_0 \left(1 - \frac{J_2 \tau_c}{d_0} \right) + (J_1 + J_2) t + J_2 \tau_c e^{-\frac{t}{\tau_c}} \end{aligned} \tag{9.30}$$

Eq. (9.30) can be written as,

$$\frac{d}{d_0} = \left(1 - \frac{J_2 \tau_c}{d_0} \right) + \frac{(J_1 + J_2)}{d_0} t + \left(\frac{J_2 \tau_c}{d_0} \right) e^{-\frac{t}{\tau_c}} \tag{9.31}$$

This leads to $$\frac{d}{d_0} = A_0 + A_1 t + A_2 e^{-A_3 t} \tag{9.32}$$

where d is the average grain diameter after aging, d_0 is the average grain diameter prior to aging, and t is the aging time. Coefficients A_0, A_1, A_2, and A_3 are functions of the alloy composition, aging temperature, and possibly other factors.

In this work, it is proposed that the degradation of the fatigue life of solder materials with aging occurs primarily due to the grain/subgrain coarsening during aging. Therefore, the shift function was assumed to vary with aging time using the same functional form as the expression in Eq. (9.32):

$$a(t) = A_0 + A_1 t + A_2 e^{-A_3 t} \tag{9.33}$$

9.4.5 Determination of Material Constants

A regression fitting technique has been developed to determine the four coefficients in the shift function for each of the two microstructure based fatigue models. For example, the uniaxial fatigue data in Figure 9.7 (SAC305, plastic strain vs. failure cycles) was used to calculate the shift factor for several aging times by using Eq. (9.18) at various strain levels as tabulated in Table 9.3. These results are plotted in Figure 9.8, and Eq. (9.33) was then fit to the extracted shift factor vs. aging time data points using a nonlinear regression analysis to determine the optimum values for coefficients A_0, A_1, A_2, and A_3. Finally the fatigue data were fit with Eq. (9.17) and the determined shift function to calculate the single values of the Coffin-Manson fatigue exponent n and fatigue ductility constant C that are valid for all aging conditions as shown in Figures (9.9(a)-(b)). The fit of Eq. (9.17) to the SAC105 fatigue data is shown in Figure 9.10, while the corresponding fit for the SAC305 fatigue data is shown in Figure 9.11. A similar approach has been used to fit the modified Morrow model to the fatigue data for SAC105 (Figure 6.5) and SAC 305 (Figure 6.12), and the results are shown in Figures 9.12 and 9.13, respectively. In all cases, the modified fatigue criteria are able to fit the experimental data well for all aging times.

9.5 Band of Fatigue Life

Figure 9.14 illustrates the band of fatigue life alloy with plastic strain range for SAC 105 solder alloy at different aging conditions. The width of band depends on the microstructure of material. Upper limit of the band indicates the fatigue life for water quenched SAC105 solder alloy and lower limit indicates the fatigue life of long term aged reflowed (aging for 360 days) SAC105 solder alloy. As described previously, initial

microstructure of water quenched solder alloy has very fine microstructure which is expected to have excellent fatigue resistance. As aging progresses, grain/sub-grain coarsens and IMC particles conglomerate which leads to decrease in fatigue life. Therefore, band of fatigue represents the possible region of plastic strain range where fatigue failure occurs for SAC105 solder alloy for any possible microstructure. Similar plot is shown indicating band of fatigue life for SAC305 solder alloy in Figure 9.15. Figures 9.16 and 9.17 illustrates the band of fatigue life for SAC105 and SAC305 solder alloy with plastic strain energy density at different aging conditions.

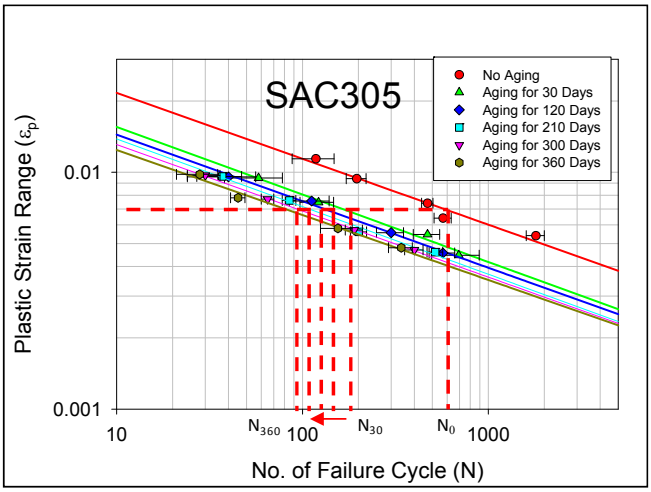

Figure 9.7 Number of Failure Cycle at Particular Strain Range for SAC305 Solder Alloy

Table 9.3 Shift Factors at Different Aging Conditions

a	N_0/N_0	N_0/N_{30}	N_0/N_{120}	N_0/N_{210}	N_0/N_{300}	N_0/N_{360}
At ε_1	1	3.401	4.367	5.24	6.34	6.72
At ε_2	1	3.663	4.484	5.352	6.43	6.79
At ε_3	1	3.484	4.296	5.135	6.29	6.6

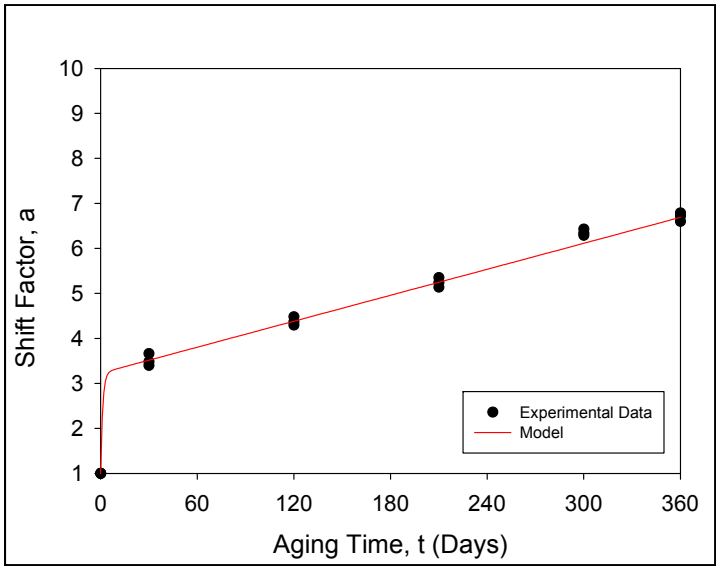

Figure 9.8 Shift Function with Aging Time for SAC305

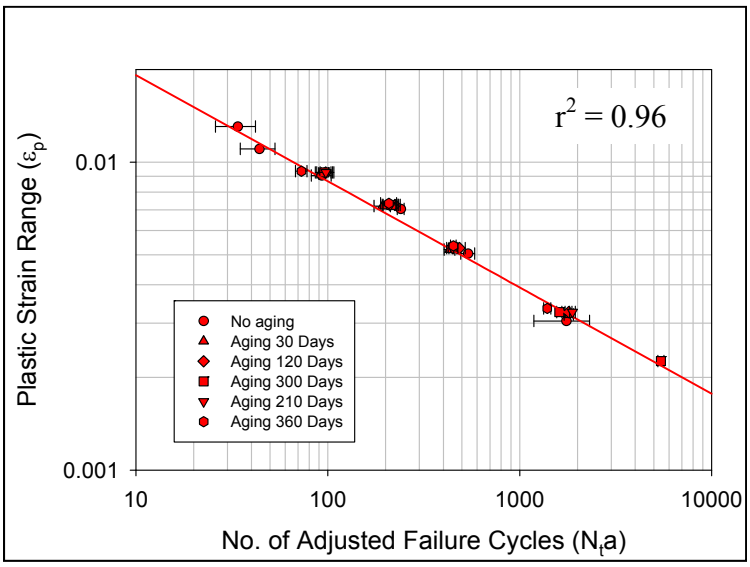

(a) SAC105

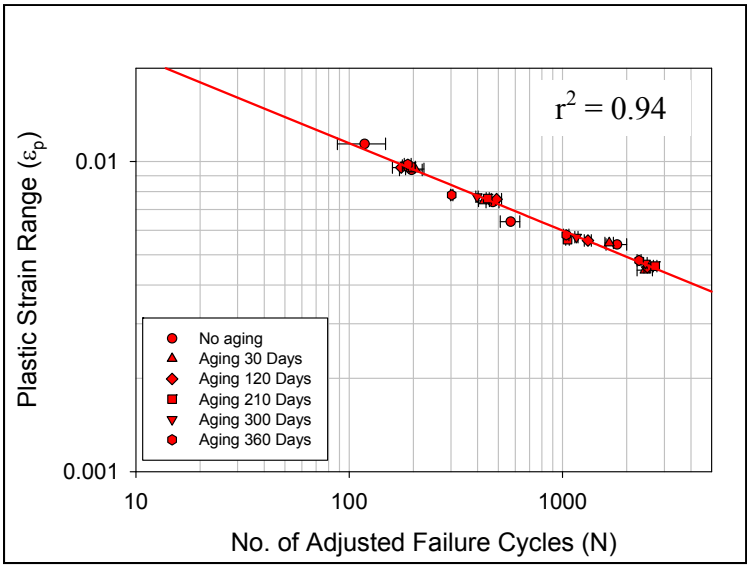

(b) SAC305

Figure 9.9 Non-linear Regression of number of Adjusted Failure Cycle Data

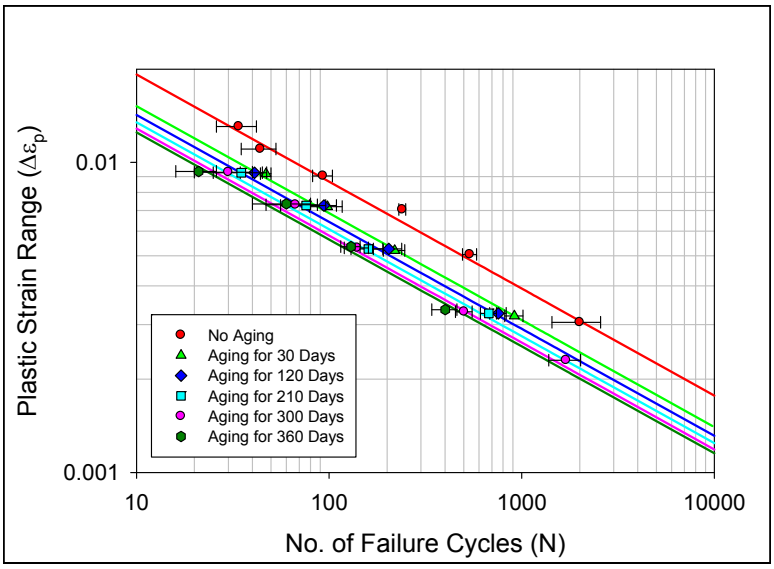

Model:

$$(N_t a)^n \Delta\varepsilon_p = C$$

$$a = A_0 + A_1 t + A_2 e^{-A_3 t}$$

Constants:

n = 0.3450
C = 0.0425
A_0 = 1.8340
A_1 = 0.00455
A_2 = -0.8340
A_3 = 0.8000

Figure 9.10 Modified Coffin-Manson Model with Shift Function for SAC105

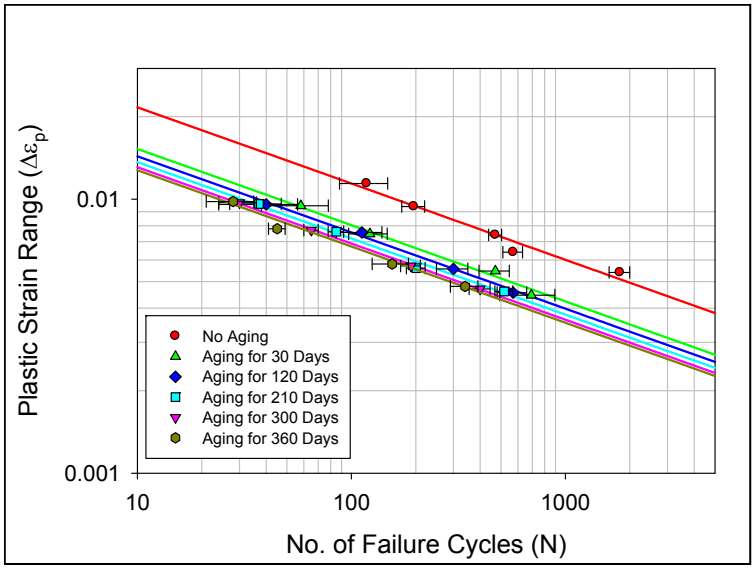

Model:

$$(N_t a)^n \Delta\varepsilon_p = C$$

$$a = A_0 + A_1 t + A_2 e^{-A_3 t}$$

Constants:

n	0.2782
C	0.0411
A_0	3.2270
A_1	0.00962
A_2	-2.2270
A_3	0.8000

Figure 9.11 Modified Coffin-Manson Model with Shift Function for SAC305

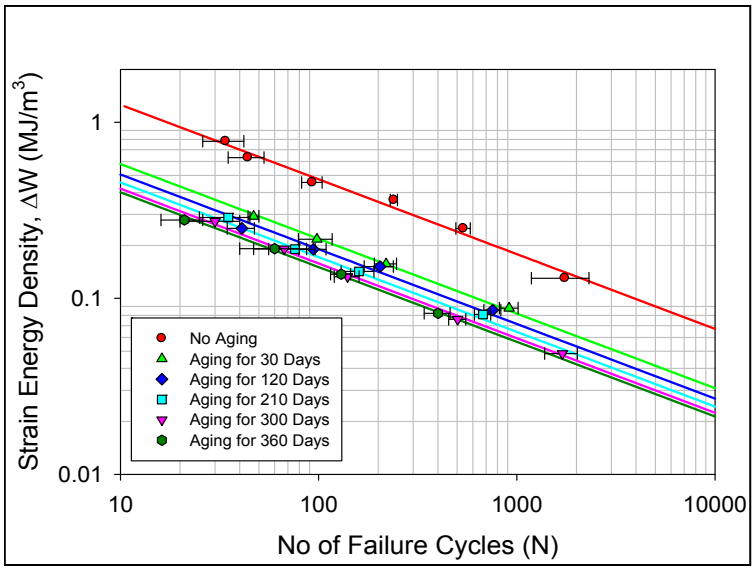

Model:

$$(N_t a)^n \Delta W = C$$

$$a = A_0 + A_1 t + A_2 e^{-A_3 t}$$

Constants:

n	0.4246
C	3.3510
A_0	5.4510
A_1	0.02625
A_2	-4.4510
A_3	0.9301

Figure 9.12 Modified Morrow Model with Shift Function for SAC105

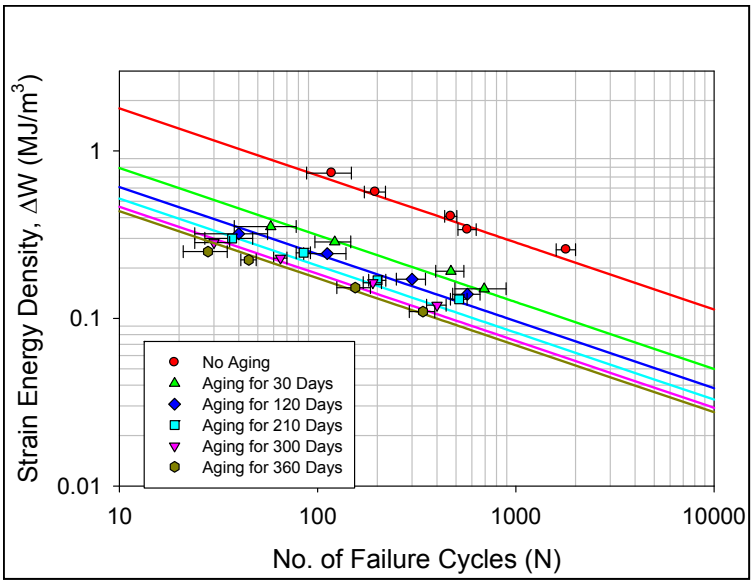

Model:

$$(N_t a)^n \Delta W = C$$

$$a = A_0 + A_1 t + A_2 e^{-A_3 t}$$

Constants:

n = 0.4000
C = 4.4504
A_0 = 5.3450
A_1 = 0.0800
A_2 = -4.3450
A_3 = 0.9301

Figure 9.13 Modified Morrow Model with Shift Function for SAC305

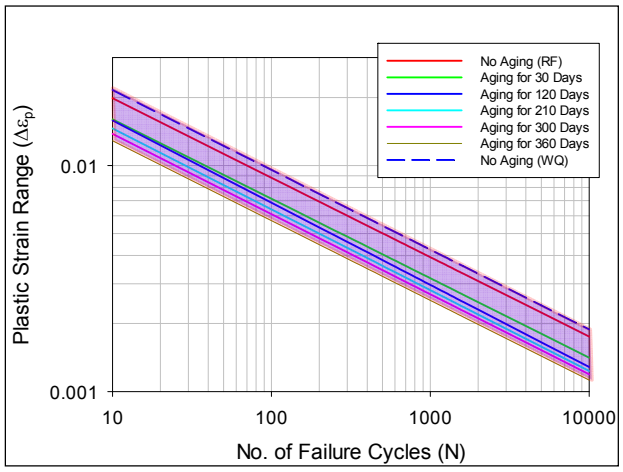

Figure 9.14 Band of Fatigue Life for SAC105 based on Plastic Strain Range

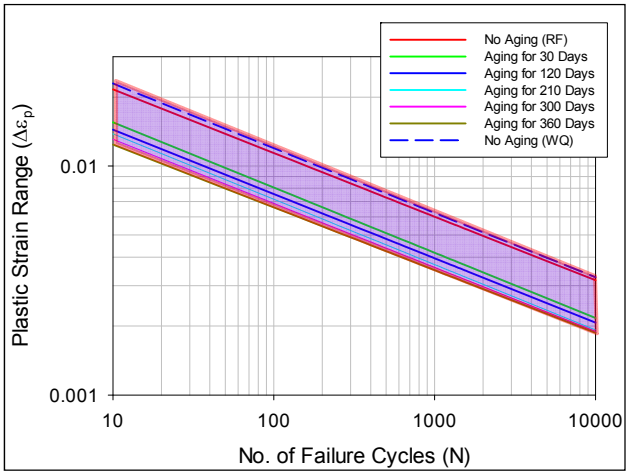

Figure 9.15 Band of Fatigue Life for SAC305 based on Plastic Strain Range

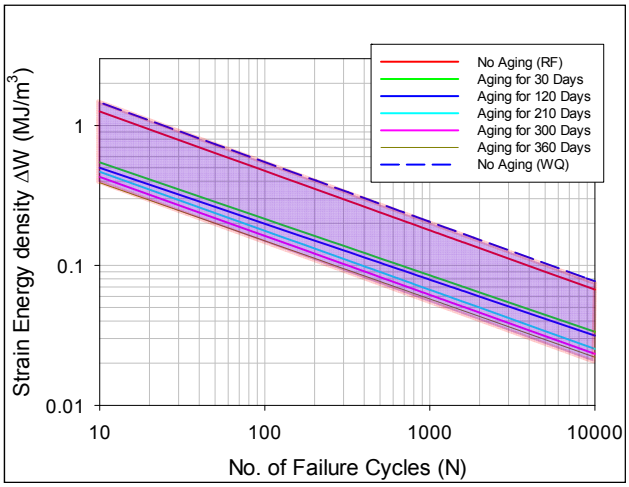

Figure 9.16 Band of Fatigue Life for SAC105 based on Plastic Strain Energy

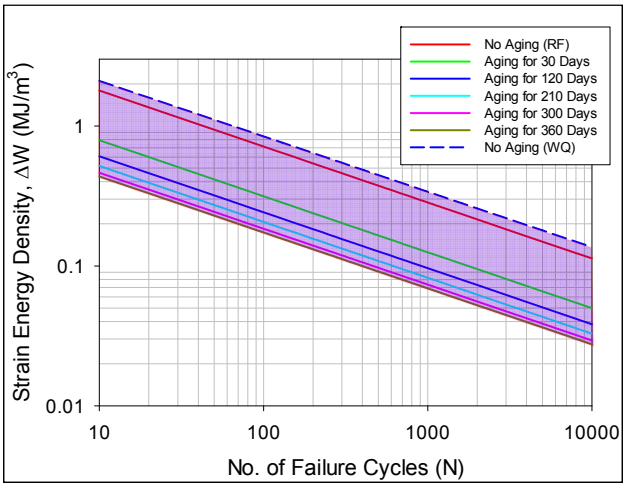

Figure 9.17 Band of Fatigue Life for SAC305 based on Plastic Strain Energy

9.6 Relation between Isothermal Fatigue Life and Thermal Fatigue Life

Thermally cycling induced solder joint fatigue is a common failure mode in electronic packaging. When subjected to temperature changes, stresses in electronic assemblies are typically developed due to the mismatches in the coefficients of thermal expansion (CTE) of the soldered components and the PCB. Mismatches in the thermal expansion coefficients of the assembly materials cause the solder joints to be subjected to thermomechanical fatigue. Therefore, it is necessary to establish a relationship between isothermal fatigue life and thermomechanical fatigue life.

Guo, et al. [65] proposed a mathematical model to predict in phase thermo-mechanical fatigue life (TMF) from isothermal fatigue life. In their investigation, TMF test was performed from 25 C to 80 C with 120 second ramp. Their relationship can be expressed as,

$$N_{f,TMF} = \frac{\Delta\sigma_{80} - \frac{4\sigma_{f80}}{\sqrt{3}}}{\Delta\sigma_{TMF} - \frac{4\sigma_{f80}}{\sqrt{3}}} \times N_{f,ISO}$$

where $N_{f,TMF}$ is number of failure cycle subjected to thermomechancial fatigue, $N_{f,ISO}$ is number of failure cycle subjected to isothermal fatigue, $\Delta\sigma_{80}$ and $\Delta\sigma_{TMF}$ are the stress range for isothermal fatigue at 80 C and thermomechanical fatigue (TMF) respectively, and σ_{f80} is flow stress at 80 C. $\Delta\sigma_{80}$ and σ_{f80} can be calculated from hysteresis loop generated during mechanical cyclic loading. The stress range, $\Delta\sigma_{TMF}$ can be obtained either isothermal fatigue at 80 C or 25 C without TMF tests. The stress range, $\Delta\sigma_{TMF}$ is approximately equal to the summation of the maximum tensile stress of isothermal fatigue at 80 C and the absolute value of the maximum compressive stress of the isothermal test at 25 C. Such a formula would be very useful if it is accurate and could be

universally applied. But no well accepted theory is available relating isothermal fatigue life to thermal fatigue life.

9.7 Application of Isothermal Fatigue Data in Reliability Prediction

Results as shown in this dissertation are isothermal tension/compression and shear fatigue. Therefore, to apply the measured results for thermal cycling induced fatigue, one must make a big assumption that the same Morrow model fatigue law and constants are valid for both situations.

In a parallel investigation, Motalab, et al. [240] developed a finite element model for reliability prediction of PBGA package assembly. In their work, the Darveaux [241] fatigue model was used to investigate aging effects on solder joint fatigue behaviors during thermal cycling. Darveaux energy dissipation based model can be written as:

$$N_f = N_i + \frac{a}{\left[\frac{da}{dN}\right]} \tag{9.35}$$

where

$$N_i = K_1(\Delta W)^{K_2} \tag{9.36}$$
$$\frac{da}{dN} = K_3(\Delta W)^{K_4}$$

Here, N_i is number of cycles to crack initiation, N_f is number of cycles to failure, and a is the fully developed crack length. It is believed from the literature that 50% drop of cyclic peak stress indicates the macro-crack initiation in the material [176]. Therefore, crack initiation data was taken from present isothermal fatigue data (see Figure 9.18). Using measured SAC305 fatigue data for different aging conditions, the evolution of reliability model parameters K_1 and K_2 with aging were determined as tabulated in Table 9.4. Empirical models for these parameters were developed, and similar to the findings for

mechanical/constitutive behavior, the values of these two parameters were affected significantly with aging. The other two reliability model parameters, K_3 and K_4 were determined from the crack growth experimental data for a 19 mm PBGA assembly. Failure data were available for this package at aging temperatures of 25, 55, 85, and 125 C, and for no aging, 6 months, and 12 months aging prior to thermal cycling. The evolution of parameters K_3 and K_4 with aging were determined from these experimental data, and the results showed that aging had significant effects on the model parameters. The reliability model parameters K_1, K_2 , K_3 and K_4 were used to estimate the life of SAC solder balls in PBGA components that were subjected to thermal cycling between -40 to 125 C in finite element analysis with various aging conditions prior to thermal cycling.

A three-dimensional finite element analysis of the 19 mm PBGA component with SAC305 interconnects was performed to calculate the stress/strain histories in the solder joints during thermal cycling accelerated life testing. Simulation of thermal cycling between -40 to 125 C was performed, and several sets of aging conditions (aging temperature and time) prior to thermal cycling were considered. For each case, the plastic energy dissipation per cycle in the critical solder ball was calculated. These values were then combined with the aging aware fatigue criterion to perform life predictions for the components with various aging conditions. The energy based criteria proposed by Darveaux was used for predicting crack initiation and crack growth in the aged solder joints using the energy dissipation values calculated from the finite element analysis. Good correlation was found between the predicted results and experimental findings for the reliability of the component as shown in Figure 9.19(a)-(b).

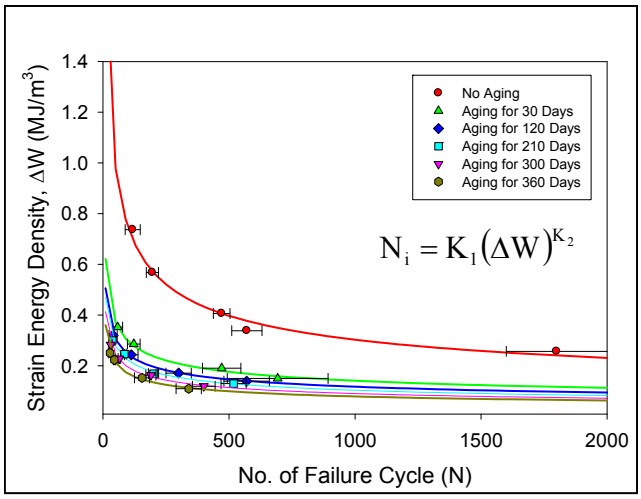

Figure 9.18 Crack Initiation Fatigue Data for SAC305

Table 9.4 Constants K_1 and K_2 for Crack Initiation

Aging Time (Days)	K_1	K_2
0	37.97	-2.8
30	3.047	-2.9
120	1.413	-3.05
210	0.647	-3.27
300	1.431	-2.66
360	0.955	-2.66

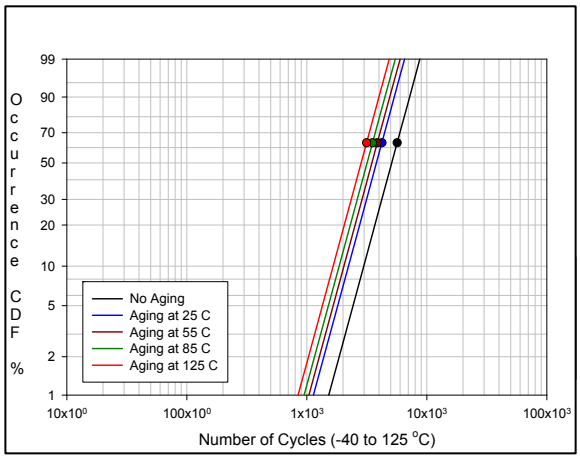

(b) Finite Element Prediction [240]

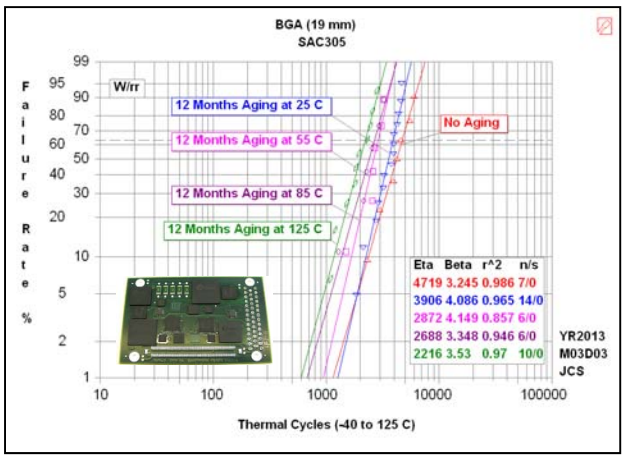

(a) Experimental Prediction [242]

Figure 9.19 Reliability Prediction of 19 mm PBGA Package

9.8 Summary and Discussion

In this chapter, microstructural damage evolution was investigated for both aged and non-aged samples for SAC105. It was observed that the crack propagation mode was changed from transgranular cracking to intergranular cracking when aging occurred. Mostly transgranular cracking was observed in non-aged samples and intergranular cracking was evident in aged samples. Many small recrystallized grains were found around the crack tips in non-aged samples and a few large irregularly shaped recrystallized grains were observed around crack tips in aged samples.

The Coffin-Manson model and Morrow model were modified using a microstructural adaptive shift function including aging effects. A mathematical technique was developed to determine the four constants in the shift function. Application of isothermal fatigue data to reliability prediction of 19 mm PBGA packages was discussed and results from the parallel investigations were summarized. There have been no universally applicable models presented in the literature for relating isothermal fatigue life, and thermomechanical fatigue life.

CHAPTER 10

SUMMARY AND CONCLUSIONS

10.1 Empirical Model for Uniaxial and Cyclic Stress-strain Behavior for Solder Material

In Chapter 4, a four-parameter hyperbolic tangent model is developed to represent experimental data of uniaxial and cyclic stress-strain of viscoplastic solder materials. Other unified empirical models for uniaxial and cyclic stress-strain behavior available in the literature are also discussed in this chapter. Comparisons are made between proposed four-parameter hyperbolic tangent model and other empirical models and based on r^2value of non-linear regression fit, four-parameter hyperbolic tangent is superior to represent the experimental data of viscoplastic solder materials. A mathematical technique is also developed to calculate the area of hysteresis loop generated during cyclic loading which indicates the energy dissipation per cycle due to damage accumulation, crack initiation and crack propagation.

10.2 Effects of Aging on Cyclic Stress-strain behavior for Lead-free Solder Materials

In Chapter 5, the effects of several parameters (aging, temperature, strain/stress limits, and solder alloy composition) on the cyclic stress-strain behavior of lead free solders have been investigated. Uniaxial SAC lead free solder specimens were subjected to cyclic (tension/compression) mechanical loading. Samples were cyclically loaded

under both strain control (constant positive and negative strain limits) and stress control (constant positive and negative stress limits). The hysteresis loop size (area) was calculated from the measured cyclic stress-strain curves for a given solder alloy and temperature. This area represents the strain energy density dissipated per cycle, which can be typically correlated to the damage accumulation in the solder material. Also plastic strain is related to movement of dislocation and cyclic stress is related to resistance of dislocation motion.

SAC105 lead free solder specimens were subjected to both strain controlled and stress controlled cyclic loading. It was observed that the hysteresis loop area changes significantly with aging, and mathematical models have been found to fit the aging induced evolution. For strain controlled cyclic testing, the hysteresis loop size decreases with aging time, while for stress controlled cyclic testing the hysteresis loop size increases with aging time. These phenomena have been explained through comparison to the aging induced degradation of the yield stress and ultimate strength extracted from the standard (non-cyclic) stress-strain curves for SAC solders and also based on theory of dislocation movement and resistance to dislocation motion.

Preliminary studies have also been made of the effects of solder composition on the cyclic stress-strain behavior by testing four SAC alloys (SAC105, SAC205, SAC305, SAC405) with varying silver content (1-4%) under strain controlled cycling. In addition, the effect of the testing temperature has also been studied by performing cyclic testing of SAC405 samples at four different temperatures (25, 50, 75, and 100 C). As expected, larger hysteresis loops were found for the lower silver content alloys and for higher

testing temperatures under stress controlled cyclic tests. Smaller hysteresis loops were found for higher temperature under strain controlled cyclic tests.

10.3 Effects of Aging on Fatigue behavior for Lead-free Solder Materials

In Chapter 6, the effects of aging on the fatigue behavior of lead free solders were investigated. Uniaxial SAC105 and SAC305 lead free solder specimens were subjected to cyclic (tension/compression) mechanical loading under strain control (constant positive and negative strain limits) until failure occurred. For both alloys, the fatigue data expressed as plastic strain change vs. cycles to failure demonstrated a nearly linear variation for all aging conditions when graphed on a log-log scale. This suggests that the Coffin-Manson fatigue law can accurately represent the data for the various aging conditions, and the largest shift in the fatigue curves occurred in the first 30 days of aging. While the slopes of the fatigue curves are nearly constant for each SAC alloy taken individually, they are different for the 2 alloy systems. A clear progression of the fatigue curves was observed with longer aging times prior to mechanical cycling. The fatigue data was also recast in terms of the energy dissipated per cycle (ΔW) in the first cycle hysteresis loop. The fatigue curves in this case were found to be well fit by the Morrow energy-based fatigue law for all aging conditions. Effects of solidification temperature profile and silver content on fatigue behavior of SAC alloys are also discussed. High silver content SAC alloy exhibits excellent fatigue resistance for both aged and non-aged conditions.

10.4 Shear Specimen Preparation and Development of Experimental Set-up

In chapter 7, a comparative study is carried out in finite element analysis considering ball shear, simple lap shear and Iosipescu shear test in this chapter. It has been investigated that ball shear test is not suitable to measure constitutive properties of pure shear of solder material. It is evident that Iosipescu design in the copper end pieces helps to provide a more uniform state of shear and also measure constitutive properties of pure shear of solder material. Finite element analysis has shown that decreasing the solder layer thickness helps to reduce stress concentration factor in the solder layer.

A quick, repeatable and novel method is developed to prepare Iosipescu shear specimen. A complete Iosipescu shear specimen assembly as used in this work is shown in this chapter. The copper end pieces are 13 x 5 x 3 mm, with 45º angular cuts. They are joined together by the 3 x 3 x 0.25 mm solder layer to be tested. During assembly, the two copper end pieces are placed into an aluminum mold with the wedge shaped ends facing each other. The mold is sized so that there is a nominal 0.25 mm clearance between the copper pieces, which is just big enough for the thin solder layer preform to fit. A spring-loaded lid is also used so that the solder perform is maintained under a small pressure during solidification. The whole mold assembly is sent through a reflow oven to melt the solder preform between the copper end pieces in the mold, and subject it to a desired temperature profile.

Shear fixtures are designed and manufactured to grip the Iosipescu shear specimen in the experimental set up. Experimental and mathematical technique has been developed for load train calibration. A four-parameter hyperbolic tangent model was again used to represent cyclic shear stress strain data for solder.

10.5 Effects of Aging on Shear Cyclic Stress-Strain and Fatigue Behaviors for Lead-free Solder Materials

In Chapter 8, the effects of aging on the cyclic shear stress-strain and fatigue behaviors of lead free solder joints are investigated. Iosipescu shear specimens for SAC105 solder are subjected to mechanical cyclic loading. It is observed that the shear hysteresis loop area changes significantly with aging, and mathematical models have been found to fit the aging induced evolution. For strain controlled cyclic testing, the shear hysteresis loop size decreases with aging time. These phenomena have been explained through comparison to the aging induced degradation of the yield stress and ultimate shear strength and microstructural damage accumulation.

The fatigue data expressed as plastic shear strain change vs. cycles to failure demonstrated a nearly linear variation for all aging conditions when graphed on a log-log scale. This suggests that the Coffin-Manson fatigue law can accurately represent the data for the various aging conditions, and the largest shift in the fatigue curves occurred in the first 30 days of aging. A clear progression of the fatigue curves was observed with longer aging times prior to mechanical cycling. The fatigue data was also recast in terms of the energy dissipated per cycle (ΔW) in the first cycle shear hysteresis loop. The fatigue curves in this case were found to be well fit by the Morrow energy-based fatigue law for all aging conditions.

A comparison of the low-cycle fatigue results of both bulk solder materials (uniaxial fatigue results) and solder joints (shear fatigue results) is made by calculating the equivalent von Mises strains and by plotting them in the same graph. It has been shown that uniaxial fatigue data and shear fatigue data for SAC105 are in good

agreement. This suggests that from uniaxial fatigue life for bulk solder, solder joint fatigue life can be estimated.

10.6 Microstructure Based Fatigue Model including Aging Effects

In Chapter 9, microstructural damage evolution has been investigated for both aged and non-aged sample for SAC105. It is observed that crack propagation mode is changed from transgranular cracking to intergranular cracking. Mostly transgranular cracking is observed in non-aged sample whereas; intergranular cracking is evident in aged sample. Many small recrystallized grains is found around crack tip in non-aged sample and few large irregularly shaped recrystallized grains is observed around crack tip in aged sample. Coffin-Manson model and Morrow model is modified using microstructural adaptive shift function including aging effects. A mathematical technique is developed to determine the constants of shift function. Application of isothermal fatigue data to reliability prediction of PBGA package is discussed from parallel investigations.

10.7 Conclusions

The main conclusions from this work are:

1. Isothermal aging affects both uniaxial and shear fatigue life of lead free solders.
2. Stress strain behavior of each cycle can modeled using four parameter hyperbolic tangent model.
3. During strain controlled cyclic tests, the hysteresis loop size decreases with aging time whereas, during stress controlled cyclic tests, the hysteresis loop size increases with aging time.

4. Both Coffin-Manson and Morrow model can be used to fit the experimental fatigue data.
5. A significant drop in the fatigue life has been found within the first 30 days of aging and degradation continues for other aging times.
6. A Good correlation has been established between uniaxial fatigue data and shear fatigue data.
7. Transgranular cracking has been found in non-aged sample whereas, intergranular cracking has been found in aged sample.
8. Microstructure adaptive fatigue failure model has been developed including aging induced shift function.
9. Entire fatigue region has been established for lead free solders which is helpful for packaging design engineers.

REFERENCES

[1] Environmental Concepts Inc., News Released in 1997, A History of Lead, http://www.gate.net/~verstraa/history.htm.

[2] Vianco, T. P., "Development of Alternatives to Lead-bearing Solders," Proceedings of the Technical Program on Surface Mount International, San Jose, CA, 1993.

[3] Reed-Hill, R. E., Physical Metallurgy Principles, PWS Publishing Company, pp. 306-307, 1994.

[4] Wood, E. P., Nimmo, K. L. "In Search of New Lead-free Electronic Solders," Journal of Electronic Materials, Vol. 23(8), pp. 709-713, 1994.

[5] Hwang, J. S., Implementing Lead-Free Electronics, McGraw-Hill, 2004.

[6] Turbini, L. J., Munie, G. C., Bernier, D., Gamalski, J., Bergman, D. W., "Examining the Environmental Impact of Lead-free Soldering Alternatives," IEEE Transactions on Electronics Packaging Manufacturing, Vol. 24, pp. 4-9, 2001.

[7] IPC Roadmap: A Guide for Assembly of Lead-Free Electronics, IPC, Northbrook, IL, 2000.

[8] "Directive 2002/95/EC of the European Parliament and of the Council 27 January 2003 on the Restriction of the Use of Certain Hazardous Substances in Electrical and Electronic Equipment," Official Journal of the European Union, Vol. 37, pp. 19-23, February 13, 2003.

[9] "Directive 2002/95/EC of the European Parliament and of the Council 27 January 2003 on Waste Electrical and Electronic Equipment," Official Journal of the European Union, Vol. 37, pp. 24-38, February 13, 2003.

[10] Japan Electronics and Information Technology Industries Association, News Released in 2002, Framework of the World Lead-free Soldering Roadmap, http://www.jeita.or.jp/english/press/2002/1217/attached.htm.

[11] Qian, Z., Abhijit, D., Peter, H., "Creep and High-temperature Isothermal Fatigue of Pb-free Solders," Proceedings of InterPACK 2003, pp. 955-960, 2003.

[12] Abtew, M., Selvaduray, G., "Lead-free Solders in Microelectronics," Materials Science and Engineering Reports, Vol. 27, pp. 95-141, 2000.

[13] The Ames Laboratory, US Department of Energy, Alternatives to Lead Based Solders, http://www.ameslab.gov/files/LeadFreeSolder_Foundation.pdf

[14] Furusawa, A., Suetsugu, K., Yamaguchi, A., Taketomo, H., "Thermoset Pb-Free Solder Using Heat-Resistant Sn-Ag Paste," National Technical Report, 1997.

[15] Nimmo, K., "Alloy Selection," Chapter 3 of Lead-free Soldering in Electronics: Science, Technology and Environmental Impact, edited by K. Suganuma, New York, Marcel Dekker, pp. 61-62, 2004.

[16] Bradley, E., "Lead-Free Solder Assembly," 53rd Electronic Components and Technology Conference, New Orleans, LA, pp. 41-46, 2003.

[17] Loomans, M. E., Fine, M. E., "Tin-Silver-Copper Eutectic Temperature and Composition," Metallurgical and Materials Transactions A, Vol. 31(A), pp. 1155-1162, 2000.

[18] Moon, K. W., Boettinger, W. J., Kattner, U. R., Biancaniello, F. S., Handwerker, C. A., "Experimental and Thermodynamic Assessment of Sn-Ag-Cu Solder Alloys," Journal of Electronic Materials, Vol. 29, pp. 1122-1136, 2000.

[19] Zhu, Q. S., Zhang L., Wang Z. G., Wu S. D., Shang J. K., "Effect of Intermetallics Ag_3Sn on the Tensile Property of Sn3.8Ag0.7Cu Solder Alloy," Acta Metallurgica Sinica, Vol. 43(1), pp. 41-46, 2007.

[20] Ganesan, S., Pecht, M., Lead-free Electronics, Wiley-Interscience Publication, pp. 51-52, 2006.

[21] Cai, Z., Reduction of Lead Free Solder Aging Effects Using Dopped SAC Alloys, PhD Dissertation, Auburn University, 2012.

[22] Pirondi, A., "Mechanical Failure in Microelectronic Packaging," Vol. IGF 13, Convegno IGF XIII Cassino, 1997.

[23] Hertzberg, R. W., Deformation and Fracture Mechanics of Engineering Materials, John Wiley & Sons Inc, 4th edition, 1996.

[24] Vianco P. T., "Fatigue and Creep of Lead-free Solder Alloys: Fundamental Properties," Chapter 3 of Lead-free Solder Interconnect Reliability, Edited by D. Shangguan, ASM International, pp. 67-106, 2006.

[25] Wiese, S., Schubert, A., Walter, H., Dudek, R., Feustel, F., Meusel, E., Michel, B., "Constitutive Behavior of Lead-free Solders vs. Lead-containing Solders - Experiments on Bulk Specimens and Flip-Chip Joints," Proceeding of the 51st Electronic Components and Technology Conference, pp. 890-902, 2001.

[26] McCabe, R. J., Fine, M. E., "Athermal and Thermally Activated Plastic Flow in Low Melting Temperature Solders at Small Stresses," Scripta Materialia, Vol. 39(2), pp. 189-195, 1998.

[27] Lau, J. H., Pao, Y. H., Solder Joints Reliability of BGA, CSP, Flip-Chip, and Fine Pitch SMT Assemblies, McGraw-Hill, 1997.

[28] Shi, X.Q., Wang, Z. P., Yang, J. Q., Pang, H. L. J., "Creep Behavior and Deformation Mechanism Map of Sn-Pb Eutectic Solder Alloy," Journal of Engineering and Material Technology. Vol. 125(1), pp. 81-89, 2003

[29] Evans, R. W., Wilshire, B., Creep of Metals and Alloys, the Institute of Metals, 1985.

[30] Weertman, J., "Steady-State Creep through Dislocation Climb," Journal of Applied Physics, Vol. 28, pp. 362-366, 1957.

[31] Herring, C., "Diffusional Viscosity of a Polycrystalline Solid," Journal of Applied Physics, Vol.21, pp. 437-445, 1950.

[32] Engelmaier, W., "Surface Mount Solder Joint Reliability: Issues, Design, Testing, Prediction," Workshop Notes, Engelmaier Associates, Inc., Mendham, NJ, 1995.

[33] Kilinski, T. J., Lesniak, J. R., Sandor, B. I., "Modern Approaches to Fatigue Life Prediction of SMT Solder Joints," Solder Joint Reliability Theory and Applications, Edited by J. H. Lau, Chapter 13, Van Nostrand Reinhold, 1991.

[34] Christensen, R. H., "Fatigue Cracking, Fatigue Damage, and Their Detection," Metal Fatigue, Edited by Sines, G. and Waisman, J. L., McGraw-Hill Book Co., New York, pp. 376. 1959.

[35] Bauschinger, J., "On the Change of the Position of the Elastic Limit of Iron and Steel under Cyclic Variations of Stress," Mitt Mech-Tech Lab, Munich, Vol. 13, No. 1, 1886.

[36] Morrow, J., "Cyclic Plastic Strain Energy and Fatigue of Metals," Internal Friction, Damping and Cyclic Plasticity, STP 378, ASTM, West Conshohocken, PA, pp. 45, 1965.

[37] Medvedev, A. S., "Aging of Tin-Lead Solders and Joints Soldered by Them," Metallovedenie i Obrabotka Metallov, No. 7, pp. 16-23, 1956.

[38] Lampe, B. T. "Room Temperature Aging Properties of Some Solder Alloys," Welding Journal, Vol. 55(10), pp. 330-340, 1976.

[39] Ding, Y., Wang, C., Li, M., and Bang, H. S., "Aging Effects on Fracture Behavior of 63Sn37Pb Eutectic Solder During Tensile Tests Under the SEM," Materials Science and Engineering, Vol. A384, 314-323, 2004.

[40] Xiao, Q., Bailey, H. J, Armstrong, W. D., "Aging Effects on Microstructure and Tensile Property of Sn3.9Ag0.6Cu Solder Alloy," Journal of Electronic Packaging, Vol. 126(2), pp. 208-212, 2004.

[41] Ma, H., Suhling, J. C., Zhang, Y., Lall, P., Bozack, M. J. "The Influence of Elevated Temperature Aging on Reliability of Lead Free Solder Joints," Proceedings of the 57th Electronic Components and Technology Conference, pp. 653-668, 2007.

[42] Zhang, Y. F., Cai, Z. J., Suhling, J. C., Lall, P., Bozack, M. J., "The Effects of SAC Alloy Composition on Aging Resistance and Reliability," Proceedings of the 59th Electronic Components and Technology Conference, pp. 370-389, 2009.

[43] Chen, W. M., McCloskey, P., O'Mathuna, S. C., "Isothermal Aging Effects on the Microstructure and Solder Bump Shear Strength of Eutectic Sn37Pb And Sn3.5Ag Solders," Microelectronics Reliability, Vol. 46(5-6), pp. 896-904, 2006.

[44] Kim, K. S., Yu, C. H., Yang, J. M., "Aging Treatment Characteristics of Solder Bump Joint for High Reliability Optical Module," Thin Solid Films, Vol. 462-463, pp. 402-407, 2004.

[45] Anderson, I. E., Harringa, J. L., "Elevated Temperature Aging of Solder Joints Based on Sn-Ag-Cu: Effects on Joint Microstructure and Shear Strength," Journal of Electronic Materials, Vol. 33(12), pp. 1485-1496, 2004.

[46] Xiao, Q., Nguyen, L., Armstrong, W. D., "Aging and Creep Behavior of Sn3.9Ag0.6Cu Solder Alloy," Proceedings of the 54th Electronic Components and Technology Conference, pp. 1325-1332, 2004.

[47] Mysore, K., Chan, D., Bhate, D., Subbarayan, G., Dutta, I., Gupta, V., Zhao, J. H., Edwards, D. R., "Aging-Informed Behavior of Sn3.8Ag0.7Cu Solder Alloys," Thermal and Thermomechanical Phenomena in Electronic Systems, ITHERM, pp.870-875, 2008.

[48] Chavali, S., Singh, Y., Kumar, P., Subbarayan, G., Dutta, I., Edwards, D. R., "Aging Aware Constitutive Models for SnAgCu Solder Alloys," Proceedings of the 61st Electronic Components and Technology Conference, pp.701-705, 2011.

[49] Chou, G. J. S., "Microstructure Evolution of SnPb and SnAgCu BGA Solder Joints During Thermal Aging," Proceedings of the 8th Symposium on Advanced Packaging Materials, pp. 39-46, 2002.

[50] Hasegawa, K., Noudou, T., Takahashi, A., and Nakaso, A., "Thermal Aging Reliability of Solder Ball Joint for Semiconductor Package Substrate," Proceedings of the 2001 SMTA International, pp.1-8, 2001.

[51] Chiu, T. C., Zeng, K., Stierman, R., Edwards, D., and Ano, K., "Effect of Thermal Aging on Board Level Drop Reliability for Pb-free BGA Packages," Proceedings

of the 54th Electronic Components and Technology Conference, pp. 1256-1262, 2004.

[52] Pang, J. H. L., Low, T. H., Xiong, B. S., Xu, L., and Neo, C. C., "Thermal Cycling Aging Effects on Sn–Ag–Cu Solder Joint Microstructure," Thin Solid Films, Vol. 462-463, pp. 370-375, 2004.

[53] Ma, H., Suhling, J. C., Lall P., Bozack, M. J., "Reliability of the Aging Lead-free Solder Joint," Proceeding of the 56th Electronic Components and Technology Conference, San Diego, California, pp. 849-864, 2006

[54] Zhang, Y., Cai, Z., Suhling, J. C., Lall, P., and Bozack, M. J., "The Effects of Aging Temperature on SAC Solder Joint Material Behavior and Reliability," Proceedings of the 58th IEEE Electronic Components and Technology Conference, pp. 99-112, Orlando, FL, May 27-30, 2008.

[55] Cai, Z., Zhang, Y., Suhling, J. C., Lall, P., Johnson, W., Bozack, M. J., "Reduction of Lead Free Solder Effects using Doped SAC Alloys," Proceedings of the 60th IEEE Electronic Components and Technology Conference, pp. 1493-1511, 2010.

[56] Motalab, M., Cai, Z., Suhling, J., Zhang, J., Evans, J., Bozack, M. J., Lall, P., "Improved Predictions of Leadfree Solder Joint Reliability that Include Aging Effects," Proceedings of the 62nd IEEE Electronic Components and Technology Conference, pp. 513-531, 2012.

[57] Mohammad Hasnine, Muhannad Mustafa, Jeffrey C. Suhling, Barton C. Prorok, Michael J. Bozack, Pradeep Lall, "Characterization of Aging Effects in Lead Free Solder Joints using Nanoindentation," Proceedings of the 63rd Electronic Components and Technology Conference, Las Vegas, Nevada, pp. 166-178, May 28-31, 2013.

[58] Hu, Q., Lee, Z. S., Zhao, Z. I., Lee, D. L., "Study of Cooling Rate on Lead-Free Soldering Microstructure of Sn-3.0Ag-0.5Cu Solder," Proceedings of International Conference on Asian Green Electronics, pp. 156-160, 2005.

[59] Jeong, S. W., Kim, J. H., Lee, H. M., "Effect of Cooling Rate on Growth of the Intermetallic Compound and Fracture Mode of Near-Eutectic Sn-Ag-Cu/Cu Pad: Before and After Aging," Journal of Electronic Materials, Vol. 33(12), pp. 1530-1544, 2004.

[60] Liang, J., Dariavach, N., Shangguan, D., "Solidification Condition Effects on Microstructures and Creep Resistance of Sn-3.8Ag-0.7Cu Lead-Free Solder," Metallurgical and Materials Transactions A, Vol. 38(7), pp. 1530-1538, 2007.

[61] Anand, L., "Constitutive Equations for the Rate-Dependent Deformation of Metals at Elevated Temperatures," Journal of Engineering Materials and Technology, Vol. 104, pp. 12-17, 1982.

[62] Pang, J. H. L., Xiong, B. S., Che, F. X., "Modeling Stress Strain Curves For Lead-Free 95.5Sn-3.8Ag-0.7Cu Solder," Proceedings of the 5th EuroSimE Conference, pp. 449-453, 2004.

[63] Nie, X., Bhate, D., Chan, D., Chen, W., Subbarayan, G., Dutta, I., "Rate-Dependent Behavior of Sn3.8Ag0.7Cu Solder over Strain Rates of 10^{-6} to 10^{2} s^{-1}," Proceedings of ITherm, pp. 676-682, 2008.

[64] Solomon, H. D., "Creep Strain Rate Sensitivity and Low Cyclic Fatigue of 60/40 Solder," Brazing and Soldering, Vol. 11, pp. 68-75. 1986,

[65] Guo, Q., Cutiongco, E. C., Keer, L. M., and Fine, M. E., "Thermomechanical Fatigue Life Prediction of 63Sn/37Pb Solder," Journal of Electronic Packaging, Vol. 114, pp.145-151, 1992.

[66] Busso, E. P., Kitano, M., and Kumazawa, T., "A Visco-plastic Constitutive Model for 60/40 Tin-lead Solder used in IC Package Joints," Journal of Engineering Materials Technology, Vol. 114, pp. 333-337, 1992.

[67] Frear, D. R., Burchett, S. N., Neilsen, M. K., and Stephens, J. J., "Microstructurally Based Finite Element Simulation of Solder Joint Behavior," Soldering and Surface Mount Technology, Vol. 2, pp. 39-42, 1997.

[68] McDowell, D. L., Miller, M. P., and Brooks, D.C., "A Unified Creep-Plasticity Theory for Solder Alloys," Fatigue of Electronic Materials, ASTM STP, Vol. 1153, pp. 42-59, 1994.

[69] Lau, J. H. (Ed.), Solder Joint Reliability, Theory and Applications, Van Nostrand Reinhold, New York, 1991.

[70] Shi, X. Q., Zhou, W., Pang, H. L. J., and Wang, Z. P., "Effect of Temperature and Strain Rate on Mechanical Properties of 63Sn/37Pb Solder Alloy." Journal of Electronic Packaging, Vol. 121, pp. 179-185, 1999.

[71] Yang, X. J., Chow, C. L., and Lau, K. J., "Time Dependent Cyclic Deformation and Failure of 63Sn/37Pb Solder Alloy," International Journal of Fatigue, Vol. 25, pp. 533-546, 2003.

[72] Hall, P. M., "Forces, Moments, and Displacements During Thermal Chamber Cycling of Leadless Ceramic Chip Carriers Soldered to Printed Boards," IEEE Transactions on Components, Hybrids, and Manufacturing Technology, Vol. 7(4), pp. 314-327. 1984.

[73] Hall, P. M., "Creep and Stress Relaxation in Solder Joints of Surface Mounted Chip Carriers," IEEE Transactions on Components, Hybrids and Manufacturing Technology, Vol. 12(4), pp. 556-565, 1987

[74] Pao, Y.-H., Badgley, S., Govila, R. and Jih, E., "An Experimental and Modeling Study of Thermal Cyclic Behavior of Sn–Cu and Sn–Pb Solder Joints," Proceedings of the Materials Research Society Symposium, Vol. 226, pp. 153-158, 1994.

[75] Pao, Y.-H., Chen, K. L. and Kuo, A. Y., "A Nonlinear and Time Dependent Finite Element Analysis of Solder Joints in Surface Mounted Components under Thermal Cycling," Proceedings of the Materials Research Society Symposium, Vol. 226, pp. 23-28, 1991.

[76] Pao, Y.-H., Govila, R., Badgley, S. and Jih, E., "An Experimental and Finite Element Study of Thermal Fatigue Fracture of Pb-Sn Solder Joints," Journal of Electronic Packaging, Vol. 115, pp. 1-8, 1993.

[77] Haacke, P. Sprecher, A. F. and Conrad, H., "Computer Simulation of Thermomechanical Fatigue of Solder Joints Including Microstructural Coarsening," Journal of Electronic Packaging, Vol. 115, pp. 153-158, 1993.

[78] Raeder, C. H., Felton, L. E., Messler, R. W., and Coffin, L. F., "Thermomechanical Stress-Strain Hysteresis of Sn-Bi Eutectic Solder Alloy," Proceedings of the IEEE International Electronics Manufacturing Technology Symposium, pp. 263-268, 1995.

[79] Dusek, M., and Hunt, C., "Low Cycle Isothermal Fatigue Properties of Lead-free Solders," Soldering and Surface Mount Technology, pp. 25-32, 2007.

[80] Hu, B., Zhou, J., Yang, Y., Wan, F., "The Effect of Temperature on Low Cycle Fatigue of an Eutectic Solder," Proceeding of International Conference on Electronic Materials and Packaging, pp. 1-5, 2006.

[81] Shi, X. Q., Pang, H. L. J., Zhou, Wang, Z. P., "A Modified Energy-Based Low Cycle Fatigue Model For Eutectic Solder Alloy," Scripta Materialia, Vol. 41(3), pp. 289-296, 1999.

[82] Herkommer, D., Punch, J. and Reid, M., "A Reliability Model for SAC Solder Covering Isothermal Mechanical Cycling and Thermal Cycling Conditions," Journal of Microelectronics Reliability, Vol. 50, pp. 116-126, 2010.

[83] Zhang, Q. and Dasgupta, A., "Constitutive and Durability Properties of Selected Lead-Free Solders," Pb-Free Electronics, Chapter 6, Edited by M. Pecht and S. Ganesan, 2nd Edition, Wiley, 2006.

[84] Zhang, Q., Dasgupta, A. and Haswell, P., "Isothermal Mechanical Durability of Three Selected Pb-Free Solders: Sn3.9Ag0.6Cu, Sn3.5Ag, and Sn0.7Cu," Journal of Electronic Packaging, Vol. 127(4), pp. 512-522, 2005.

[85] Whitelaw, R. S., Neu, R. W. and Scott, D. T., "Deformation Behavior of Two Lead-Free Solders: Indalloy 227 and Castin Alloy," Journal of Electronic Packaging, Vol. 121(2), pp. 99-107, 1999.

[86] Korhonen, T. K., Lahman, P. L., Korhonen, M. A. and Henderson, W. D., "Isothermal Fatigue Behavior of the Near Eutectic Sn-Ag-Cu Alloy Between -25 ºC and 125 ºC," Journal of Electronic Materials, Vol. 36(2), pp. 173-178, 2007.

[87] Kanchanomai, C., Miyashita, Y., Mouth, Y. and Mannan, S. L., "Low Cycle Fatigue and Fatigue Crack Growth Behaviour of Sn-Ag Eutectic Solder," Soldering and Surface Mount Technology, Vol. 14(3), pp. 30-36, 2002.

[88] Shang, J. K., Zeng, Q. L., Zhang, L. and Zhu, Q. S., "Mechanical Fatigue of Sn-rich Pb-Free Solder Alloys," Journal of Material Science: Materials in Electronics, Vol. 18, pp. 211-227, 2007.

[89] Andersson, C., Lai, Z., Liu, J., Jiang, H. and Yu, Y., "Comparison of Isothermal Mechanical Fatigue Properties of Lead-Free Solder Joints and Bulk Solders," Material Science and Engineering A, Vol. 394, pp. 20-27, 2005.

[90] Pang, J. H. L., Xiong, B. S. and Low, T. H., "Low Cycle Fatigue Models for Lead-Free Solders," Journal of Thin Solid Films, Vol. 462-463, pp. 408-412, 2004.

[91] Kanda, Y., Kariya, Y., Oto, Y., "Influence of Cyclic Strain-Hardening Exponent on Fatigue Ductility Exponent for a Sn-Ag-Cu Micro-Solder Joint," Journal of Electronic Materials, Vol. 41, No. 3, pp. 580-587, 2012.

[92] Kim, I., Lee, S., "Fatigue Life Evaluation of Lead-free Solder under Thermal and Mechanical Loads," Proceedings of the 57th IEEE Electronic Components and Technology Conference, pp. 95-104, 2007.

[93] Chen, X., Song, J., Kim, K. S., "Fatigue Life of 63Sn-37Pb Solder Related to Load Drop Under Uniaxial and Torsional Loading," International Journal of Fatigue, Vol. 28, pp. 767-776, 2006.

[94] Sun, P., Andersson, C., Wei, X., Cheng, Z., Shangguan, D., Liu, J., "Coffin-Manson Constant Determination for a Sn-8Zn-3Bi Lead-free Solder Joint," Soldering and Surface Mount Technology, Vol. 18 (2), pp. 4-11, 2006.

[95] Fossum, A. F., Vianco, P. T., Neilsen, M. K., Pierce, D. M., "A Practical Viscoplastic Damage Model for Lead-free Solder," Journal of Electronic Packaging, Vol. 128 pp. 71-81, 2006.

[96] Takahashi, T., Hioki, S., Shohji, I., Kamiya, O., "An Evaluation of Fatigue Damage in Low-Cycle Range for Sn-3.5Ag, Sn-0.7Cu Lead-free Solders and Sn-Pb Eutectic Solder Using Image Processing to Surface Fracture," Proceedings of InterPACK 2005, pp. 1-7, 2005.

[97] Andersson, C., Sun, P., Liu, J., "Low Cycle Fatigue of Sn-based Lead-free Solder Joints and the Analysis of Fatigue Life Prediction Uncertainty," Proceedings of High Density Microsystem Design and Packaging and Component Failure Analysis conference, pp. 272-279, 2006.

[98] Lee, K. O., Yu, J., Park, T. S., Lee, S. B., "Low-Cycle Fatigue Characteristics of Sn-Based Solder Joints," Journal of Electronic Materials, Vol. 33(4), pp. 249-257, 2004.

[99] Kanchanomai, C., Mutoh, Y., "Low Cycle Fatigue Prediction Model for Pb-Free Solder 96.5Sn-3.5Ag," Journal of Electronic Materials, Vol. 33(4), 2004.

[100] Lau, J., Lee, R., Shangguan, D., "Thermal Fatigue-Life Prediction of Lead-Free Solder Joints," Proceedings of International Mechanical Engineering Congress and Exposition (IMECE04), pp. 1-6, 2004.

[101] Pang, J. H. L., Xiong, B. S., Low, T. H., "Creep and Fatigue Characterization of Lead Free 95.5Sn-3.8Ag-0.7Cu Solder," Proceedings of the 54th IEEE Electronic Components and Technology Conference, pp. 1333-1337, 2004.

[102] Li, G. Y., Chan, Y. C., "Aging Effects on Shear Fatigue Life and Shear Strength of Soldered Thick Film Joints," IEEE Transaction on Components, Packaging and Manufacturing Technology-Part B, Vol. 21(4), 1998.

[103] Bansal, A., Lee, T. K., Liu, K. C., Xue, J., "Effects of Isothermal Aging and In-Situ Current Stress on The Reliability of Lead-Free Solder Joints," Proceedings of the 60th Electronic Components and Technology Conference, pp. 1529-1535, 2010.

[104] Venkatadri, V., Liang, Y., Yan, X., Cotts, E., Srihari, K., Borgesen, P., "Accelerating The Effects of Aging on The Reliability of Lead Free Solder Joints in a Quantitative Fashion," Proceedings of the 59th Electronic Components and Technology Conference, pp. 398-405, 2009.

[105] Mustafa, M., Cai, Z. J., Suhling, J. C., Lall, P., "The Effects of Aging on The cyclic Stress-Strain Behavior And Hysteresis Loop Evolution of Lead Free Solders," Proceedings of the 61th Electronic Components and Technology Conference, pp. 927-939, 2011.

[106] Mustafa M, Roberts J. C., Suhling J. C., Lall P., "The Effects of Aging on the Cyclic Stress-Strain and Fatigue Behaviors of Lead Free Solders," Proceedings of InterPACK 2013, Burlingame, CA, pp. 1-12, 2013.

[107] Mustafa, M., Roberts, J.C., Suhling, J.C., Lall, P., "Effects of Aging on Shear Cyclic Stress-strain and Fatigue Behavior of Lead-free Solder Joints," Proceedings of ITherm, pp. 142-151, Orlando, FL, May 27-30, 2014.

[108] Mustafa M., Roberts, R. C., Suhling J., Lall P., "The Effects of Aging on the Fatigue Life of Lead-free Solders," 64th Electronic Components and Technology Conference (ECTC), pp 666-683, Orlando, FL, May 27-30, 2014.

[109] Hsuan, T. C., Lin, K. L., "Effects of Aging Treatment of Mechanical Properties and Microstructure of Sn-8.5Zn-0.5Ag-0.01Al-0.1Ga Solder," Materials Science and Engineering, A, Vol. 456, pp. 202-209, 2007.

[110] Chuang, C. M., Liu, T. S., Chen, L. H., "Effect of Aluminum Addition on Tensile Properties of Naturally Aged Sn-9Zn Eutectic Solder," Journal of Materials Science, Vol. 37(1), pp. 191-195, 2002.

[111] Ding, Y., Wang, C., Tian, Y., and Li, M., "Influence of Aging on Deformation Behavior of 96.5Sn3.5Ag Lead Free Solder Alloy During In Situ Tensile Tests," Journal of Alloys and Compounds, Vol. 428, pp. 274-285, 2007.

[112] Darveaux, R., "Shear Deformation of Lead Free Solder Joints," Proceedings of the 55th Electronic Components and Technology Conference, pp. 882-893, 2005.

[113] Wiese, S., Wolter, K. J., "Creep of Thermally Aged SnAgCu Solder Joints," Microelectronics Reliability, Vol. 47, pp. 223-232, 2007.

[114] Dutta, I., Pan, D., Marks, R. A., Jadhav, S. G., "Effect of Thermo-mechanically Induced Microstructural Coarsening on the Evolution of Creep Response of SnAg-based Microelectronic Solders," Materials Science and Engineering A, Vol. 410-411, pp. 48-52, 2005.

[115] Zhang, Q., Dasgupta, A., Haswell, P., "Partitioned Viscoelastic Constitutive Properties of the Pb-Free Sn3.9-Ag0.6-Cu Solder," Journal of Electronic Materials, Vol. 33(11), pp.1338-1349, 2004.

[116] Haythornthwaite, R. M., "A More Rational Approach to Strain-hardening Data," Engineering Plasticity, pp. 201-218, Cambridge University Press, 1968.

[117] Phillips, A., Introduction to Plasticity, New York, Ronald Press, 1956.

[118] Johnson, G. R., Cook, W. H., "A Constitutive Model and Data for Metals Subjected to Large Strains, High Strain Rates and High Temperatures," Proceedings of the Seventh International Symposium on Ballistic, pp. 541-547, 1983.

[119] Zerilli, F. J., Armstrong, R. W., "Dislocation-Mechanics-Based Constitutive Relations for Material Dynamics Calculations," Journal of Applied Physics, Vol. 61(5), pp. 1816-1825, 1987.

[120] Bodner, S. R., Partom Y., "Constitutive Equations for Elastic-Viscoplastic Strain-Hardening Materials," Journal of Applied Mechanics, pp. 385-389, 1975.

[121] Khan, A.S., Huang, S., "Experimental and Theoretical Study of Mechanical Behavior of 1100 Aluminum in the Strain Rate Range 10^{-5}-10^{4}," International Journal of Plasticity, Vol. 8, pp. 397-424, 1992.

[122] Anand, L., "Constitutive Equations for Hot Working of Metals," Journal of Plasticity, Vol. 1, pp. 213–231, 1985.

[123] Mises, R., "Mechanik Der Festin Körper Im Plastisch Deformation Zustand," Gottingen Nachrichten, Math. Phys., Vol. 4(1), pp. 582-592, 1928.

[124] Prandtl, L., "Ein Gadenkenmodell Zur Kinetischen Theorie Der Festen Körper, ZAMM, Vol. 8, pp. 85-106, 1923.

[125] Ilyshim, A. A., "On the Theory of Small Elastic-Plastic Deformations (in Russian), Prikl. Mat. Mekh., Vol. 10(3), pp. 347-356, 1946.

[126] Ludwik, P., "Elemente Der Technologischen Mechanik," Berlin, Springer, 1909.

[127] Swift, H. W., "Plastic Instability under Plane Stress," Journal of Mechanics and Physics of Solids, Vol. 1(1), pp. 1-18, 1952.

[128] Ramberg, W., Osgood, W., "Description of Stress-Strain Curves by Three Parameters," National Advisory Committee for Aeronautics, No. 902, pp. 1-27, 1943.

[129] Szuwalski, K., Życzkowski, M., "On the Phenomenon of Decohesion in Perfect Plasticity, International Journal of Solids and Structures, Vol. 9(1), pp. 85-98, 1973.

[130] Betten, J., "Bemerkungen Zum Versuch von Hohenemser," ZAMM, Vol. 55, pp. 149-158, 1975.

[131] McDowell, D. L., "Description of Nonproportional Cyclic Ratcheting Behavior," European Journal of Mechanics, A/Solids, Vol. 13, pp. 593–604, 1994.

[132] Anderson, O. and Berkyto, E., "Some Factors Affecting the Stress Strain Characteristics of Paper," Svensk Papperstidning, Vol. 54(13), pp. 437-444, 1951.

[133] Suhling, J. C., Constitutive Relations and Failure Predictions for Nonlinear Orthotropic Media, Ph.D Dissertation, University of Wisconsin – Madison, 1985.

[134] Kujawski, D., "A Fatigue Criterion Based on Strain Energy Density," Theoretical and Applied Mechanics, Vol. 7(1), pp. 15-22, 1989.

[135] Feltner, C., E., Morrow, J. D., "Microplastic Strain Hysteresis Energy as a Criterion for Fatigue Fracture," Journal of Basic Engineering ASSME, pp. 15-22, 1961.

[136] Lin, H., Multiaxial Plasticity and Fatigue Life Predictions of Anisotropic AL-6061-T6, Ph.D. Dissertation, Northeastern University, Boston, MA, 1993.

[137] Lin, X., Haicheng, G., "Plastic Energy Dissipation Model for Lifetime Prediction of Zirconium and Zircaloy-4 Fatigued at RT and 400 C," Journal of Engineering Materials and Technology, Vol. 120, pp. 114-118, 1998.

[138] Gołoś, K., "Plastic Strain Energy Under Cyclic Multiaxial States of Stress," Mechanika Teoretyczna i Stosowana, Vol. 26 (1), pp. 171-177, 1988.

[139] Kaleta, J., "Doświadczalne Podstawy Formułowania energetycznych hipotez zmęczeniowuch, Oficyna Wydawnicza Politechniki Wrocławskiej, 1998.

[140] Mroziński, S., Topoliński, T., "New Energy Model of Fatigue Damage Accumulation and Its Verification for 45-Steel, Journal of Theoretical and Applied Mechanics, Vol. 37(2), pp. 223-240, 1999.

[141] Ellyin, F., "A Criterion For Fatigue Under Multiaxial Fatigue Failure," Biaxial and Multiaxial Fatigue, EGF3, K. J. Miller and M. W. Brown, Editors, MEP, London, pp. 571-583, 1989.

[142] Gołoś, K., "Trwałość Zmęczeniowa Stali w Ujęciu Energetyczym," Prace Naukowe, Mechanika, z. 123, Politechnika Warszawska, 1989.

[143] Gołoś, K., Ellyin, F., "A Total Strain Energy Theory for Cumulative Fatigue Damage," Journal of Pressure Vessel Technology, Vol. 110, pp. 35-41, 1988.

[144] Łagoda, T., "Energetyczne Modele Trwałości Zmęczeniowej Materiałow konstrukcyjnych w Warunkach Jednoosiowych i Wieloosiowych Obciążeń Losowych," Studia I Monografie Politechniki Opolskiej, z. 121, Opole, 2001.

[145] Smith, K. N., Watson, P., Topper, T. H., "A Stress-strain Function for the Fatigue of Metals," Journal of Materials, Vol. 5, pp. 767-776, 1970.

[146] Zhang, Y., The Effects of Aging on the Mechanical Behavior of Lead Free and Mixed Formulation of Solder Alloys, Ph.D. Dissertation, Auburn University, Auburn, AL, 2010.

[147] Ma, H., Characterization of Lead-Free Solders for Electronic Packaging, Ph.D. Dissertation, Auburn University, Auburn, AL, 2007.

[148] Cai, Z., Zhang, Y., Suhling, J.C., Lall, P., Johnson, R.W., Bozack, M.J., "Reduction of Lead Free Solder Aging Effects using Doped SAC Alloys," Proceedings of the 60th Electronic Components and Technology Conference, pp. 1493-1511, 2010.

[149] Kariya, Y., Hosoi, T., Kimura, T., Terashima, S., Tanaka, M., "Low Cycle Fatigue Properties of Ni added Low Silver Content Sn-Ag-Cu Chip Interconnects," Materials Transactions, Vol. 45(3), pp. 689-694, 2004.

[150] Ritchie, R. O., "Mechanisms Fatigue-Crack Propagation in Ductile and Brittle Solids," International Journal of Fracture, Vol. 100, pp. 55-83, 1999.

[151] Stephens, R. I., Metal Fatigue in Engineering, John Wiley and Sons Inc., 2001.

[152] Manson, S. S., Thermal Stress and Low Cycle Fatigue, McGraw-Hill, 1966.

[153] Morrow, J. D., "Cycle Plastic Strain Energy and Fatigue of Metals," STP 378, ASTM, pp. 45-87, 1964.

[154] Englemaier, W., "Effects of Power Cycling on Leadless Chip Carrier Mounting Reliability and Technology," Proceedings of International Electronics Packaging Conference (IEPS), San Diego, CA, pp. 15-20, 1982.

[155] Englemaier, W. and Attarwala, A. I., "Surface-Mount Attachment Reliability of Clip-Leaded Ceramic Chip Carriers on FR-4 Circuit Boards," IEEE Transactions of Components, Hybrids and Manufacturing Technology, Vol. 12(2), pp. 284-296, 1989.

[156] Wild, R. N., "Some Fatigue Properties of Solders and Solder Joints," IBM Technical Report 73Z000421, 1973.

[157] Solomon, H. D., "Low Cycle Fatigue of 60/40 Solder Plastic Strain Limited vs. Displacement Limited Testing," Electronic Packaging: Materials and Processes, J. A. Sartell, Editor, ASM, pp. 29-47, 1985.

[158] Englemaier, W., "BGA and CGA Solder Attachments: Results of Low-Acceleration Test and Analysis," Proceedings of Surface Mount International Conference, San Jose, CA, pp. 344-358, 1995.

[159] Englemaier, W., "Surface Mount Solder Joint Reliability: Issues Design, Testing, Prediction" Workshop Notes, Englemaier Associates, Inc., Mendham, NJ, 1995.

[160] Englemaier, W., "Functional Cycles and Surface Mounting Attachment Reliability," Surface Mount Technology, ISHM Technical Monograph Series 6984-002, pp. 87-98, 1984.

[161] Englemaier, W., "Performance Considerations: Thermal-Mechanical Effects," Section 6: Soldering and Mounting Technology, Electronic Materials Handbook, Vol. 1, ASM International, pp. 740-753, 1989.

[162] Englemaier, W., "Reliability for Surface Mount Solder Joints: Physics and Statistics of Failure," Proceedings Surface Mount International Conference, Vol. 1, pp. 433-443, 1992.

[163] Englemaier, W., "Long-Term Reliability Requirement And Their Assurance For Surface Mount Solder Joints For U.S. Air Force (AVIP) Avionics," Proceedings of 18th Annual Electronics Manufacturing Seminar, pp. 151-165, 1994.

[164] Englemaier, W., "Solder Joint Reliability, Accelerated Testing and Result Evaluation," Solder Joint Reliability: Theory and Applications, John Lau, Editor, Van Nostrand Reinhold, New York, 1990.

[165] Akay, H., Zhang, H., Paydar, N., "Experimental Correlations of an Energy-based Fatigue Life Prediction Method for Solder Joints," Proceedings of InterPACK 1997, Vol. 2, pp. 1567-1674, 1997.

[166] Wu, S. X., Chin, J., Grigorich, T., Wu, X., Mui, G., Yeh, C., "Reliability Analysis for Fine Pitch BGA Packaging," Proceedings of Electronic Components and Technology Conference, pp. 737-741, 1998.

[167] Syed, A., "Accumulated Creep Strain and Energy Density Based Thermal Fatigue Life Prediction Models for SnAgCu Solder Joints," Proceedings of Electronic Components and Technology Conference, pp. 737-746, 2004.

[168] Jung, W., Lau, J. H., Pao, Y. H., "Non-linear Analysis of Full-Matrix and Perimeter Plastic Ball Grid Array Solder Joints," Journal of Electronic Packaging, Vol. 119, pp. 163-170, 1997.

[169] Dudek, R., Walter, H., Doering, R., Michel, B., "Thermal Fatigue Modelling for SnAgCu and SnPb Solder Joints," Proceedings of EuroSimE, pp.557-564, 2004.

[170] Pang, J. H. L., Che, F., "Isothermal Cyclic Bend Fatigue Test Method for Lead Free Solder Joints," Proceedings of ITherm 2006, pp. 1011-1017, 2006.

[171] Chi, F. X., Pang, H. L. J., Zhu, W. H., Sun, A. Y. S., "Cyclic Bend Fatigue Reliability Investigation for Sn-Ag-Cu Solder Joints," Proceedings of Electronic Packaging Technology Conference, pp. 313-317, 2006.

[172] Cortez, R., Cutiongco, E. C., Fine, M. E., "Correlation of Uniaxial Tension-Tension, Torsion, and Multiaxial Tension-Torsion Fatigue Failure in a 63Sn-37Pb Solder Alloy," Proceedings of the Electronic Components and Technology Conference, pp. 354-359, 1992.

[173] Kariya, Y., Otsuka, M., "Mechanical Fatigue Characteristics Sn-3.5Ag-X (X=Bi, Cu, Zn and In) Solder Alloys," Journal of Electronic Materials, Vol. 27(11), pp. 1229-1235, 1998.

[174] Pang, J. H. L., Xiong, B. S., Low, T. H., "Low Cycle Fatigue of Lead-free 99.3Sn-0.7Cu Solder Alloy," International Journal of Fatigue, Vo. 26, pp. 865-872, 2004.

[175] Kanchanomai, C., Miyashita, Y., Mutoh, Y., "Low Cycle Fatigue Behavior of Sn-Ag, Sn-Ag-Cu and Sn-Ag-Cu-Bi Lead Free Solders," Journal of Electronic Materials, Vol. 31(5), pp. 456-465, 2002.

[176] Park, S. T. and Lee, S. B., "Low Cycle Fatigue Testing of Ball Grid Array Solder Joints under Mixed-Mode Loading Conditions," Journal of Electronic Packaging, Vol. 125, pp. 237-244, 2005.

[177] Coffin, L. F., "A Study of the Effects of Cyclic Thermal Stresses on Ductile Metal," ASME Transactions, Vol. 76, pp. 931-950, 1954.

[178] Manson, S. S., "Fatigue: A Complex Subject – Some SPL Approximations," Experimental Mechanics, Vol. 5, pp. 193-226, 1965.

[179] Kariya Y., Niimi T., Otsuka M., "Isothermal Fatigue Properties of Sn-Ag-Cu Alloy Evaluated by Micro Size Specimen," Materials Transactions, Vol. 46(11), pp. 2309-2315, 2005.

[180] Kariya, Y. and Plumbridge, W. J., "Mechanical properties of Sn-3.0mass%Ag-0.5mass%Cu alloy", Proceedings of the 7th Symposium on Microjoining and Assembly Technology in Electronics, pp. 383-388, 2001.

[181] Kariya, Y., Hirata, Y., Otksuka, M., "Effects of Thermal Cycles on the Mechanical Strength of Quad Flat Packleads/Sn-3.5Ag-X (X= Bi and Cu) Solder Joints," Journal of Electronic Materials, Vol. 28, pp. 1262-1269, 1999.

[182] Terashima, S., Kariya, Y., Hosoi, T., Tanaka, M., "Effect of Silver Content on Thermal Fatigue Life of Sn-xAg-0.5Cu Flip-Chip Interconnects," Journal of Electronic Materials, Vol. 32(12), pp. 1527-1533, 2003.

[183] Abtew, M., Coyle, R., Kinyanjui, R., "Solder Joint Reliability of Pb-free Tin-Silver-Copper Ceramic Ball Grid Array (CBGA) Packages as a Function of Cooling Rate and Silver Content," Proceedings of the SMTAI, pp. 1-10, 2011.

[184] Kim, D., Filho, J. M. D., Park, C., Mawer, A., Moon, T. J., Masada, G. Y., "Crack Length Analysis of SnPb and SnAg Solder Joints in Plastic Ball Grid Array Packages from Dye Penetration Studies," Proceedings of the Electronic Components and Technology Conference, pp. 1746-1753, 2003.

[185] Unal, O., Barnard, D. J., Anderson, I. E., "A Shear Test Method to Measure Shear Strength of Metallic Materials and Solder Joints Using Small Specimens," Scripta Materialia, Vol. 40(3), pp. 271-276, 1999.

[186] Cook, B. A., Anderson, I. E., Harringa, J. L., Terpstra, R. L., Foley, J. C., and Laabs, F. C., "Shear Deformation in Sn-3.5Ag and Sn-3.6 Ag-1.0Cu Solder Joints Subjected to Asymmetric Four Point Bend Tests," Journal of Electronic Materials, Vol. 30(9), pp. 1214-1221, 2001.

[187] Zhang, Q., Dasgupta, A., Haswell, P., "Partitioned Viscoplastic-Constitutive Properties of the Pb-Free Sn3.9Ag0.6Cu Solder," Journal of Electronic Materials, Vol. 33(11), pp. 1338-1349, 2004.

[188] Mukherjee, S., Dasgupta, A., "An Evaluation of a Modified Iosipescu Specimen For Measurement of Elastic-Plastic Properties of Solder Materials,", Proceedings of the ASME 2010 International Mechanical Engineering Congress and Exposition, pp. 351-356, 2010.

[189] Dirnfeld, S. F, and Ramon, J. J., "Microstructure Investigation of Copper–Tin Intermetallics and the Influence of Layer Thickness on Shear Strength," Welding Journal, pp. 373-377, 1990.

[190] Vianco, P. T. and Rejent J. A. "Properties of Ternary Sn–Ag–Bi Solder Alloys. Part II. Wettability and Mechanical Properties Analyses," Journal of Electronic Materials, Vol. 28(10), pp. 1138–43, 1999.

[191] Wright, C., "Effect of Solid-State Reactions Upon Solder Lap Shear Strength," IEEE Trans Parts Hybrids Package, Volume PHP-13, Issue 3, pp. 202-207, 1977.

[192] Reader, C. H., Felton, L. E., Tanzi, V. A., and Knorr, D. B., "The Effect of Aging on Microstructure, Room Temperature Deformation, and Fracture of Sn-Bi/Cu Solder Joints," Journal of Electronic Materials, vol. 23, no. 7, pp. 611–617,1994.

[193] Shieu, F. S., Chang, Z. C., Sheen, J. G., and Chen, C. F., "Microstructure and Shear Strength of a Au-In Microjoint," Intermetallics, Vol. 8, pp. 623-627, 2000.

[194] Frear, D., Grivas, D. and Morris, J. W., "Parameters Affecting Thermal Fatigue Behavior of 60Sn-40Pb Solder Joints," Journal of Electronic Materials, Vol. 18, pp. 671-680, 1989.

[195] Darveaux, R., "Shear Deformation of Lead Free Solder Joints," Proceedings of Electronic Components and Technology Conference, pp. 882-892, 2005.

[196] Iosipescu, N., "New Accurate Procedure for Single Shear Testing of Metals," Journal of Materials, Vol. 2(3), pp. 537-566, 1967.

[197] Kwon, S., Lee, Y., Han, B., "Advanced Micro Shear Testing for Solder Alloy using Direct Local Measurement," Proceedings of InterPack 2003, Paper 35325, 2003.

[198] Reinikainen, T., Ren, W., "An Optimized Shear Test Sample for Assessing Solder Deformation Properties," Proceedings of EuroSimE, 2001.

[199] Kariya, Y., Sat, K., Asari, S., Kanda, Y., "Effect of Joint Size on Low-Cycle Fatigue Properties of Sn-Ag-Cu Solder Joint," Proceedings of ITherm 2010, pp. 1-4, 2010.

[200] Lee, H., Hu, S., Hong, T., Chen, Y., "The Shear Strength and Fracture Behavior of Sn-Ag-xSb Solder Joints with Au/Ni-P/Cu UBM," Journal of Electronic Materials, Vol. 37(6), pp. 867-873, 2008.

[201] Andersson, C., Lai, Z., Liu, J., Jiang, H., Yu, Y., "Comparison of Isothermal Mechanical Fatigue Properties of Lead-free Solder Joints and Bulk Solders," Journal of Materials and Engineering A, Vol. 394, pp. 20-27, 2005.

[202] Darveaux, R., "Constitutive Relations for Tin-based Solder Joints," IEEE Transactions on Components, Hybrids and Manufacturing Technology, Vol. 15(6), pp. 1013-1024, 1992.

[203] Liang, J., Downes, S., Dariavach, N., Shangguan, D., Heinrich, S. M., "Effects of Load and Thermal Conditions on Pb-Free Solder Joint Reliability," Journal of Electronic Materials, Vol. 33(12), pp. 1507-1515, 2004.

[204] Lee, S., Kim, I., "Fatigue and Fracture Assessment for Reliability in Electronics Packaging," International Journal of Fracture, Vol. 150(1-2), pp. 91-104, 2008.

[205] Henshall, G., Sweatman, J., Coyle, R., Parker, R., Tisdale, S., Hua, F., Liu, W., Healey, R., Pandher, R. S., Daily, D., Currie, M., Nguyen, J., "iNEMI Lead-free Alloy Alternatives Project Report: Thermal Fatigue Experiments and Alloy Test Requirements," Proceedings of SMTAI, pp. 317-324, 2009.

[206] Tamin, M. N., Liew, Y. B., "Numerical Modeling of Cyclic Stress-strain Behavior of Sn-Pb Solder Joint During Thermal Fatigue," National Seminar on Computational and Experimental Mechanics (CEM), pp. 351-360, 2005.

[207] The Engineering Tool Box, Coefficients of Linear Thermal Expansion, http://www.engineeringtoolbox.com/linear-expansion-coefficients-d_95.html, 2013.

[208] Haswell, P., Durability Assessment and Microstructural Observations of Selected Solder Alloys, Ph.D. Dissertation, University of Maryland College Park, MD, 2001.

[209] Ma, H., and Suhling, J. C., "A Review of Mechanical Properties of Lead-Free Solders for Electronic Packaging," Journal of Materials Science, Vol. 44, pp. 1141-1158, 2009.

[210] Prasad, S., Carson, F., Kim, G. S., Lee, J. S., Roubaud, P., Henshall, G., Kundar, S., Garcia, A., Herber, R., Bulwith., R., "Board Level Reliability of Lead-Free Packages," Proceedings of SMTAI, pp. 272-276, 2000.

[211] Bansal, A., Lee, T., Liu, K., Jie, X., "Effects of Isothermal Aging and In-Situ Current Stress on the Reliability of Lead-Free Solder Joints," Proceedings of the Electronic Components and Technology Conference, pp. 1529-1535, 2010.

[212] Pang, J. H. L., Xiong, B. S., Neo, C. C., Zhang, X. R., and Low, T. H., "Bulk Solder and Solder Properties for Lead Free 95.5Sn-3.8Ag-0.7Cu Solder Alloy," Proceedings of Electronic Components and Technology Conference, pp. 673-679, 2003.

[213] Pang, J. H. L., Low, T. H., Xiong, B. S., Xu, L., Neo, C. C., "Thermal Cycling Aging Effects on Sn–Ag–Cu solder Joint Microstructure, IMC and Strength," Thin Solid Films, Vol. 462-463, pp. 370-375, 2004.

[214] Zhang, Q., Dasgupta, A., and Haswell, P., "Isothermal Mechanical Durability of Three Selected PB-Free Solders: Sn3.9Ag0.6Cu, Sn3.5Ag, and Sn0.7Cu," Journal of Electronic Packaging, Vol. 127, pp. 512-522, 2005.

[215] Snugovsky, L., Perovic, D. D., and Rutter, J. W., "Experiments on the Aging of Sn-Ag-Cu Solder Alloys," Powder Metallurgy, Vol. 48, pp. 193-198, 2005.

[216] Darveaux, R., and Reichman, C., "Mechanical Properties of Lead-Free Solders," Proceedings of the Electronic Components and Technology Conference, pp. 695-706, 2007.

[217] Lee, S. W. R., Tsui, Y. K., Huang, X., Yan, C. C., "Effects of Room Temperature Storage Time on the Shear Strength of PBGA Solder Balls," Proceedings of the 2002 ASME International Mechanical Engineering Congress and Exposition, pp. 1-4, 2002.

[218] Coyle, R. J., Solan, P. P., Serafino, A. J., Gahr, S. A., "The Influence of Room Temperature Aging on Ball Shear Strength and Microstructure of Area Array Solder Balls," Proceedings of the Electronic Components and Technology Conference, pp. 160-169, 2002.

[219] Solomon, H. D., "Fatigue of 60/40 Solder," IEEE Transaction on Components, Hybrids and Manufacturing Technology, Vol. CHMT-9(9), pp. 423-432, 1986.

[220] Stowell, E. Z., "Stress and Strain Concentration at a Circular Hole in an Infinite Plate," NACA TN 2073, National Advisory Committee for Aeronautics, 1956.

[221] Gonyea, D.C., "Method for Low Cycle Fatigue Design Including Biaxial Stress and Notch Effects," Fatigue at Elevated Temperatures, STP 520, ASTM, pp. 678-687, 1973.

[222] Pang, J. H. L, Tan, T., Sitaraman, S. K., "Thermo-<echanical Analysis of Solder Joint Fatigue and Creep in a Flip Chip on Board Package Subjected to Temperature Cycling Loading," Proceedings of the Electronic Components and Technology Conference, pp. 878-883, 1998.

[223] Knecht, S., Fox, L., "Intergrated Matrix Creep: Application to Accelerated Testing and Lifetime Prediction," Solder Joint Reliability Theory and Applications, Edited by J. Lau, Van Nostrand Reinhold, pp. 508-544, 1991.

[224] Syed, A. R., "Factors Affecting Creep-fatigue Interaction in Eutectic Sn/Pb Solder Joints," Proceedings of InterPACK 1997, Vol. 2, pp. 1535-1542, 1997.

[225] Syed, A. R., "Thermal Fatigue Reliability Enhancement of Plastic Ball Grid Array (PBGA) Packages," Proceedings of Electronic Components and Technology Conference, pp. 1211-1216, 1996.

[226] Syed, A., Panczak, T., Darveaux, R., Lee, S., Lee, C., Partridge, J., "Solder Joint Reliability of Chip Array BGA," Proceedings of SMTA, Pan Pacific Microelectronics Symposium, pp. 1-10, 1998.

[227] Gustafasson, G., "Solder Joint Reliability of a Lead-less RF-Transistor," Proceedings of Electronic Components and Technology Conference, pp. 87-91, 1998.

[228] Pan, T., "Critical Accumulated Strain Energy (CASE) Failure Criterion for Thermal Cyclic Fatigue of Solder Joints," Journal of Electronic Packaging, Transactions of the ASME, Vol. 116 (8), pp. 163-170, 1998.

[229] Stolkarts, V., Moran, B., Keer, L. M., "Constitutive and Damage Model for Solders," Proceedings of the Electronic Components and Technology Conference, pp. 379-385, 1998.

[230] Solomon, H. D., "Predicting Thermal and Mechanical Fatigue Lives from Isothermal Low Cycle Data," Solder Joint Reliability – Theory and Applications, Edited by Lau, J. H., pp. 406-454, 1991.

[231] Chen, H. T., Mattila, T., Li, J., Liu, X. W., Li, M. Y., Kivilahti, J. K., "Localized Recrystallization and Cracking Behavior of Lead-free Solder Interconnections Under Thermal Cycling," Proceedings of International Conference on Electronic Packaging Technology & High Density Packaging (ICEPT-HDP), pp. 562-568, 2009.

[232] Mattila, T. T., Vuorinen, V., Kivilahti, J. K., "Impact of Printed Wiring Board Coatings on the Reliability of Lead-free Chip-scale Package Interconnections," Journal of Materials Research, Vol. 19(11), pp. 3214-3223, 2004.

[233] Senkov, O., Myshlyaev, M., "Grain Growth in a Superplastic Zn-22%Al Alloy," Acta Metallurgica, Vol. 34(1), pp. 97-106, 1986.

[234] Hillert, M., "On the Theory of Normal and Abnormal Grain Growth," Acta Metallurgica, Vol. 13, pp. 227-238, 1965.

[235] Martin, J. W., Doherty, R. D., Stability of Microstructure in Metallic Systems, pp. 173-221, Cambridge University Press, 1976.

[236] Lifshitz, I. M., Sliyozov, V. V., "The Kinetics of Precipitation from Supersaturated Solid Solutions," Journal of the Physics and Chemistry of Solids, Vol. 19, pp. 35-50, 1961.

[237] Ardell, A. J., "The Effect of Volume Fraction on Particle Coarsening: Theoretical Considerations," Acta Metallurgica, Vol. 20, pp. 61-70, 1972.

[238] Speight, M. V., "Growth Kinetics of Grain–Boundary Precipitates," Acta Metallurgica, Vol. 16, pp. 133, 1968.

[239] Ardell, A. J., "On the Coarsening of Grain Boundary Precipitates," Acta Metallurgica, Vol. 20, pp. 601-609, 1972.

[240] Motalab, M., Mustafa, M., Suhling, J. C., Zhang, J., Evans, J., Bozack, M. J., Lall, P., "Correlation of Reliability Models Including Aging Effects with Thermal Cycling Reliability Data," Proceedings of Electronic Components and Technology Conference (ECTC), pp. 986-1004, 2013.

[241] R. Darveaux, "Effect of Simulation Methodology on Solder Joint Crack Growth Correlation," Proceedings of the Electronic Components and Technology Conference, pp. 1048-1058, 2000.

[242] Zhang, J., Thirugnanasambandam, S., Evans, J. L., Bozack, M. J., Zhang, Y., Suhling, J. C., "Correlation of Aging Effects on the Creep rate and Reliability in Lead Free Solder Joints," SMTA Journal, Vol. 25(3), pp. 19-28, 2012.

APPENDIX A

OTHER PROPOSED EMPIRICAL MODELS FOR VISCOPLASTIC STRESS-STRAIN BEHAVIOR FOR SOLDER ALLOYS

A.1 Model #1: Hyperbolic Tangent Model with Linear Term

Model:

$$\sigma = C_1 \tanh(C_2\varepsilon) + C_3 \tanh(C_4\varepsilon) + C_5 \tanh(C_6\varepsilon) + C_7\varepsilon$$

Elastic Modulus, E:

$$E = C_1C_2 + C_3C_4 + C_5C_6 + C_7$$

Ultimate Stress:

$$\sigma_u = C_1 + C_3 + C_5 \quad \text{If} \quad C_2 > C_4 > C_6$$

A.2 Model #1: Non-linear Regression Fit

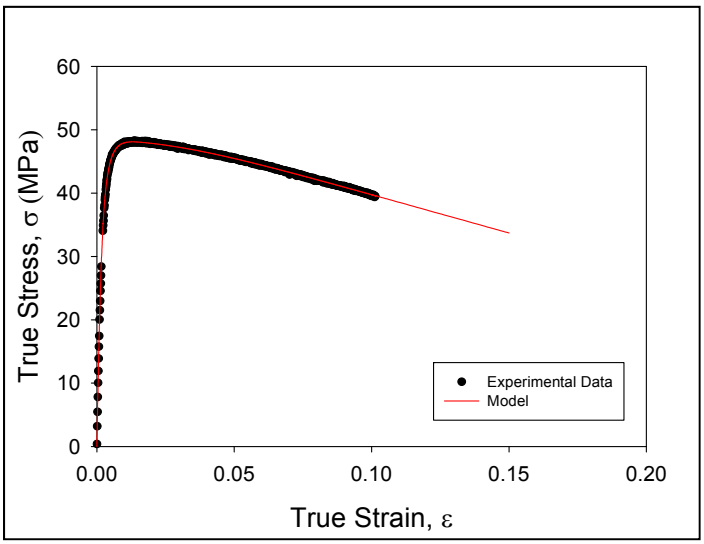

Figure A1 Non-Linear Regression Fit for Sn-Pb Solder (Sample 1)

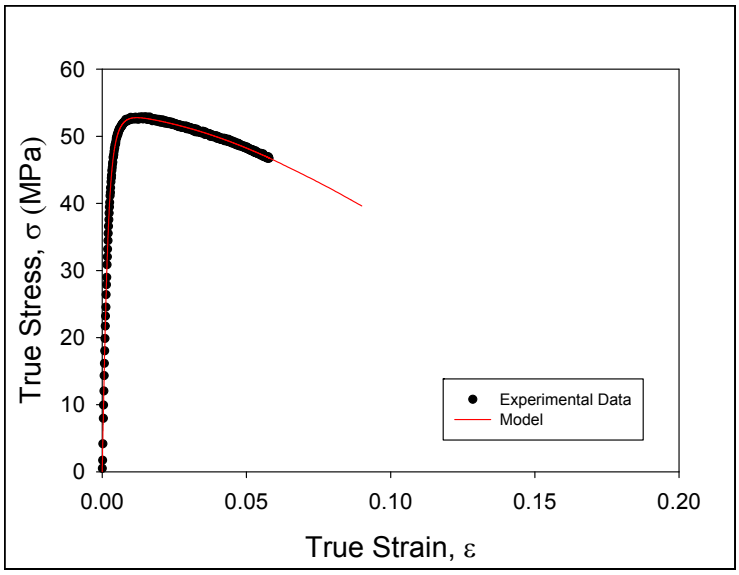

Figure A2 Non-Linear Regression Fit for Sn-Pb Solder (Sample 2)

A.3 Model #2: Polynomial Hyperbolic Tangent Model

Model:

$$\sigma = \left(C_0 + C_1\varepsilon + C_2\varepsilon^2 + C_3\varepsilon^3 + C_4\varepsilon^4\right)\tanh\left(C_5\varepsilon\right)$$

Elastic Modulus, E:

$$E = C_0 C_5$$

A.4 Model #2: Non-linear Regression Fit

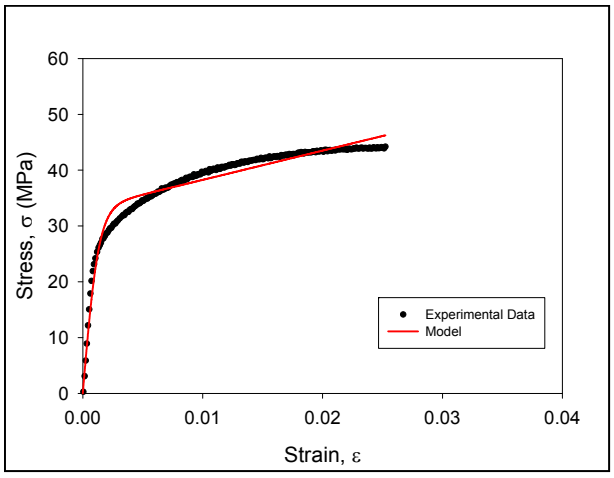

Figure A3 Non-Linear Regression Fit Using Model #2
Considering 1st Order Polynomial

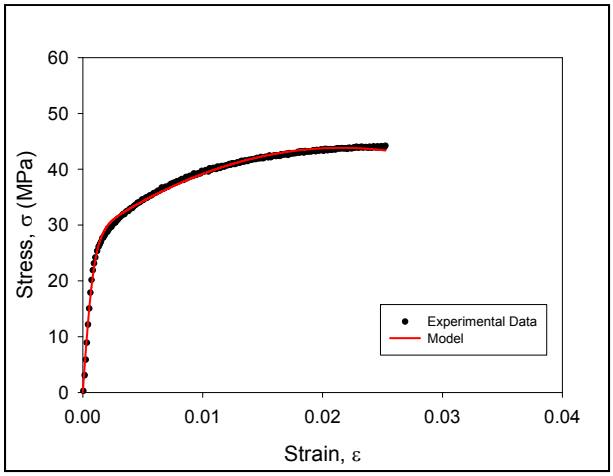

Figure A4 Model #2 Considering 2nd Order Polynomial

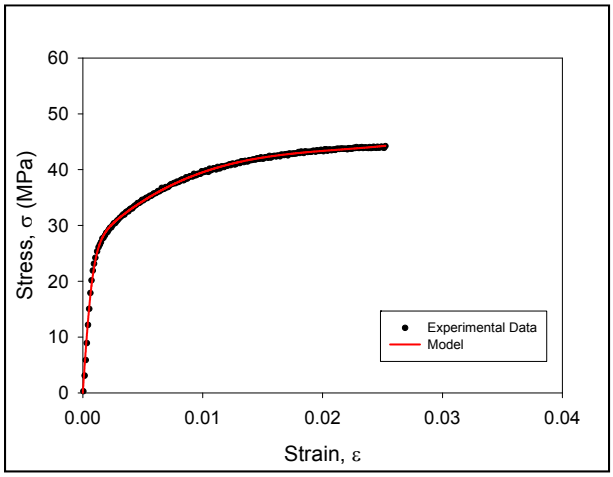

Figure A5 Model #2 Considering 3rd Order Polynomial

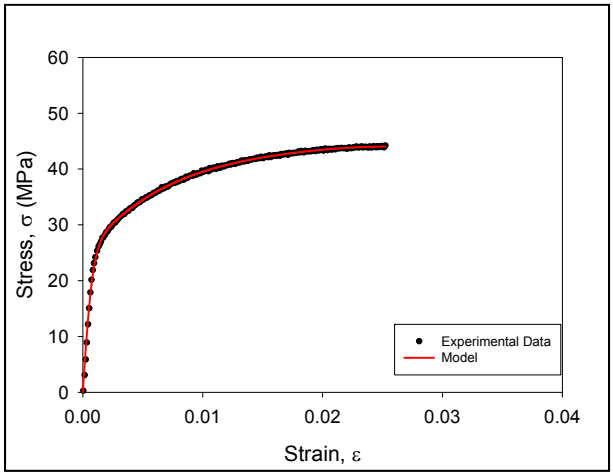

Figure A6 Model #2 Considering 4th Order Polynomial (Best Fit)

A.5 Model #2: Examples (4th Order Polynomial)

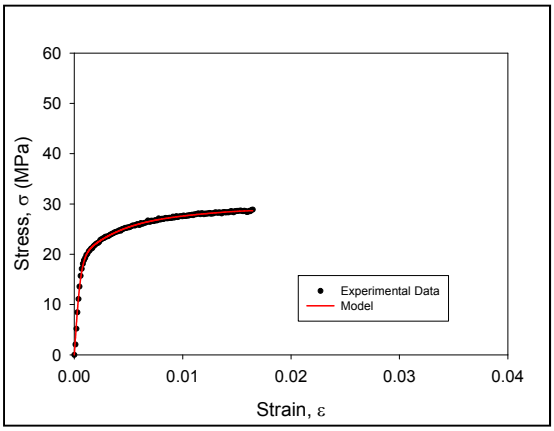

Figure A7 Non-Linear Regression Fit for SAC105 Solder Using Model #2

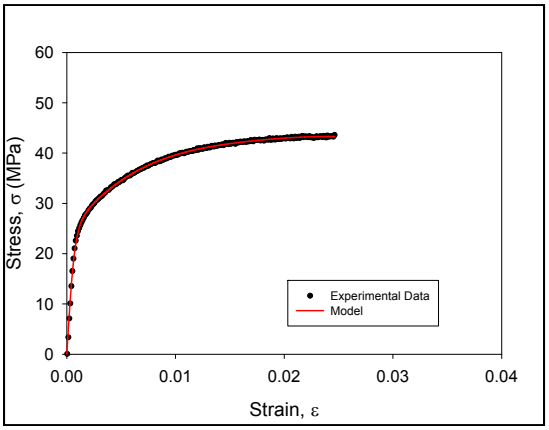

Figure A8 Non-Linear Regression Fit for SAC405 Solder Using Model #2

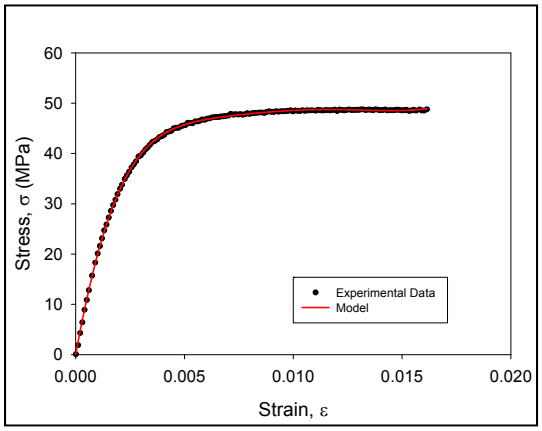

Figure A9 Non-Linear Regression Fit for Sn-Pb Solder Using Model #2

A.6 Model #2: Examples (4th Order Polynomial) for True Stress-Strain Behavior

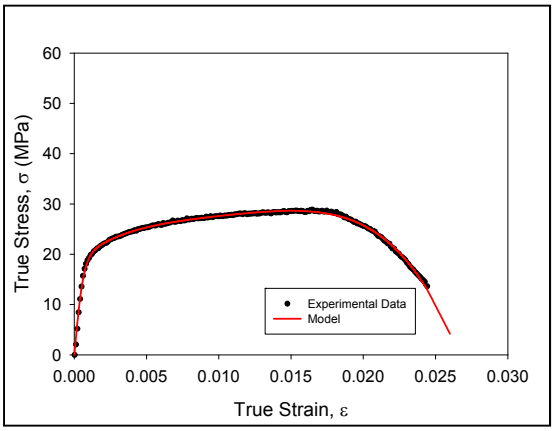

Figure A10 Non-Linear Regression Fit for SAC105 Solder Using Model #2

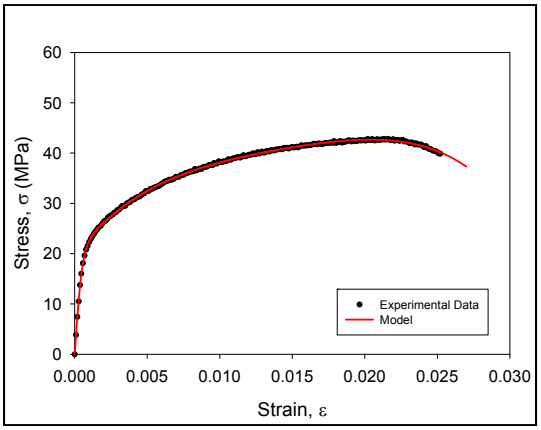

Figure A11 Non-Linear Regression Fit for SAC405 Solder Using Model #2

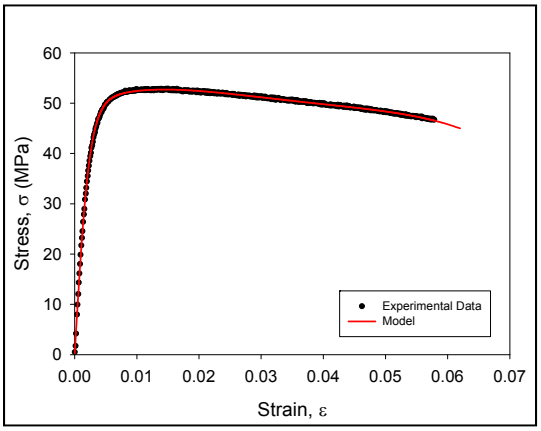

Figure A12 Non-Linear Regression Fit for Sn-Pb Solder Using Model #2

A.7 Model #3: Dual Polynomial Hyperbolic Tangent Model

Model:

$$\sigma = \left(C_0 + C_1\varepsilon + C_2\varepsilon^2\right) \tanh \left(C_3\varepsilon + C_4\varepsilon^2 + C_5\varepsilon^3\right)$$

Elastic Modulus:

$$E = C_0 C_3$$

A.8 Model #3: Non-linear Regression Fit

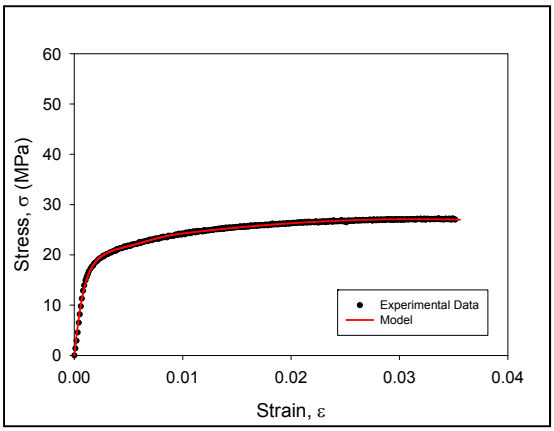

Figure A13 Non-Linear Regression Fit for SAC105 Solder Using Model #3

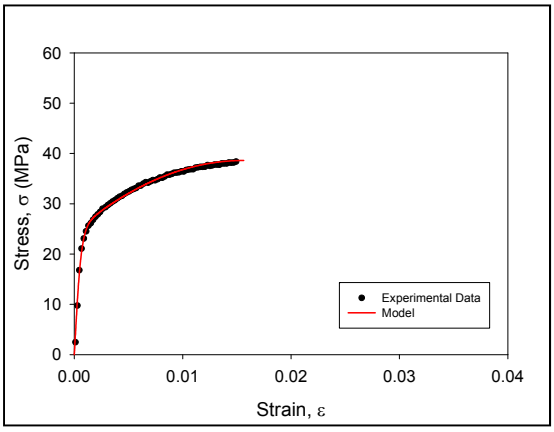

Figure A14 Non-Linear Regression Fit for SAC405 Solder Using Model #3

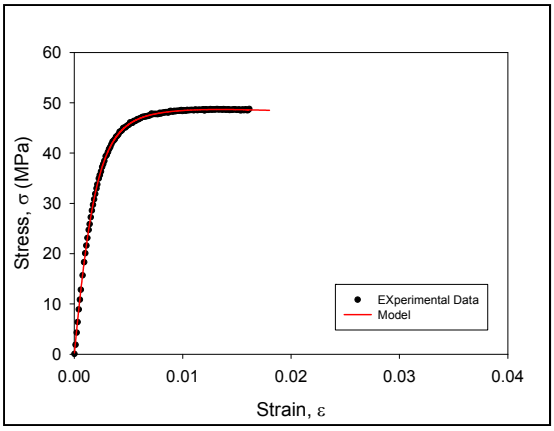

Figure A15 Non-Linear Regression Fit for Sn-Pb Solder Using Model #3

APPENDIX B

COMPUTER CODE IN MATLAB

B.1 Example Code For Calculation of Area of Hysteresis Loop

```
clear;clc;
data=[
0.038648877 0.15200544  0
1.292432308 0   1
20.53607692 1.056   1
29.02531538 2.58    1
32.31081538 4.5 1
33.39237692 6.432   1
25.82143846 7.884   1
4.877232308 6.912   1
-11.42102308    5.712   1
-21.2095    4.212   1
-26.56289231    2.376   1
-29.86199231    0.6 1
-31.63739231    -1.308  1
-30.60344615    -3.384  1
-28.69880769    -5.484  1
-26.44725385    -7.608  2
-6.196874615    -6.816  2
8.468838462 -5.508  2
17.12813077 -3.948  2
22.80123077 -2.208  2
26.86219231 -0.444  2
29.78036923 1.392   2
32.38563846 3.252   2
34.17463846 5.22    2
34.9501 7.104   2
17.46144615 7.488   2
-2.29917    6.48    2
-16.35267692    5.184   2
-24.14808462    3.492   2
-27.03905385    1.572   2
-27.08666923    -0.408  2
-25.87586154    -2.436  2
-24.63784615    -4.464  2
-23.25698462    -6.528  2
-15.12146154    -7.56   3
-0.816273077    -6.312  3
9.400746154 -4.824  3
15.50919231 -3.108  3
19.88986154 -1.356  3
23.56989231 0.456   3
```

```
26.73294615 2.292   3
29.44025385 4.104   3
32.00471538 5.964   3
29.69873846 7.872   3
7.013147692 6.864   3
-10.06736923    5.64    3
-19.77422308    4.164   3
-23.22977692    2.304   3
-23.43384615    0.324   3
-23.21616923    -1.656  3
-22.39309231    -3.648  3
-21.24351538    -5.7    3
-20.09392308    -7.752  4
-4.4827 -6.66   4
5.924783846 -5.148  4
12.30532308 -3.492  4
16.7268 -1.728  4
20.30479231 0.048   4
23.49506154 1.992   4
26.53568462 3.804   4
29.50147692 5.688   4
31.97750769 7.548   4
11.98561538 7.212   4
-6.462163077    6.036   4
-16.82883077    4.572   4
-20.42043846    2.676   4
-21.2163    0.768   4
-21.12106923    -1.236  4
-20.37962308    -3.3    4
-19.65177692    -5.316  4
-19.00556154    -7.32   4
-7.570934615    -6.984  5
3.074629231 -5.424  5
10.06736923 -3.792  5
14.41402308 -2.028  5
18.02603846 -0.24   5
21.04624615 1.608   5
24.26372308 3.408   5
27.08666923 5.328   5
29.82118462 7.236   5
11.67950769 7.2 5
-5.727517692    6.108   5
-15.57721538    4.584   5
-18.77428462    2.688   5
-19.4205    0.744   5
-19.42730769    -1.416  5
-18.74026923    -3.42   5
-18.15527692    -5.424  5
-17.81516154    -7.416  5
-6.006410769    -6.78   6
3.577997692 -5.28   6
9.890507692 -3.564  6
13.97867692 -1.824  6
17.16894615 0.108   6
20.22997692 1.908   6
23.04611538 3.732   6
25.88266154 5.616   6
```

```
28.3723 7.464   6
9.244292308 7.02    6
-6.734254615    5.796   6
-15.09425385    4.236   6
-17.67231538    2.34    6
-18.42056923    0.42    6
-18.17568462    -1.572  6
-17.87638462    -3.528  6
-17.339 -5.604  6
-17.16894615    -7.644  7
-4.407875385    -6.552  7
4.380666154 -4.968  7
9.679638462 -3.228  7
13.63176154 -1.488  7
16.51593077 0.396   7
19.52933846 2.196   7
22.4135 4.032   7
25.25005385 5.904   7
28.15462308 7.716   7
6.836289231 6.972   7
-7.815815385    5.712   7
-14.76093846    4.044   7
-16.91046154    2.088   7
-17.28458462    0.12    7
-17.36621538    -1.86   7
-17.06691538    -3.96   7
-16.80843077    -5.964  7
-14.74053077    -7.896  8
-3.224279231    -6.42   8
4.843221538 -4.848  8
10.10138462 -3.108  8
13.55013846 -1.224  8
16.30506154 0.648   8
19.04637692 2.532   8
21.89653077 4.464   8
24.40656923 6.336   8
19.81503077 7.62    8
1.265223846 6.552   8
-10.67957692    5.136   8
-15.10105385    3.3 8
-16.20982308    1.392   8
-16.61116154    -0.564  8
-16.39348462    -2.7    8
-16.20302308    -4.692  8
-15.99215385    -6.744  8
-9.713653846    -7.32   9
-0.040813662    -5.844  9
7.155995385 -4.068  9
11.16933846 -2.268  9
14.56367692 -0.24   9
17.10092308 1.608   9
19.52253846 3.468   9
22.35908462 5.316   9
25.26365385 7.2 9
9.972138462 7.008   9
-5.394206154    5.784   9
-12.81549231    4.092   9
```

```
-15.09425385    2.22    9
-15.86971538    0.204   9
-15.98535385    -1.764  9
-15.72686154    -3.78   9
-15.47517692    -5.724  9


];

strain=data(:,2);stress=data(:,1);c=data(:,3);
NN=6;
for a=1:NN
    d1=min(find(c==a));
    d2=max(find(c==a));
    ind=find(strain(d1:d2)==max(strain(d1:d2)))-1+d1;
    if length(ind)>1
        ind=ind(find(stress(ind)==max(stress(ind))));
    end

    x0=strain(d1);y0=stress(d1);
    x=strain(d1:ind-1);y=stress(d1:ind-1);

    fo_ = fitoptions('method','NonlinearLeastSquares','Lower',[0 0 0
0],'upper',[inf inf inf inf],'MaxFunEvals',5000,'MaxIter',40000000);
    ok_ = isfinite(x) & isfinite(y);
    if ~all( ok_ )
        warning( 'GenerateMFile:IgnoringNansAndInfs', ...
            'Ignoring NaNs and Infs in data' );
    end
    st_ = [1 1 1 1];
    ft_ = fittype('a*tanh(b*(x-x0))+c*tanh(d*(x-x0))+y0',...
     'dependent',{'y'},'independent',{'x'},...
     'coefficients',{'a', 'b', 'c', 'd'},...
     'problem',{'x0','y0'},'options',fo_);
    cf_ = fit(x(ok_),y(ok_),ft_,'Startpoint',st_,'problem',{x0,y0});
    if 0
         cv_ = { 33.084082879035726, 1.0879076416858526,
280.38410959158659, 0.0018144557597358562};
         cf_ = cfit(ft_,cv_{:});
    end
    cv = coeffvalues(cf_);


C1(a,1)=cv(1);C2(a,1)=cv(2);C3(a,1)=cv(3);C4(a,1)=cv(4);X0(a,1)=x0;Y0(a
,1)=y0;

    x0=strain(ind);y0=stress(ind);
    x=strain(ind:d2);y=stress(ind:d2);

    fo_ = fitoptions('method','NonlinearLeastSquares','Lower',[0 0 0
0],'upper',[inf inf inf inf],'MaxFunEvals',5000,'MaxIter',40000000);
    ok_ = isfinite(x) & isfinite(y);
    if ~all( ok_ )
        warning( 'GenerateMFile:IgnoringNansAndInfs', ...
            'Ignoring NaNs and Infs in data' );
```

```
    end
    st_ = [1 1 1 1];
    ft_ = fittype('-a*tanh(b*(-x+x0))-c*tanh(d*(-x+x0))+y0',...
     'dependent',{'y'},'independent',{'x'},...
     'coefficients',{'a', 'b', 'c', 'd'},...
     'problem',{'x0','y0'},'options',fo_);
    cf_ = fit(x(ok_),y(ok_),ft_,'Startpoint',st_,'problem',{x0,y0});
    if 0
         cv_ = { -33.084082879035726, -1.0879076416858526, -
280.38410959158659, -0.0018144557597358562};
         cf_ = cfit(ft_,cv_{:});
    end
    cv = coeffvalues(cf_);


C1(a,2)=cv(1);C2(a,2)=cv(2);C3(a,2)=cv(3);C4(a,2)=cv(4);X0(a,2)=x0;Y0(a
,2)=y0;
end
for i=1:1:NN-1;
for xi=0:0.000001:9.00

f=C1(i,1)*tanh(C2(i,1)*(xi-X0(i,1)))+C3(i,1)*tanh(C4(i,1)*(xi-
X0(i,1)))+Y0(i,1);
ff=-C1(i,2)*tanh(C2(i,2)*(-xi+X0(i,2)))-C3(i,2)*tanh(C4(i,2)*(-
xi+X0(i,2)))+Y0(i,2);
dif=abs(f-ff);
if(dif<=0.001)
    xxi(i)=xi;
end

end
end
for ii=1:1:NN-1;
for xi=-9.00:0.000001:0

f=C1(ii+1,1)*tanh(C2(ii+1,1)*(xi-
X0(ii+1,1)))+C3(ii+1,1)*tanh(C4(ii+1,1)*(xi-X0(ii+1,1)))+Y0(ii+1,1);
ff=-C1(ii,2)*tanh(C2(ii,2)*(-xi+X0(ii,2)))-C3(ii,2)*tanh(C4(ii,2)*(-
xi+X0(ii,2)))+Y0(ii,2);
dif=abs(f-ff);
if(dif<=0.001)
    xxii(ii)=xi;

end

end
end
r=1;

for i=1:NN-2
   for xi=xxi(i):-0.01:xxii(i)
       xp(i,r)=xi;
       upp(i,r)=-C1(i,2)*tanh(C2(i,2)*(-xi+X0(i,2)))-
C3(i,2)*tanh(C4(i,2)*(-xi+X0(i,2)))+Y0(i,2);
       r=r+1;
```

```
    end
    for xi=xxii(i):0.01:xxi(i+1)
        xp(i,r)=xi;
        upp(i,r)=C1(i+1,1)*tanh(C2(i+1,1)*(xi-
X0(i+1,1)))+C3(i+1,1)*tanh(C4(i+1,1)*(xi-X0(i+1,1)))+Y0(i+1,1);
        r=r+1;
    end
    r=1;

end
xxp=xp';
upx=upp';
syms x;
for i=1:NN-1
    fl=-C1(i,2)*tanh(C2(i,2)*(-x+X0(i,2)))-C3(i,2)*tanh(C4(i,2)*(-
x+X0(i,2)))+Y0(i,2);
    fu=C1(i+1,1)*tanh(C2(i+1,1)*(x-
X0(i+1,1)))+C3(i+1,1)*tanh(C4(i+1,1)*(x-X0(i+1,1)))+Y0(i+1,1);
    fll=eval(int(fl,x,xxii(i),xxi(i)));
    fuu=eval(int(fu,x,xxii(i),xxi(i)));
    ar(i)=(fuu-fll);
    arr=ar;
    area=arr';
    area=area/1000;
end
inn=1;
for xi=0:0.01:xxi(1)
in(inn)=C1(1,1)*tanh(C2(1,1)*(xi-X0(1,1)))+C3(1,1)*tanh(C4(1,1)*(xi-
X0(1,1)))+Y0(1,1);
ix(inn)=xi;
inn=inn+1;
end
im=in';
ixx=ix';
```

B.2 Example Code For Determination of Peak Cyclic Stress

```
clear;clc;
data=[
0.008780468 0.001266712 0
1.046221785 0.0002  1
2.73532121  0.0021  1
4.26988316  0.0042  1
5.7271761   0.0068  1
7.11492704  0.0092  1
9.23982318  0.0118  1
10.68320663 0.0143  1
11.9766911  0.0171  1
13.307265   0.0196  1
14.7367346  0.0219  1
15.9514088  0.0249  1
17.0378118  0.028   1
16.4474678  0.0314  1
14.9546365  0.0292  1
13.5081629  0.0271  1
11.9102338  0.0252  1
10.395766   0.0226  1
8.97401796  0.0203  1
7.54454182  0.0178  1
6.03470652  0.0158  1
4.51250844  0.0136  1
3.12321188  0.0111  1
1.72309816  0.0085  1
0.230261519 0.0064  1
-1.24866694 0.004   1
-2.56842041 0.0013  1
-3.83254137 -0.0012 1
-5.22338246 -0.0036 1
-6.56013557 -0.0063 1
-7.72071525 -0.0091 1
-8.9137475  -0.0122 1
-10.20104949    -0.0147 1
-11.8159706 -0.0185 1
-12.8312838 -0.0215 1
-13.9238671 -0.0245 1
-15.0628081 -0.0273 2
-14.4183892 -0.0312 2
-12.7385575 -0.0292 2
-11.2101813 -0.0268 2
-9.87806396 -0.0247 2
-8.36822866 -0.0222 2
-6.81048677 -0.0202 2
-5.36401208 -0.0177 2
-3.94226295 -0.0152 2
-2.60550984 -0.0126 2
-1.11112747 -0.0104 2
0.358528032 -0.0079 2
1.64119338  -0.0053 2
3.03203447  -0.003  2
4.51714312  -0.0006 2
5.88789551  0.0017  2
```

```
7.1813778   0.0045  2
8.46558855  0.0072  2
9.92288149  0.0094  2
11.2070857  0.0123  2
12.4171274  0.0149  2
13.6565228  0.0177  2
14.950004   0.0202  2
16.1631195  0.023   2
17.2464378  0.0263  2
18.2602032  0.0294  2
17.427247   0.033   2
15.4012531  0.0299  2
14.0196781  0.0277  2
12.4387639  0.0255  2
10.9381936  0.0232  2
9.53653535  0.0208  2
8.10396906  0.0183  2
6.66676591  0.016   2
5.09975139  0.0138  2
3.73054571  0.0113  2
2.35824879  0.0088  2
0.92413688  0.0064  2
-0.560972751    0.0043  2
-1.88845334 0.0016  2
-3.15566445 -0.001  2
-4.53105261 -0.0037 2
-5.97443606 -0.0058 2
-7.22464862 -0.0086 2
-8.43622613 -0.0115 2
-9.79616027 -0.0139 2
-11.1112747 -0.0165 2
-12.3058602 -0.0193 2
-13.4896111 -0.0223 2
-14.6934725 -0.0251 2
-15.8169573 -0.028  3
-15.15863   -0.0316 3
-13.4834308 -0.0297 3
-11.9365137 -0.0275 3
-10.48849012    -0.0249 3
-9.07446691 -0.0225 3
-7.59399403 -0.0204 3
-6.0470693  -0.0183 3
-4.61604754 -0.0157 3
-3.31329371 -0.0132 3
-1.87763618 -0.0108 3
-0.429615434    -0.0085 3
0.917955272 -0.0059 3
2.25316298  -0.0034 3
3.65018546  -0.001  3
5.08893423  0.0013  3
6.82748641  0.0049  3
8.13796725  0.0076  3
9.52417257  0.0099  3
10.83310888 0.0125  3
12.0895061  0.0155  3
13.2686245  0.0182  3
14.6192871  0.0205  3
```

```
15.8354982  0.0235  3
16.9188165  0.0264  3
17.9248538  0.0298  3
17.1398031  0.0331  3
15.6639649  0.0308  3
14.2329475  0.0287  3
12.7401053  0.0265  3
11.1931773  0.0242  3
9.70807301  0.0217  3
8.31723192  0.0193  3
6.40096069  0.0164  3
4.87567137  0.0141  3
3.51264708  0.0115  3
2.17743959  0.0089  3
0.761871959 0.0066  3
-0.735600561    0.0044  3
-2.02753734 0.0016  3
-3.33183788 -0.0009 3
-4.7180432  -0.0032 3
-6.55704433 -0.0065 3
-7.78253024 -0.0096 3
-9.02037893 -0.0123 3
-10.18559547    -0.0143 3
-11.2905361 -0.0164 3
-12.4573048 -0.0192 3
-13.6348863 -0.0222 3
-14.8047397 -0.025  3
-15.9483132 -0.0278 4
-15.3193505 -0.0314 4
-13.6302429 -0.0294 4
-12.064774  -0.0272 4
-10.6538453 -0.0245 4
-9.23827756 -0.0223 4
-7.7377138  -0.0202 4
-6.18924454 -0.0178 4
-4.86639983 -0.0152 4
-3.46783173 -0.013  4
-2.00744755 -0.0104 4
-0.817505668    -0.0083 4
0.338438133 -0.0064 4
1.46656448  -0.0042 4
2.53596784  -0.0021 4
4.00562356  0   4
5.37482924  0.0026  4
6.64204035  0.0054  4
7.90925146  0.0079  4
9.34490899  0.0103  4
10.69093364 0.013   4
11.9009688  0.0156  4
13.0893631  0.0185  4
14.446206   0.021   4
15.6253353  0.0239  4
16.6823737  0.027   4
16.3006666  0.0307  4
15.0442672  0.0288  4
13.4448012  0.0261  4
11.2719952  0.0237  4
```

```
9.84870263  0.0213  4
8.46404293  0.0186  4
7.00365875  0.0164  4
5.45518949  0.0143  4
4.05816592  0.0117  4
2.70441426  0.0092  4
1.32748048  0.0068  4
-0.179264016    0.0047  4
-1.50519953 0.002   4
-2.84504388 -0.0006 4
-4.16634297 -0.003  4
-5.63445307 -0.0054 4
-6.93566237 -0.008  4
-8.16423843 -0.011  4
-9.44072217 -0.0135 4
-10.83001873    -0.0158 4
-12.038505  -0.0189 4
-13.220719  -0.0216 4
-14.3581231 -0.0245 4
-15.5913273 -0.0274 5
-14.9886336 -0.0307 5
-13.3149931 -0.029  5
-11.7927863 -0.0265 5
-10.40040286    -0.0242 5
-8.94774569 -0.0216 5
-7.43636586 -0.0196 5
-5.96516452 -0.0172 5
-4.59441322 -0.0146 5
-3.25611449 -0.0121 5
-1.78336753 -0.01   5
-0.327620428    -0.0076 5
0.978225078 -0.0048 5
2.338159    -0.0023 5
3.7645439   0   5
5.17547587  0.0025  5
6.45350414  0.0053  5
7.73153241  0.0077  5
9.13937314  0.0103  5
10.45758208 0.0129  5
11.6861625  0.0156  5
12.9240101  0.0184  5
14.2159435  0.0209  5
15.4058856  0.0238  5
16.532466   0.0269  5
17.5771438  0.03    5
16.8600873  0.0333  5
15.3873447  0.0311  5
13.9223193  0.029   5
12.4217599  0.0266  5
10.86401692 0.0248  5
9.41445099  0.0221  5
8.02206428  0.0195  5
6.59567938  0.0173  5
5.04875465  0.0151  5
3.6532767   0.0125  5
2.32888637  0.0101  5
0.947317474 0.0077  5
```

```
-0.564063446    0.0053  5
-1.88381757 0.0026  5
-3.16339146 0   5
-4.52023436 -0.0023 5
-5.92343932 -0.0049 5
-7.24010155 -0.0075 5
-8.47331556 -0.0104 5
-9.75288836 -0.0127 5
-11.117455  -0.0153 5
-12.3151252 -0.0183 5
-13.455614  -0.0212 5
-14.5868378 -0.0241 5
-15.7906883 -0.0268 5
-16.8137296 -0.0302 6
-16.0271311 -0.0338 6
-14.5111155 -0.0315 6
-12.9286426 -0.0295 6
-11.3832624 -0.027  6
-10.00169503    -0.0248 6
-8.64176089 -0.0221 6
-7.11647157 -0.02   6
-5.62518044 -0.0176 6
-4.31469851 -0.015  6
-2.93158443 -0.0128 6
-1.47120134 -0.0104 6
-0.063360556    -0.0079 6
1.26721111  -0.0052 6
2.57305618  -0.0027 6
4.01180495  -0.0003 6
5.40882743  0.0023  6
6.68994694  0.0048  6
7.9324314   0.0075  6
9.29700131  0.0099  6
10.65229968 0.0125  6
11.882417   0.0153  6
13.0229167  0.0182  6
14.307122   0.0207  6
15.5511499  0.0235  6
16.5340138  0.0268  6
17.5740591  0.0299  6
16.8322705  0.0334  6
15.3054421  0.0314  6
13.8589576  0.0287  6
12.403219   0.0266  6
10.81920048 0.0245  6
9.36190754  0.022   6
7.9957931   0.0195  6
6.55240856  0.0174  6
4.9962112   0.0151  6
3.60073434  0.0124  6
2.33661338  0.01    6
0.907137676 0.0077  6
-0.562518153    0.0052  6
-1.90545298 0.0025  6
-3.22520645 0.0001  6
-4.54186977 -0.0023 6
-5.98525431 -0.0047 6
```

```
-7.25710119 -0.0077 6
-8.50731375 -0.0104 6
-9.74979821 -0.0128 6
-11.1112747 -0.0154 6
-12.2842237 -0.0184 6
-13.4401687 -0.0212 6
-14.6084743 -0.0239 6
-15.810777  -0.0269 6
-16.7998212 -0.0302 7
-16.0472198 -0.0341 7
-14.0382299 -0.0311 7
-12.4681176 -0.029  7
-10.9490173 -0.0266 7
-9.57208025 -0.0241 7
-8.1348771  -0.022  7
-6.58486113 -0.0197 7
-5.19556566 -0.0172 7
-3.85263116 -0.0148 7
-2.50660542 -0.0121 7
-1.027677288    -0.0099 7
0.353891826 -0.0072 7
1.63192075  -0.0047 7
2.94703845  -0.0021 7
4.48005478  0   7
6.2139701   0.0035  7
7.46109142  0.0064  7
8.75921057  0.009   7
10.17941408 0.0113  7
11.3848102  0.0142  7
12.6133819  0.0169  7
13.820328   0.0196  7
15.0365391  0.0225  7
16.158487   0.0255  7
17.1722524  0.0286  7
16.4088382  0.0322  7
14.933  0.0301  7
13.5097107  0.0278  7
11.916425   0.0256  7
10.38031307 0.0235  7
8.98638074  0.0208  7
7.61871959  0.0184  7
6.07797625  0.0163  7
4.6206844   0.0139  7
3.26538712  0.0112  7
1.9348154   0.0086  7
0.460523038 0.0067  7
-0.953499082    0.0043  7
-2.26707138 0.0015  7
-3.56828068 -0.0011 7
-4.93130497 -0.0036 7
-6.36078111 -0.0059 7
-7.58935826 -0.0087 7
-8.78084489 -0.0116 7
-10.14387027    -0.014  7
-11.4744409 -0.0167 7
-12.6133819 -0.0196 7
-13.7523338 -0.0224 7
```

```
-14.933 -0.0253 7
-16.0812169 -0.0284 8
-15.3950728 -0.0319 8
-13.8064196 -0.0299 8
-12.2316748 -0.0277 8
-10.75893111    -0.0252 8
-9.38817981 -0.0226 8
-7.91852409 -0.0208 8
-6.41023332 -0.0184 8
-5.01630099 -0.0157 8
-3.67954788 -0.0131 8
-2.29488818 -0.0109 8
-0.80514267 -0.0087 8
0.559427349 -0.006  8
1.86990917  -0.0033 8
3.22829769  -0.0009 8
4.6902264   0.0015  8
6.38396214  0.0051  8
7.63417361  0.0078  8
9.03428733  0.0103  8
10.37722292 0.0127  8
11.6382461  0.0155  8
12.8065626  0.0184  8
14.0691314  0.0208  8
15.2853425  0.0237  8
16.3377484  0.027   8
15.575882   0.0301  8
14.1448537  0.0279  8
12.5824804  0.026   8
10.9907425  0.0238  8
9.55817185  0.0214  8
8.1766023   0.0188  8
6.71621812  0.0164  8
5.17083901  0.0143  8
3.78308807  0.0118  8
2.43242656  0.0093  8
1.010678084 0.0071  8
-0.432706238    0.0045  8
-1.80036717 0.0021  8
-3.05985127 -0.0005 8
-4.40124015 -0.003  8
-5.89098566 -0.0054 8
-7.08092776 -0.0084 8
-8.33577609 -0.0109 8
-9.62462261 -0.0136 8
-11.0077356 -0.0159 8
-12.2069536 -0.0189 8
-13.3489902 -0.022  8
-14.5111155 -0.0246 8
-15.7118704 -0.0276 9
-14.9190916 -0.0312 9
-13.2918088 -0.029  9
-11.7557045 -0.027  9
-10.36640467    -0.0242 9
-8.90447596 -0.0218 9
-7.43482024 -0.0196 9
-5.95898313 -0.0173 9
```

```
-4.57277672 -0.0149 9
-3.26229588 -0.0123 9
-1.74473357 -0.0102 9
-0.321438929    -0.0076 9
0.981315882 -0.0051 9
2.31961483  -0.0026 9
3.75372674  -0.0003 9
5.13684082  0.0024  9
6.41950595  0.0051  9
7.67589881  0.0076  9
9.05592383  0.0099  9
10.38649555 0.0126  9
11.57798    0.0157  9
12.820471   0.0185  9
14.0768595  0.0212  9
15.2513454  0.0239  9
16.3222922  0.027   9
15.949861   0.0304  9
14.4910268  0.0289  9
13.0507335  0.0265  9
11.4327157  0.0243  9
9.94606143  0.0219  9
8.58303714  0.0195  9
7.14428837  0.0173  9
5.56336545  0.015   9
4.13852617  0.0125  9
2.80640883  0.01    9
1.40474949  0.0077  9
-0.081905107    0.0054  9
-1.42947614 0.0028  9
-2.71832266 0.0003  9
-4.06125716 -0.0025 9
-5.44591686 -0.0048 9
-6.75639879 -0.0074 9
-8.01897304 -0.0102 9
-9.30009255 -0.0128 9
-10.6538453 -0.0152 9
-11.8947885 -0.0181 9
-13.0260014 -0.0211 9
-14.1726705 -0.0239 9
-15.3857969 -0.0265 9
-16.4382028 -0.03   10
-15.9575891 -0.0339 10
-14.419937  -0.0317 10
-12.7710177 -0.0297 10
-11.3446328 -0.0274 10
-9.92133587 -0.0249 10
-8.55985611 -0.0225 10
-6.96657041 -0.0204 10
-5.5185501  -0.0179 10
-4.16479735 -0.0152 10
-2.87286068 -0.0127 10
-1.40320496 -0.0105 10
0.026271453 -0.0082 10
1.34911589  -0.0054 10
2.61787262  -0.0029 10
4.08289257  -0.0006 10
```

```
5.42428145  0.002   10
6.69767395  0.0047  10
7.99270186  0.0073  10
9.35109038  0.0098  10
10.70793328 0.0124  10
11.8978732  0.0151  10
13.0677266  0.0182  10
14.3303063  0.0208  10
15.4877882  0.0238  10
16.5216532  0.0267  10
17.496789   0.0299  10
16.6560938  0.0335  10
15.2096202  0.0313  10
13.7538816  0.0292  10
12.2780434  0.0269  10
10.72029715 0.0246  10
9.29236554  0.0222  10
7.92006971  0.0196  10
6.50450197  0.0173  10
4.90194364  0.0153  10
3.56209929  0.0125  10
2.16971258  0.01    10
0.802051866 0.0077  10
-0.676876157    0.0053  10
-2.02444719 0.0027  10
-3.26075026 0   10
-4.63768295 -0.0023 10
-6.05170507 -0.0047 10
-7.74235066 -0.0085 10
-8.93847415 -0.0112 10
-10.25822871    -0.0138 10
-11.551711  -0.0163 10
-12.7153841 -0.0192 10
-13.8404167 -0.0222 10
-14.976273  -0.0252 10
];

strain=data(:,2);stress=data(:,1);c=data(:,3);
NN=10;
for a=1:NN
    d1=min(find(c==a));
    d2=max(find(c==a));
    ind=find(stress(d1:d2)==max(stress(d1:d2)))-1+d1;
   if length(ind)>1
        ind=ind(find(strain(ind)==max(strain(ind))));
    end
    %x0=strain(d1);y0=stress(d1);
    %x=strain(d1:ind-1);y=stress(d1:ind-1);

    %X0(a,1)=x0;Y0(a,1)=y0;

    %x0=strain(ind);
    y0=stress(ind);
    %x=strain(ind:d2);
    y=stress(ind:d2);
```

```
    %X0(a,2)=x0;
    Y0(a,2)=y0;
end
```